NASA Contractor Report 172188

NASA-CR-172188
19830025620

A FUEL-EFFICIENT CRUISE PERFORMANCE MODEL FOR GENERAL AVIATION PISTON ENGINE AIRPLANES

Richard C. H. Parkinson

PRINCETON UNIVERSITY
Princeton, New Jersey

Grant NGL 31-001-252
August 1983

National Aeronautics and
Space Administration

Langley Research Center
Hampton, Virginia 23665

A FUEL-EFFICIENT

CRUISE PERFORMANCE MODEL FOR

GENERAL AVIATION PISTON ENGINE AIRPLANES

Table of Contents

CHAPTER 1

INTRODUCTION AND GUIDE FOR THE READER

Table of Contents

CHAPTER 1

INTRODUCTION AND GUIDE FOR THE READER

INTRODUCTION

Purpose and Motivation of this Study

Purpose:

The purpose of this study is to define a fuel-efficient airplane cruise performance model, suitable for airborne microprocesser implementation, which facilitates maximizing Specific Range. The study is confined to General Aviation (GA) airplanes powered by Spark-Ignition (SI) piston engines and propellers. Airplanes of fixed design only are considered; design optimization for fuel-efficient operation is not considered.

Specific Range is the ground distance the airplane flies per unit mass of fuel consumed in cruising flight. The term Cruising Flight means straight and level steady flight. Specific range defines the Point Economy (that is, the instantaneous fuel economy) of the airplane. In this study: the Specific Range of the airplane is denoted R* (ground nautical miles/lbm); and R* is referred to as the Point Economy Function.

Motivation:

This study is motivated by two conservation objectives:

1. To minimize the fuel consumption of GA airplanes.
2. To improve the safety of GA operations.

Avionics and controls, particularly the airborne microprocessor, are perceived as means to these ends.

In order to satisfy the first objective, the total fuel M_f (lbm) used on each GA airplane trip must be minimized, taking account of the design and operational constraints which may be imposed.

Each trip is characterized by a flight trajectory consisting of: a horizontal profile consisting of a number of legs between waypoints; and a vertical profile consisting of climb, cruise and descent segments. M_f is determined by R* throughout the cruise segments, by the manner in which the airplane is operated during climb and descent, and by the horizontal and vertical profiles flown.

Optimizing (minimizing) M_f involves the implementation of a rather sophisticated airborne computation/guidance/control system, utilizing fuel-efficient models of the airplane performance in cruise, climb and descent. Such a system is envisaged as being microprocessor-based, and would enable the pilot

1. To accurately compute the trip minimum fuel requirement $M_{f_{min}}$ (lbm) and the corresponding flight trajectory/control trajectories (taking account of constraints), during flight planning and during flight plan revisions enroute
2. To fly the airplane in accordance with the computed trajectories, thereby achieving the computed $M_{f_{min}}$.

This study does not address M_f optimization, but rather concentrates on developing a fuel-efficient cruise performance

model suitable for microprocessor implementation, as required by that optimization.

It may be some time before procedures and hardware for optimizing M_f for GA aircraft are developed. In the interim period, a significant reduction in M_f can be achieved by optimizing (maximizing) R* in cruise (taking account of constraints); since the majority of M_f is consumed in cruise. This study addresses such optimization of R* using the cruise performance model developed herein.

Implementation of the cruise performance model and the R* optimization procedures here developed, in an airborne microprocessor, will enable the pilot:

1. To accurately compute the operating point yielding maximum R*, with or without constraints, with little or no increase in pilot workload
2. To fly the airplane in the manner prescribed by the cruise performance model, thereby achieving the computed maximum R*.

This study therefore contributes to achieving the first conservation objective, in two ways: by developing the fuel-efficient cruise performance model required for M_f and R* optimization; and by developing computational procedures for optimizing R* using this cruise performance model.

Fuel exhaustion and fuel mismanagement together are a major cause of GA accidents. An M_f optimization system implemented in GA airplanes will be a powerful tool for reducing the number of

fuel exhaustion related accidents. The simpler microprocessor system incorporating R* optimization advocated herein can contribute to reducing the number of fuel exhaustion related accidents: using this system

1. The destination fuel reserve expected can be approximately computed during flight planning and at any time enroute, from
   a) Fuel onboard
   b) R* computations for various stages of the trip
   c) Climb and descent fuel requirements (these are not addressed by this system)
2. The flight plan can be modified as necessary to ensure an adequate destination fuel reserve.

This study therefore contributes to achieving the second conservation objective.

Inclusion of a fuel quantity monitoring/warning/tank-switching system in any airborne microprocessor system could greatly reduce the number of fuel mismanagement related accidents.

The Point Economy Function R*

Properties of the atmosphere, airframe, propeller and engine all contribute to the value of R*. Fundamentals of R* are discussed in Appendix A. From Equations A.3, A.7 and A.8,

$$R^* = \frac{V_T + V_w}{E\dot{m}_f} \text{ ground nautical miles/lbm} \qquad (1.1)$$

$$= \frac{V_T + V_w}{E\dot{m}_f c} \qquad (1.2)$$

where

c = engine brake specific fuel consumption, lbm/BHP.hr

E = number of engines, each driving one propeller

$\dot{m}_f$ = fuel mass flow rate per engine, lbm/hr

P_E = brake horsepower per engine

V_T = airplane true airspeed, knots

V_w = geocentric true windspeed along track, knots.

R* is determined by many parameters, both design and operational: design parameters define the design of the airplane; while operational parameters are those which characterize the environment and operation of the airplane. The parameters contributing to the value of R* through each of the variables on the right hand side of Equation 1.2 are listed in Table 1.1. That table lists 19 operational parameters affecting R*, for an airplane powered by a naturally aspirated SI piston engine.† The parameters pertaining to a turbocharger and aftercooler are not separately listed in Table 1.1.

Antecedents

Airplane designers have long struggled to improve the performance of airplanes, and part of that struggle has been to

†Note that in Table 1.1, and throughout this work: the term Gross Weight means the All Up Weight of the airplane in cruise. Gross Weight does not mean some maximum All Up Weight of the airplane.

increase specific range R* (1-17). The four major characteristics of the airplane which affect R* are:

1. The gross weight W, lb
2. The power-off lift/drag ratio L/D_{OFF} of the airframe
3. The propulsive efficiency η_p of the propeller and airframe
4. The brake specific fuel consumption c of the engine, lbm/BHP.hr.

R* has been increased by

1. Increasing L/D_{OFF} and η_p: by the application of continuously improving aerodynamic theory and practice
2. Decreasing W: by improving
   a) Structural design
   b) Materials strength/weight ratios
   c) Engine brake horsepower/weight ratio
3. Decreasing c: by improving
   a) Engine indicated thermal efficiency
   b) Engine mechanical efficiency (brake horsepower/indicated horsepower)
   c) Fuel heat content and detonation resistance.

The aerodynamic theories appropriate to piston engine GA airplane airframes and propellers were well established by 1935,† when the classic work "Aerodynamic Theory" edited by W.F. Durand was first published (1).

---

†With the exception of an adequate compressible flow theory to describe the flow over the outer regions of the propeller blades.

With regard to the airframe contribution to gross weight: the advent of high strength aluminum alloys in the form of rolled sheet and extrusions, and of composite materials; and the development of structural theories and manufacturing technologies for the construction of rivetted, welded and bonded structures; has led to the construction of airframes with increasing payload/structural weight ratios.

With regard to the development of aircraft powerplants, Chirivella (16) states:

> The early development of power plants for aircraft was characterized by a broad variety of approaches and designs for engines to drive the propeller, which was at that time the only propulsive element available. Some of those early designs were seen for a short period, but 20 years after the first flight of the Wright brothers only the gasoline and diesel engines survived as competitive power sources. Although the diesel engine proved to be an adequate and reliable machine, it was overwhelmed by the success of the gasoline engine due primarily to the better power-to-weight ratio, which is most important in aviation.
>
> The first 20 years of the development of the aircraft gasoline engine were mostly characterized by perfecting design details and manufacturing procedures. The motivation to increase the engine power-to-weight ratio brought about a wide variety of cylinder arrangements around the crankshaft. For large engines this culminated in the powerful (3500-hp) radial air-cooled engines of the type produced by Pratt & Whitney and the Wright Aeronautical Corporation.
>
> In the late twenties, the demands for larger power plants for takeoff and altitude performance, triggered the introduction of supercharging. In the 30's the evolution of aircraft piston engines was marked by a great increase in power output from engines of a given size. This effort required considerable redesign and endurance testing, which even to this day is the method used in engine development. These great increases in power and

constraints in engine sizes resulted in formidable engine cooling requirements. The pioneering work that NACA conducted in the study of cowl and pressure baffles is worth mentioning here. This gave rise to what is presently known as cooling drag. Other achievements during the same period were improvements in lubrication, valve mechanics, fuel injection, and water injection at takeoff.

In the 40's and 50's, the radial gasoline engine had become highly perfected, and had conquered the challenge of reliability and power-weight ratio (about 1-hp/lb). Then the new challenge was to lower specific fuel consumption to meet the requirements of the long-range strategic bombers and the transatlantic nonstop air liners, such as the B-29 and the DC-7. Further development on the large radial engines lowered cruise brake specific fuel consumption (BSFC) to 0.42 lb/hp/h. The efficiency loss required for crankshaft geared superchargers can be reduced if the supercharger is driven by a turbine powered by the exhaust gases. This is the concept of turbocharging, and although it was used in large engines during World War II (the Boeing Super-Fortress), its real significance at that time was superseded by the role it played in the development of the jet engine. Turbocharged piston engines gave rise to the efficient turbocompound radial, the Wright Turbocompound R-3350. This is a turbocharged engine where the excess power in the turbine shaft is delivered to the propeller. The turbocompound engines produced the best power-weight ratio and the lowest BSFC (0.38 lb/hp/h) of all radial piston engines in the late fifties, but their price was very high and their performance was obscured by dramatic developments underway in jet engine technology. At this point, the costly R & D supporting the large gasoline engines came to an end, and, in a matter of 10 years, the gasoline engine became a power plant exclusively for general aviation.

. . . From the brief historical review given above it is evident that considerable knowledge and experience were gained on aircraft piston engines during those 40 years of development, and that has resulted in the great reliability and performance of modern general aviation engines . . .

. . . Most gasoline aircraft engines of the past as well as the present were designed to burn rich fuel/air mixtures. This provided a means to cool the

> engine and to operate at higher manifold pressures (which means higher power-to-weight ratio). This trend has been inherited by general aviation and has resulted in exhaust gases rich in carbon monoxide and unburned hydrocarbons. The BSFC, even in the best engines, has remained at a relatively high value (about 0.45). The maximum manifold pressure that can be used during takeoff and still prevent detonation has led manufacturers to run the engine at high speed to meet the power requirements. Unfortunately, this has given rise to noisier takeoffs and climbouts.
>
> It is known that if an engine designed for rich operation is considerably leaned out, it will stumble, run unstable, and even misfire. There is experience, however, in the large radial engines used in the 50's, which indicates that lean operation is possible by adjusting the spark timing. These techniques were conducted to increase the range of large transport aircraft: those using the Wright R-3350 engine, for example. These aircraft were equipped with torquemeters, gas analyzers, and two spark advance settings; the pilot had to actually tune the engine in flight to improve efficiency and meet mission range objective. Most of these techniques were known before the war, as shown by the excellent historical paper presented by Hersey in 1939 on "Fuel-Economy Possibilities of Otto-Cycle Aircraft Engines"[†].

The development of aircraft piston engine technology virtually ceased with the advent of the jet engine, with the exception of the continued development of the turbocharger, the improvement of GA engine reliability, and the increase in engine Time Between Overhauls. According to Chirivella (16):

> . . . The advent of jet engines put an end to the large funding allocated to the research and development of the piston engine, and there is no doubt that further improvements would have appeared if the jet engine introduction had been delayed a few years.

[†]Hersey, D.S., "Fuel-Economy Possibilities of Otto-Cycle Aircraft Engines", Pratt & Whitney, SAE Transactions, Vol. 44, No. 6, 1939 (as given by Chirivella, 16).

There is still a large amount of piston engine work and information which awaits a go-ahead by engine manufacturers. How much of this information is applicable to the horizontally opposed cylinder configuration used nowadays by general aviation is not clear, but there is strong evidence of multiple commonalities.

The present day GA piston engine airplane represents a technology which is approximately 30 years old, with respect to airframes, propellers and engines. The use of variable ignition timing as a means for decreasing engine brake specific fuel consumption is not currently practiced: all commercially available GA airplane piston engines employ fixed ignition timing.

During the last decade, the energy crisis has stimulated fresh efforts to improve the fuel economy of GA airplanes. These efforts have included the following.

1. Increased propulsive efficiency of GA propellers is being pursued by the NASA-Langley Research Center, Hamilton Standard, the McCauley Accessory Division of the Cessna Aircraft Company, and by various universities throughout the United States (including Ohio State and Mississippi State).
2. Decreased engine brake specific fuel consumption in GA spark-ignition piston engines is being pursued by the NASA-Lewis Research Center, AVCO-Lycoming and Teledyne Continental Motors. The combined effort of the Jet Propulsion Laboratory, AVCO-Lycoming and the Beech Aircraft Corporation reported in Reference 16 is a significant contribution to a methodology for decreasing the

brake specific fuel consumption of GA SI piston engines.

It is hoped that these efforts, as well as efforts by the airframe manufacturers to reduce structural weight and increase airframe L/D_{OFF}, will make significant improvements to the individual contributions of the airframe, propeller and engine to GA airplane range and specific range, R*.

Approach of this Study

Systems Approach:

The approach taken in this study is to consider the airplane to be of fixed design, and to treat the airframe, propeller, engine and atmosphere together as an airplane-atmosphere system.

1. The cruise performance of this system is modelled as the cruise performance of two subsystems:
   a) The Airframe-Propeller-Atmosphere (APA) subsystem: the cruise performance model of this subsystem is called the APA subsystem input-output model.
   b) The Engine-Atmosphere subsystem. In modelling the performance of this subsystem, detailed attention is given only to naturally aspirated SI piston engines employing ignition timing optimized for maximum brake torque: the subsystem incorporating such an engine is called the Naturally aspirated Engine-Atmosphere (NEA) subsystem. The cruise performance model of the NEA subsystem is called the NEA subsystem input-output

model. No account is taken of emission control in modelling the NEA subsystem performance. The performance of turbocharged SI piston engines is not modelled, due to the unavailability of suitable turbocharger performance data.

Each subsystem (APA, NEA) input-output model is developed for standard and non-standard atmospheric conditions.[+] The modelling of each subsystem is entirely static: no dynamics are considered.

2. The APA and NEA subsystem models are combined to form the cruise performance model of the complete airplane-atmosphere system.
3. Computational procedures are developed for maximizing R* with or without constraints. These procedures consider the performance of the complete airplane-atmosphere system.

Figure 1.1 is an airplane-atmosphere system block diagram, drawn from the perspective of the pilot. The nomenclature of Figure 1.1 is that previously given in Table 1.1, plus:

D_{OFF} = airframe power-off drag

E = number of engines each driving one propeller

G = transmission gear ratio

H_p = pressure altitude

L = airframe lift

N_c = commanded propeller rotational speed

[+]The Standard Atmosphere used in this work is the U.S. Standard Atmosphere, 1962 (18).

Q_a = propeller shaft torque

Q_E = engine brake torque

T_p = propulsive thrust

β = propeller blade angle

γ = airplane flight path angle to horizontal

σ = atmospheric air density ratio.

In Figure 1.1: $\{V_T, \dot{m}_f\}$ are outputs corresponding to the control inputs $\{P_m, N_c\}$ and to given values of the remaining inputs at the left. R* is computed from the circled output variables in Figure 1.1 using Equation 1.1.†

The APA and NEA subsystem block diagrams developed in this work are shown in Figures 4.8 and 5.30, and are combined in Figure 6.1 to form the complete airplane-atmosphere system block diagram. Figure 6.1 is equivalent to Figure 1.1. Since the modelling herein is static, the propeller governor is not modelled explicitly: the commanded propeller speed N_c is equal to the actual propeller speed N at all times in the steady state.

A new unique systems approach has been adopted in this study because it offers an immediate payoff in fuel savings and safety benefits without airplane redesign. The APA and NEA subsystem models developed might be used by designers:

1. To identify airplane components/systems in which redesign would be beneficial to specific range

†Note particularly that, in drawing Fig. 1.1, it is assumed that the airplane has a "constant speed" propeller and variable ignition timing. Practically, now, the former is often the case; the latter never.

2. To estimate the impact of redesign on specific range.

Issues of redesign, however, are not addressed in this study.

Modelling Technique:

The modelling technique used in this study is the following:

1. Mathematical models of
   a) The standard atmosphere and any non-standard atmosphere
   b) The performance of the airframe, propeller and naturally aspirated SI piston engine

   are adopted or developed as necessary and synthesized into an appropriate overall model. Theoretical models are based on material in the open literature, and on information obtained from the GA industry.
2. Where possible, the theoretical models are modified and quantified in accordance with experimental data. These data were obtained from the open literature, from the GA industry and from interested individuals.

The amount of experimental data available for appropriately modelling the performance of GA airframes, propellers and SI piston engines is perhaps surprisingly small, considering that design and test methodologies have been well developed for some time.

The performance of the airframe and propeller, computed and illustrated in this study, approximates the performance of the Lockheed LASA 60 airframe and propeller--the Lockheed LASA 60 is a typical, single engine GA airplane, owned and operated by

Princeton University. The performance of the naturally aspirated engine, computed and illustrated in this study, approximates the performance of a 470 cubic inch displacement naturally aspirated SI piston engine: this performance does not represent that of any particular GA engine.

GUIDE FOR THE READER

Chapter 2 establishes what can be done to maximize the specific range of GA airplanes, using cruise performance data currently available to the GA community in Pilot Operating Handbooks. The construction of cruise performance models from Pilot Operating Handbook (POH) data is described, and the uses and limitations of such models for maximizing R* are discussed. The limited usefulness of such models for maximizing R* constitutes the motivation for the study of Chapters 3 through 6.

Chapters 3 through 6 develop a new cruise performance model of the airplane-atmosphere system. This model is suitable for airborne microprocessor implementation. It overcomes the limitations of the POH cruise performance model developed in Chapter 2. Mathematical details are relegated to Appendices as described below.

Chapter 3 reconsiders the performance of the airframe in the atmosphere.

Chapter 4 combines the propeller performance with the airframe-atmosphere performance described in Chapter 3, and develops the APA subsystem input-output model.

Chapter 5 discusses the performance of naturally aspirated SI piston engines, and develops the NEA subsystem input-output model.

Chapter 6 integrates the APA and NEA subsystem input-output models to form the new cruise performance model of the airplane-atmosphere system. The implementation, use, and engine control requirements of this new model are discussed. The percentage increases in R* offered by the implementation of this new model in any GA airplane, relative to R* achieved when operating that airplane in accordance with current GA practice, are estimated. Finally, this new model is compared with the POH cruise performance model developed in Chapter 2.

Chapter 7 presents conclusions and recommendations as a result of this study.

Appendix A discusses the fundamentals of the Point Economy Function R*. The reader is urged to read this appendix prior to commencing a detailed reading of Chapters 3 through 6.

Appendix B describes the standard and non-standard atmosphere models used throughout this study.

Appendix C develops the airframe performance model used in Chapters 3 and 4.

Appendix D develops the propeller performance model used in Chapter 4.

Appendix E develops the naturally aspirated SI piston engine performance model used in Chapter 5.

Appendix F presents a brief discussion of autoignition, detonation and knock in spark-ignition piston engines.

Following Appendix F, there is a tabulation of the nomenclature used throughout the chapters of this study (other symbols used in the appendices are defined locally). For historical reasons, and in consideration of other peoples' work, a conventional notation has been maintained throughout; this has sometimes resulted in the same symbol being used for different quantities. For the same reasons, English rather than Metric units have been used throughout.

Finally, the list of References is presented. Reference numbers in this list are cited in parentheses throughout the text.

Interesting Results

Without unduly anticipating the logical conclusions, presented in their separate place, it may be appropriate here to consider briefly some of the difficulties overcome in, and interesting results of, the research. Given that the problem of maximizing specific range, R^*, is significant, one finds that it is not amenable to theoretical solution. On the other hand, one finds that costly experimental or test data which have been accumulated are inadequate for the purpose at hand. The thesis is the proposition, in detail, of a prescription for experiments to be made.

I first review classical airplane cruise performance. In principle this is very well understood. A new irterpretation,

however, of that performance is given inasmuch as

1. The effects of wind and auxiliary equipment power on R* are presented in terms of new Equivalent Quantities.
2. The effects of center of gravity (c.g.) position on R* are specifically formulated in terms of
   a) R* appropriate to a reference c.g. position, and
   b) A correction factor for variations in c.g. position.

Next, classical propeller performance is reconsidered. A compact representation of the combined performance of the airframe and the propeller in terms of novel Corrected Quantities is made. In particular,

1. Propeller performance is presented in terms of a novel non-dimensional quantity, the Speed-Thrust Coefficient, C_R. This, in conjunction with the well known propeller advance ratio, facilitates computations of the effects of equivalent airspeed, gross weight, c.g. position, propeller shaft speed and atmospheric density ratio on propulsive efficiency.
2. The effects of compressibility on propeller performance are represented by a correction factor, f_{comp}. Such a correction factor is not new, but has passed out of use since the advent of modern computational fluid mechanics. This study identifies the importance of f_{comp} for compact computations of General Aviation (GA) airplane cruise performance; and recommends further effort in quantifying f_{comp} for GA propellers.

3. Corrected Quantities are then formulated which facilitate representation of the Airframe-Propeller-Atmosphere (APA) subsystem cruise performance for all values of gross weight and altitude.

Further then, I synthesize a fuel-efficient steady state performance model of naturally aspirated Spark-Ignition (SI) piston aero engines from a widely scattered literature. Using this model, novel Corrected Quantities are identified. The cruise performance of the Naturally aspirated MBT ignition timing Engine-Atmosphere (NEA) subsystem is then represented in terms of these Corrected Quantities.

The subsystem integration is summarized in a single block diagram illustration (Figure 6.1). This figure is an original, logical abstraction of the developments and models which are presented in the body of the work. It shows the connection between the important inputs and "controls" and the overall system performance which is of interest.

All this appears to have significant implications for efficient and safe GA airplane operation. Finally, I present calculations of the fuel savings which might be obtained by improved computer-aided operating practices. Increased specific range, R*, is conservatively estimated to be 20% to 26%.

TABLE 1.1

PARAMETERS CONTRIBUTING TO R*

Variable	Contributing Parameters	
V_T	V_E	Equivalent airspeed
	P_{atmos}	Atmospheric ambient air absolute pressure
	T_{atmos}	Atmospheric ambient air temperature
V_w		Geocentric wind speed and direction
	ψ	Airplane heading
P_E	C_D	Airframe power-off drag coefficient
		$C_D = C_D[V_E, W, h]$
		where W = airplane gross weight
		$h\bar{c}$ = longitudinal center of gravity position
		$\bar{c}$ = mean aerodynamic chord of the wing
	V_T	Airplane true airspeed
	P_{atmos}	
	T_{atmos}	
	P_{AUX}	Auxiliary equipment power
	η_p	Propulsive efficiency = $\eta_p[V_E, W, h, N, \sigma, M_T]$
		where N = propeller shaft rotational speed
		σ = atmospheric air density ratio
		M_T = propeller helical tip Mach number
c	The following apply to naturally aspirated and turbo-charged SI piston engines:	
	$\dot{m}_f$	Fuel mass flow rate per engine

TABLE 1.1

(concluded)

		Engine geometry and grade of fuel	These define the Indicated Horsepower (IHP)
	F	Fuel-dry air mass ratio	
	τ	Ignition timing	
	N_E	Engine shaft rotational speed	
	P_m	Inlet manifold absolute pressure	
	T_m	Inlet manifold temperature	
	P_e	Exhaust absolute back-pressure	
	CHT	Cylinder head temperature	
		Detonation	
		Engine geometry	These define the Lost Horsepower (LHP)
	N_E		
	T_m		
	P_m		
	P_e		
	IHP	Indicated horsepower	
The following apply to Turbocharged SI piston engines:			
		Turbocharger characteristics	
		Aftercooler characteristics	
		Throttling absolute pressure losses	

AIRPLANE - ATMOSPHERE SYSTEM BLOCK DIAGRAM

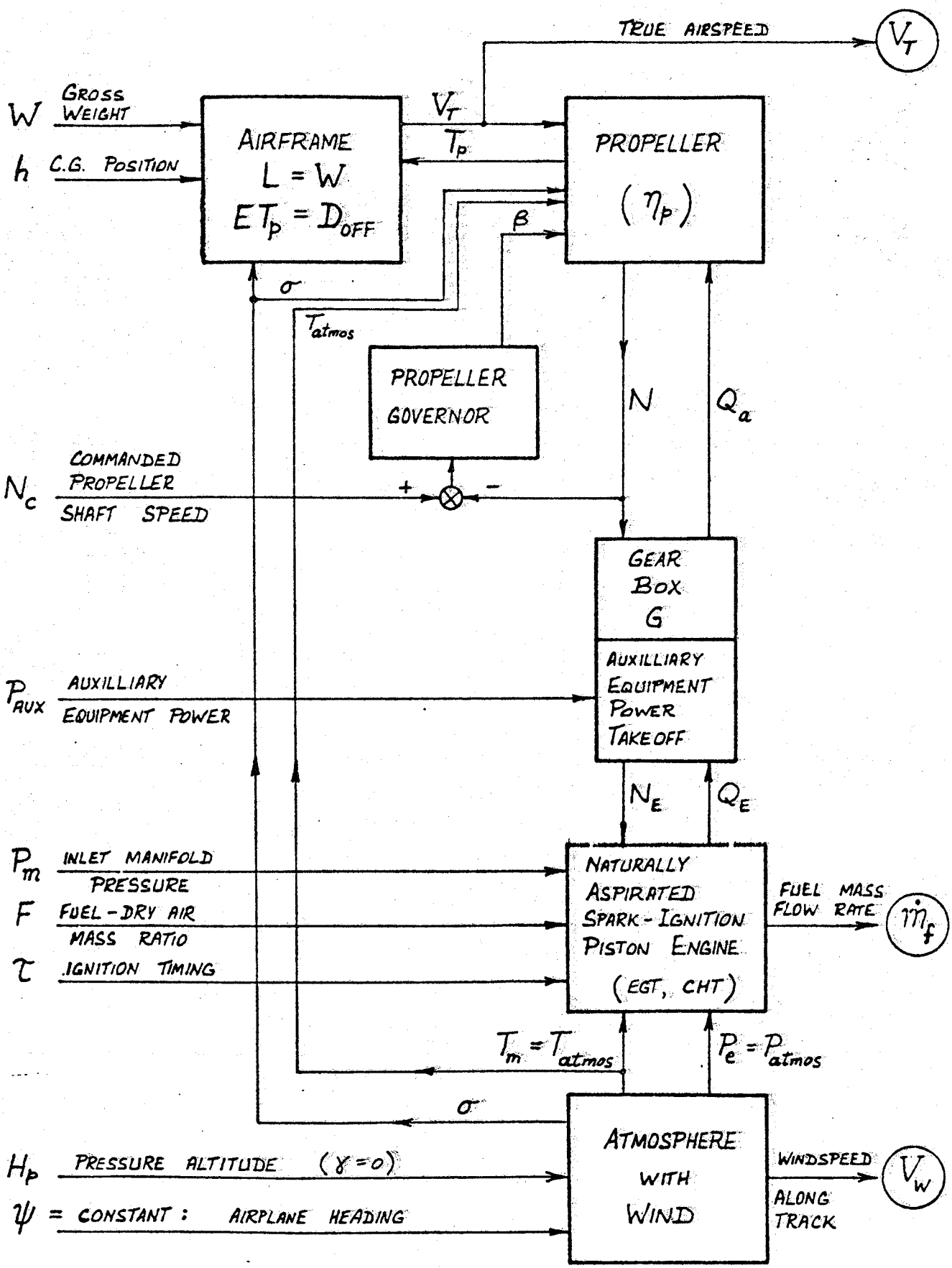

FIGURE 1.1

CHAPTER 2

USES AND LIMITATIONS OF POH CRUISE PERFORMANCE DATA FOR MAXIMIZING R*

Table of Contents

CHAPTER 2

USES AND LIMITATIONS OF POH CRUISE PERFORMANCE DATA FOR MAXIMIZING R*

INTRODUCTION

The manufacturers of GA airplanes provide detailed cruise performance data for each airplane sold. These data are available in the airplane Pilot Operating Handbook (POH) and in the Federal Aviation Administration approved Flight Manual for each airplane.

This chapter describes the construction of cruise performance models from POH data, and examines the usefulness and limitations of such models for maximizing R*.

The pilot operating handbooks of a number of typical GA airplanes are first examined. The construction of cruise performance models incorporating the common cruise performance variables in this POH sample is described, and this is illustrated for two GA airplanes. The use of a POH cruise performance model for maximizing R* is discussed, and illustrated for one GA airplane. Finally, the limitations of POH cruise performance models for maximizing R* are discussed.

PILOT OPERATING HANDBOOK DATA

A sample of Pilot Operating Handbooks was examined in order to determine what variables are commonly included in the cruise performance data of such handbooks.

Ten airplane types and four manufacturers were represented in the sample. These are listed in Table 2.1, along with the operating

point variables included in the POH cruise performance data and the operating conditions pertaining to those data. Single and twin engined airplanes are included in the list, some with naturally aspirated engines and others with turbocharged engines.

The five variables common to each airplane listed in Table 2.1 are:

1. Pressure altitude
2. Engine rotational speed
3. Engine inlet Manifold Absolute Pressure (MAP)
4. Fuel flow rate
5. True airspeed (TAS)

This constitutes the majority of the listed variables.

Some of the sampled POH's specify a leaning criterion to establish the given fuel flow rates, such as an Exhaust Gas Temperature (EGT) relative to peak EGT, or a Turbine Inlet Temperature (TIT) relative to peak TIT. However, it is not clear in every case what leaning procedure results in the given POH fuel flow rates. In those cases where the leaning criterion appropriate to the cruise performance data is clearly established in the POH: the POH informs the pilot of the TAS and fuel flow rate which will result when the airplane is flown at various pressure altitudes, with various combinations of MAP and RPM, under certain operating conditions (one of which is the leaning criterion). In those cases where the leaning criterion appropriate to the cruise performance data is not clearly established in the POH: the POH informs the pilot of the TAS which will result

when the airplane is flown at various pressure altitudes, with various combinations of MAP, RPM and fuel flow rate, under certain operating conditions (excluding a leaning criterion).

Sufficient information is given in each POH for the computation of R* (Equation A.7) throughout the operating range documented, given a knowledge of the prevailing windspeed along track. However, in no case listed in Table 2.1 does the form of data presentation facilitate maximizing R* in current operations.

CONSTRUCTION OF A CRUISE PERFORMANCE MODEL FROM POH DATA

This section shows how the POH cruise data for an airplane may be used to construct a cruise performance model which facilitates the computation of operating points which maximize R* in the cruise operation of that airplane: a cruise performance model constructed from POH cruise data is referred to as a POHCPM. The cruise data for the 1974 Cessna Centurion and the 1974 Cessna Turbo Centurion are used for this purpose[†]: the former airplane employs a naturally aspirated engine, and the latter a turbocharged engine.

The cruise operating point variables, presented in the POH data for each of these two airplanes, are the first six variables listed in Table 2.1. The POH data format for these two airplanes is that shown in Table 2.2. The POHCPM of each of these airplanes, constructed here from their POH data, is comprised of the following plots:

[†]The data for these airplanes were taken from the airplane Owner's Manual in each case. The information contained in these manuals is issued for more modern airplanes in the POH. These two Owner's Manuals are here referred to as Pilot Operating Handbooks in keeping with this practice.

1. Fuel flow rate $\dot{m}_{f_t}$ (lbm/hr) versus true airspeed V_T (statute mph), for constant values of pressure altitude (ft). Such plots are referred to as Fuel Flow Diagrams.
2. MAP (inches Hg) versus V_T (statute mph), for constant values of pressure altitude (ft) and engine RPM. Such plots are referred to as Power Diagrams.

The source POH data for each of these models, and hence the models themselves, apply only to the following operating conditions:

1. Extended range mixture (fuel-air mass ratio): established by leaning to a specified EGT increment rich of peak EGT
2. Standard atmosphere
3. Specified gross weight
4. Fixed (but unspecified) longitudinal center of gravity (c.g.) position
5. Undercarriage retracted
6. Flaps up
7. Cowl flaps: position not determined by author. However, cowl flap position was commensurate with required Cylinder Head Temperature (CHT) in each case
8. Some specific configuration of avionics aerials and other external equipments.

Fuel Flow Diagrams

The POH fuel flow data for the 1974 Cessna Centurion and Turbo Centurion are plotted against TAS for fixed values of pressure

altitude, in Figures 2.1 and 2.2. Plots such as Figures 2.1 and 2.2 are referred to as Fuel Flow Diagrams. A least squares cubic polynomial of the form

$$\dot{m}_{f_t} = a_o + a_1 V_T + a_2 V_T^2 + a_3 V_T^3 \qquad (2.1)$$

is fitted through the fuel flow data at each pressure altitude in these two figures. The data points for each pressure altitude fall very close to the fitted curve, the standard deviation being less than 0.5 lbm/hr in every case, except for the Turbo Centurion at 20,000 ft where the standard deviation is 0.73 lbm/hr. Each data point corresponds to a recommended combination of MAP and RPM. For this Cessna data, it is apparent that every combination of MAP and RPM, given in the POH and yielding a given TAS, corresponds to a fuel flow rate $\dot{m}_{f_t}$ lying very close to the relevant altitude curve. The curves of Figures 2.1 and 2.2 are therefore taken to apply to all combinations of MAP and RPM within the limits of the POH data.[†]

The hatched boundaries of Figures 2.1 and 2.2 represent the recommended upper cruise power limits for the respective airplanes (see also Reference 4, p. 414). Such boundaries correspond either to the maximum percentage of maximum continuous power (brake horsepower) which the manufacturer recommends for continuous normal cruise operation; or to the maximum available cruise brake horsepower when this is altitude limited; whichever is the smaller power level. Occasionally, as in the case of the 1974 Centurion, some of the tabulated data points lie outside this boundary and are presented in the

[†]This close proximity of $\dot{m}_{f_t}$ to a single curve, for various combinations of MAP and RPM at one altitude, should not be taken as an indication that MAP and RPM have no effect on R* (see Chapter 5).

POH merely for interpolation purposes. The boundary should be drawn (as in Figure 2.1) on the basis of the manufacturer's recommendation and not as the upper power limit of the data tabulated for each pressure altitude. The recommended power boundaries of Figures 2.1 and 2.2 both represent 75% maximum continuous brake horsepower, or less when altitude limited.

Power Diagrams

The engine MAP and RPM corresponding to the ($\dot{m}_{f_t}$, V_T) data points of Figure 2.1, at sea level and 10,000 ft, are plotted in Figure 2.3 for the Centurion. Similar plots corresponding to the ($\dot{m}_{f_t}$, V_T) data points of Figure 2.2, at sea level and 20,000 ft, are shown in Figure 2.4 for the Turbo Centurion. It is apparent from Figures 2.3 and 2.4 that a great deal of redundant engine setting data are available to the pilot for the cruise operation of these airplanes: at each TAS and pressure altitude, an infinite number of (MAP, RPM) combinations may be selected. At each TAS, one recommended combination of MAP and RPM would suffice. In Figures 2.3 and 2.4, a straight line has been drawn through the set of data points appropriate to each pressure altitude. Each straight line represents an arbitrary trajectory of (MAP, RPM) over the TAS range at each pressure altitude: points (a, a'), (b, b') etc. on these straight lines correspond to (2200), (2300) RPM etc. respectively. When all of the (MAP, RPM) data for one airplane are plotted against TAS, and a straight line inscribed for each pressure altitude, a unique combination of (MAP, RPM)

may be prescribed for flight at any TAS and pressure altitude by interpolating between the inscribed straight lines.

Figures 2.5 and 2.6 show the results of the above construction for the Centurion and Turbo Centurion respectively. The straight lines of constant pressure altitude correspond to the inscribed straight lines in that construction. Points a, a' etc. in Figure 2.5 (2.6) correspond to points a, a' etc. respectively in Figure 2.3 (2.4). Lines of constant RPM are shown dotted in Figures 2.5 and 2.6.

Plots such as Figures 2.5 and 2.6 are referred to as Power Diagrams. The fuel flow rate shown in the Fuel Flow Diagram drawn for a specific set of operating conditions, corresponds to the MAP and RPM in the Power Diagram drawn for the same set of operating conditions, at the same TAS and pressure altitude. Consequently, variations in $\dot{m}_{f_t}$ with MAP and RPM, at any TAS and pressure altitude, are accounted for in these Diagrams.

The POHCPM

Figures 2.1 and 2.5 constitute a POHCPM of the 1974 Cessna Centurion, for the operating conditions stated in Figure 2.1. Figures 2.2 and 2.6 constitute a POHCPM of the 1974 Cessna Turbo Centurion, for the operating conditions stated in Figure 2.2.

The cruise performance of any GA airplane, flying in specified atmospheric conditions with a specified gross weight and c.g. position, may be completely described by one Fuel Flow Diagram and one corre-

sponding Power Diagram. (The units used in these Diagrams would be Nautical mph or Statute mph, and lb/hr or gallons/hr, in accordance with the POH data.) Different Fuel Flow and Power Diagrams are required to describe the airplane performance for different values of:

1. Atmospheric temperature at fixed pressure altitude,
2. Gross weight,
3. C.G. position.

Each pair of Diagrams would be appropriate to:

1. A mixture (fuel-air mass ratio) established by a specified leaning criterion,†
2. Undercarriage retracted,
3. Flaps up,
4. Cowl flaps either closed, or opened the amount necessary to achieve a specified CHT,
5. A specified configuration of avionics aerials and other external equipments.

The cruise performance of any GA airplane in all operating conditions should be well represented by linear interpolation between pairs of Fuel Flow and Power Diagrams for the conditions 1-12 listed in Table 2.3. Such a set of Diagrams, for a given airplane, would constitute a POHCPM applicable to all operating conditions of that airplane. In the event that the Diagrams are found to be influenced little by c.g. position, pairs of Diagrams for conditions 1-6 only

†Discussions with the GA manufacturers indicate that good repeatability of fuel flow rate, in given atmospheric conditions and at a given MAP and RPM, is achieved using a leaning criterion based on EGT or TIT, although no repeatability statistics were made available to the author.

will suffice to describe the performance. The value of R* increases continuously as the c.g. is moved from the forward limit to the aft limit (see Chapter 3) so that the choice of conditions 1-6 only would be a conservative one. If the range of gross weights were great, it may be desirable to include an intermediate gross weight in the POHCPM. Three values of any one parameter in Table 2.3 affords the use of parabolic rather than linear interpolation for that parameter.

While the use of Fuel Flow and Power Diagrams reduces POH cruise data to a simple form for fixed conditions, the prospect of manually interpolating between 6 or more pairs of such Diagrams is a daunting one. However, this task is a simple one for a computer, and may be performed enroute by a microprocessor installed in the airplane.

The POHCPM may be stored in a microprocessor as sets of coefficients of cubic polynomials (describing the Fuel Flow Diagrams: see Equation 2.1) and straight lines (describing the Power Diagrams).

The following section describes some of the uses of a POHCPM.

APPLICATIONS OF POH CRUISE PERFORMANCE MODELS

One obvious function of a POHCPM of a given airplane is to inform the pilot of the engine power (MAP, RPM) settings required to fly that airplane in any given operating conditions. The model is entered with values for:

1. TAS
2. Pressure altitude
3. Atmospheric temperature relative to standard
4. Gross weight

5. Center of gravity position

and values of MAP and RPM are returned. The corresponding fuel flow rate, also obtainable from the POHCPM, would be established by the pilot using the leaning criterion appropriate to the POHCPM (or established directly using fuel flow instrumentation).

However, a POHCPM has some more important uses than the computation of MAP and RPM (and fuel flow rate) for specified flight conditions. In this section we examine the use of cruise performance models for various optimizations. In particular, we examine the computation of the operating point, for a particular airplane, which satisfies the following alternative requirements:

1. Achieve maximum groundspeed, with an R* constraint
2. Achieve maximum possible R*
3. Maximize R* while flying at a prescribed TAS
4. Maximize R* while flying at a prescribed groundspeed.

The use of cruise performance models for the computation of R* is first described, with the aid of the POHCPM of the 1974 Cessna Centurion: Figures 2.1 and 2.5. The above four optimizations are then discussed in turn, using the POHCPM of the 1974 Cessna Turbo Centurion: Figures 2.2 and 2.6. Throughout these discussions, the operating conditions are assumed to conform to the conditions pertaining to Figures 2.1 and 2.2. Zero and non-zero wind conditions are considered: computations involving the latter employ the wind profile shown in Figure 2.7.

The Computation of R*

The value of R* for given operating conditions is obtained from the Fuel Flow Diagram, which is a graphical representation of Equation A.7:

$$R^* = \frac{V_G}{\dot{m}_{f_t}} = \frac{V_T + V_w}{\dot{m}_{f_t}} \quad \text{ground miles/lb}^{\dagger} \tag{2.2}$$

where

V_G = groundspeed, mph

V_T = TAS, mph

V_w = true windspeed component along track (see Appendix A), mph

Headwind: $V_w < 0$

Tailwind: $V_w > 0$

$\dot{m}_{f_t}$ = Total fuel mass flow rate to all engines, lbm/hr (gallons/hr).

Consider the Fuel Flow Diagram of the 1974 Cessna Centurion: Figure 2.1.

In zero wind conditions, operation at any TAS and pressure altitude is represented by a point on Figure 2.1: the horizontal coordinate of the point gives the TAS ($=V_G$), the vertical coordinate gives the fuel flow rate, while the inverse slope of the radial line from the origin to the point gives the value of R*. For example, flight at 2,500 ft pressure altitude and 169 mph TAS (Point A in Figure 2.1) results in a fuel flow rate $\dot{m}_{f_t}$ = 87 lb/hr from which R* = 169/87 = 1.94 ground miles/lb.

---

†(Nautical or Statute) miles/(lb or gallon) in accordance with POH data. The present examples use statute miles/lb.

In non-zero wind conditions, R* is again readily obtained from Figure 2.1. The windspeed may be represented by plotting V_w along the abscissa; headwinds plotted to the right of the origin and tailwinds to the left. Then for any operating point (TAS, Pressure Altitude: Point A say) and wind condition (Point B say), the groundspeed is the base BC of the triangle ABC, and the value of R* is given by the inverse slope of the hypotenuse BA.

The MAP and RPM required for flight at any given TAS and pressure altitude are obtained from the corresponding Power Diagram (Figure 2.5), and are independent of windspeed. The MAP and RPM corresponding to point A in Figure 2.1 are: MAP = 24 in. Hg, RPM ≈ 2425.

We now address the four optimization problems previously mentioned, using the POHCPM of the 1974 Cessna Turbo Centurion shown in Figures 2.2 and 2.6.

Flight at Maximum Groundspeed

We here demonstrate the use of the POHCPM for computation of the operating point yielding maximum groundspeed with an R* constraint.

In zero wind conditions, maximum groundspeed is achieved by flying at the altitude where the maximum TAS is achieved. This altitude and the corresponding maximum TAS is represented for the Turbo Centurion by point A on the power boundary of Figure 2.2.

It may be impossible to fly at point A because of insufficient fuel capacity; that is, R* at point A may be unacceptably small. Let us assume that a fuel constraint exists which requires R* to be greater than or equal to some minimum value R^*_c. Plotting a line with

slope $1/R_c^*$ (lb per hr/mph) on Figure 2.2 may result in line OB, in which case the altitude and TAS required for flight at maximum groundspeed while not violating the fuel constraint will be given by the point on the power boundary furthest to the right and on or below the line OB: point B in the case drawn. Clearly if line OB intersects the power boundary above A, then maximum groundspeed may be achieved without violating the fuel constraint by flying at A.

However, only a few specific altitudes are available to the pilot, many being precluded by topography, weather, cabin environment requirements, air traffic control or perhaps NOTAMs.[†] As a result, it may not be possible to fly at A or B in Figure 2.2. The operating point for maximum groundspeed is then determined as the point at an available altitude on or within the power boundary, on or below line OB and furthest to the right. For example, if all altitudes above 20,000 ft were unavailable, the operating point for maximum groundspeed would be point C.

In non-zero wind conditions with no fuel constraint, maximum groundspeed is obtained in all cases by flying at point A on the power boundary of Figure 2.2. When the fuel consumption constraint $R^* \geq R_c^*$ is imposed, the procedure for determining the altitude and TAS for maximum groundspeed is similar to that used in the zero wind case. In fact the analysis varies from the zero wind case only inasmuch as the line OB with slope $1/R_c^*$ is drawn for each altitude separately, the origin 0 being shifted along the abscissa to the wind component prevailing at each altitude.

[†]NOTAM: Notice to airmen.

For each cruising altitude the procedure is as follows. Consider cruise at 10,000 ft pressure altitude when the minimum tolerable value of R* is R^*_c = 2.35 miles/lb, and the winds aloft V_w are given by Figure 2.7:

1. V_w = 15 mph tailwind
2. Plot point D on Figure 2.2 corresponding to this windspeed V_w
3. Plot line DE with slope $1/R^*_c$ = 1/2.35 (lb per hr/mph). It is possible to fly at any operating point on the 10,000 ft line, on or below line DE.
4. To achieve the maximum allowable TAS and hence maximum groundspeed, assume flight at point E. The groundspeed is given by V_G = 177 + 15 = 192 mph.

Flight at other pressure altitudes is treated in similar fashion. The results of these computations for all pressure altitudes from sea level to 25,000 ft are shown in Figure 2.8. There the computations are tabulated and the maximum groundspeed achievable at each pressure altitude is plotted against pressure altitude. The maximum possible groundspeed is achieved at 25,000 ft even though the largest headwind exists there. The value of R* is the same at each pressure altitude. The engine fuel flow rate, MAP and RPM required for a chosen pressure altitude and TAS are obtained from Figures 2.2 and 2.6.

Flight at Maximum Possible R*

We here demonstrate the use of the POHCPM for computation of the operating point yielding the maximum possible value of R*.

In zero wind conditions, the maximum value of R* achievable at a particular altitude is obtained by flying at the point of tangency of a radial line from the origin to the appropriate altitude curve of Figure 2.2. At sea level this flight condition is at point F in Figure 2.2; at 25,000 ft it is at point G. The pressure altitude and TAS offering the maximum possible R* correspond to the point in Figure 2.2 at which the slope of the tangent line from the origin is least (Equation 2.2).

In non-zero wind conditions the tangent line is drawn from the appropriate wind reference rather than from the origin. For example, when flying at 25,000 ft with a 40 mph headwind, maximum R* is achieved at H in Figure 2.2 rather than at G. The pressure altitude and TAS offering the maximum possible R* correspond to the point at which the slope of the tangent line drawn from the appropriate wind reference is least.

It is of interest to determine the altitude variation of the maximum value of R* achievable at each altitude (R^*_{max}) for the Turbo Centurion. For zero wind conditions, inspection of Figure 2.2 reveals that the value of R^*_{max} increases continuously from sea level to 25,000 ft as follows:

Sea level (point F): $R^*_{max} = 130/57 = 2.28$ miles/lb

25,000 ft (point G): $R^*_{max} = 175/70 = 2.50$ miles/lb.

This represents a variation of 9.65% of the lower value. For non-zero wind conditions, the variation depends upon the wind profile. Using the wind profile of Figure 2.7 the value of R^*_{max} from sea level to

25,000 ft has been computed and plotted in Figure 2.9. The computations, tabulated in Figure 2.9, were performed as follows at each pressure altitude:

1. V_w was taken from Figure 2.7 and inscribed on the abscissa of Figure 2.2 as the wind reference
2. V_T and the fuel flow rate $\dot{m}_{f_t}$ were determined from Figure 2.2, at the point of tangency of the straight line drawn from the wind reference to the appropriate altitude curve
3. $V_G = V_T + V_w$
4. $R^*_{max} = V_G/\dot{m}_{f_t}$

The computed values of R^*_{max} plotted in Figure 2.9 show a maximum variation of (2.67 - 2.39)/2.39 or 11.7% of the lower value. In this example the wind profile has increased the percentage variation of R^*_{max} with altitude from that obtained in the zero wind case.

At any pressure altitude on the curve of Figure 2.9, the TAS may be obtained from a linear interpolation of the TAS values tabulated in that figure. For these values of pressure altitude and TAS, the engine fuel flow rate, MAP and RPM are determined from Figures 2.2 and 2.6.

When a fuel constraint dictates a minimum value of R*, some altitudes in Figure 2.9 may be excluded from candidacy for a particular operation. Other constraints may also preclude operation at certain altitudes in Figure 2.9. In such cases, Figure 2.9 clearly shows the available pressure altitude yielding the maximum possible value of R*.

Flight at a Prescribed TAS

To achieve an approximate trip duration, a pilot may choose to fly at a particular TAS. We here demonstrate the use of the POHCPM to compute the operating point which maximizes R* at a specified TAS. The method of computation is independent of the choice of TAS: it is here illustrated for a TAS of 185 mph, for which all operating points lie along the line JK in Figure 2.2.

In zero wind conditions, the value of R* is determined at each altitude as $R^* = V_T/\dot{m}_{f_t}$ at the intersection of line JK and the appropriate altitude curve. In this case the value of R* increases continuously from 5,000 ft to 25,000 ft as follows:

5,000 ft: R* = 185/98 = 1.89 miles/lb

25,000 ft: R* = 185/74 = 2.50 miles/lb.

This represents a variation of 32.3% of the lower value. Note that flight below 5,000 ft is not possible at this TAS due to the presence of the power boundary.

In non-zero wind conditions, the altitude variation of R* is determined as follows. At each pressure altitude:

1. The fuel flow rate $\dot{m}_{f_t}$ is obtained from the intersection of the line JK and the appropriate altitude curve
2. The wind component V_w is obtained from Figure 2.7
3. $V_G = V_T + V_w$
4. $R^* = V_G/\dot{m}_{f_t}$

Figure 2.10 tabulates these computations for V_T = 185 mph and shows R* plotted against pressure altitude. For the wind profile used, the

value of R* varies little above 15,000 ft, reaching a maximum at 25,000 ft even though the maximum headwind exists there. The maximum variation of R* in Figure 2.10 is (2.42 - 2.02)/2.02 or 19.8% of the lower value. In this example the wind profile has significantly decreased the percentage variation of R* with altitude, from that obtained in the zero wind case.

At any pressure altitude the engine fuel flow rate, MAP and RPM required for flight at a TAS of 185 mph are obtained from Figures 2.2 and 2.6.

A fuel constraint which dictates a minimum value of R*, or some other constraint, may preclude operation at certain altitudes. In this event, Figure 2.10 clearly shows the available pressure altitude yielding the maximum value of R* at the prescribed TAS.

Flight at a Prescribed Groundspeed

This mode of operation may be selected to satisfy a particular trip duration. We here demonstrate the use of the POHCPM to compute the operating point which maximizes R* at a specified groundspeed. The method of computation is independent of the choice of groundspeed: it is here illustrated for a groundspeed of 200 mph.

In zero wind conditions, the method is identical to that shown above for a prescribed TAS. In this case the value of R* increases continuously from 13,500 ft on the power boundary to 25,000 ft as follows:

13,500 ft: R* = 200/98 = 2.04 miles/lb

~~25,000 ft: R* = 200/81.5 = 2.45 miles/lb.~~

This represents a variation of 20.1% of the lower value.

In non-zero wind conditions, the altitude variation of R* is determined as follows. At each pressure altitude:

1. The wind component V_w is obtained from Figure 2.7
2. The TAS is computed as $V_T = V_G - V_w$
3. The fuel flow rate $\dot{m}_{f_t}$ is obtained at the intersection of this V_T line and the appropriate pressure altitude curve in Figure 2.2
4. $R^* = V_G/\dot{m}_{f_t}$

Figure 2.11 tabulates these computations for V_G = 200 mph and shows R* plotted against pressure altitude. For the wind profile used, the value of R* reaches a maximum at 25,000 ft where the maximum headwind occurs. The maximum variation of R* in Figure 2.11 is (2.38 - 2.22)/2.22 or 7.21% of the lower value. The wind profile employed in this example has significantly reduced the percentage variation of R* with altitude, from that obtained in the zero wind case.

At any pressure altitude on the curve of Figure 2.11, the TAS may be obtained from a linear interpolation of the TAS values tabulated in that figure. For these values of pressure altitude and TAS, the engine fuel flow rate, MAP and RPM are determined from Figures 2.2 and 2.6.

As for the previous analyses, a fuel constraint which dictates a minimum value of R*, or some other constraint, may preclude operation at certain altitudes. In this event, Figure 2.11 shows the available

pressure altitude yielding the maximum value of R* at the prescribed groundspeed.

LIMITATIONS OF POH DATA FOR MAXIMIZING R*

A POHCPM can only maximize R* subject to the constraints imposed by the source POH data. Two sets of such constraints are listed below: these constraints constitute typical significant limitations of POH data for maximizing R*.

1. POH cruise data pertain to specific values of (see Figure 1.1):
   a) Gross weight W: data for more than one value of gross weight are often unavailable
   b) C.G. position h: data taken for more than one c.g. position has not been observed by the author for any GA airplane
   c) Pressure altitude and atmospheric conditions: data for specific pressure altitudes and standard atmospheric conditions are usually provided, and in many cases data for certain non-standard atmospheric conditions at these pressure altitudes are also provided.

   Interpolation for performance in all cruise flight conditions is only possible when multiple data sets are provided.
2. POH data give the performance which can be expected when the airplane is operated in accordance with the manufacturer's recommendations. Those recommendations constrain the following engine variables (see Figure 1.1):
   a) Inlet MAP P_m

b) Engine rotational speed N_E

c) Fuel-air mass ratio F

d) Engine ignition timing τ

The effect of each of these variables on R* is discussed in detail in Chapters 4 and 5. Current GA airplane manufacturers' recommendations for setting these variables are not appropriate to maximum R*.

As a result of the foregoing limitations, it is concluded that a POHCPM, constructed from currently available POH cruise data, is an inadequate tool for maximizing R*.

SUMMARY AND CONCLUSIONS

Summary

The POH cruise performance data for ten airplanes have been considered. The construction of cruise performance models based on POH data, the use of such models for the solution of various optimization problems, and the limitations of such models for maximizing R* have been discussed.

Conclusions

1. On the basis of computations performed herein, it is concluded that variations in R* over the cruise envelopes of GA airplanes are sufficiently large to warrant the development of airborne microprocessor cruise performance models capable of performing fuel-use optimization computations.

2. It is concluded that a POHCPM, constructed from currently available POH cruise data, is an inadequate tool for maximizing R*.

TABLE 2.1

SAMPLE PILOT OPERATING HANDBOOKS EXAMINED

MANUFACTURER	AIRPLANE TYPE
Cessna	1974 Centurion†
	1974 Turbo Centurion†
	1980 Centurion 210N
	1980 Turbo Centurion T210N
Beech	Baron B55
	Baron 58P
Piper	Arrow IV PA-28RT-201
	Seneca II PA-34-200T
Mooney	M20J-201
	M20K-231

CRUISE OPERATING POINT VARIABLES PRESENTED

Pressure altitude
RPM
MAP
Fuel lb/hr and/or gal/hr
TAS and CAS (1)
% BHP (2)
Miles/gallon (3)

Operating Conditions††

Mixture - see Chapter 2.
ISA Temperature ±Δ OAT (4)
1 or 2 gross weights (5)
No wind
Fixed c.g. position
Undercarriage retracted
Flaps up
Cowl Flaps closed (6,7)

(1) CAS given for Beechcraft only.
(2) Except Beechcraft.
(3) Mooney M20K-231 only.
(4) Non-standard OAT for some airplanes only.
(5) 2 gross weights Mooney only.
(6) All airplanes listed have cowl flaps except Piper Arrow IV.
(7) Ascertained for all but the two 1974 Cessna airplanes.

†Owner's Manual

††The cruise data for each airplane apply to some specific airframe geometry, including avionics aerials and other optional external equipments. These details were not examined.

TABLE 2.2

CRUISE PERFORMANCE

EXTENDED RANGE MIXTURE

Standard Conditions — Zero Wind — Gross Weight- 3800 Pounds

7500 FEET

RPM	MP	% BHP	TAS MPH	LBS./ HOUR	384 LBS. (NO RESERVE)		534 LBS. (NO RESERVE)	
					ENDR. HOURS	RANGE MILES	ENDR. HOURS	RANGE MILES
2550	23	75	187	94	4.1	765	5.7	1065
	22	71	183	89	4.3	790	6.0	1095
	21	67	178	84	4.6	810	6.4	1130
	20	63	172	79	4.9	835	6.8	1160
2500	23	73	185	91	4.2	780	5.8	1080
	22	69	180	86	4.4	800	6.2	1115
	21	65	175	82	4.7	820	6.5	1145
	20	61	168	77	5.0	845	7.0	1175
2400	23	68	179	85	4.5	805	6.3	1120
	22	64	174	81	4.8	825	6.6	1150
	21	60	168	76	5.0	845	7.0	1175
	20	57	162	72	5.3	865	7.4	1200
2300	23	64	173	80	4.8	830	6.6	1150
	22	60	168	76	5.0	845	7.0	1175
	21	57	162	72	5.3	865	7.4	1200
	20	53	155	68	5.7	875	7.9	1220
2200	23	59	166	74	5.1	855	7.2	1185
	22	56	160	71	5.4	870	7.5	1205
	21	52	154	67	5.7	880	7.9	1220
	20	49	146	64	6.1	880	8.4	1225
	19	46	136	59	6.4	875	9.0	1220

CRUISE PERFORMANCE

EXTENDED RANGE MIXTURE

Standard Conditions — Zero Wind — Gross Weight- 3800 Pounds

10,000 FEET

RPM	MP	% BHP	TAS MPH	LBS./ HOUR	384 LBS. (NO RESERVE)		534 LBS. (NO RESERVE)	
					ENDR. HOURS	RANGE MILES	ENDR. HOURS	RANGE MILES
2550	21	69	187	87	4.4	825	6.1	1145
	20	65	181	82	4.7	845	6.5	1175
	19	61	174	77	5.0	870	6.9	1210
	18	56	166	72	5.3	890	7.4	1235
2500	21	67	184	85	4.5	835	6.3	1160
	20	63	177	80	4.8	855	6.7	1190
	19	59	171	74	5.1	880	7.2	1220
	18	55	163	70	5.5	895	7.7	1245
2400	21	63	177	79	4.9	860	6.8	1195
	20	59	171	74	5.1	880	7.2	1220
	19	55	163	70	5.5	895	7.6	1245
	18	51	154	66	5.8	900	8.1	1250
2300	21	59	170	74	5.2	880	7.2	1225
	20	55	163	70	5.5	895	7.6	1245
	19	51	155	66	5.8	900	8.1	1250
	18	48	144	62	6.2	895	8.6	1245
2200	21	54	162	70	5.5	895	7.7	1245
	20	51	154	66	5.8	900	8.1	1250
	19	48	144	62	6.2	895	8.6	1245
	18	44	134	58	6.6	885	9.2	1230

TABLE 2.3

FLIGHT CONDITIONS REQUIRED FOR POH CRUISE PERFORMANCE MODEL

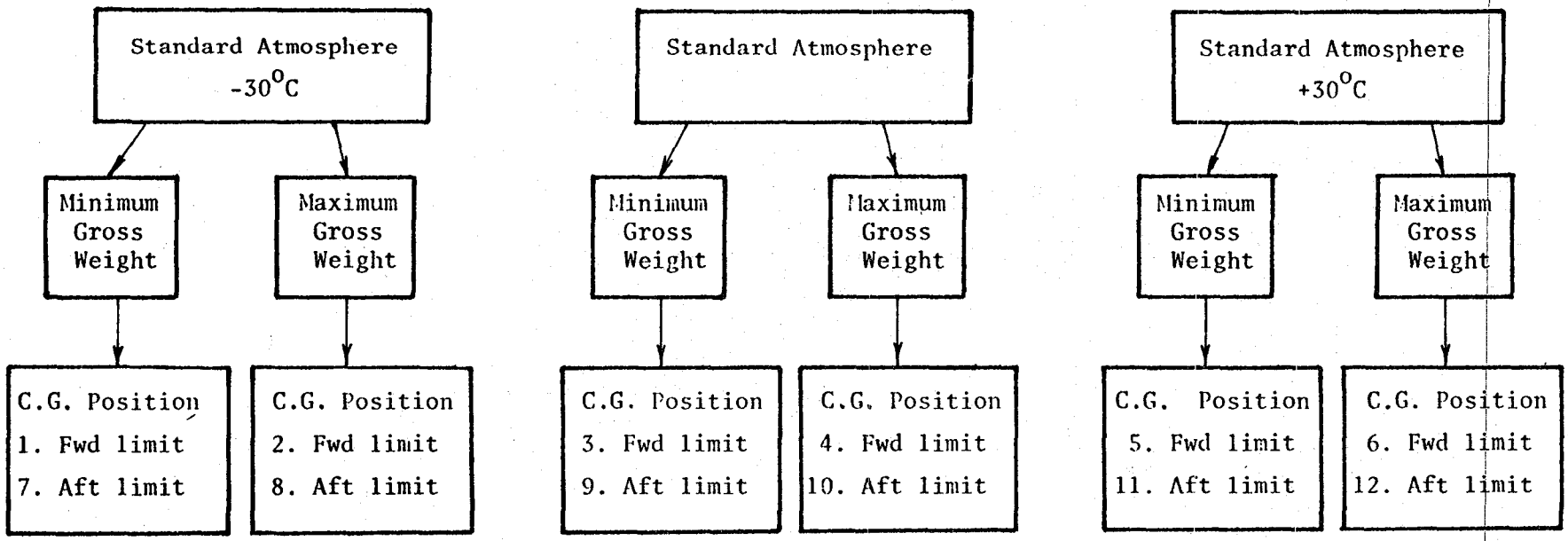

1974 CESSNA CENTURION : MANUFACTURERS FUEL CONSUMPTION DATA

FUEL FLOW DIAGRAM

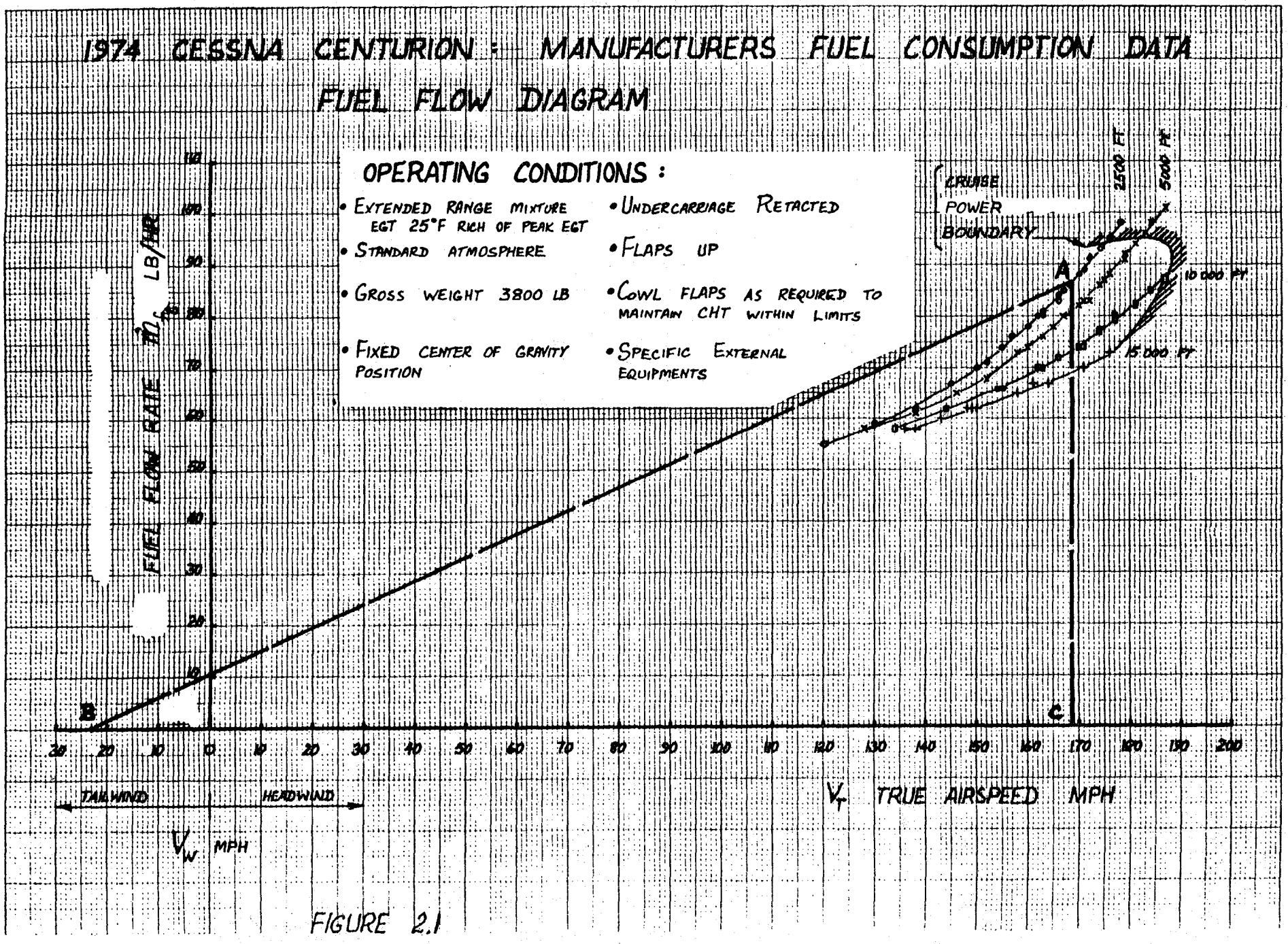

FIGURE 2.1

1974 CESSNA TURBO-CENTURION : MANUFACTURERS FUEL CONSUMPTION DATA

FUEL FLOW DIAGRAM

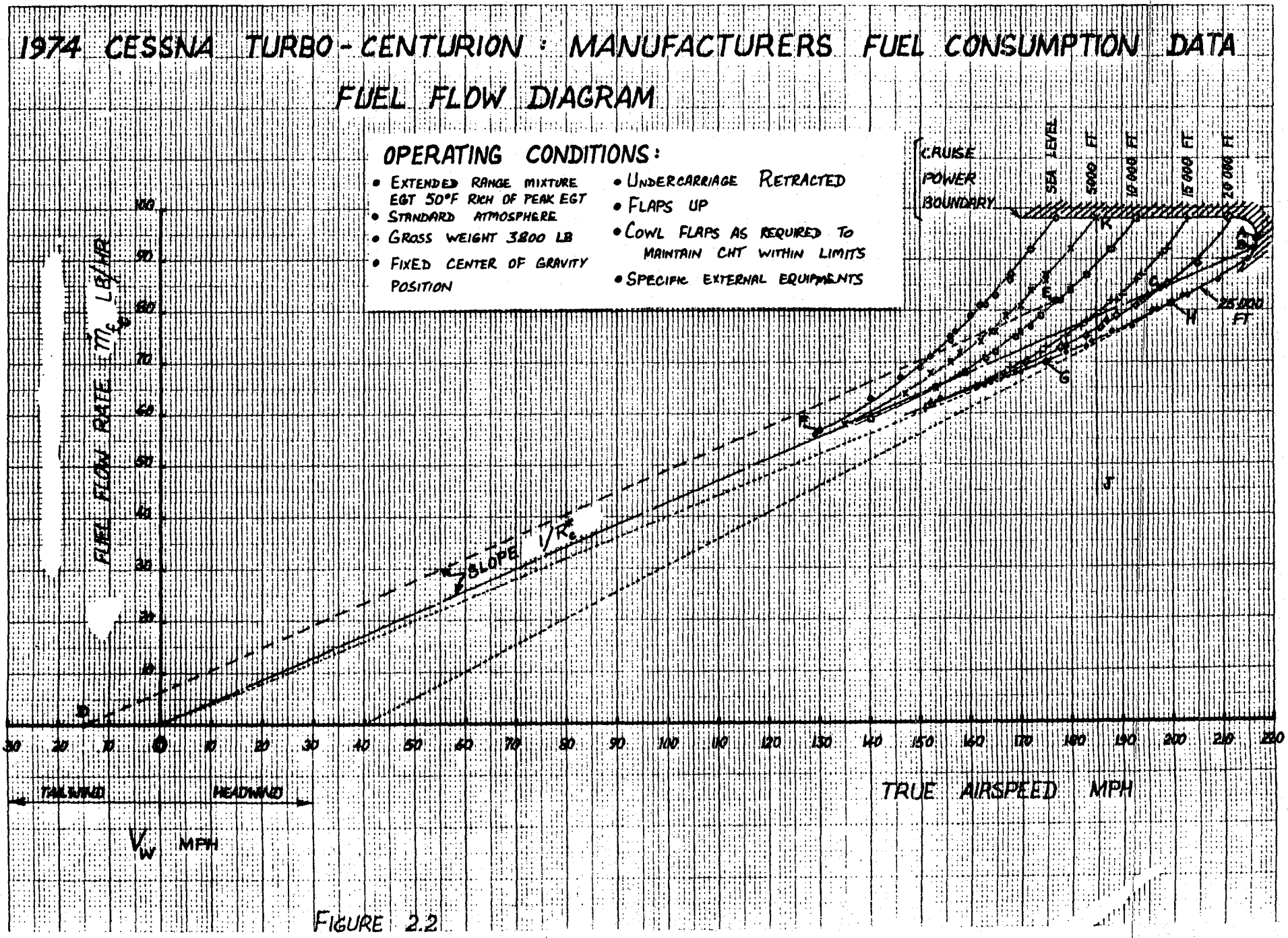

FIGURE 2.2

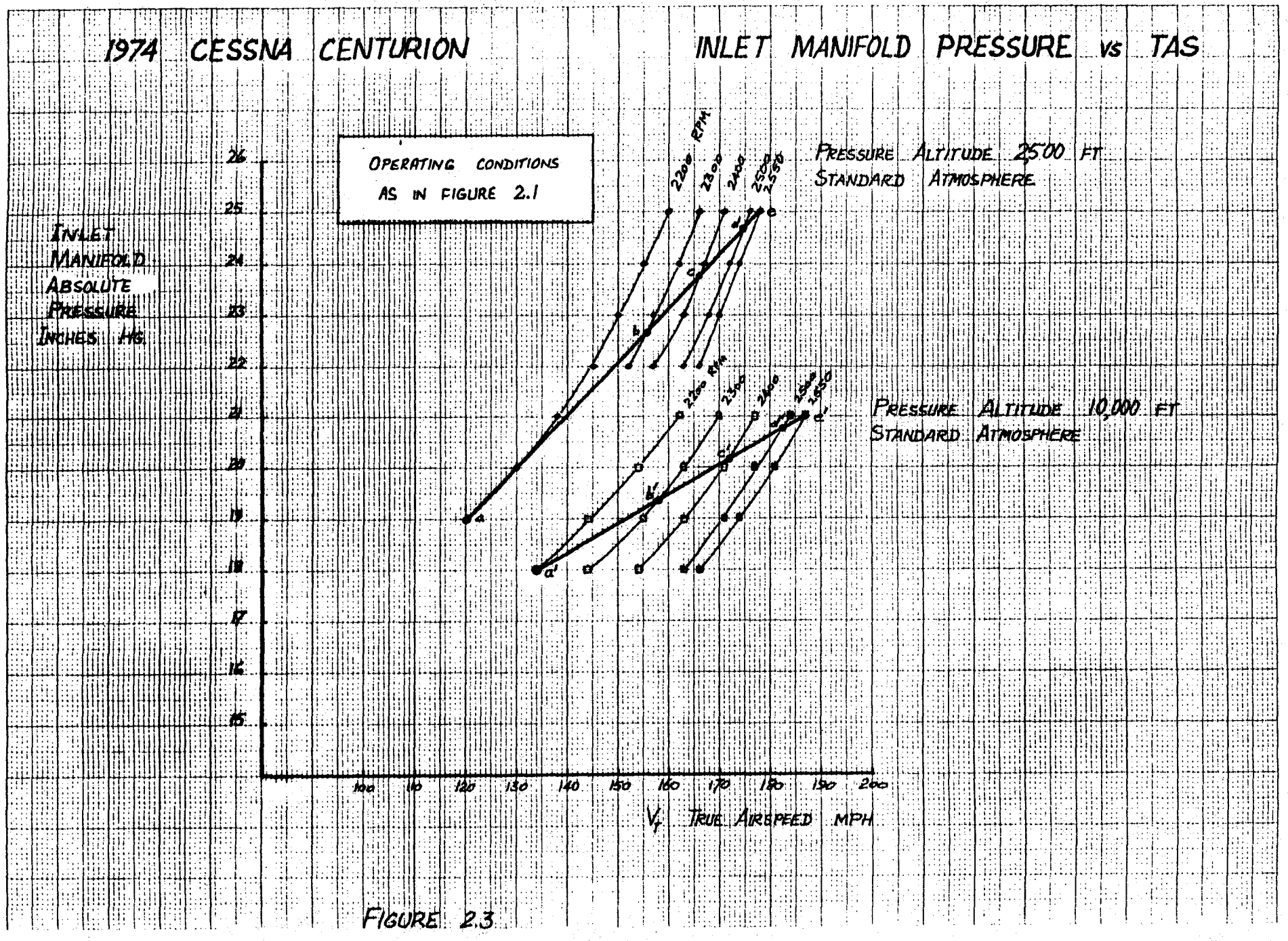
1974 CESSNA CENTURION
INLET MANIFOLD PRESSURE Vs TAS
OPERATING CONDITIONS
AS IN FIGURE 2.1
PRESSURE ALTITUDE 25.00 FT
STANDARD ATMOSPHERE
PRESSURE ALTITUDE 10,000 FT
STANDARD ATMOSPHERE
INLET MANIFOLD ABSOLUTE PRESSURE INCHES HG.
26
25
24
23
22
21
20
19
18
17
16
15
2200 RPM
2300
2400
2500
2550
2200 RPM
2300
2400
2500
2550
a
b
c
d
a'
b'
c'
d'
100
110
120
130
140
150
160
170
180
190
200
V_t TRUE AIRSPEED MPH

FIGURE 2.3

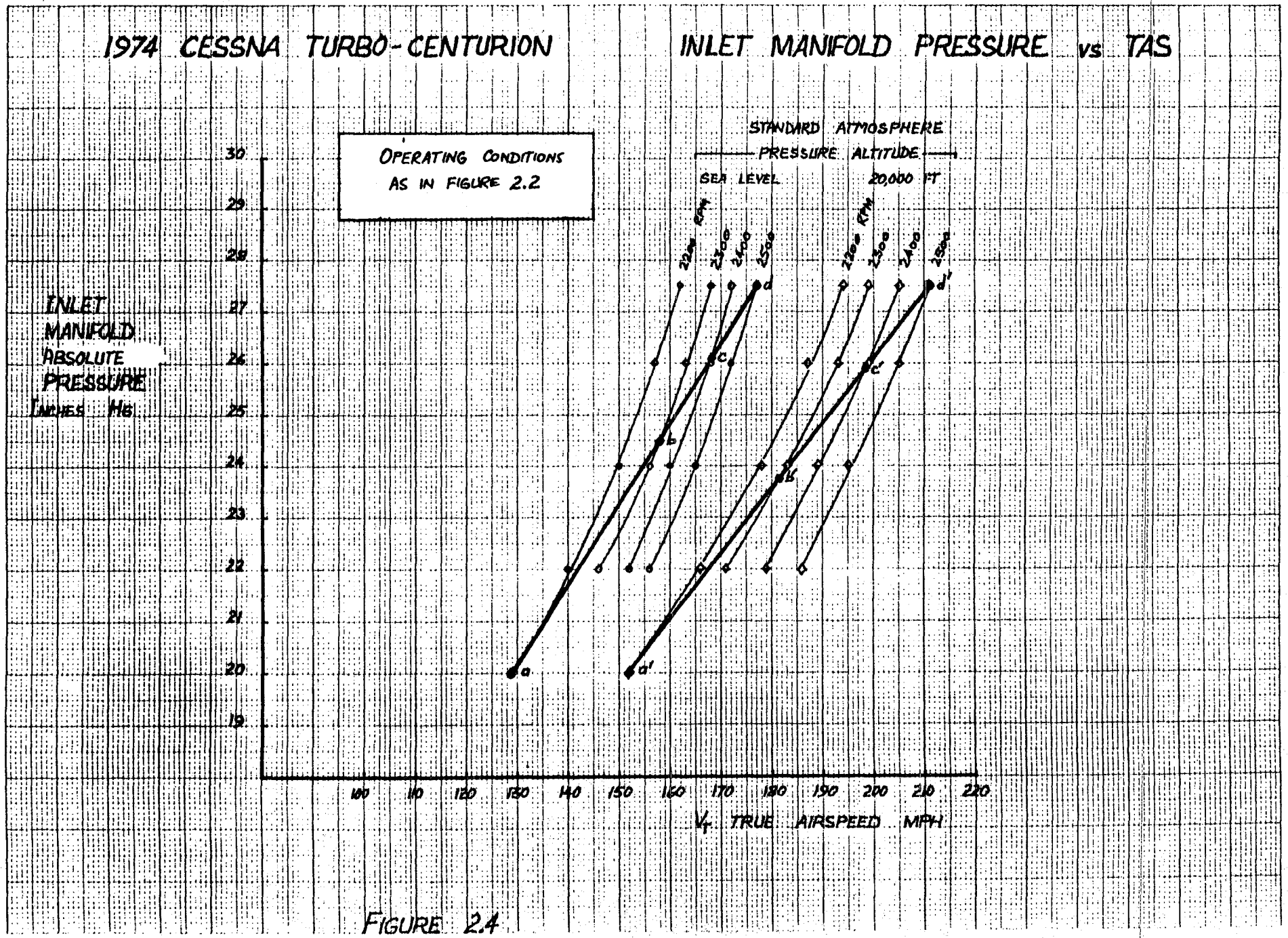
1974 CESSNA TURBO-CENTURION
INLET MANIFOLD PRESSURE vs TAS
OPERATING CONDITIONS AS IN FIGURE 2.2
STANDARD ATMOSPHERE
PRESSURE ALTITUDE
SEA LEVEL
20,000 FT
2200 RPM
2300
2400
2500
INLET MANIFOLD ABSOLUTE PRESSURE INCHES HG
30
29
28
27
26
25
24
23
22
21
20
19
a
b
c
d
a'
b'
c'
d'
100
110
120
130
140
150
160
170
180
190
200
210
220
V_t TRUE AIRSPEED MPH

FIGURE 2.4

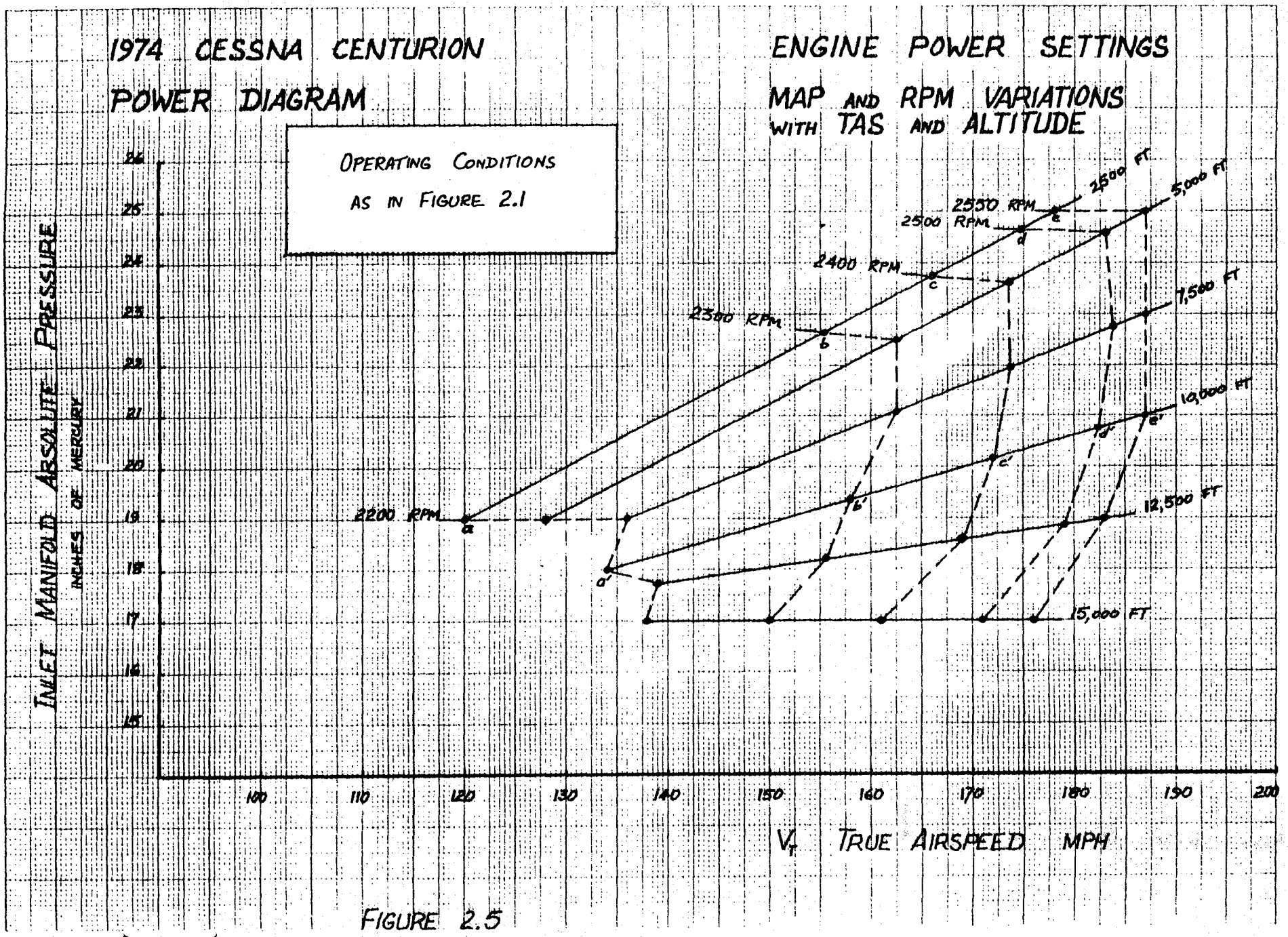
1974 CESSNA CENTURION
POWER DIAGRAM
ENGINE POWER SETTINGS
MAP AND RPM VARIATIONS
WITH TAS AND ALTITUDE
OPERATING CONDITIONS
AS IN FIGURE 2.1
INLET MANIFOLD ABSOLUTE PRESSURE
INCHES OF MERCURY
26
25
24
23
22
21
20
19
18
17
16
15
2200 RPM
2300 RPM
2400 RPM
2500 RPM
2550 RPM
a
b
c
d
e
a'
b'
c'
d'
e'
2,500 FT.
5,000 FT.
7,500 FT
10,000 FT
12,500 FT
15,000 FT
100
110
120
130
140
150
160
170
180
190
200
V_T TRUE AIRSPEED MPH

FIGURE 2.5

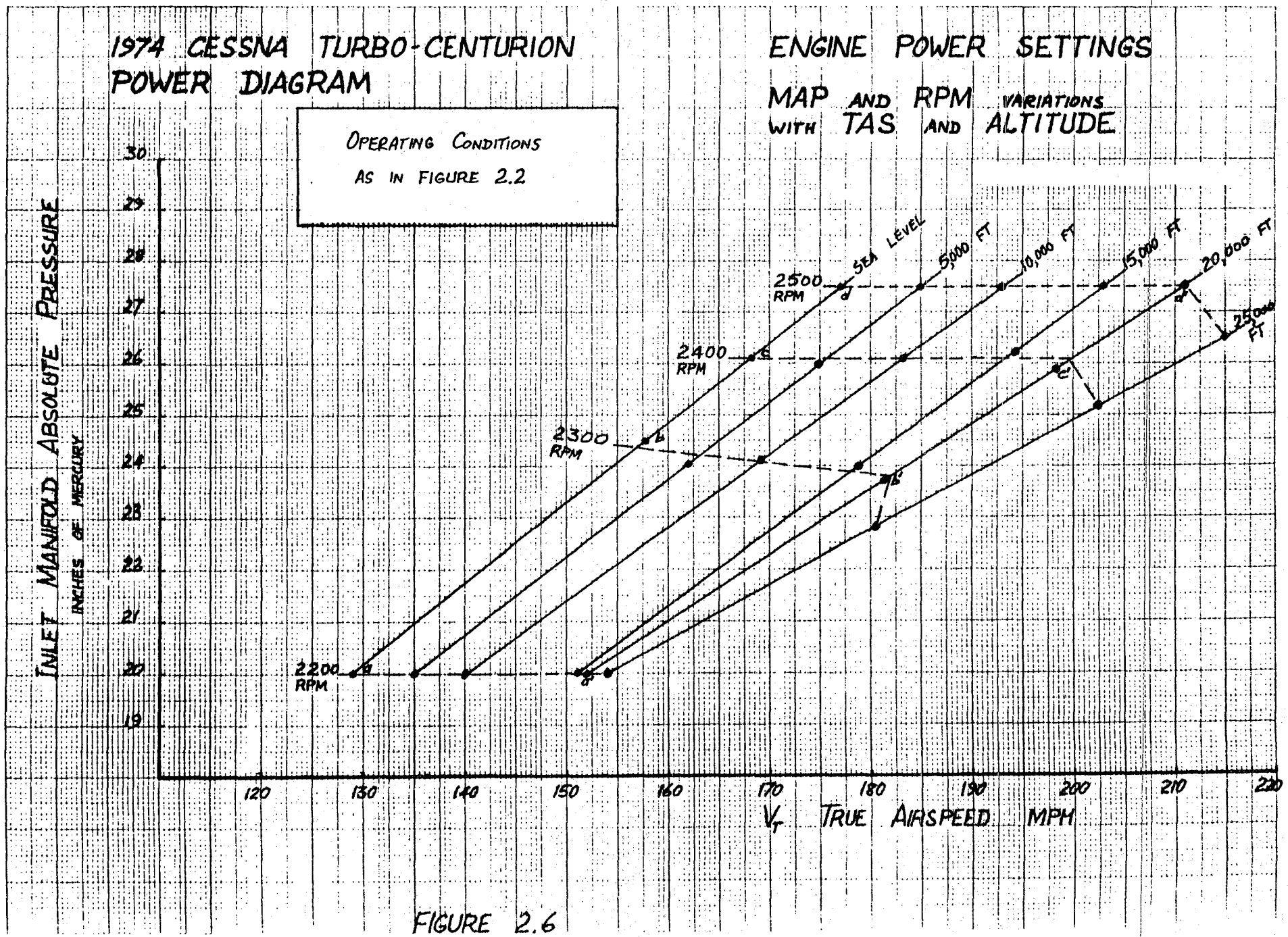
1974 CESSNA TURBO-CENTURION
POWER DIAGRAM
ENGINE POWER SETTINGS
MAP AND RPM VARIATIONS
WITH TAS AND ALTITUDE
OPERATING CONDITIONS
AS IN FIGURE 2.2
INLET MANIFOLD ABSOLUTE PRESSURE
INCHES OF MERCURY
30
29
28
27
26
25
24
23
22
21
20
19
SEA LEVEL
5,000 FT
10,000 FT
15,000 FT
20,000 FT
25,000 FT
2500 RPM
2400 RPM
2300 RPM
2200 RPM
a
b
c
d
e
f
g
120
130
140
150
160
170
180
190
200
210
220
V_T TRUE AIRSPEED MPH

FIGURE 2.6

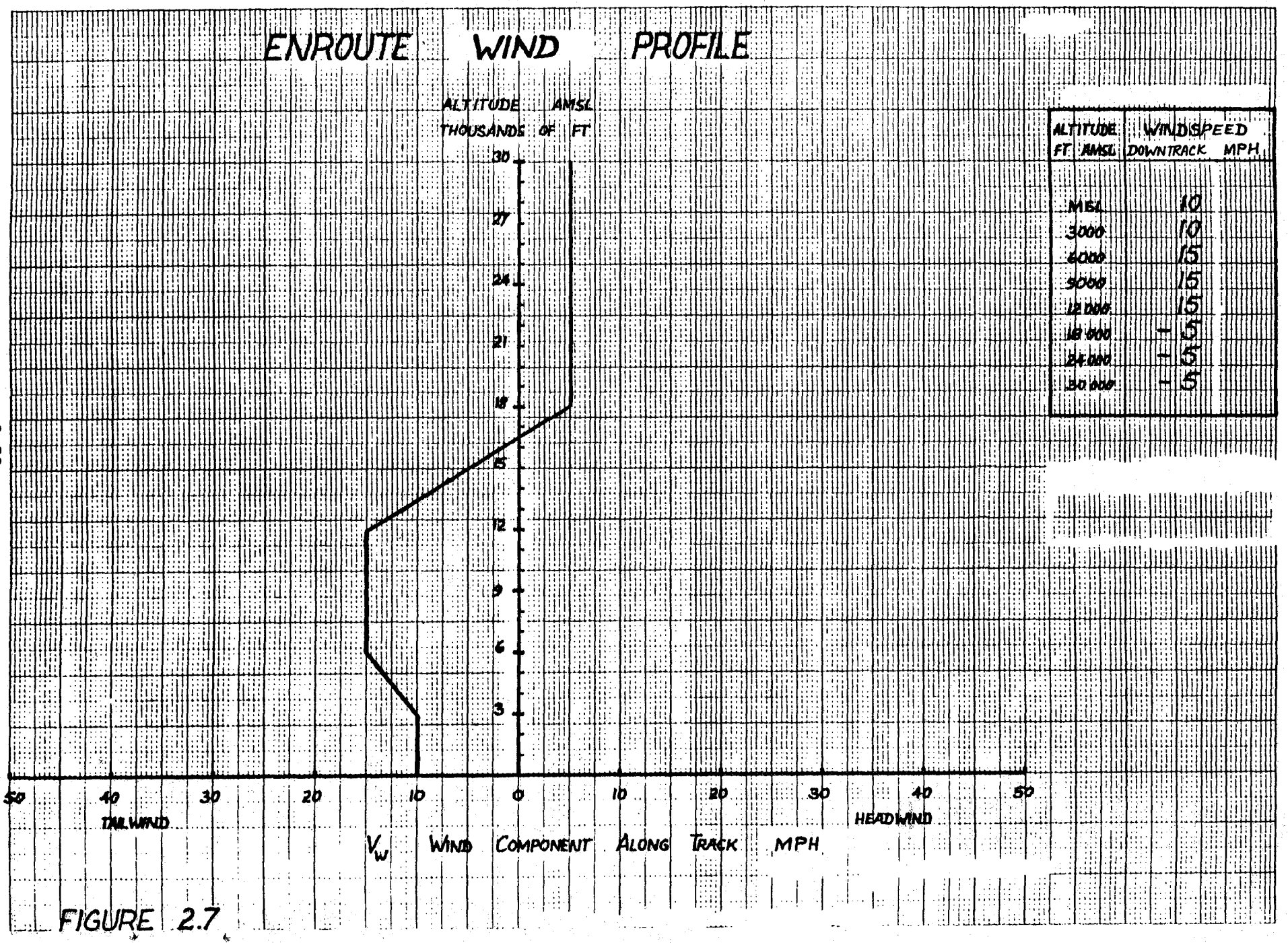
ENROUTE WIND PROFILE
ALTITUDE AMSL
THOUSANDS OF FT
30
27
24
21
18
15
12
9
6
3
50
40
30
20
10
0
10
20
30
40
50
TAILWIND
HEADWIND
V_W WIND COMPONENT ALONG TRACK MPH
ALTITUDE FT. AMSL
WINDSPEED DOWNTRACK MPH
MSL 10
3000 10
6000 15
9000 15
12000 15
18000 -15
24000 -15
30000 -15

FIGURE 2.7

MAXIMUM ACHIEVABLE GROUNDSPEED WITH FUEL CONSTRAINT

PRESS. ALT. FT	V_w MPH	V_t MAX. MPH	V_g MAX. MPH	$\dot{m}_{f_c}$ LB/HR	R^* STATUTE MILES/LB
MSL	10	147	157	67	2.34
5000	13	162	175	74	2.36
10,000	15	177	192	82	2.34
12,000	15	185	200	85	2.35
15,000	5	190	195	83	2.35
20,000	-5	186	181	77	2.35
25,000	-5	212	207	88	2.35

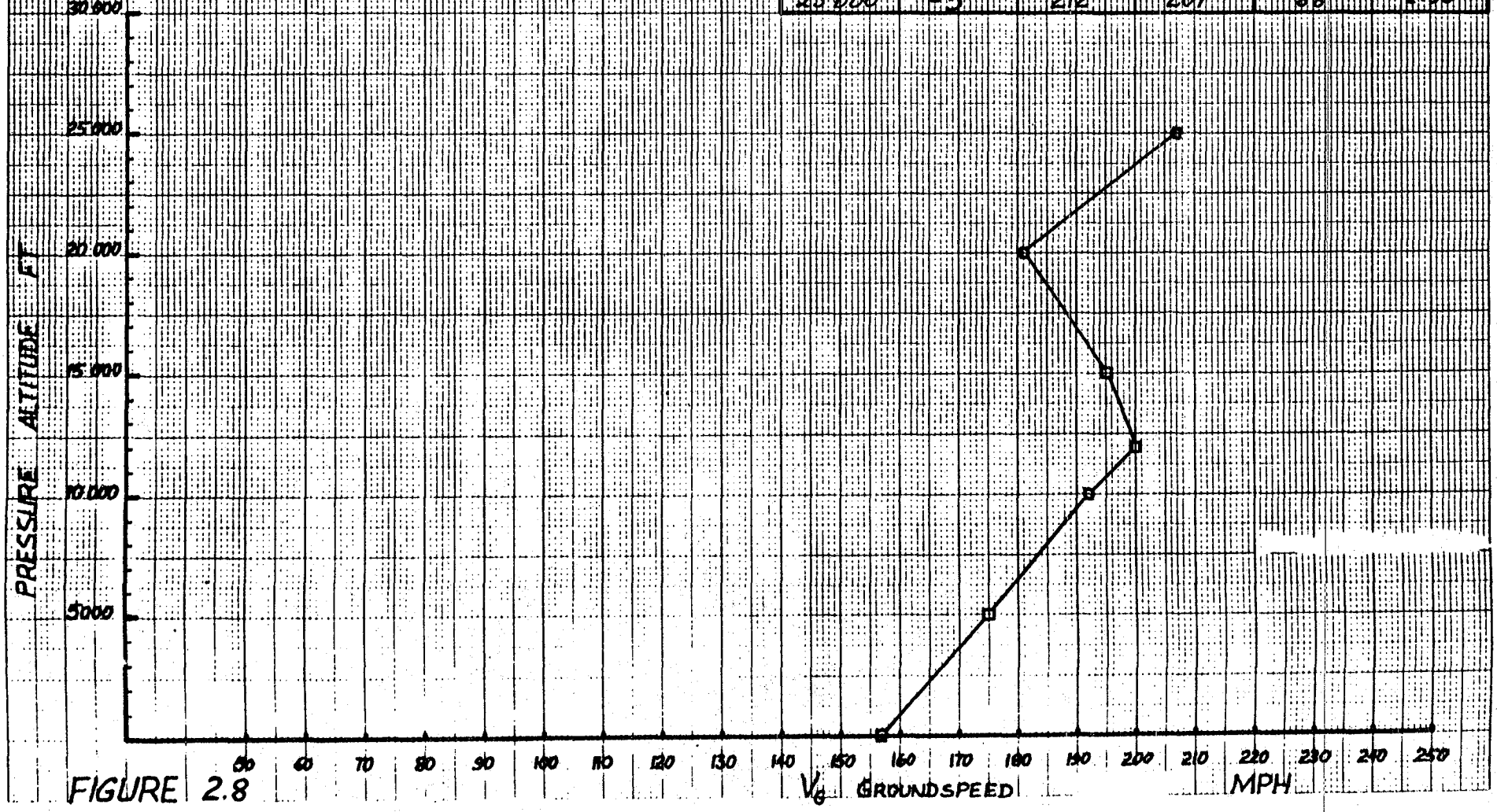

FIGURE 2.8

MAXIMUM R* ANALYSIS

PRESS. ALT. FT	V_w MPH	V_t MPH	V_G MPH	$\dot{m}_{f_t}$ LB/HR	R* G. MILES/LB.
M.S.L.	10	~ 125	135	54	2.50
5000	13	~ 130	143	56	2.55
10 000	15	135	150	57	2.63
12 000	15	145	160	60	2.67
15 000	5	150	155	61	2.54
20 000	-5	163	158	66	2.39
25 000	-6	182	177	73	2.42

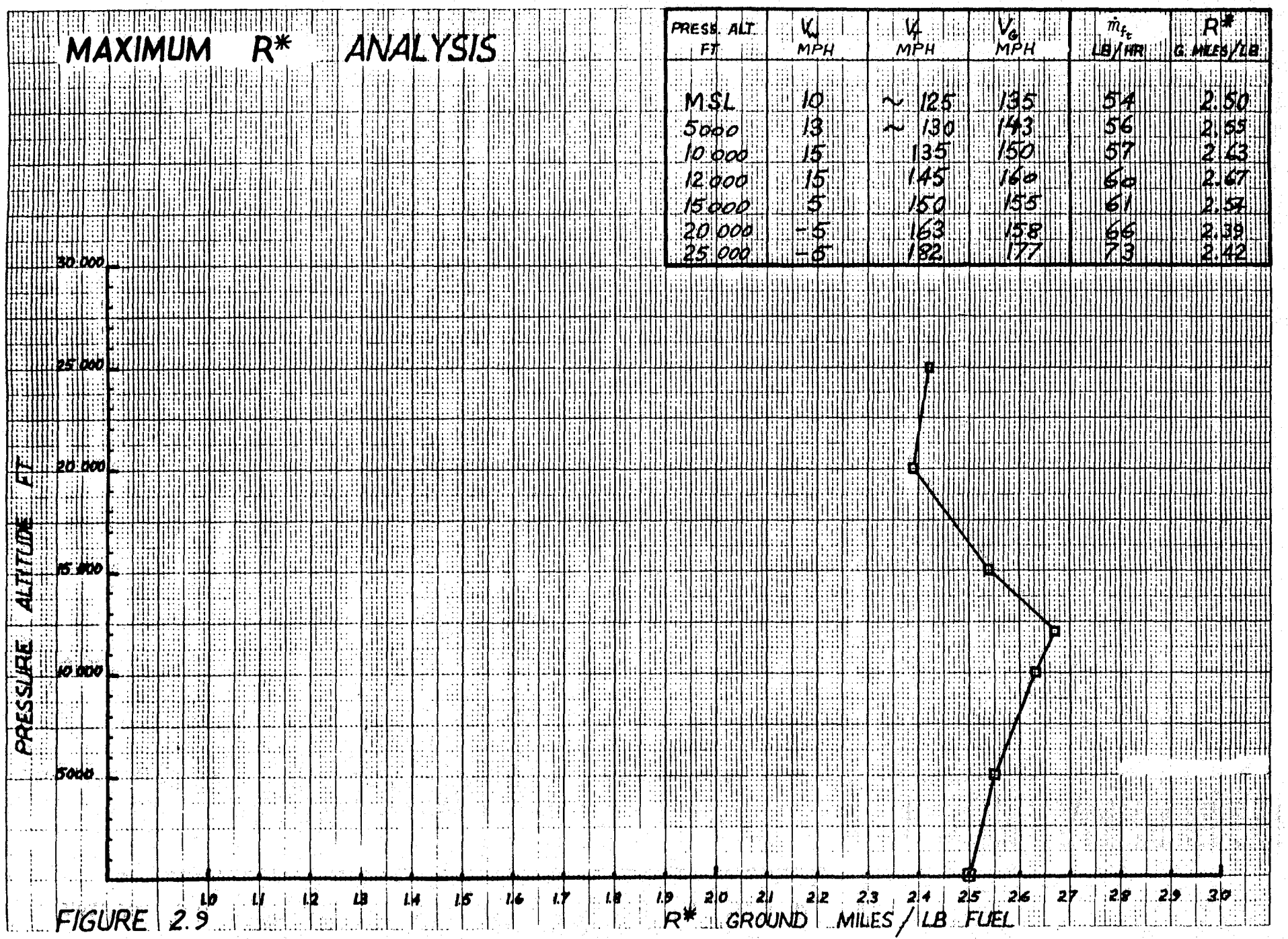

FIGURE 2.9

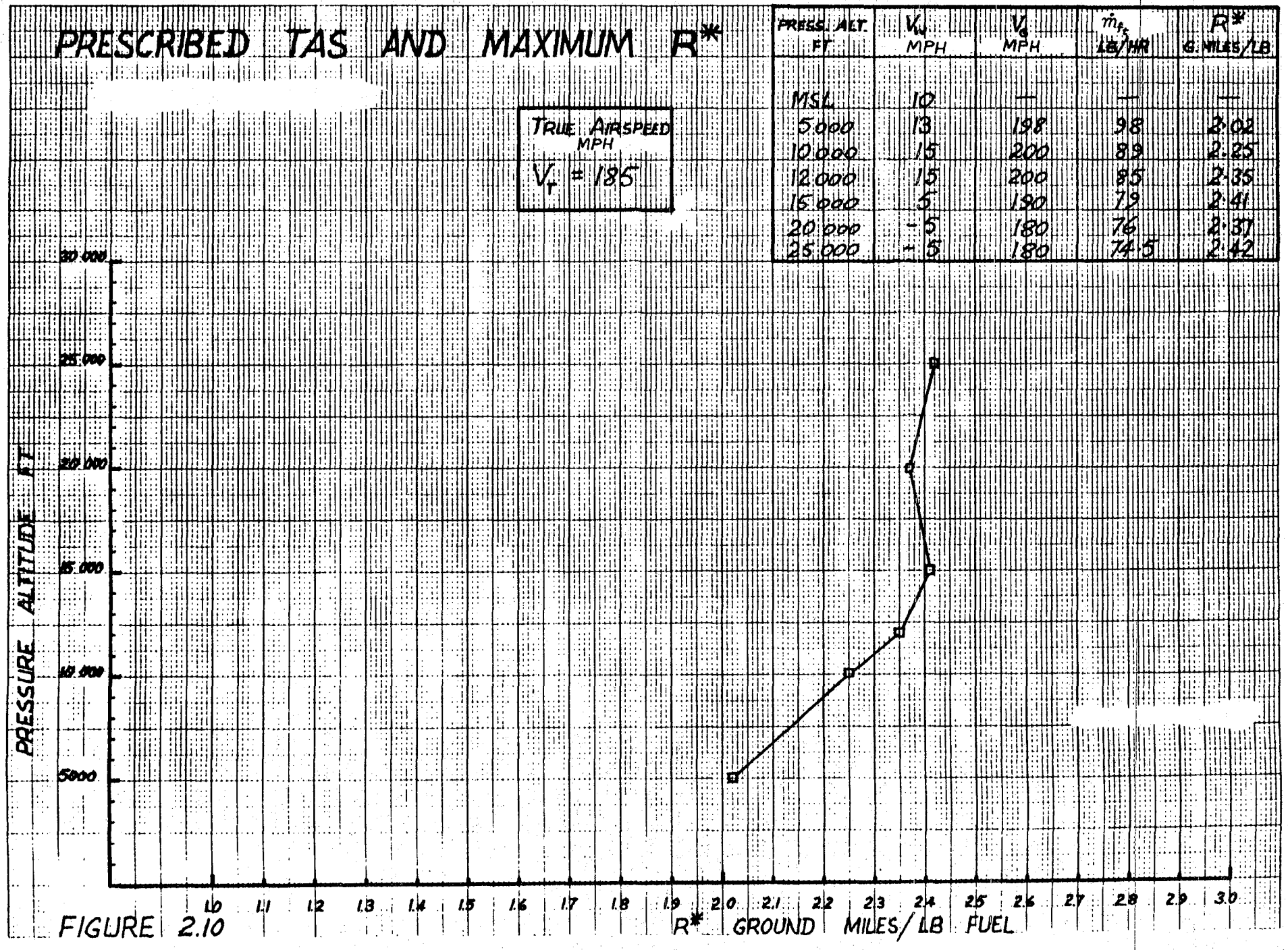
PRESCRIBED TAS AND MAXIMUM R*
TRUE AIRSPEED MPH
V_T = 185
PRESS. ALT. FT
V_W MPH
V_G MPH
$\dot{m}_{f_c}$ LB/HR
R* G. MILES/LB
MSL 10 — — —
5000 13 198 98 2.02
10,000 15 200 89 2.25
12,000 15 200 85 2.35
15,000 5 190 79 2.41
20,000 -5 180 76 2.37
25,000 -5 180 74.5 2.42
PRESSURE ALTITUDE FT
30,000
25,000
20,000
15,000
10,000
5000
1.0 1.1 1.2 1.3 1.4 1.5 1.6 1.7 1.8 1.9 2.0 2.1 2.2 2.3 2.4 2.5 2.6 2.7 2.8 2.9 3.0
R* GROUND MILES/LB FUEL

FIGURE 2.10

PRESCRIBED GROUNDSPEED AND MAXIMUM R*

GROUNDSPEED MPH
V_G = 200

PRESS. ALT. FT	V_W MPH	V_T MPH	$\dot{m}_{f_c}$ LB/HR	R^* G. MILES/LB
MSL	10	190	—	—
5000	13	187	—	—
10 000	15	185	89	2.25
12 000	15	185	85	2.35
15 000	5	195	88	2.27
20 000	-5	205	90	2.22
25 000	-5	205	84	2.38

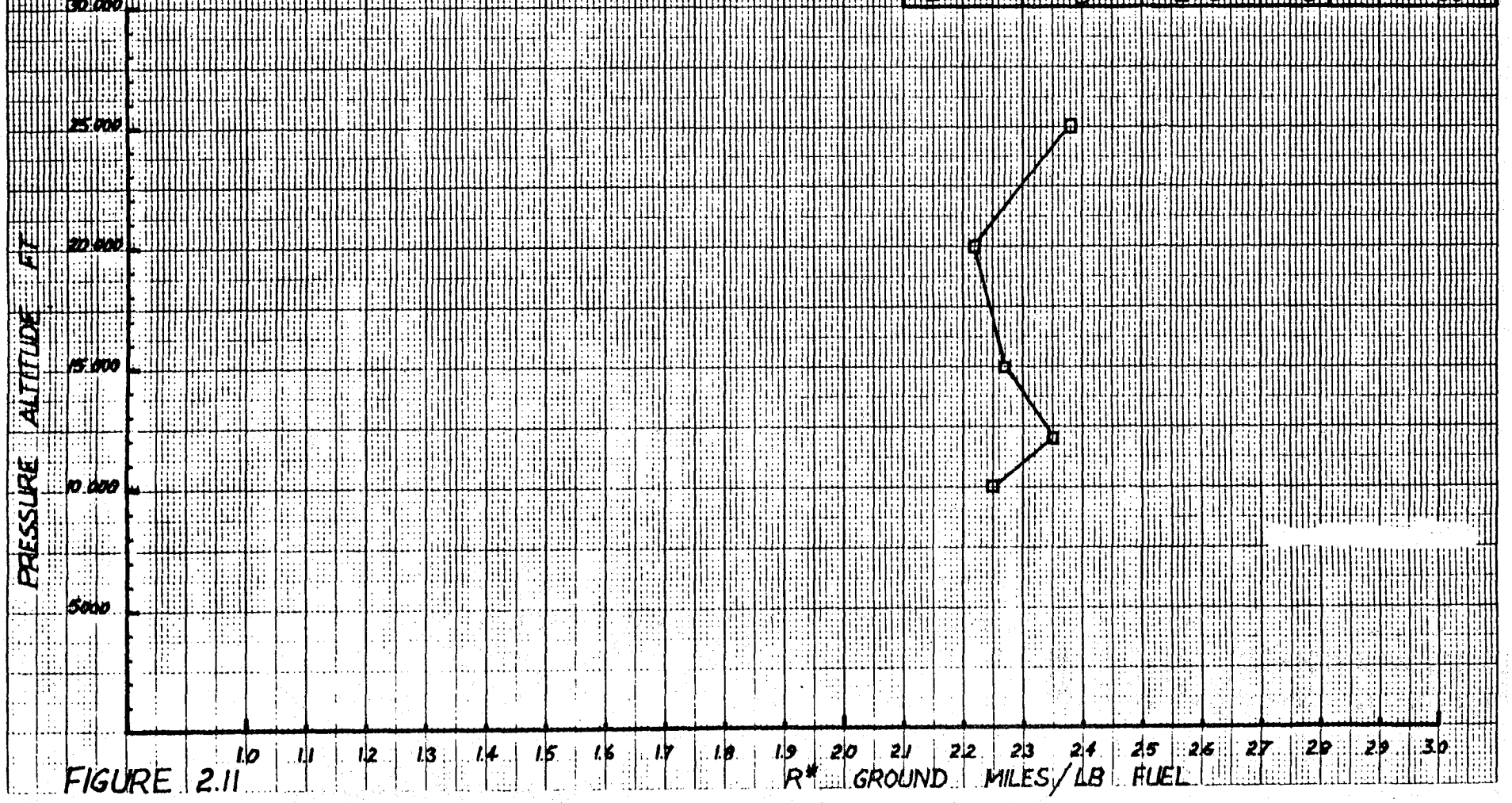

FIGURE 2.11

CHAPTER 3

THE AIRFRAME AND THE ATMOSPHERE

Table of Contents

CHAPTER 3

THE AIRFRAME AND THE ATMOSPHERE

INTRODUCTION

In this chapter we commence the development of an airplane-atmosphere system performance model suitable for maximizing R*. Detailed consideration is given to the airframe and the atmosphere only, while the propeller and engine contributions to R* are represented by the variables η_p (the propulsive efficiency) and c (the engine brake specific fuel consumption).

The model developed incorporates the following airframe and atmosphere variables:

1. Equivalent airspeed (EAS) V_E, knots
2. Altitude, represented by the atmospheric air density ratio σ
3. Airplane gross weight W, lbf
4. Windspeed along track V_w, knots
5. Auxiliary equipment power P_{AUX}, horsepower
6. Airplane longitudinal center of gravity (c.g.) position $\overline{hc}$.

The airframe model of Appendix C is first discussed. The effect of each of the above variables on R* is then examined, and each of those effects is illustrated for the LASA 60 airplane under the assumption that η_p and c are constants. An expression for R* (different from equivalent expressions for R* in Appendix A) is derived which, after expansion in later chapters, will prove most useful to the task of airborne computations.

THE AIRFRAME MATHEMATICAL MODEL

The general airframe mathematical model presented in Appendix C constitutes expressions for:

1. The airframe drag and power required, power-off and power-on (Equations C.1 - C.8)
2. The airframe drag coefficient, power-off and power-on (Equations C.9, C.10, C.29 - C.31).

The approximate geometric and aerodynamic characteristics of the Lockheed LASA 60 airplane are presented in Table 3.1. For this airplane, the longitudinal range of movement of the c.g. is assumed to be limited to $0.15 \leq h \leq 0.30$ by considerations of stability and control power.

Experimental power-off drag data for the LASA 60 with an unspecified c.g. position is presented in Reference 19, and reproduced here in Figure 3.1. The power-off drag polar for the LASA 60 was computed, using Equation C.29 and Table 3.1, for $h = 0.15$ and $h = 0.30$. Plots of these computations are superimposed on Figure 3.1. The computed curves fit the experimental data over the range $0.09 \leq C_L^2 \leq 1.2$. Deviation from the data when $C_L^2 > 1.2$ is considered unimportant: such C_L^2 values correspond to flight at speeds well below the minimum drag speed for which $C_L^2 \simeq 0.8$.

The power-off drag coefficient of the LASA 60, with the c.g. at the aft limit ($h = 0.3$), is represented in this work by:

$$C_D = 0.0402 + 0.052\, C_L^2 \qquad (3.1)$$

Equation 3.1 represents an approximate straight line fit through the experimental data of Figure 3.1, plus an increment to the lift-independent term to account for modifications made to the LASA 60 owned by Princeton University since those experimental data were collected.

The relationship between the drag coefficient power-off C_D and the drag coefficient power-on $C_{D_{ON}}$ is discussed in Appendix C. The difference between C_D and $C_{D_{ON}}$ arises because, in powered flight, the following parameters have values different from those pertaining to power-off flight:

1. $C_{D_{pm}}$
2. C_{m_o}
3. a_{o_w} with corresponding values of δ_w, τ_w and e_t
4. η_t
5. i_w

In Appendix D it is shown that variations in lift-independent drag with power result in

$$D_{ON} = f_D \, D_{OFF} \tag{3.2}$$

where the slipstream interference factor f_D is a constant. Equation 3.2 reflects changes in $C_{D_{pm}}$ and η_t (the term $\xi_t^2 \, K_t S_t \eta_t / S$ in κ_0 only)

in Equation C.29, due to power. Substitution of Equations C.1 and C.5 in Equation 3.2 yields:

$$C_{D_{ON}} = f_D \, C_D \tag{3.3}$$

Changes in items 2, 3 and 5 above, and additional effects of changing η_t, alter this relationship between $C_{D_{ON}}$ and C_D for fixed values of C_L and h. The effects of such changes on C_D were studied for the LASA 60 using Equation C.29. The data set of Table 3.1 was used as a base, and items 2-5 above were separately varied. $C_{D_{pm}}$ and the term $\xi_t^2 K_t S_t \eta_t / S$ in κ_0 were constants in these computations. The range of variation of items 2-5, and the corresponding maximum percentage variations in $|C_L/C_D|$ from the value pertaining to the basic data set at the same C_L and h, are shown in Table 3.2. The actual percentage variations in C_L/C_D, which varied with C_L and h, are the negative percentage contributions to f_D resulting from the variations in items 2-5. Table 3.2 applies to the range of lift coefficient $0.3 \leq C_L \leq 1.2$ and to the range of c.g. position $0.15 \leq h \leq 0.3$.

For most GA airplanes it is considered that the incremental changes in items 2-5 above, due to power, will lie well within the incremental changes shown in Table 3.2. The corresponding maximum percentage variations in $|C_L/C_D|$ shown in Table 3.2 are taken to indicate that the effects of power on drag, in addition to those considered in the formulation of Equation 3.3, are small for GA airplanes.

f_D is taken to be a constant in this work, except in the discussion of center of gravity position in this chapter.

DEPENDENCE OF R* ON AIRFRAME OPERATION AND ATMOSPHERIC CONDITIONS

In this section, an expression for R* is derived which is equivalent to the various expressions for R* in Appendix A. The new expression models the airframe and atmosphere contributions to R* in detail, while expressing the propeller and engine contributions to R* in terms of the variables η_p and c. The airframe and atmosphere contributions to R* are illustrated for the LASA 60 under the assumption that η_p and c are constants.

It is assumed initially that all of the variables contributing to the value of R* are constrained to have specific constant values, with the exception of equivalent airspeed, altitude and gross weight. A simple expression for R*, which accounts for these three variables is presented. That expression is then expanded as V_w, P_{AUX} and h are consecutively introduced into it as explicit variables.

Airspeed, Altitude and Gross Weight

In this discussion, the following assumptions are made:

η_p = constant = 0.75 in all Figures

c = constant = 0.45 lb/BHP.hr in all Figures

$V_w = 0$

$P_{AUX} = 0$

h = constant = 0.3 in all Figures.

With these assumptions, the most convenient form for R* is

$$R^* = \frac{V_E}{P_R\sqrt{\sigma}} \frac{\eta_p}{c} \tag{3.4}$$

which is obtained from Equation A.12. Consideration of Appendix C (Equations C.4, C.9, C.11 and C.29) reveals that $P_R\sqrt{\sigma}$ is a function only of V_E, W and h for a given airplane. Therefore with the above assumptions, $P_R\sqrt{\sigma}$ and R* in Equation 3.4 are functions of V_E and W only. Figure 3.2 shows R* computed for the LASA 60, plotted against V_E for a range of gross weights. The family of curves in Figure 3.2 applies to all altitudes.

Line A in Figure 3.2 represents the variation of R^*_{max} with gross weight (R^*_{max} is the maximum achievable value of R* for a given gross weight). Since R^*_{max} corresponds to flight at maximum L/D_{OFF} under the stated assumptions, line A also depicts the variation of minimum drag EAS with gross weight. The variation of R^*_{max} and the minimum drag EAS along line A are shown in Figure 3.3, the former being presented as a proportion of its value at W = 3,000 lb.

Equations C.11 and A.15 show that for flight at minimum drag (md) EAS with zero wind,

EAS_{md} is proportional to $\sqrt{W}$

R^*_{max} is proportional to $1/W$

These are the forms of the curves of Figure 3.3.

Consider the following two flight conditions:

1. Flight at constant EAS as the gross weight varies
2. Flight at constant power as the gross weight varies.

Lines B and C in Figure 3.2 represent flight at constant EAS with varying gross weight, the EAS corresponding to minimum drag for

W = 3,000 lb and W = 3,400 lb respectively. R* varies from R^*_{max} along line B (C) at every gross weight except W = 3,000 (3,400) lb. This variation is expressed as an R* penalty, defined by

$$R^* \text{ PENALTY} = \left[\frac{R^* - R^*_{max}}{R^*_{max}} \right] \times 100\ \%$$

Lines B and C in Figure 3.4 correspond with lines B and C in Figure 3.2 and depict this R* penalty.

Similarly lines D and E in Figure 3.2 represent flight at constant power with varying gross weight, the power level corresponding to that required at minimum drag EAS for a gross weight of 3,000 lb and 3,400 lb respectively. These lines D and E are straight with a slope given by differentiating Equation 3.4 with P_R constant:

$$\left.\frac{\partial R^*}{\partial V_E}\right|_{P_R} = \frac{\eta_p}{P_R \sqrt{\sigma}\, c} \qquad (3.5)$$

The slopes of lines D, E in Figure 3.2 are therefore different and invariant with flight density altitude. Curves D, E in Figure 3.4 correspond with lines D, E in Figure 3.2 and depict the R* penalty (also independent of density altitude) for flight at constant power as the gross weight varies.

It is clear from Figure 3.2 that both V_E and W have a significant effect on R*. The curves of Figures 3.2 and 3.4 indicate that as airplane gross weight decreases during a trip due to fuel burn, it is more fuel-efficient to fly at constant EAS than to fly at constant

power, whenever the EAS exceeds the minimum drag speed. At constant V_E and W, R* is independent of altitude.

Wind

In this discussion the following assumptions are made:

η_p = constant = 0.75 in all Figures

c = constant = 0.45 lb/BHP.hr in all Figures

P_{AUX} = 0

h = constant = 0.3 in all Figures.

The effect of wind on R* is clearly seen from Equation A.12. With the above assumptions this is written

$$R^* = \left[1 + \frac{V_w\sqrt{\sigma}}{V_E}\right] \frac{V_E}{P_R\sqrt{\sigma}} \frac{\eta_p}{c} \qquad (3.6)$$

The effect of wind is to multiply the right hand side of Equation 3.4 by the factor $(1 + V_w \sqrt{\sigma}/V_E)$. For any given gross weight, $P_R \sqrt{\sigma}$ is a function of V_E only. Therefore, for a given gross weight and EAS, the effect of a given equivalent windspeed on R* is identical at all altitudes. The altitude yielding the maximum value of R*, at any gross weight and EAS, is that at which the equivalent windspeed $V_w \sqrt{\sigma}$ is a maximum. If a constant tailwind (headwind) V_w exists at all altitudes, maximum R* is achieved by flying at sea level (the highest altitude possible).

A plot of $P_R \sqrt{\sigma}$ versus V_E facilitates the computations in Equation 3.6. In particular, the EAS yielding maximum R* in any equivalent wind

condition is readily obtained from such a plot, as illustrated for the LASA 60 in Figure 3.5. The equivalent windspeed is inscribed on the abscissa, tailwinds to the left and headwinds to the right of the origin. The straight line drawn from this $V_W \sqrt{\sigma}$ point yields the EAS for maximum R* at the point of tangency to the appropriate gross weight curve. This construction is shown in Figure 3.5: points A, B and C represent the operating points yielding maximum R* corresponding to equivalent windspeeds $V_W \sqrt{\sigma}$ = -20, 0, + 20 knots respectively, for W = 2,600 lb and any altitude.

Computed performance for the LASA 60 is shown in Figures 3.6-3.8.

Figure 3.6 shows the EAS required to achieve maximum R*, plotted against V_W, for three values of the gross weight W and two density altitudes. When the abscissa of Figure 3.6 is relabelled Equivalent Windspeed $V_W \sqrt{\sigma}$ without a scale change, the sea level curve for each gross weight will apply to all altitudes and the 10,000 ft density altitude curves will cease to be meaningful.

Figure 3.7 shows the ratio of the maximum value of R* obtainable with wind to the maximum value of R* obtainable with zero wind, plotted against $V_W \sqrt{\sigma}$, for three values of gross weight. These curves apply to all altitudes.

If an airplane is flown at the minimum drag speed in non-zero wind conditions, the maximum possible R* is not achieved. The

variation from the maximum is expressed as an R* penalty, defined by

$$R^* \text{ PENALTY} = \left[\frac{R^*_{md} - R^*_{max}}{R^*_{max}} \right] \times 100\ \%$$

where R^*_{md} = R* at minimum drag EAS

R^*_{max} = maximum achievable R*

both computed for the appropriate gross weight and the prevailing V_w and σ. Figure 3.8 shows this R* penalty plotted against $V_w\sqrt{\sigma}$, for three values of gross weight. These curves apply to all altitudes. The R* penalty is in general more severe for headwinds than for tailwinds.

The effect of equivalent windspeed on R* and upon the EAS for maximum R* is clearly significant.

Auxiliary Equipment Power

In this discussion, the following assumptions are made:

η_p = constant = 0.75 in all Figures

c = constant = 0.45 lb/BHP.hr in all Figures

h = constant = 0.3 in all Figures.

The auxiliary equipment power delivered per engine is defined by Equations A.4 and A.5a. When c is defined equal to c', then P_{AUX} is defined to be zero.

Equation A.12 shows the dependence of R* on P_{AUX}:

$$R^* = \left[1 + \frac{V_w \sqrt{\sigma}}{V_E} \right] \frac{V_E}{(P_R \sqrt{\sigma} + E\, \eta_p\, P_{AUX} \sqrt{\sigma})} \frac{\eta_p}{c} \qquad (3.7)$$

A plot of $(P_R \sqrt{\sigma} + E\, \eta_p\, P_{AUX} \sqrt{\sigma})$ versus V_E, for any value of the equivalent auxiliary equipment power $P_{AUX} \sqrt{\sigma}$, would appear similar to the curves of Figure 3.5. The effect of P_{AUX} is to shift the plot of $P_R \sqrt{\sigma}$ versus V_E vertically by the constant amount $E\, \eta_p\, P_{AUX} \sqrt{\sigma}$. Consequently, as P_{AUX} increases (decreases) from zero:

1. The value of R* decreases (increases) in every flight condition,
2. The EAS yielding maximum R* increases (decreases) for any given equivalent windspeed.

Figure 3.9 shows the effects of $P_{AUX} > 0$ on R^*_{max} (the maximum achievable value of R* at a given gross weight) and on the EAS required for R^*_{max}, computed for the LASA 60. The curves are drawn for three values of the gross weight, two density altitudes and zero wind conditions. When the abscissas of Figure 3.9 are read as $P_{AUX} \sqrt{\sigma}$, the sea level curves for each gross weight apply to all altitudes, and the 10,000 ft density altitude curves cease to be meaningful.

When the Equivalent Quantities V_E, $V_w \sqrt{\sigma}$ and $P_{AUX} \sqrt{\sigma}$, and the gross weight are constants in Equation 3.7, R* is independent of altitude.

Equation 3.7 is now rewritten as:

$$R^* = \left[1 + \frac{V_w \sqrt{\sigma}}{V_E}\right] \left[\frac{1}{1 + \dfrac{E\, \eta_p\, P_{AUX} \sqrt{\sigma}}{P_R \sqrt{\sigma}}}\right] \frac{V_E}{P_R \sqrt{\sigma}} \quad \frac{\eta_p}{c} \tag{3.8}$$

The form of Equation 3.8 is convenient for the following discussion of the effects of center of gravity position on R*.

Center of Gravity Position

The airframe model of Appendix C assumes that the airplane is laterally symmetric about its longitudinal center line, with respect to geometry and mass distribution. The airplane center of gravity (c.g.) is assumed to lie on the longitudinal center line, at a distance $h\bar{c}$ aft of the leading edge of the mean aerodynamic chord of the wing.

We now consider the effect on R* of varying h. Considering the right hand side of Equation 3.8, the quantities which are functions of h are

1. $P_R\sqrt{\sigma}$ - see Equations C.4 and C.29
2. η_p - Equation D.48 shows that η_p depends upon f_D, which has been shown above to demonstrate small variations with h.

$P_R\sqrt{\sigma}$ and η_p always appear together in Equation 3.8 as the ratio $\eta_p/P_R\sqrt{\sigma}$. Instead of introducing h as an independent variable into $P_R\sqrt{\sigma}$ and η_p, it is more convenient to:

1. Compute $\eta_p/P_R\sqrt{\sigma}$ for a reference c.g. postion $h_{ref}\bar{c}$, and
2. Adjust that computed value for variations in h from h_{ref}, by means of a correction factor which is some function of $dh = h - h_{ref}$.

This procedure is equivalent to expanding $\eta_p/P_R\sqrt{\sigma}$ into a Taylor Series in dh.

Accordingly, we define

$$\left[\frac{\eta_p}{P_R\sqrt{\sigma}}\right]_{h_{ref}} = \frac{\eta_p}{P_R\sqrt{\sigma}} \quad \text{at } h = h_{ref}$$

$$R^*_{h_{ref}} = R^* \text{ at } h = h_{ref}$$

Equation 3.8 is now written:

$$R^*_{h_{ref}} = \left[1 + \frac{V_w\sqrt{\sigma}}{V_E}\right] \left\{\frac{1}{1 + E\,P_{AUX}\sqrt{\sigma}\left[\frac{\eta_p}{P_R\sqrt{\sigma}}\right]_{h_{ref}}}\right\} \frac{V_E}{c}\left[\frac{\eta_p}{P_R\sqrt{\sigma}}\right]_{h_{ref}} \tag{3.9}$$

Now from Equation A.13,

$$P_R\sqrt{\sigma} = D_{OFF}\,V_E/325.65 \quad \text{horsepower}$$

Therefore

$$\frac{\eta_p}{P_R\sqrt{\sigma}} = \frac{325.65\,\eta_p}{D_{OFF}\,V_E}$$

and invoking Equations D.47 and 3.2,

$$\frac{\eta_p}{P_R\sqrt{\sigma}} = \frac{325.65\,\eta_a}{V_E\,f_J\,W}\quad\frac{L}{f_D\,D_{OFF}} \tag{3.10}$$

$$= \frac{325.65\,\eta_a}{V_E\,f_J\,W}\quad\frac{L}{D_{ON}} \tag{3.11}$$

where η_a = propeller efficiency in the presence of the body,

f_J = constant.

Equation 3.10 shows that, if f_D were truly a constant, variations in $\eta_p/P_R\sqrt{\sigma}$ with h could be evaluated in terms of the variation in L/D_{OFF} with h, assuming η_a is independent of h. However, f_D varies slightly with power condition, h and C_L, as previously discussed. The variation of $\eta_p/P_R\sqrt{\sigma}$ with h is therefore more accurately computed from the variation of L/D_{ON} with h, as shown by Equation 3.11.

We here evaluate the variation of L/D_{OFF} with h for the LASA 60 airplane, and propose a general model for such variations for GA airplanes. A general model for the variation of L/D_{ON} with h is then proposed, and used to describe variations of R* with h for GA airplanes (η_a is assumed to be independent of h in this discussion - the validity of this assumption is addressed in Chapter 4).

Using Equation C.29 and Table 3.1, the percentage variation in L/D_{OFF} from that pertaining to the nominal forward c.g. limit was computed for the LASA 60, as h and C_L were varied. The full lines A, B and C of Figures 3.10 and 3.11 show the results of these computations for C_L = 0.4, C_L = 0.8 and h = 0.3 respectively. These percentage variations in L/D_{OFF} with h and C_L may be visualized as the height of a surface, as shown schematically in Figure 3.12. Lines A, B and C in Figure 3.12 correspond to lines A, B and C respectively in Figures 3.10 and 3.11.

The form of Figure 3.12 is considered to be typical of GA airplanes. The height of that surface for any particular airplane is a function of

C_L, the position of the c.g. behind the nominal forward limit, and all the geometric and aerodynamic characteristics of the airplane. The height of the surface behind the aft c.g. limit (nominally h = 0.3 for the LASA 60) is not of interest for current GA airplanes, since the aft c.g. limits of such airplanes are prescribed by stability considerations[†].

From this discussion of L/D_{OFF} for the LASA 60, the following model is proposed for variations in L/D_{OFF} with h for GA airplanes:

$$\left[\frac{L}{D_{OFF}}\right]_h = \left[\frac{L}{D_{OFF}}\right]_{h_{ref}} (1 + \zeta C_L \, dh) \tag{3.12}$$

where

$\left[\frac{L}{D_{OFF}}\right]_h$ = L/D_{OFF} corresponding to the c.g. position $h\bar{c}$

$\left[\frac{L}{D_{OFF}}\right]_{h_{ref}}$ = L/D_{OFF} corresponding to the c.g. position $h_{ref}\,\bar{c}$

$dh = h - h_{ref} > 0$ for $h\bar{c}$ aft of $h_{ref}\,\bar{c}$

ζ = positive constant

[†]Note however, that the maximum increases in L/D_{OFF} along lines A and B in Figure 3.10 occur for h > 0.3, and correspond to positive tail loads. Laitone (20) has shown that induced drag is minimized with a positive tail load (upload) for all values of $C_L > 0$.

and both $h\bar{c}$ and $h_{ref}\,\bar{c}$ lie anywhere within the allowable c.g. range. This linearization appears justified on the basis of Figures 3.10 and 3.11. For the LASA 60 airplane defined by Table 3.1, lines A, B and C of Figures 3.10 and 3.11 (corresponding to $h_{ref} = 0.15$) give $\zeta \simeq 0.375$.

The sensitivity of ζ to all the geometric and aerodynamic characteristics appearing in Equation C.29 for C_D was not studied. However, as an indication of this sensitivity, the following studies were performed:

1. The dotted curves of Figures 3.10 and 3.11 give the effects on ζ of a single variation in $C_{D_{pm}}$, while all other variables retain their values in Table 3.1. For those dotted curves, $h_{ref} = 0.15$ and $\zeta \simeq 0.467$. A low lift-independent drag coefficient therefore contributes to a high drag-sensitivity to c.g. position at any C_L.
2. Figure 3.13 gives the effects on ζ of varying C_{m_o} at $C_L = 0.8$, while all other variables retain their values in Table 3.1. For those curves, $h_{ref} = 0.15$ and:
   (a) for $C_{m_o} = 0$, $\zeta \simeq 0.217$
   (b) for $C_{m_o} = -0.25$, $\zeta \simeq 0.479$
3. Individual variations in the parameters given in Table 3.2 (with the exception of C_{m_o}), within the limits given therein, were performed while all other variables retained their values in Table 3.1.

The resulting deviations of the surface of Figure 3.12 from the surface corresponding to the basic data set of Table 3.1 were not large in the region ($0.3 \leq C_L \leq 1.2$, $0.15 \leq h \leq 0.30$). The corresponding variations in ζ (with $h_{ref} = 0.15$) from the basic value of 0.375 were not computed, but are expected to be small.

The effect of c.g. position on L/D_{ON} may be determined from the foregoing discussion. Running propellers effect changes in $C_{D_{pm}}$ and in the parameters listed in Table 3.2, as previously discussed. It has just been shown that variations of these quantities do not change the form of Equation 3.12, but merely the value of ζ. For powered flight we therefore replace ζ in Equation 3.12 by ξ and write

$$\left[\frac{L}{D_{ON}}\right]_h = \left[\frac{L}{D_{ON}}\right]_{h_{ref}} (1 + \xi C_L \, dh) \qquad (3.13)$$

where ξ is a positive constant. The values of $C_{D_{pm}}$ and the parameters in Table 3.2, used to compute ξ for a given airplane, should be average values pertaining to the powered flight of that airplane. The above sensitivity study of the effects on ζ of variations in $C_{D_{pm}}$ and in the parameters in Table 3.2 indicates that ξ will probably differ little from ζ for most GA airplanes.

From Equation 3.11 we see that the percentage variation of $\eta_p/P_R \sqrt{\sigma}$ is identical to the percentage variation of L/D_{ON} with h.

Therefore,

$$\left[\frac{\eta_p}{P_R\sqrt{\sigma}}\right]_h = \left[\frac{\eta_p}{P_R\sqrt{\sigma}}\right]_{h_{ref}} (1 + \xi C_L\, dh) \qquad (3.14)$$

Using Equations 3.9 and 3.14, we now write R* for the c.g. position $h\bar{c}$:

$$R^* = \left[1 + \frac{V_w\sqrt{\sigma}}{V_E}\right]\left\{\frac{1}{1 + EP_{AUX}\sqrt{\sigma}\left[\frac{\eta_p}{P_R\sqrt{\sigma}}\right]_{h_{ref}} (1 + \xi C_L\, dh)}\right\}\frac{(1+\xi C_L\, dh)V_E}{c}\left[\frac{\eta_p}{P_R\sqrt{\sigma}}\right]_{h_{ref}} \qquad (3.15)$$

where both $h\bar{c} = (h_{ref} + dh)\,\bar{c}$ and $h_{ref}\,\bar{c}$ lie anywhere within the allowable c.g. range. When $h\bar{c}$ is aft of $h_{ref}\,\bar{c}$, $dh > 0$. Equation 3.15 is applicable to standard and non-standard atmospheric conditions.

This analysis has conveniently accounted for variations of f_D with h. Henceforth f_D is considered to be a constant when $h = h_{ref}$.

Conclusions

The following conclusions may be drawn from Equation 3.15, when η_p(at $h = h_{ref}$) and c are assumed to be constants:

1. When all Equivalent Quantities, gross weight and c.g. position $h\bar{c}$ are constants, R* is independent of altitude and when, in addition, $P_{AUX} = 0$:

2. R* increases as the c.g. is moved aft within the allowable c.g. range. The maximum value of R* is achieved, in all flight conditions, with the c.g. at the aft limit.

3. The percentage increase in R*, for a given aft shift in c.g. position, increases with increasing C_L and hence
   (a) Increases with increasing W
   (b) Increases with decreasing EAS
4. The percentage increase in L/D_{OFF}, shown by the full lines of Figures 3.10 and 3.11, are taken to be indicative of the effect of c.g. position on R* for the LASA 60.

The influence of c.g. position on the second term of Equation 3.15 is negligible when P_{AUX} is small, for all values of η_p.

It is apparent that c.g. position can have a significant effect on R*. The magnitude of this effect for any particular GA airplane, characterized by ξ, depends upon the geometric and aerodynamic characteristics of that airplane.

A CONVENIENT R* MODEL

Equation 3.15 is equivalent to the numerous expressions for R* in Appendix A.

In Equation 3.15, $P_R\sqrt{\sigma}$ at $h = h_{ref}$ is a function of V_E and W only, and all other airframe and atmosphere variables are explicitly represented. The reason for expressing R* in this form will become apparent in the following chapter, where the variable nature of η_p is discussed.

SUMMARY

Airframe and atmosphere contributions to R* have been examined. Equation 3.15 has been derived and will be further developed, in the

next chapter, into a model for R* which is convenient for airborne computations.

Assuming that the propulsive efficiency and the engine brake specific fuel consumption are constants, it has been shown that: equivalent airspeed, gross weight and equivalent windspeed have significant effects on R*; longitudinal c.g. position can have a significant effect on R*, depending upon the airplane design and operation; auxiliary equipment power in general has a small effect on R*; and when all Equivalent Quantities, gross weight and c.g. position are constants, R* is independent of altitude.

TABLE 3.1

LOCKHEED LASA 60 CHARACTERISTICS

The symbols used are defined in Appendix C.

$S = 210 \text{ ft}^2$

$S_t = 55.43 \text{ ft}^2$

$\bar{c} = 5.46 \text{ ft}$

$\ell = 16.2 \text{ ft}$

$h_o = 0.2$

$A_w = 7.13$	$A_t = 3.98$
$b_w = 38.687 \text{ ft}$	$b_t = 14.854 \text{ ft}$
$K_w = 0.011$	$K_t = 0.011$
$\xi_w = 0.4$	$\xi_t = 0$
$g_o = 2.0 \text{ ft}$	$\delta_t = 0.028$

In power-off flight:

$C_{m_o} = -0.15$	$i_w = 5.80$ degrees
$a_{o_w} = 5.73 \text{ radian}^{-1}$	$e_t = 1.575$
$\delta_w = 0.063$	$\eta_t = 1.0$
$\tau_w = 0.2$	$C_{D_{pm}} = 0.0393$

Values for δ_w, τ_w, K_w, ξ_w, a_{o_w}, e_t, δ_t, K_t, ξ_t and i_w were determined with the assumptions that:

1. The wing is untwisted, has a rectangular planform, and has a uniform NACA 4412 section.
2. The tailplane is untwisted, has a rectangular planform, and has a uniform NACA 0012 section.

TABLE 3.2

LOCKHEED LASA 60

EFFECTS OF PARAMETER VARIATION ON AIRFRAME LIFT TO DRAG RATIO

PARAMETER	PARAMETER RANGE OF VARIATION	ABSOLUTE % VARIATION C_L/C_D AT FIXED C_L AND h. $0.3 \leq C_L \leq 1.2$ $0.15 \leq h \leq 0.30$
C_{m_o}	- 0.1 to - 0.2	< 2.5%
a_{o_w}	5.73 ± 25% per radian [with corresponding changes in δ_w, τ_w and e_t - see Appendix C]†	< 1.5%
η_t	0.8 to 1.6	< 0.5%
i_w	2.80 to 8.80 degrees	< 0.5%

†These variations together yield variations of +19% and -21% in the three dimensional lift curve slope of the wing.

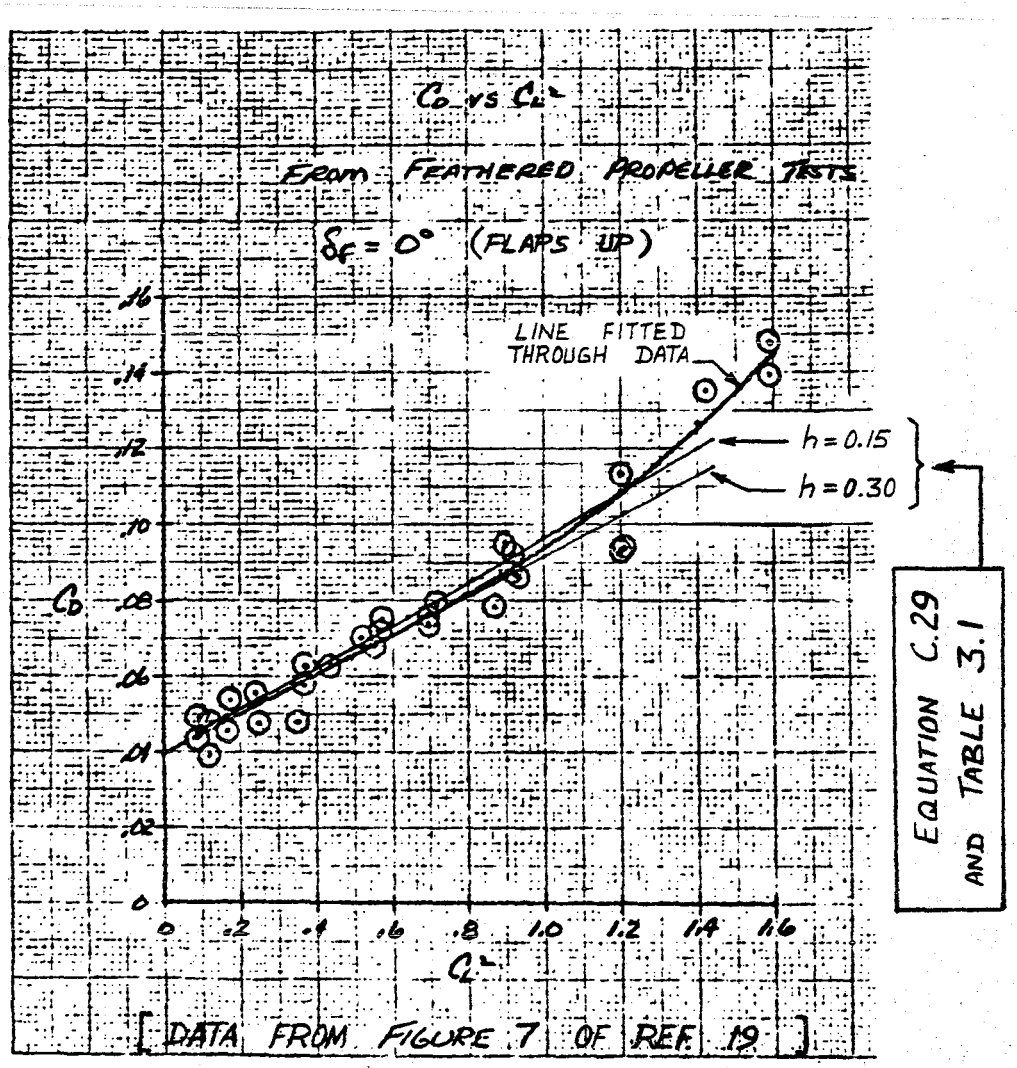

FIGURE 3.1 LOCKHEED LASA 60 : C_D VERSUS C_L^2
DATA FROM FEATHERED PROPELLER TESTS.

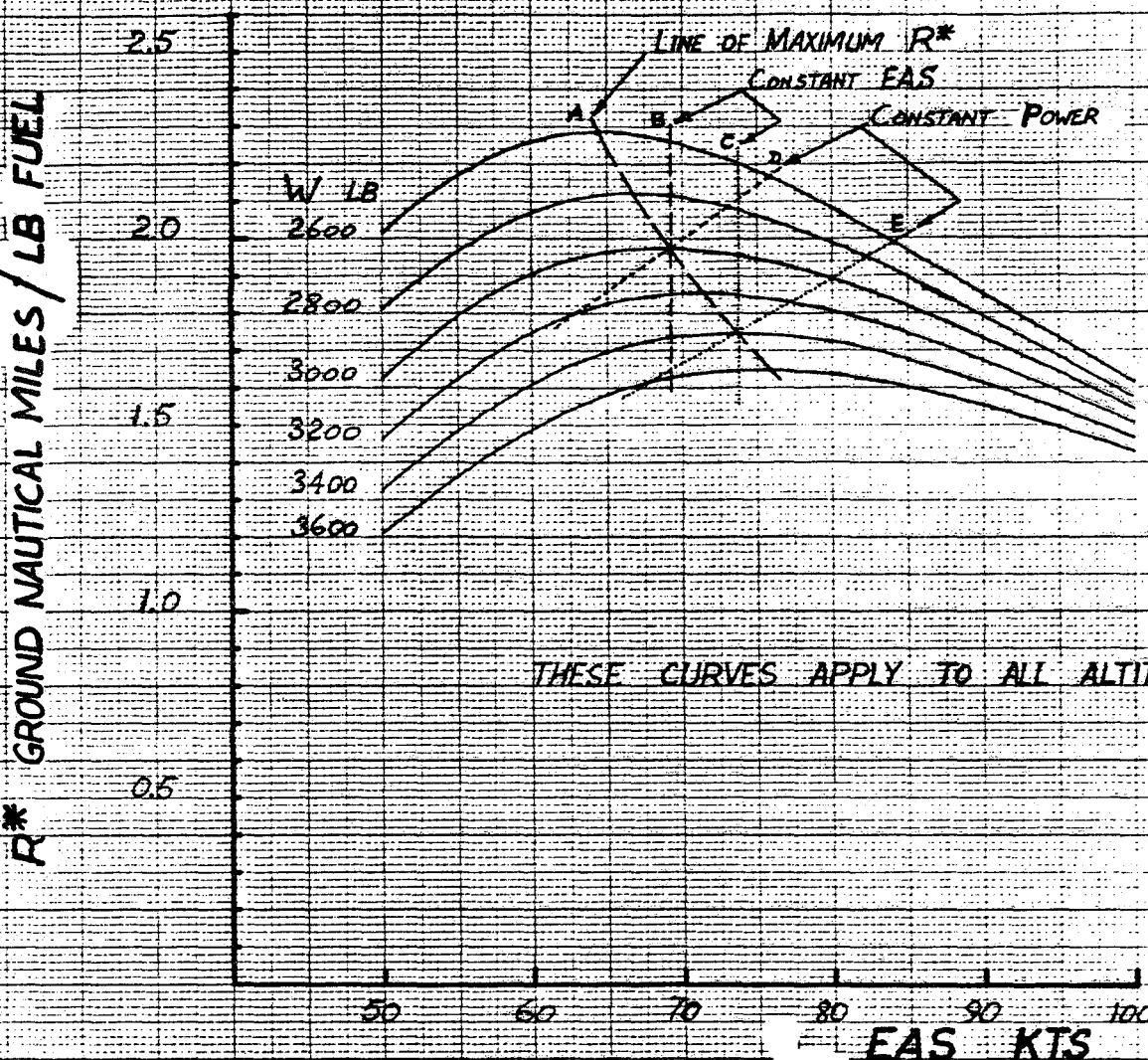

FLIGHT CONDITION:

(MAXIMUM GROSS WEIGHT = 3532 LB)
(EMPTY WEIGHT = 2400 LB APPROXIMATELY)

POWER-OFF DRAG POLAR : $C_D = 0.0402 + 0.052 C_L^2$

PROPULSIVE EFFICIENCY : $\eta_{LP} = 0.75$ CONSTANT

BRAKE SPECIFIC FUEL CONSUMPTION : BSFC = 0.45 LB/BHP HR CONSTANT

AUXILIARY EQUIPMENT POWER USED : $P_{AUX} = 0$

CENTER OF GRAVITY POSITION : $h = 0.3$ CONSTANT

ZERO WIND CONDITIONS

STANDARD AND NON-STANDARD ATMOSPHERES

VARIATION OF R* WITH EAS & GROSS WEIGHT

FIGURE 3.2

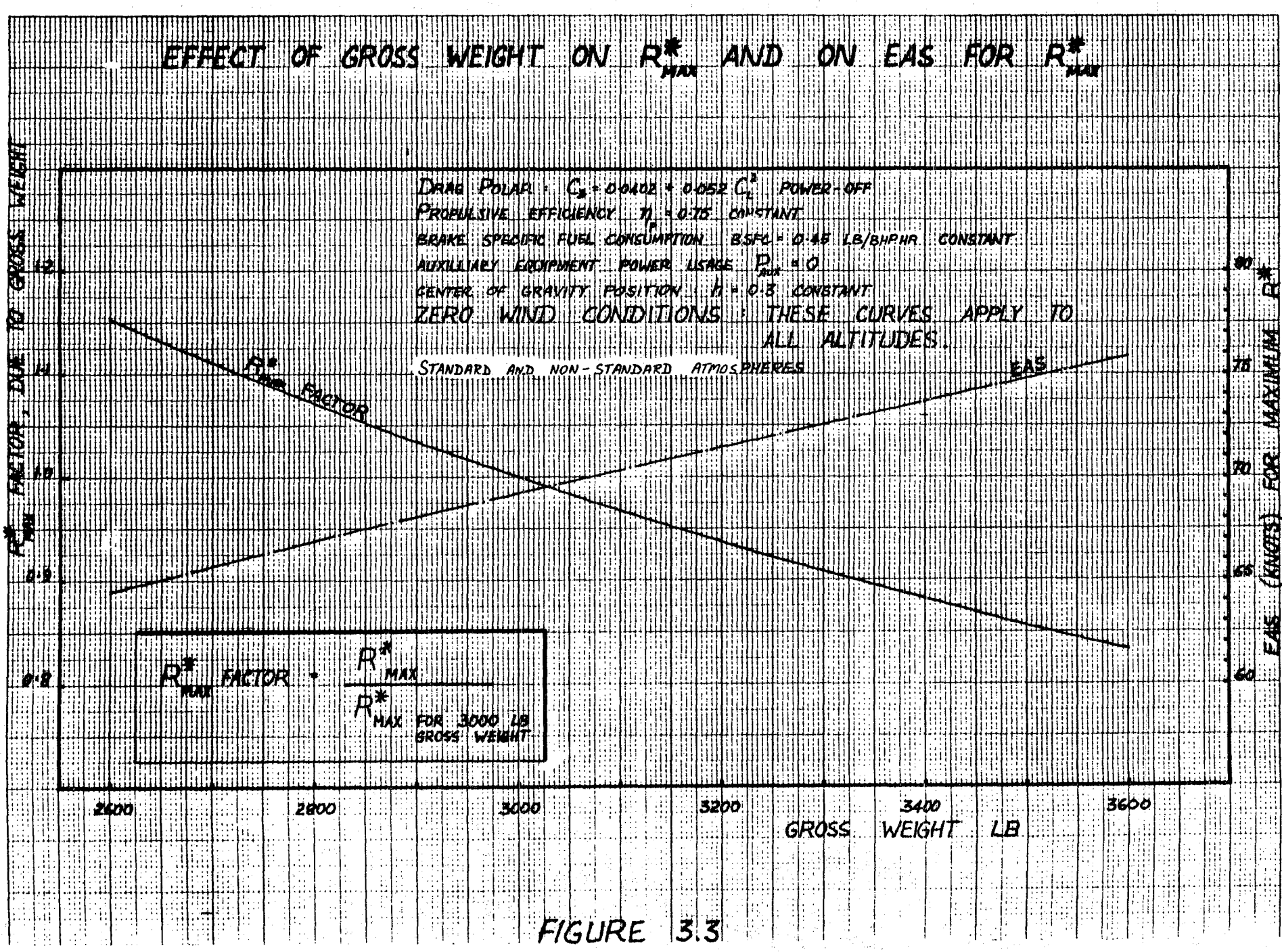
EFFECT OF GROSS WEIGHT ON R^*_{MAX} AND ON EAS FOR R^*_{MAX}
DRAG POLAR : $C_D = 0.0402 + 0.052\,C_L^2$ POWER-OFF
PROPULSIVE EFFICIENCY $\eta_p = 0.75$ CONSTANT
BRAKE SPECIFIC FUEL CONSUMPTION B.S.F.C. = 0.45 LB/BHP HR CONSTANT
AUXILLIARY EQUIPMENT POWER USAGE $P_{aux} = 0$
CENTER OF GRAVITY POSITION $h = 0.3$ CONSTANT
ZERO WIND CONDITIONS : THESE CURVES APPLY TO ALL ALTITUDES.
STANDARD AND NON-STANDARD ATMOSPHERES
R^*_{MAX} FACTOR
EAS
R^*_{MAX} FACTOR = $\frac{R^*_{MAX}}{R^*_{MAX}\text{ FOR 3000 LB GROSS WEIGHT}}$
R^*_{MAX} FACTOR, DUE TO GROSS WEIGHT
EAS (KNOTS) FOR MAXIMUM R^*
1.2
1.1
1.0
0.9
0.8
80
75
70
65
60
2600
2800
3000
3200
3400
3600
GROSS WEIGHT LB

FIGURE 3.3

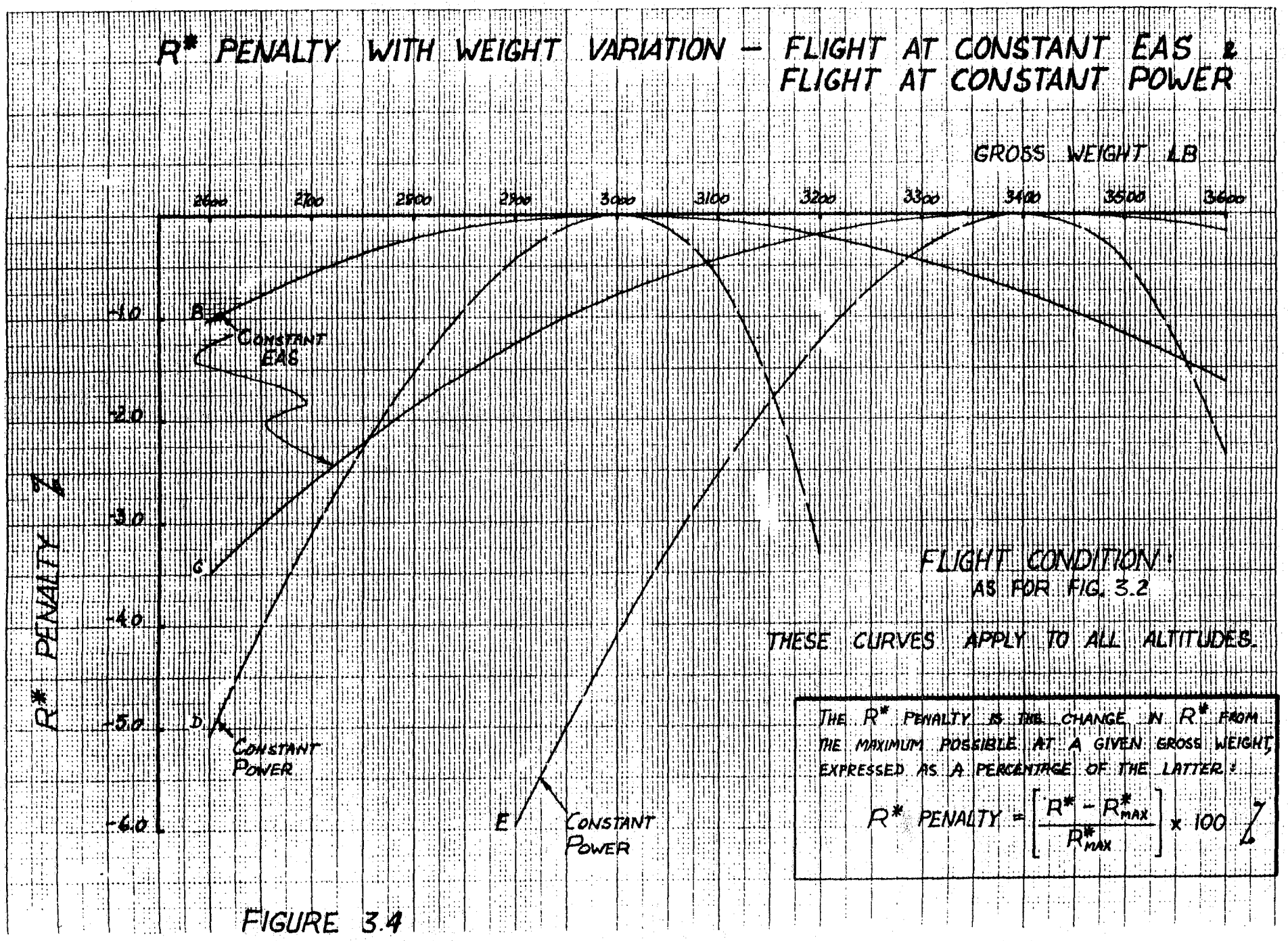
R* PENALTY WITH WEIGHT VARIATION – FLIGHT AT CONSTANT EAS & FLIGHT AT CONSTANT POWER
GROSS WEIGHT LB
2600
2700
2800
2900
3000
3100
3200
3300
3400
3500
3600
R* PENALTY %
-1.0
-2.0
-3.0
-4.0
-5.0
-6.0
B
CONSTANT EAS
C
D
CONSTANT POWER
E
CONSTANT POWER
FLIGHT CONDITION:
AS FOR FIG. 3.2
THESE CURVES APPLY TO ALL ALTITUDES.
THE R* PENALTY IS THE CHANGE IN R* FROM THE MAXIMUM POSSIBLE AT A GIVEN GROSS WEIGHT, EXPRESSED AS A PERCENTAGE OF THE LATTER:
R* PENALTY = [(R* − R*max) / R*max] × 100 %

FIGURE 3.4

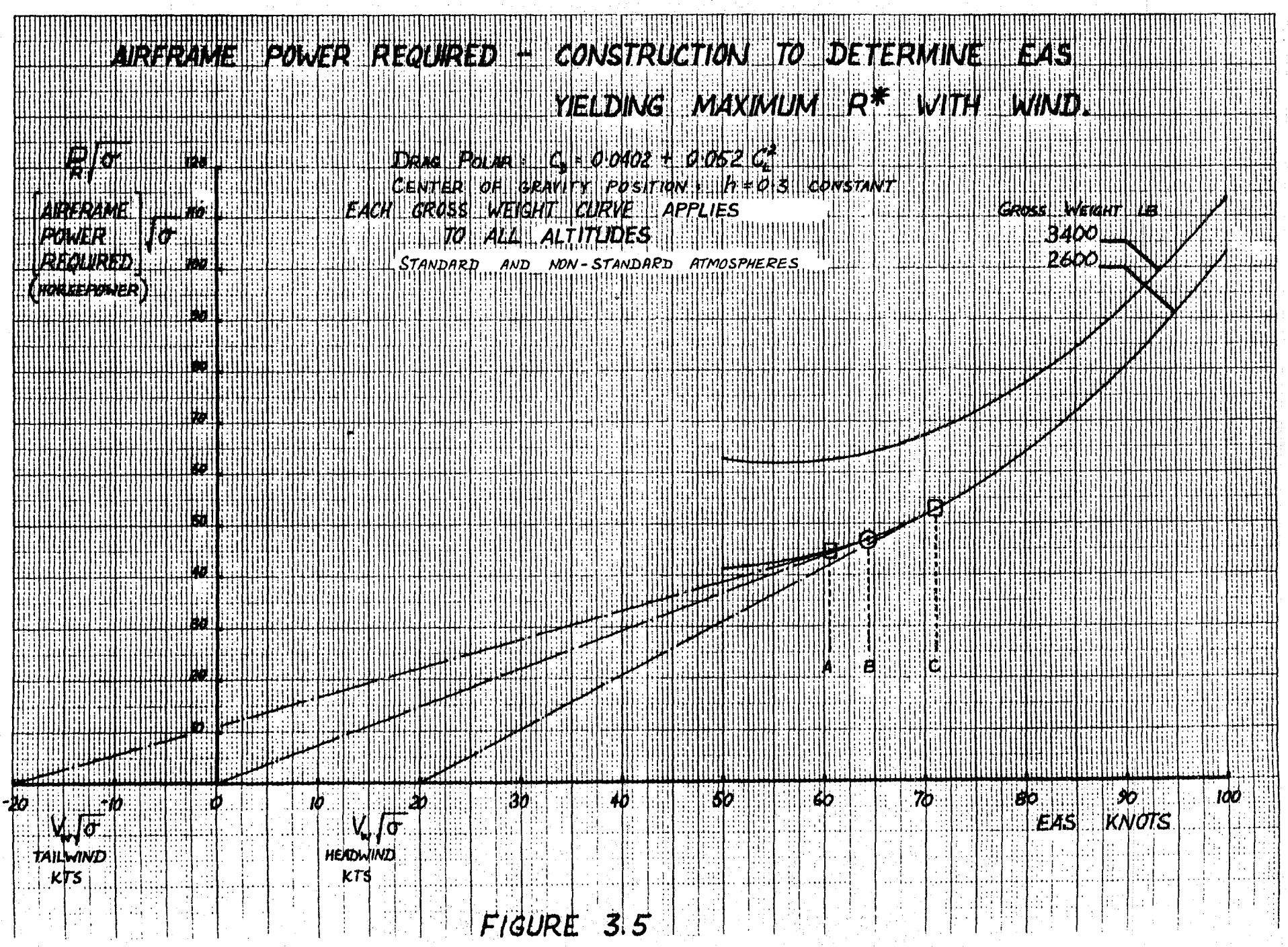
AIRFRAME POWER REQUIRED - CONSTRUCTION TO DETERMINE EAS YIELDING MAXIMUM R* WITH WIND.
DRAG POLAR : $C_D = 0.0402 + 0.052\,C_L^2$
CENTER OF GRAVITY POSITION : $h = 0.3$ CONSTANT
EACH GROSS WEIGHT CURVE APPLIES TO ALL ALTITUDES
STANDARD AND NON-STANDARD ATMOSPHERES
$\frac{P}{R}\sqrt{\sigma}$
AIRFRAME POWER REQUIRED (HORSEPOWER) $\sqrt{\sigma}$
GROSS WEIGHT LB
3400
2600
A
B
C
$V_w\sqrt{\sigma}$ TAILWIND KTS
$V_w\sqrt{\sigma}$ HEADWIND KTS
EAS KNOTS

FIGURE 3.5

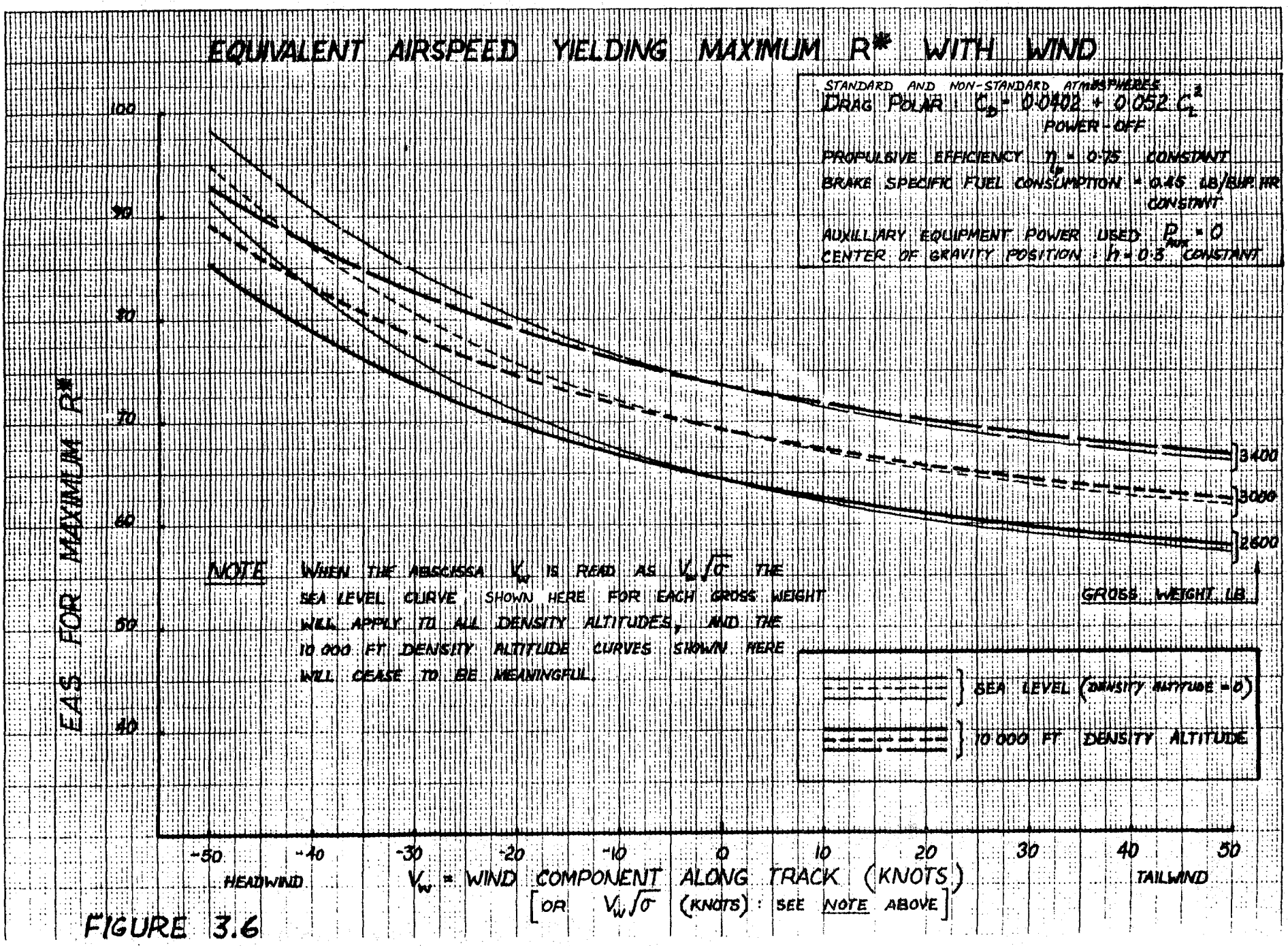
EQUIVALENT AIRSPEED YIELDING MAXIMUM R* WITH WIND
STANDARD AND NON-STANDARD ATMOSPHERES
DRAG POLAR : $C_D = 0.0402 + 0.052\,C_L^2$
POWER-OFF
PROPULSIVE EFFICIENCY $\eta_p = 0.75$ CONSTANT
BRAKE SPECIFIC FUEL CONSUMPTION = 0.45 LB/BHP HR CONSTANT
AUXILLIARY EQUIPMENT POWER USED $P_{AUX} = 0$
CENTER OF GRAVITY POSITION : $h = 0.5$ CONSTANT
EAS FOR MAXIMUM R*
100
90
80
70
60
50
40
3400
3000
2600
GROSS WEIGHT LB.
NOTE WHEN THE ABSCISSA V_w IS READ AS $V_w\sqrt{\sigma}$ THE SEA LEVEL CURVE SHOWN HERE FOR EACH GROSS WEIGHT WILL APPLY TO ALL DENSITY ALTITUDES, AND THE 10 000 FT DENSITY ALTITUDE CURVES SHOWN HERE WILL CEASE TO BE MEANINGFUL.
SEA LEVEL (DENSITY ALTITUDE = 0)
10 000 FT DENSITY ALTITUDE
-50
-40
-30
-20
-10
0
10
20
30
40
50
HEADWIND
TAILWIND
V_w = WIND COMPONENT ALONG TRACK (KNOTS)
[OR $V_w\sqrt{\sigma}$ (KNOTS) : SEE NOTE ABOVE]

FIGURE 3.6

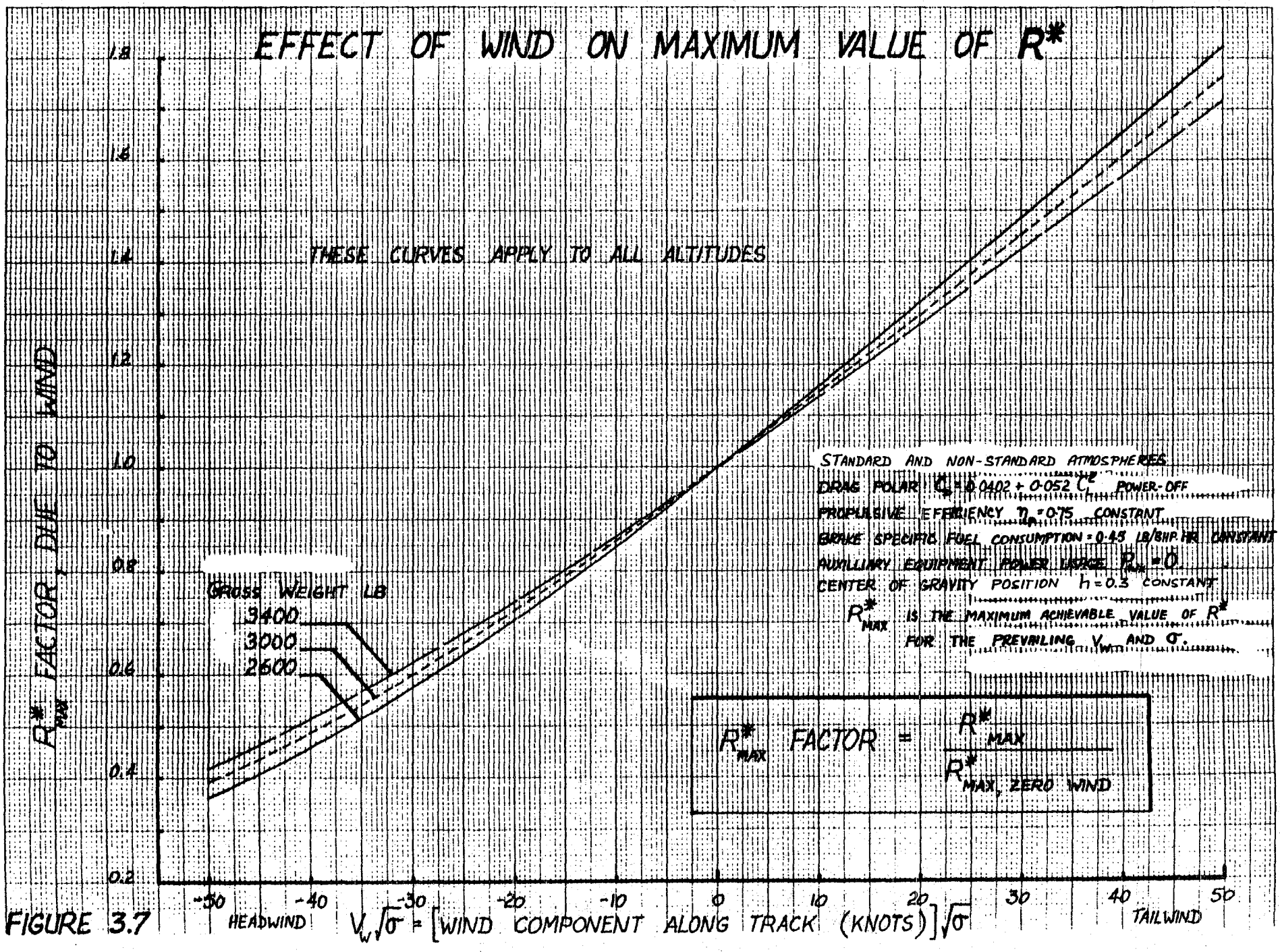
EFFECT OF WIND ON MAXIMUM VALUE OF R*
THESE CURVES APPLY TO ALL ALTITUDES
R*MAX FACTOR, DUE TO WIND
1.8
1.6
1.4
1.2
1.0
0.8
0.6
0.4
0.2
GROSS WEIGHT LB
3400
3000
2600
STANDARD AND NON-STANDARD ATMOSPHERES
DRAG POLAR $C_D = 0.0402 + 0.052\,C_L^2$ POWER-OFF
PROPULSIVE EFFICIENCY $\eta_p = 0.75$ CONSTANT
BRAKE SPECIFIC FUEL CONSUMPTION = 0.45 LB/BHP HR CONSTANT
AUXILIARY EQUIPMENT POWER LARGE $P_{aux} = 0$
CENTER OF GRAVITY POSITION $h = 0.3$ CONSTANT
R^*_{MAX} IS THE MAXIMUM ACHIEVABLE VALUE OF R^* FOR THE PREVAILING V_w AND σ.
R^*_{MAX} FACTOR = $\dfrac{R^*_{MAX}}{R^*_{MAX,\ ZERO\ WIND}}$
-50
-40
-30
-20
-10
0
10
20
30
40
50
HEADWIND
TAILWIND
$V_w\sqrt{\sigma}$ = [WIND COMPONENT ALONG TRACK (KNOTS)]$\sqrt{\sigma}$

FIGURE 3.7

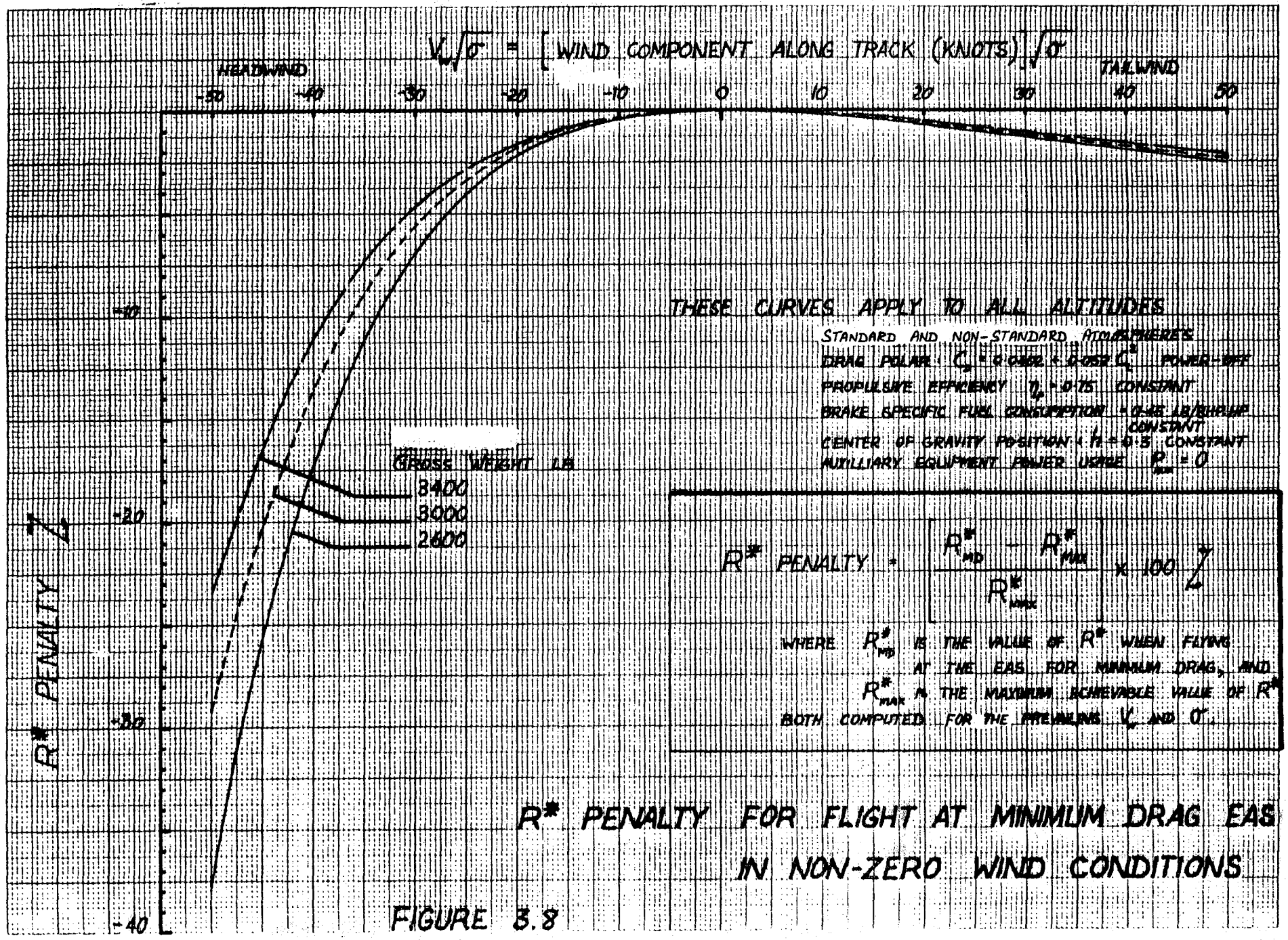

R^* PENALTY FOR FLIGHT AT MINIMUM DRAG EAS IN NON-ZERO WIND CONDITIONS

FIGURE 3.8

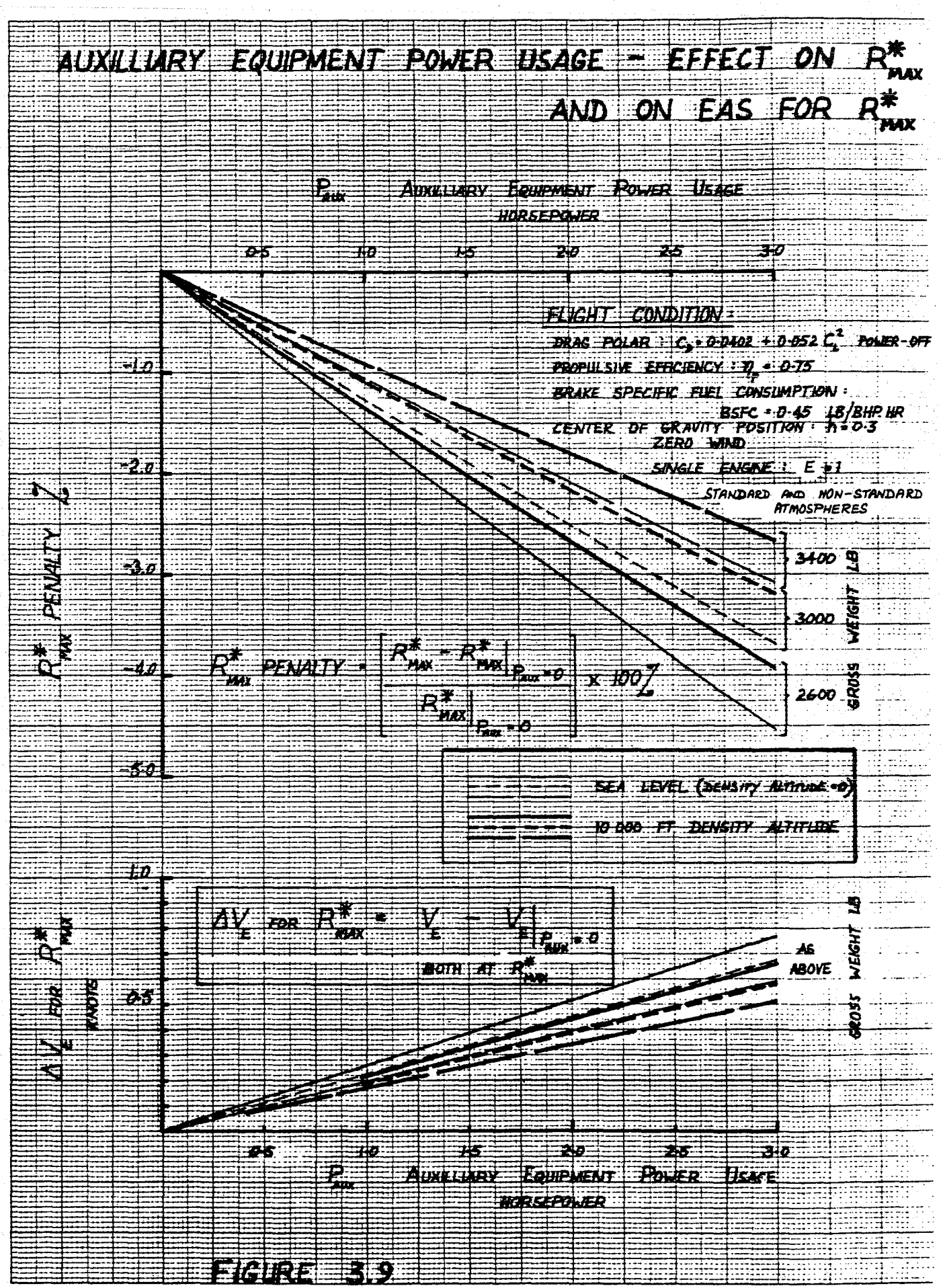

FIGURE 3.9

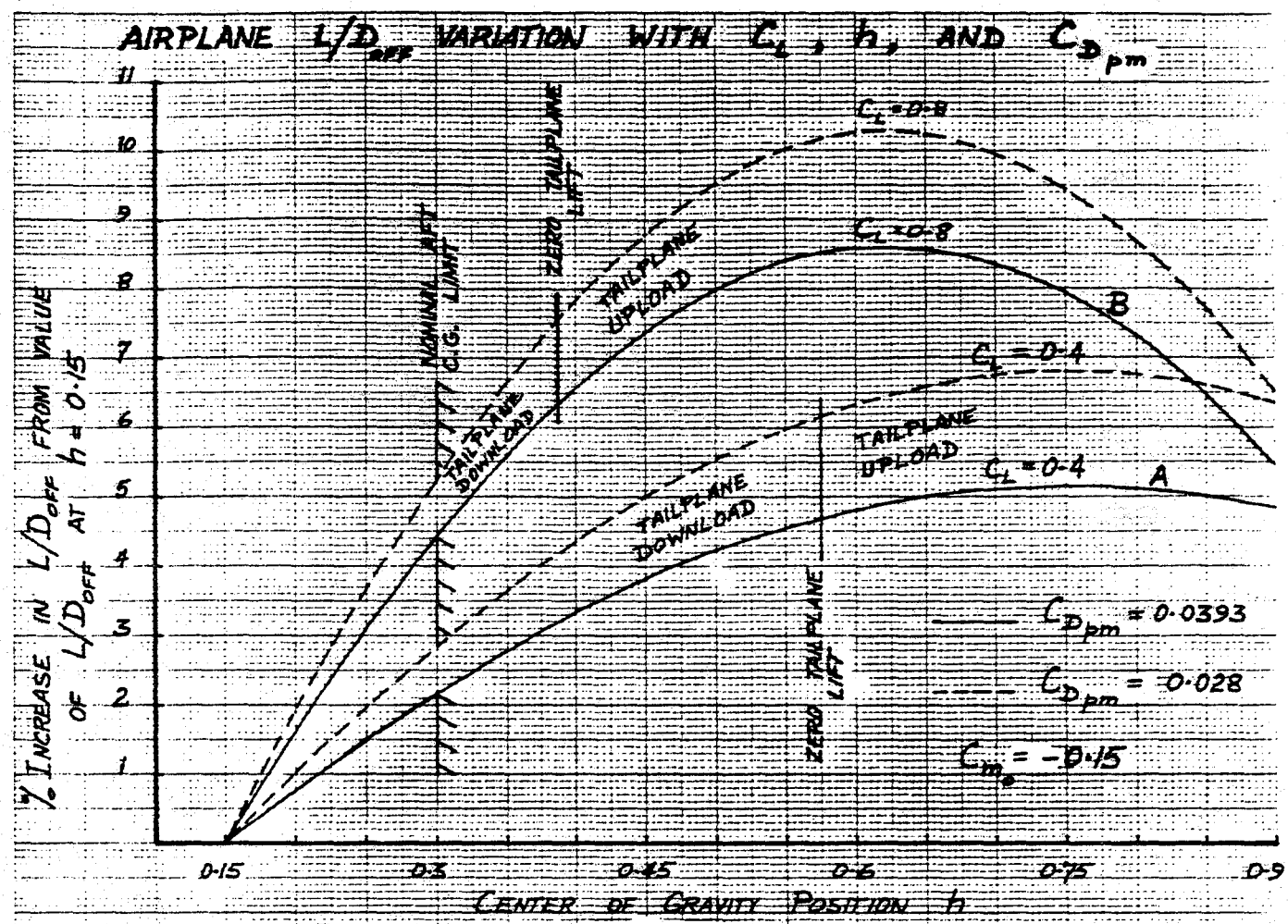

FIGURE 3.10

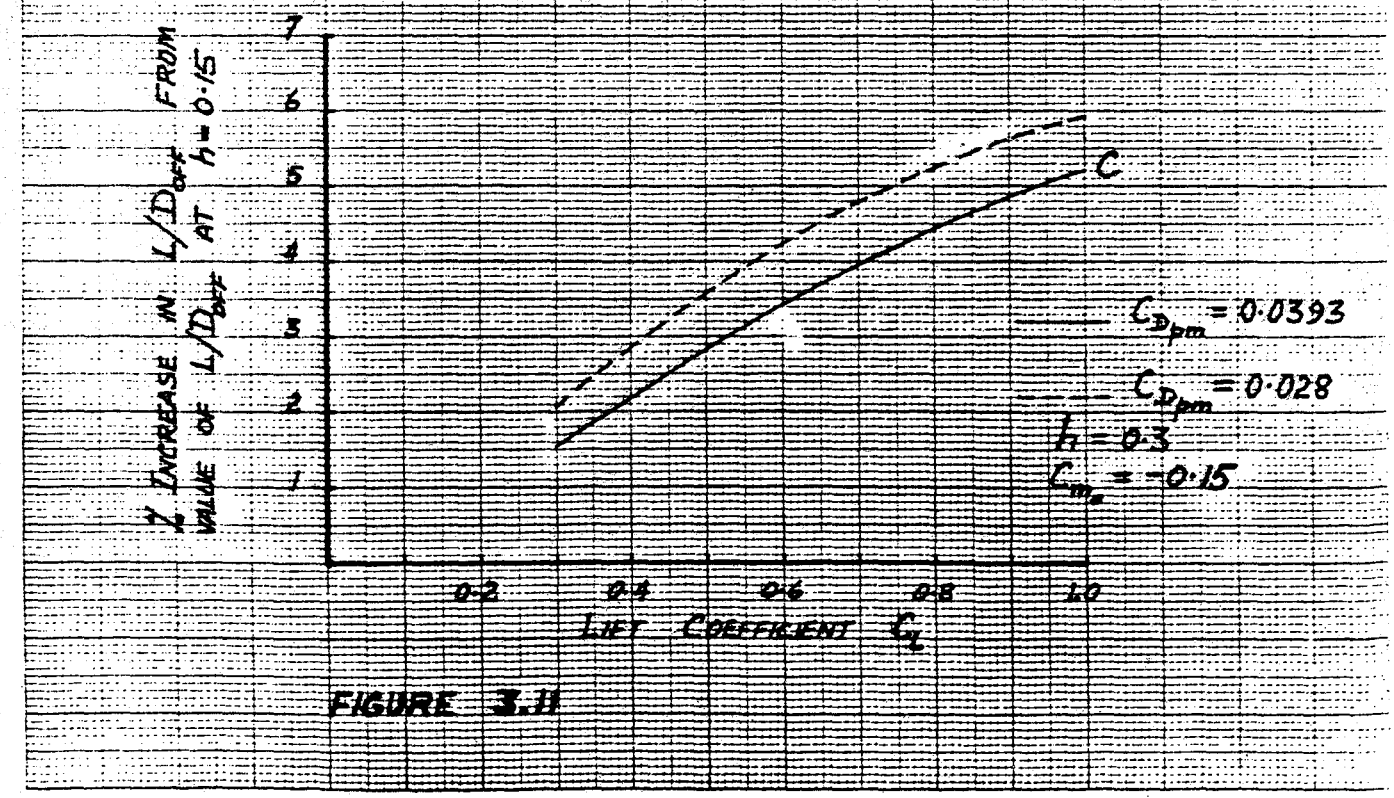

FIGURE 3.11

SCHEMATIC VARIATION OF AIRPLANE L/D_{OFF} WITH h AND C_L

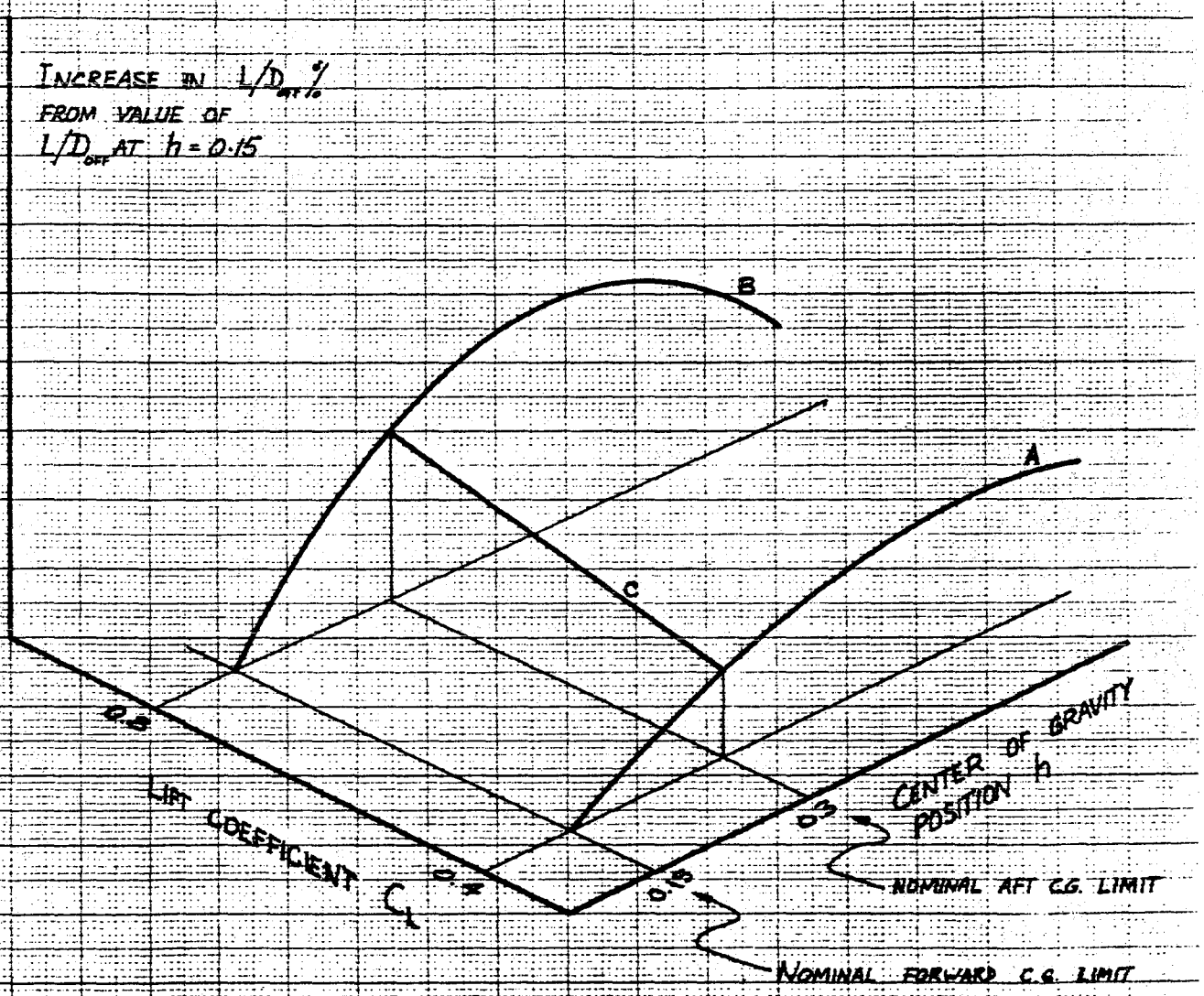

FIGURE 3.12

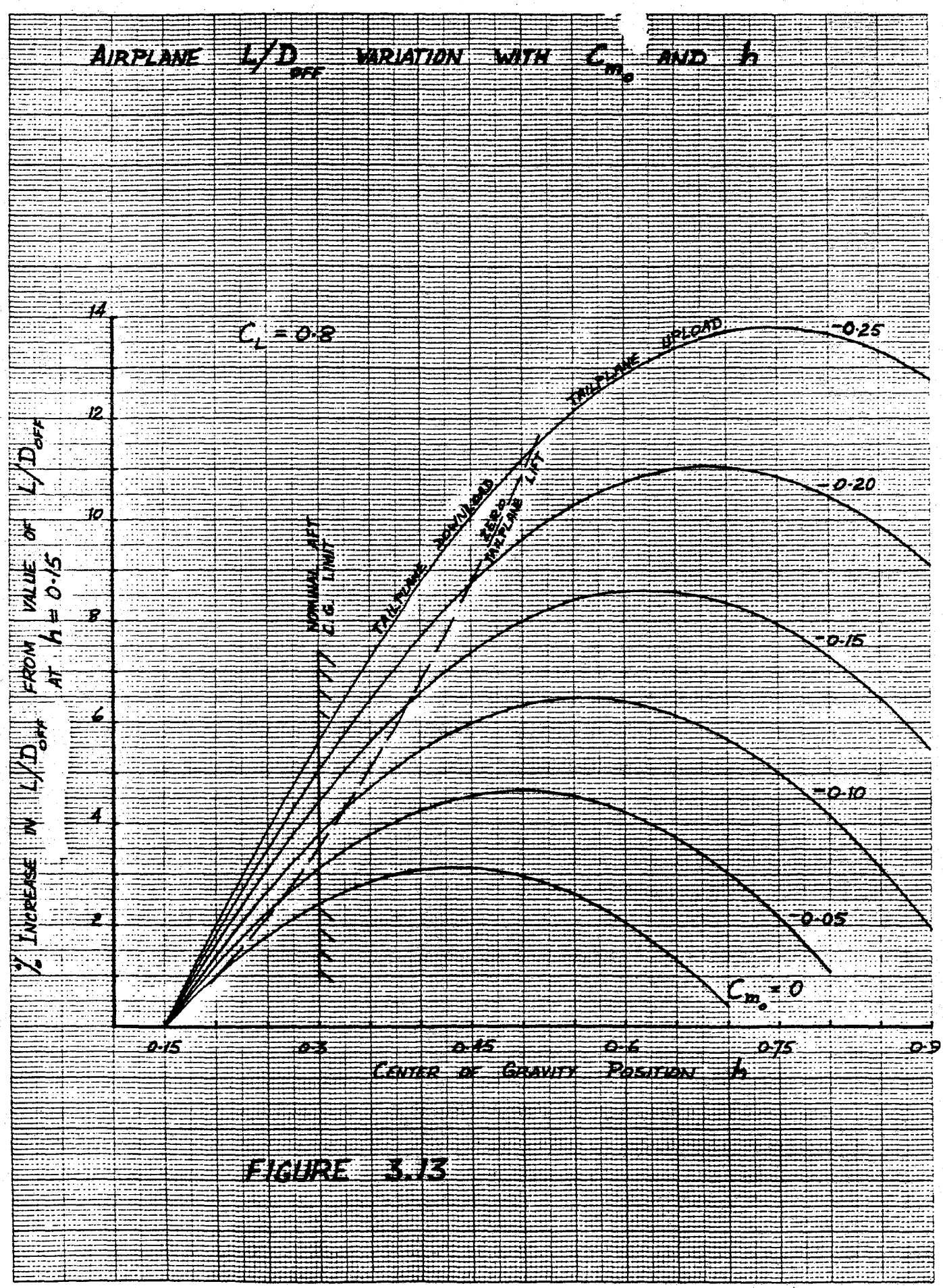

FIGURE 3.13

CHAPTER 4

THE AIRFRAME-PROPELLER-ATMOSPHERE SUBSYSTEM

Table of Contents

CHAPTER 4

THE AIRFRAME-PROPELLER-ATMOSPHERE SUBSYSTEM

INTRODUCTION

This chapter develops an input-output model for the cruise performance of the airframe-propeller-atmosphere subsystem. The inputs to this model are airplane operational variables; the outputs are the quantities R*c (knots/brake horsepower) and the engine brake torque Q_E (lb ft).

This subsystem model is developed by considering the performance of the McCauley C33/90M-4 constant speed propeller, in conjunction with the airframe-atmosphere model of the Lockheed LASA 60 airplane discussed in Chapter 3. The McCauley C33/90M-4 constant speed propeller is installed on the LASA 60 airplane owned by Princeton University.

It is shown that, by presenting the performance of the airframe-propeller-atmosphere subsystem in terms of Corrected Quantities; a compact input-output model of this subsystem, suitable for microprocessor applications, is obtained. The input-output model of this subsystem developed here for the LASA 60 airplane is assumed to typify such models for propeller-driven GA airplanes.

The propeller performance model is discussed first. The remainder of the chapter is a discussion of the airframe-propeller-atmosphere subsystem performance, in which the input-output model of that subsystem is developed.

THE PROPELLER PERFORMANCE MODEL

The propeller performance model used in this work is presented in Appendix D. The performance items of interest here are:

1. The propulsive efficiency η_p: required for the computation of R*c
2. The propeller shaft speed N (RPM) and torque Q_a (lb ft)
3. The propeller blade angle β degrees (measured between the plane of propeller rotation and the flat face of the blade at a radius of 0.75R, where R is the propeller tip radius): required to compute the contribution of compressibility to η_p and Q_a.

For straight and level steady flight it is shown (Equations D.56, D.58 and D.59) that:

$$\eta_p = \eta_p \ [V_E, W, h, N, \sigma, M_T] \tag{4.1}$$

$$Q_a = Q_a \ [V_E, W, h, N, \sigma, M_T] \tag{4.2}$$

$$\beta = \beta \ [V_E, W, h, N, \sigma] \tag{4.3}$$

Appendix D describes the computation of η_p, Q_a and β in terms of:

1. The performance of the free propeller in the absence of compressibility effects. The absence of compressibility effects is denoted by the superscript i (incompressible)
2. The propeller-body interference factors f_D and f_J
3. The compressibility correction factor f_{comp}.

It is shown (Equations D.49, D.48 and D.40) that

$$\eta_p = \eta_p^i f_{comp} \tag{4.4}$$

$$\eta_p^i = \frac{\eta_a^i}{f_D f_J} \tag{4.5}$$

$$Q_a = Q_a^i / f_{comp} \tag{4.6}$$

where (Equations D.55 and D.57)

$$\eta_a^i = \eta_a^i \ [V_E, W, h, N, \sigma] \tag{4.7}$$

$$Q_a^i = Q_a^i \ [V_E, W, h, N, \sigma] \tag{4.8}$$

f_D and f_J are constants whose magnitudes are dependent upon the airplane geometry.

The method used to compute η_p, Q_a and β for the McCauley C33/90M-4 constant speed propeller operating on the Lockheed LASA 60 airplane is summarized on page D-29.

AIRFRAME-PROPELLER-ATMOSPHERE SUBSYSTEM PERFORMANCE

We here develop the Airframe-Propeller-Atmosphere (APA) subsystem input-output model. This model consists of:

1. A model of the collective contribution of the airframe, propeller and atmosphere to R*: this contribution is the quantity R*c knots/brake horsepower
2. A model of the engine brake torque Q_E lb ft

in all straight and level steady flight conditions. The airplane operational variables are the inputs to this model; R*c and Q_E are its outputs.

The model of R*c is developed by introducing a model for the propulsive efficiency η_p into Equation 3.15. The model of Q_E is developed from a model of the propeller shaft torque Q_a (lb ft) which is developed below.

A model of the propeller blade angle β is also developed below, this being required for the computation of f_{comp} which influences both R*c and Q_a.

The development of the airframe-propeller-atmosphere subsystem input-output model proceeds in the following manner:

1. R*c, Q_a and β are expressed in terms of
   a) The kernel functions S*, Q* and β* respectively
   b) A number of simple correction factors, and an incremental correction in the case of β.
2. Utilizing Corrected Quantities, the kernel functions S*, Q* and β* are represented in compact form.
3. A corrected performance model of R*c, Q_a and β is defined and discussed.
4. Q_E is defined in terms of Q_a.
5. The input-output model is defined from the results of Steps 3 and 4. The suitability of this input-output model to microprocessor applications, and the allocation of numerical values to this model for GA airplanes, are then briefly discussed.

The Kernel Functions S*, Q* and β*

Consider Equation 3.15 for R*; and specifically the quantity

$V_E \left[\eta_p / P_R\sqrt{\sigma}\right]_{h_{ref}}$ therein. Invoking Equation 4.4, this quantity is written

$$V_E \left[\frac{\eta_p}{P_R\sqrt{\sigma}}\right]_{h_{ref}} = V_E \left[\frac{\eta_p^i}{P_R\sqrt{\sigma}}\right]_{h_{ref}} f_{comp} \tag{4.9}$$

We now define S* to be:

$$S^* = V_E \left[\frac{\eta_p^i}{P_R\sqrt{\sigma}}\right]_{h_{ref}} \quad \text{knots/BHP} \tag{4.10}$$

(BHP = brake horsepower). It was shown in Chapter 3 that $P_R\sqrt{\sigma}$ is a function of $\{V_E, W, h\}$ only. This fact, together with Equations 4.5 and 4.7, gives the functional relation

$$S^* = S^* \left[V_E, W, h, N, \sigma\right]_{h_{ref}} \tag{4.11}$$

Substituting Equations 4.9 and 4.10 into Equation 3.15 yields:

$$R^*c = \left[1 + \frac{V_w\sqrt{\sigma}}{V_E}\right] \frac{(1 + \xi C_L dh) f_{comp}\, S^*}{\Lambda} \quad \text{knots/BHP} \tag{4.12}$$

where the auxiliary equipment power loading factor Λ is

$$\Lambda = 1 + E\, P_{AUX}\sqrt{\sigma} \left[\frac{\eta_p}{P_R\sqrt{\sigma}}\right]_{h_{ref}} (1 + \xi C_L dh)$$

$$= 1 + E\, P_{AUX}\sqrt{\sigma} \left[\frac{\eta_p^i}{P_R\sqrt{\sigma}}\right]_{h_{ref}} (1 + \xi C_L dh) f_{comp}$$

$$= 1 + E\, P_{AUX}\sqrt{\sigma} \left[\frac{S^*}{V_E}\right] (1 + \xi C_L dh) f_{comp} \tag{4.13}$$

S* constitutes the kernel of R*c; this kernel being corrected for the effects of wind, auxiliary equipment power, center of gravity position and compressibility by means of Equation 4.12.

Consider now the propeller shaft torque Q_a. From Equation D.29,

$$\frac{\eta_p^{(i)}}{P_R} = \frac{550}{EP_a^{(i)}}$$

where E = number of engines, each driving one propeller

$P_a^{(i)}$ = propeller shaft power, ft lb/sec

$= 2\pi n Q_a^{(i)}$

$n = N/60$ = propeller shaft speed, revolutions/second.

Thus

$$Q_a^{(i)} = \frac{5252.1}{EN\sqrt{\sigma}\left[\frac{\eta_p^{(i)}}{P_R\sqrt{\sigma}}\right]} \tag{4.14}$$

With the center of gravity located at $h = h_{ref}$,

$$Q_a^i\Big|_{h_{ref}} = \frac{5252.1}{EN\sqrt{\sigma}\left[\frac{\eta_p^i}{P_R\sqrt{\sigma}}\right]_{h_{ref}}} \tag{4.15}$$

With the center of gravity located at $h = h_{ref} + dh$,

$$Q_a = \frac{5252.1}{EN\sqrt{\sigma}\left[\frac{\eta_p}{P_R\sqrt{\sigma}}\right]_h}$$

Invoking Equations 3.14, 4.4 and 4.15,

$$Q_a = \frac{Q_a^i\Big|_{h_{ref}}}{(1 + \xi C_L dh) f_{comp}} \tag{4.16}$$

We now define Q* to be

$$Q^* = Q_a^i\Big|_{h_{ref}} \qquad \text{lb ft} \tag{4.17}$$

From this and Equation 4.8 we have the functional relation

$$Q^* = Q^* \left[V_E, W, h, N, \sigma\right]_{h_{ref}} \tag{4.18}$$

Invoking Equation 4.17, Equation 4.16 becomes

$$Q_a = \frac{Q^*}{(1 + \xi C_L dh) f_{comp}} \qquad \text{lb ft} \tag{4.19}$$

Q* constitutes the kernel of the propeller shaft torque Q_a; this kernel being corrected for the effects of center of gravity position and compressibility by means of Equation 4.19.

S* and Q* are related (Equations 4.10, 4.15 and 4.17) by

$$S^* = \frac{5252.1\ V_E}{EN\sqrt{\sigma}\ Q^*} \tag{4.20}$$

Finally, consider the propeller blade angle β, expressed functionally by Equation 4.3: β is required only for the computation of f_{comp}. When the center of gravity is located at $h = h_{ref}$, β is denoted by the kernel function β*. Hence (Equation 4.3),

$$\beta^* = \beta\Big|_{h_{ref}} = \beta^* \left[V_E, W, h, N, \sigma\right]_{h_{ref}} \quad \text{degrees} \tag{4.21}$$

With the center of gravity located at $h = h_{ref} + dh$, this kernel function is corrected by the increment Δβ:

$$\beta = \beta^* + \Delta\beta \quad \text{degrees} \tag{4.22}$$

The Speed-Thrust Coefficient plot (C_R^i:J^2) facilitates the computation of $\Delta\beta$. Figure 4.1 shows that, when the lines of constant β in the C_R^i:J^2 plot for the McCauley C33/90M-4 free propeller are approximated by straight lines radiating from the origin at an equal spacing of θ degrees,

$$\Delta\beta = \frac{-\kappa \cos\psi \sin(\psi - \frac{\theta dh}{|dh|}) \left[(1 + \xi C_L dh)^{\frac{1}{2}} - 1\right]}{\theta\pi/180} \quad \text{degrees} \tag{4.23}$$

where ψ = angle from the abscissa to the straight radial line which approximates the β^* line on the C_R^i:J^2 plot, degrees

κ = increment of β^* between lines of constant β^* on the C_R^i:J^2 plot, degrees.

Equation 4.23 is assumed to typify the $\Delta\beta$ performance of propeller-driven GA airplanes. For the McCauley C33/90M-4 free propeller,[†]

$$\Delta\beta = -32.74\cos(1.75\beta^* - 2)\sin(1.75\beta^* - 2 - \frac{3.5dh}{|dh|}) \left[(1 + \xi C_L dh)^{\frac{1}{2}} - 1\right] \text{ degrees.}$$

Figure 4.1 shows that the straight radial line approximation of the constant β^* lines, in the $C_{R_a}^i$:J_a^2 plot for the McCauley C33/90M-4 propeller, is a good approximation in the region [$1.8 \leq C_{R_a}^i \leq 3.2$, $10 \leq \beta^*$ degrees ≤ 23]. This is the normal region of operation for the LASA 60 airplane.[††]

The kernel functions S*, Q* and β^* are functions of the same set of variables {V_E, W, h, N, σ} with h = h_{ref}.

[†] Note that $\Delta\beta$ is a function of {β^*, C_L and dh} only.

[††] Departures of β^* from this range during fuel-economical operations may necessitate modification of the expression $\psi = 1.75\beta^* - 2$ degrees (Figure 4.1) to accommodate all operational values of β^* in the linear approximation of Figure 4.1.

S, Q* and β* at Sea Level with Specified Gross Weight and C.G. Position:*

We now examine the functional dependence of S*, Q* and β* on $\{V_E, N\}$; when the variables W, h and σ are constrained to be $[W = W_0, h = h_{ref}, \sigma = 1]$, this flight condition being denoted by the subscript 0. Note that $V_{E_0} = V_T$.

Consider S_0^*, Q_0^* and β_0^* for the LASA 60 airplane when

1. $W = W_0 = 3400$ lb
2. $h = h_{ref} = 0.3$.

Figure 4.2 shows contours of S_0^*, Q_0^* and β_0^* plotted for variations in V_{E_0} and N_0. The S_0^* contours define a three-dimensional surface with a single peak: for any given V_{E_0}, the N_0 yielding maximum S_0^* falls on the inscribed line passing through the peak. The Q_0^* contours define a second three-dimensional surface: the height of the S_0^* surface at any point (V_{E_0}, N_0) may be computed from the height of the Q_0^* surface at the same point (V_{E_0}, N_0) using Equation 4.20. Two lines of constant propeller blade angle β_0^* are also shown in Figure 4.2, constituting contours of a third three-dimensional surface. Radial lines from the origin $(V_{E_0}, N_0) = (0, 0)$ in Figure 4.2 represent lines of constant propeller advance ratio J_{a_0} .

Figure 4.2 is assumed to typify the S_0^*, Q_0^* and β_0^* performance of propeller-driven GA airplanes.

We now examine how the functions S*, Q* and β* vary from the functions S_0^*, Q_0^* and β_0^*, as W and σ vary from the fixed values $[W = W_0, \sigma = 1]$. This is done most efficiently by introducing a number of Corrected Quantities.

Corrected Quantities

Definitions:

The following Corrected Quantities are defined:

$$D_{OFF_c} = D_{OFF}\left[\frac{W_0}{W}\right] \quad \text{Corrected airframe drag, lb} \tag{4.24}$$

$$P_{AUX_c} = P_{AUX}\sqrt{\frac{W_0^3\sigma}{W^3}} \quad \text{Corrected auxiliary equipment power, horsepower} \tag{4.25}$$

$$P_{R_c} = P_R\sqrt{\frac{W_0^3\sigma}{W^3}} \quad \text{Corrected airframe power required (power-off), horsepower} \tag{4.26}$$

$$S^*_c = S^*\left[\frac{W}{W_0}\right] \quad \text{Corrected S*, knots/BHP} \tag{4.27}$$

$$V_{w_c} = V_w\sqrt{\frac{W_0\sigma}{W}} \quad \text{Corrected geocentric windspeed along track, knots} \tag{4.28}$$

$$X = V_E\sqrt{\frac{W_0}{W}} \quad \text{Corrected airspeed, knots} \tag{4.29}$$

$$Y = N\sqrt{\frac{W_0\sigma}{W}} \quad \text{Corrected propeller shaft speed, RPM} \tag{4.30}$$

$$Z = Q^*\left[\frac{W_0}{W}\right] \quad \text{Corrected Q*, lb ft} \tag{4.31}$$

These corrected quantities apply to standard and non-standard atmospheric conditions.

Significance:

Consider an airplane in straight and level steady flight, in the following flight condition (denoted by subscript 0):

1. Sea level, standard atmosphere: Density ρ_0, slugs/ft^3
2. Gross weight W_0, lb
3. Center of gravity position $h = h_{ref}$
4. True airspeed V_0, ft/sec

True airspeed $V_{T_0} = 0.5921\ V_0$, knots (4.32)

5. Propeller shaft speed N_0, RPM

In this flight condition, the following equations apply:

$$L_0 = W_0 = \left[C_L\right]_0 \tfrac{1}{2}\rho_0 V_0^2 S \quad \text{lb} \tag{4.33}$$

$$D_{OFF_0} = \left[C_D\right]_0 \tfrac{1}{2}\rho_0 V_0^2 S \quad \text{lb} \tag{4.34}$$

$$P_{R_0} = D_{OFF_0} V_0/550 \quad \text{horsepower} \tag{4.35}$$

$$J_{a_0} = 60\ f_J V_0/N_0 d \tag{4.36}$$

$$Q_0^* = \frac{5252.1}{EN_0\left[\frac{n_p^i}{P_R}\right]_0} \quad \text{lb ft} \tag{4.37}$$

$$S_0^* = \frac{5252.1\ V_{T_0}}{EN_0 Q_0^*} \quad \text{knots/BHP} \tag{4.38}$$

Now consider the same airplane in straight and level steady flight, in the following flight condition (no subscript):

1. Above sea level, standard or non-standard atmosphere: density ρ, slugs/ft^3
2. Gross weight W, lb
3. Center of gravity position $h = h_{ref}$
4. True airspeed V, ft/sec

   True airspeed $V_T = 0.5921\ V$, knots

   Equivalent airspeed $V_e = V\sqrt{\rho/\rho_0} = V\sqrt{\sigma}$, ft/sec

   Equivalent airspeed $V_E = 0.5921\ V_e$, knots (4.39)
5. Propeller shaft speed N, RPM.

In this flight condition the following equations apply:

$$L = W = C_L \tfrac{1}{2}\rho_0 V_e^2 S \quad \text{lb} \tag{4.40}$$

$$D_{OFF} = C_D \tfrac{1}{2}\rho_0 V_e^2 S \quad \text{lb} \tag{4.41}$$

$$P_R\sqrt{\sigma} = D_{OFF}V_e/550 \quad \text{horsepower} \tag{4.42}$$

$$J_a = 60f_J V/Nd = 60f_J V_e/N\sqrt{\sigma}d \tag{4.43}$$

$$Q^* = \frac{5252.1}{EN\sqrt{\sigma}\left[\dfrac{\eta_p^i}{P_R\sqrt{\sigma}}\right]} \quad \text{lb ft} \tag{4.44}$$

$$S^* = \frac{5252.1\ V_E}{EN\sqrt{\sigma}\ Q^*} \quad \text{knots/BHP} \tag{4.45}$$

We now prescribe that, for these two flight conditions:

$$\left[C_L\right]_0 = C_L \tag{4.46}$$

$$J_{a_0} = J_a \tag{4.47}$$

Consequently:

1. From Equations 4.32, 4.33, 4.39, 4.40, 4.46 and 4.29,

$$V_0 = V_e\sqrt{\frac{W_0}{W}} \tag{4.48}$$

$$V_{T_0} = V_E\sqrt{\frac{W_0}{W}} = X \tag{4.49}$$

Hence constant C_L corresponds to constant X.

2. Since $\left[C_L\right]_0 = C_L$, $\left[C_D\right]_0 = C_D$ (Appendix C).
Therefore, from Equations 4.34, 4.41, 4.48 and 4.24,

$$D_{OFF_0} = D_{OFF}\left[\frac{W_0}{W}\right] = D_{OFF_c} \tag{4.50}$$

3. From Equations 4.35, 4.42, 4.48, 4.50 and 4.26,

$$P_{R_0} = P_R\sqrt{\frac{W_0^3\sigma}{W^3}} = P_{R_c} \tag{4.51}$$

4. From Equations 4.36, 4.43, 4.47, 4.48, and 4.30,

$$N_0 = N\sqrt{\frac{W_0\sigma}{W}} = Y \tag{4.52}$$

5. Since $\left[C_D\right]_0 = C_D$, the Speed-Thrust Coefficient $C^i_{R_a}$ (Equation D.53) is the same in both flight conditions.

This in conjunction with Equation 4.47 yields (Figure D.6)

$$\beta_0^* = \beta^* \tag{4.53}$$

$$\left[\eta^i_a\right]_0 = \eta^i_a \tag{4.54}$$

and thus from Equation 4.5,

$$\left[\eta^i_p\right]_0 = \eta^i_p \tag{4.55}$$

Then from Equations 4.37, 4.44, 4.51, 4.52, 4.55 and 4.31,

$$Q_0^* = Q^*\left[\frac{W_0}{W}\right] = Z \tag{4.56}$$

6. From Equations 4.38, 4.45, 4.49, 4.52, 4.56 and 4.27,

$$S_0^* = S^*\left[\frac{W}{W_0}\right] = S_c^* \tag{4.57}$$

These results may be summarized as follows:

Straight and level steady flight of a propeller-driven airplane under the conditions

1. $h = h_{ref}$ = constant
2. C_L = constant
3. J_a = constant

with variations in W and σ[†], results in invariance of the quantities

$$X, Y, Z, S_c^*, \beta^*, \eta_p^i, D_{OFF_c}, P_{R_c}.$$

The significance of these results in the present work is apparent from the converse statement:

Straight and level steady flight of a propeller-driven airplane under the conditions

1. $h = h_{ref} = \text{constant}$
2. $X = \text{constant}$
3. $Y = \text{constant}$

with variations in W and σ[†], results in invariance of the quantities

$$C_L, J_a, Z, S_c^*, \beta^*, \eta_p^i, D_{OFF_c}, P_{R_c}.$$

These results are an extension of the ideas presented by Pye (12) pp. 37, 38.

The Corrected Quantities P_{AUX_c} and V_{w_c} are addressed in the discussion of the Corrected Performance Model below.

Corrected Performance Plots

Contour Plots of S_c^*, Z and β^*:

The flight condition of Figure 4.2 corresponds to the flight condition denoted by the subscript 0 in the foregoing discussion of Corrected Quantities. Invoking the results of the latter discussion, Figure 4.2 does not change when the various quantities in Figure 4.2 are relabelled as follows:

[†]In standard or non-standard atmospheric conditions.

$$X = V_{T_0} \qquad \text{(Equation 4.49)}$$

$$Y = N_0 \qquad \text{(Equation 4.52)}$$

$$Z = Q^*_0 \qquad \text{(Equation 4.56)}$$

$$S^*_c = S^*_0 \qquad \text{(Equation 4.57)}$$

$$\beta^* = \beta^*_0 \qquad \text{(Equation 4.53)}$$

Figure 4.2 is duplicated as Figure 4.3† in which this relabelling has been performed: Figure 4.3 shows contours of S^*_c, Z and β^* plotted for variations in X and Y for the LASA 60 airplane operating with $h = h_{ref} = 0.3$.

From Equations 4.20, 4.27 and 4.29-4.31 we have

$$S^*_c = \frac{5252.1}{E} \frac{X}{YZ} \qquad \text{knots/BHP} \qquad (4.58)$$

$$S^* = \frac{5252.1}{E} \frac{X}{YZ} \frac{W_0}{W} \qquad \text{knots/BHP} \qquad (4.59)$$

Also, from the definition of Z (Equation 4.31),

$$Q^* = Z\left[\frac{W}{W_0}\right] \qquad \text{lb ft} \qquad (4.60)$$

The contour plots of Figure 4.3 constitute a complete definition of the functions S*, Q* and β^* (Equations 4.11, 4.18 and 4.21) for the LASA 60 airplane operating with $h_{ref} = 0.3$. Note that in Chapter 3 where both η_p and c were assumed to be constants, the maximum value of R* ($=R^*_{max}$) occurred at the airframe minimum drag EAS: Figure 3.3 shows this EAS to be 73.7 kts for the LASA 60 when W = 3400 lb. Introduction of the η^i_p model in this chapter has increased the EAS for maximum S* to 77.5 kts for that aircraft with the same gross weight.

†Note that Figure 4.3 applies to standard and non-standard atmospheric conditions.

Figure 4.3 is assumed to typify the variations of $\{S_c^*, Z, \beta^*\}$ with $\{X, Y\}$, and hence the variations of $\{S^*, Q^*, \beta^*\}$ with $\{V_E, W, N, \sigma\}$, for propeller-driven GA airplanes. Note that each such plot is constructed for a specific value of W_0 and a specific value of h_{ref}; and that for the representation of $\{S^*, Q^*, \beta^*\}$ variations with $\{V_E, W, N, \sigma\}$, the values of W_0 and h_{ref} used in the construction of such a plot may be selected arbitrarily.

X,Y,Z Plots and X,Y,β Plots:*

Figure 4.4 shows vertical sections through the X,Y,Z surface of Figure 4.3, for several constant values of Y. Plots such as Figure 4.4 will henceforth be referred to as X,Y,Z plots. For a given airplane: an X,Y,Z plot and Equations 4.59 and 4.60 together yield S* and Q* for any set {W, X, Y}.

Figure 4.5 shows vertical sections through the X,Y,β* surface of Figure 4.3 for several constant values of Y. Plots such as Figure 4.5 will henceforth be referred to as X,Y,β* plots.

Propulsive Efficiency η_p^*:

It is of interest to observe the functional nature of the propulsive efficiency $\left[\eta_p^i\right]_{h_{ref}}$, denoted η_p^*. From Equations 4.5 and 4.7,

$$\eta_p^* = \left[\eta_p^i\right]_{h_{ref}} = \eta_p^* \left[V_E, W, h, N, \sigma\right]_{h_{ref}} \tag{4.61}$$

A plot showing η_p^* contours for variations in X and Y would completely

define the function in Equation 4.61 as a three-dimensional surface, for a given airplane and a chosen h_{ref}.

Vertical sections through the X,Y,η_p^* surface, for several constant values of X, are shown in Figure 4.6 for the LASA 60 airplane with $h_{ref} = 0.3$. As X increases, the maximum value of η_p^* achievable also increases. Variations of η_p^* with Y at constant X are solely responsible for variations of S_c^* with Y at constant X in Figure 4.3.

Figure 4.6 is assumed to typify the η_p^* performance of propeller-driven GA airplanes. It is clear from this figure that η_p^* varies greatly with the airplane operating condition.

Corrected Performance Model of R*c, Q_a and β

Formulation:

We now formulate a model for R*c, Q_a and β based on the corrected quantities and corrected performance plots of the foregoing discussion.

The following definitions (Equations 4.25, 4.28-4.30) are collected here for convenience:

$$P_{AUX_c} = P_{AUX}\sqrt{\frac{W_0^3\sigma}{W^3}} \qquad \text{horsepower} \qquad (4.62)$$

$$V_{w_c} = V_w\sqrt{\frac{W_0\sigma}{W}} \qquad \text{knots} \qquad (4.63)$$

$$X = V_E\sqrt{\frac{W_0}{W}} \qquad \text{knots} \qquad (4.64)$$

$$Y = N\sqrt{\frac{W_0\sigma}{W}} \qquad \text{RPM} \tag{4.65}$$

With these definitions we have:

1. From Equation 4.12,

$$R^*c = \left[1 + \frac{V_{w_c}}{X}\right] \frac{(1 + \xi C_L dh) f_{comp} S^*}{\Lambda} \qquad \text{knots/BHP} \tag{4.66}$$

2. From Equation 4.59,

$$S^* = \frac{5252.1}{E} \frac{X}{YZ} \frac{W_0}{W} \qquad \text{knots/BHP} \tag{4.67}$$

3. From Equations 4.13 and 4.67,

$$\Lambda = 1 + 5252.1 \, (1 + \xi C_L dh) f_{comp} \left[\frac{P_{AUX_c}}{YZ}\right] \tag{4.68}$$

4. From Equations 4.19 and 4.31,

$$Q_a = \frac{WZ}{W_0 \, (1 + \xi C_L dh) f_{comp}} \qquad \text{lb ft} \tag{4.69}$$

5. From Equations 4.22 and 4.23,

$$\beta = \beta^* + \Delta\beta \qquad \text{degrees} \tag{4.70}$$

$$\Delta\beta = \frac{-\kappa \cos\psi \sin(\psi - \frac{\theta dh}{|dh|}) \left[(1 + \xi C_L dh)^{\frac{1}{2}} - 1\right]}{\theta\pi/180} \text{ degrees} \tag{4.71}$$

The computation of f_{comp} is performed using f_{comp} plots (see page D-11).

For given values of X and Y: Z is obtained from an X,Y,Z plot appropriate to $\{W_0, h_{ref}\}$; and β^* is obtained from an X,Y,β^* plot appropriate to $\{W_0, h_{ref}\}$.

An X,Y,Z plot, an X,Y,β^* plot, a set of f_{comp} plots, and Equations 4.62-4.71 together constitute the Corrected Performance

Model for R*c, Q_a and β for a given airplane.

Note that:

- R^*cW/W_0 is constant for constant $\{V_{w_c}, X, Y, dh, f_{comp}, P_{AUX_c}\}$
- $Q_a W_0/W$ is constant for constant $\{X, Y, dh, f_{comp}\}$
- β is constant for constant $\{X, Y, dh\}$.

Following are some remarks on this modelling method. First: the influence of center of gravity movement on propulsive efficiency is examined. Second: some typical values of f_{comp} for GA airplanes are given. Third: the effect of corrected windspeed on peak R^*W/W_0 and on the operating condition for peak R^*W/W_0 is examined.

Center of Gravity Effects:

Throughout this chapter computations of R*c and Q_a, for c.g. positions displaced a distance $dh\bar{c}$ from the reference c.g. position $h_{ref}\,\bar{c}$, have been performed by multiplying S* and dividing Q* by the factor $(1 + \xi C_L dh)$.

The factor $(1 + \xi C_L dh)$ was derived in Chapter 3 under the assumption that η_a was independent of h. This is not precisely correct. Consider movement of the c.g. while maintaining constant X and constant Y. This results in:

1. Constant C_L, but varying C_D (Equation C.29)
2. Varying $C_{R_a}^i$ (Equation D.53)
3. Constant J_a
4. Varying η_a^i and β (Figure D.6).

On the basis of Figure 3.10, it is assumed that a typical maximum variation in $C_{D_{ON}}$ with c.g. movement is 4%. This results in a 2% variation in $C_{R_a}^i$ (Equation D.53). From Figure D.6, a 2% variation in $C_{R_a}^i$ at constant J_a results in a maximum variation in η_a^i of approximately 1.5%.

Therefore the factor $(1 + \xi C_L dh)$ is expected to introduce a maximum error of 1.5% in R*c and Q_a; and a maximum error of 1.5% in the increment of Λ due to P_{AUX_c} (Equation 4.68). The latter error is expected to give a negligibly small error in Λ.

Compressibility Effects:

Computations of f_{comp} were performed for the LASA 60 airplane, using the Hamilton Standard Method (21): the results of these computations are given in Table 4.1.

A detailed study of propeller compressibility effects, using the approach involving f_{comp}, has not been performed by this author; such a study is desirable (see Appendix D). The following should be considered in an investigation of this matter (22):

1. Computation of propeller performance in incompressible flow may be performed using Goldstein-Lock analysis (8) which employs 2-Dimensional (2-D) airfoil data. This is accepted practice in the propeller industry.
2. It is accepted practice in the propeller industry to compute propeller performance, in compressible flow, using Goldstein-Lock analysis and 2-D airfoil data which

incorporate variations in airfoil lift and drag coefficients with Mach number. However, this computational method ignores two phenomena which may be important to the actual performance:

a) Three-dimensional flow near the blade tip: Radial flow near the blade tip (due to the tip vortices in the wake, and the proximity of the tip itself) reduces the effect of compressibility in the tip region. Consequently, a 2-D analysis will tend to overestimate the compressibility effect.

b) The effect of compressible flow on the wake-induced velocity: Compressibility effects should be accounted for in application of the Biot-Savart law to the computation of the velocity induced at each blade element by the wake.

The effects of these two phenomena on the performance should be assessed, and included in the analysis of propeller compressibility effects if necessary.

Full scale propeller tests will be required to give confidence in the use of any developed method for computing propeller compressibility effects.

Wind Effects:

Equation 4.66 expresses the effect of wind on R* in terms of the Corrected Windspeed V_{w_c}.

Figure 4.7 shows variations in X,Y and R^*W/W_0 at the operating condition for maximum R^*W/W_0, as corrected windspeed varies; for

the LASA 60 airplane [$h = h_{ref} = 0.3$, $f_{comp} = 1$, $P_{AUX_c} = 0$, $c = 0.45$ lb/BHP.hr]. Similar curves exist for the constraints [$h = \text{constant} \neq h_{ref}$, $f_{comp} = \text{constant} \neq 1$, $P_{AUX_c} = \text{constant} \neq 0$, $c = \text{constant} \neq 0.45$ lb/BHP.hr].

The wind has no effect on Q_a or β when X is fixed.

Engine Rotational Speed and Brake Torque

The engine rotational speed N_E (RPM) and brake torque Q_E (lb ft) are required in Chapter 5 for the computation of engine brake specific fuel consumption c (lb/BHP.hr). It is convenient to compute these quantities here, in terms of the propeller shaft speed N (RPM) and torque Q_a (lb ft). Figure A.2 shows the notation used in this derivation.

N_E is simply determined by the transmission gear ratio G:

$$N_E = GN \quad \text{revolutions/minute} \tag{4.72}$$

The engine brake torque Q_E is determined as follows:

$$P_E = P_S + P_{AUX} \quad \text{horsepower}$$

$$= P_S \left[1 + \frac{P_{AUX}}{P_S}\right]$$

$$\therefore \; Q_E = \frac{Q_a}{G}\left[1 + \frac{5252.1\, P_{AUX}}{NQ_a}\right] \quad \text{lb ft}$$

Substitution for Q_a (Equation 4.69), N (Equation 4.65), and P_{AUX} (Equation 4.62) yields

$$Q_E = \frac{Q_a}{G}\left\{1 + 5252.1\,(1 + \xi C_L dh) f_{comp}\left[\frac{P_{AUX_c}}{YZ}\right]\right\}$$

Invoking Equation 4.68, Q_E becomes

$$Q_E = \frac{Q_a \Lambda}{G} \quad \text{lb ft} \tag{4.73}$$

Input-Output Model

The input-output model of the Airframe-Propeller-Atmosphere (APA) subsystem consists of the set of relationships which determine R*c and Q_E (the outputs of the model) in terms of the airplane operational variables (the inputs to the model). These relationships have all been formulated in the foregoing discussion. Figure 4.8 depicts this model, with its inputs and outputs, in block diagram form.

Implementation:

The APA subsystem input-output model is well suited to implementation in an airborne microprocessor, for the following reasons:

1. The X,Y,Z plot; the X,Y,β* plot; and presumably the f_{comp} plots; may be stored as sets of coefficients of cubic polynomials. The memory space required for this storage is very small.
2. All of the required equations are algebraic equations, in which the most complex functions are trigonometric functions.

Allocation of numerical values to the non-operational variables in the model, for a particular airplane, is readily accomplished by the airframe manufacturer. In particular:

1. The X,Y,Z plot is constructed from propeller shaft torquemeter readings of Q_a, in conjunction with Equation 4.69.

2. The X,Y,β^* plot is computed from the propeller manufacturer's data. The parameters κ, ψ and θ required by Equation 4.71 for $\Delta\beta$ are obtained from a $C_R^i:J^2$ plot of the same propeller data.
3. The f_{comp} plots could be computed for the airframe manufacturer by the propeller manufacturer.
4. The value of ξ may be estimated by the airframe manufacturer from propeller shaft torquemeter readings of Q_a, in conjunction with Equation 4.69.

SUMMARY

A propeller performance model has been discussed. The APA subsystem input-output model has been developed. This model has been presented in block diagram form in Figure 4.8, and appears suited to microprocessor applications due to its simplicity and minimal storage requirements.

TABLE 4.1

COMPRESSIBILITY CORRECTION FACTOR f_{comp}

Flight Condition: Lockheed LASA 60, W = 3400 LB

$C_D = 0.0402 + 0.052\ C_L^2$ (power-off)

$h = h_{ref} = 0.3$ $\quad f_J = 0.98$

$P_{AUX} = 0$ $\quad f_D = 1.08$

Standard Atmosphere

Entries in this Table are $f_{comp} = \eta_p / \eta_p^i$

DENSITY ALTITUDE ft	EAS knots	PROPELLER RPM		
		2000	2300	2600
Sea Level	80	1.0	1.0	1.0
	100	1.0	1.0	1.0
10,000	80	1.0	1.0	0.994
	100	1.0	1.0	0.976

Note: Values of f_{comp} were computed using the Hamilton Standard Method of Propeller Performance Calculation, 1941 (21).

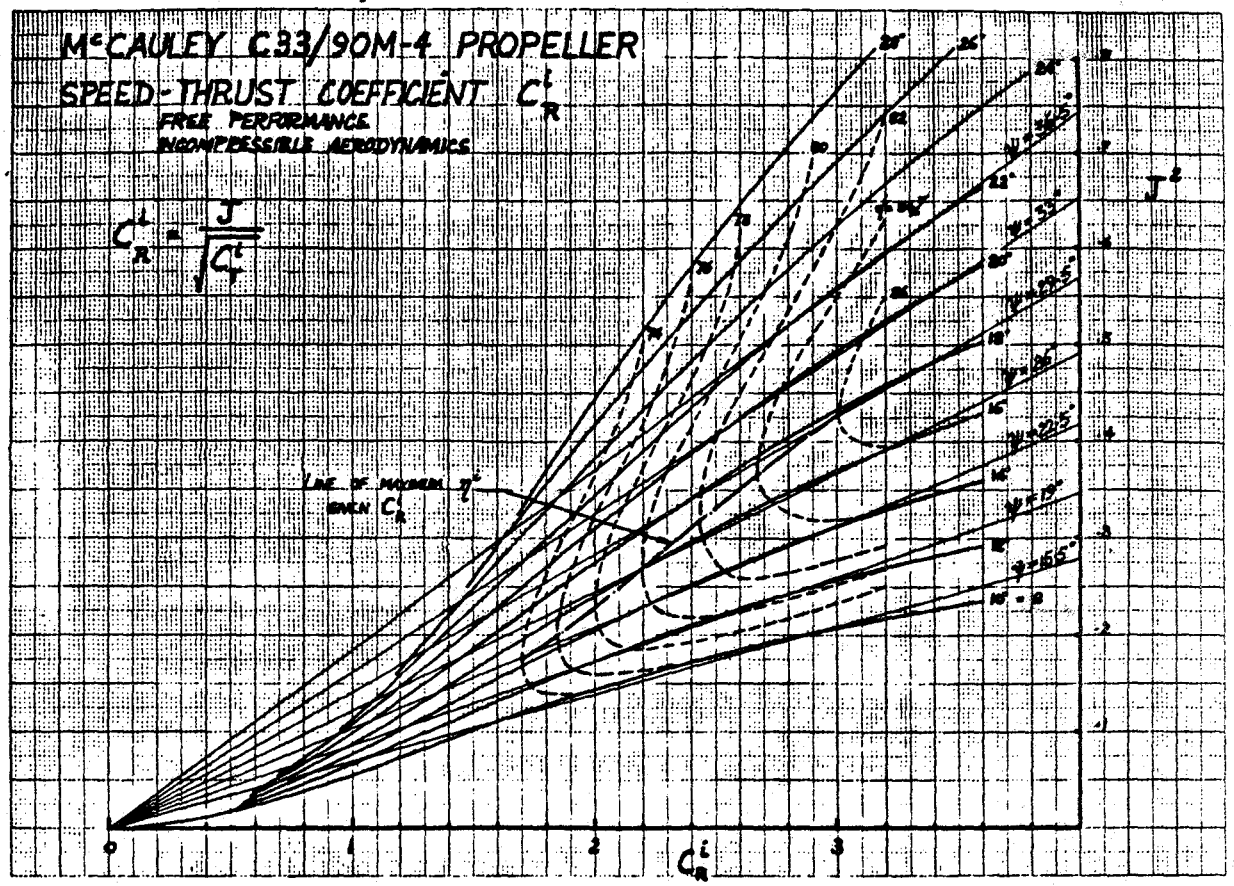

$\theta = 3.5$ degrees $\qquad \psi = 1.75\beta^* - 2$ degrees
$K = 2$ degrees

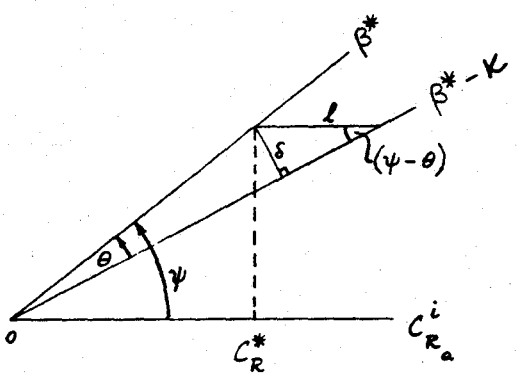

$$\delta = \frac{C_R^* \, \theta \, \pi/180}{\cos\psi} \qquad \ell = \frac{\delta}{\sin(\psi \pm \theta)} = \frac{C_R^* \, \theta \, \pi/180}{\cos\psi \sin(\psi \pm \theta)}$$

$+\theta$ FOR $-\Delta C_{R_a}^i$
$-\theta$ FOR $+\Delta C_{R_a}^i$

$$\left.\frac{\Delta\beta^\circ}{\Delta C_{R_a}^i}\right|_{J_a} = \frac{-K}{\ell} = \frac{-K\cos\psi \, \sin(\psi \pm \theta)}{C_R^* \, \theta \, \pi/180}$$

Now $\dfrac{C_{D_{ON}}|_h}{C_{D_{ON}}|_{h_{ref}}} = \dfrac{1}{(1 + \xi C_L dh)}$ SO THAT $\dfrac{C_{R_a}^i}{C_R^*} = (1 + \xi C_L dh)^{\frac{1}{2}}$ FROM EQUATION D.53

$$\therefore \Delta C_{R_a}^i = C_{R_a}^i - C_R^* = C_R^* \left[(1 + \xi C_L dh)^{\frac{1}{2}} - 1\right]$$ AND $+dh \rightarrow +\Delta C_{R_a}^i$, $-dh \rightarrow -\Delta C_{R_a}^i$

$$\therefore \Delta\beta^\circ = \frac{-K\cos\psi \, \sin\left(\psi - \frac{\theta \, dh}{|dh|}\right) C_R^* \left[(1 + \xi C_L dh)^{\frac{1}{2}} - 1\right]}{C_R^* \, \theta \, \pi/180}$$

$$= \frac{-K\cos\psi \, \sin\left(\psi - \frac{\theta \, dh}{|dh|}\right)\left[(1 + \xi C_L dh)^{\frac{1}{2}} - 1\right]}{\theta \, \pi/180}$$

$\therefore$ SUBSTITUTING FOR θ, ψ AND K: $\Delta\beta^\circ = -32.74 \cos(1.75\beta^* - 2) \sin\left(1.75\beta^* - 2 - 3.5\frac{dh}{|dh|}\right)\left[(1 + \xi C_L dh)^{\frac{1}{2}} - 1\right]$

FIGURE 4.1 EFFECT OF C.G. POSITION ON PROPELLER BLADE ANGLE.

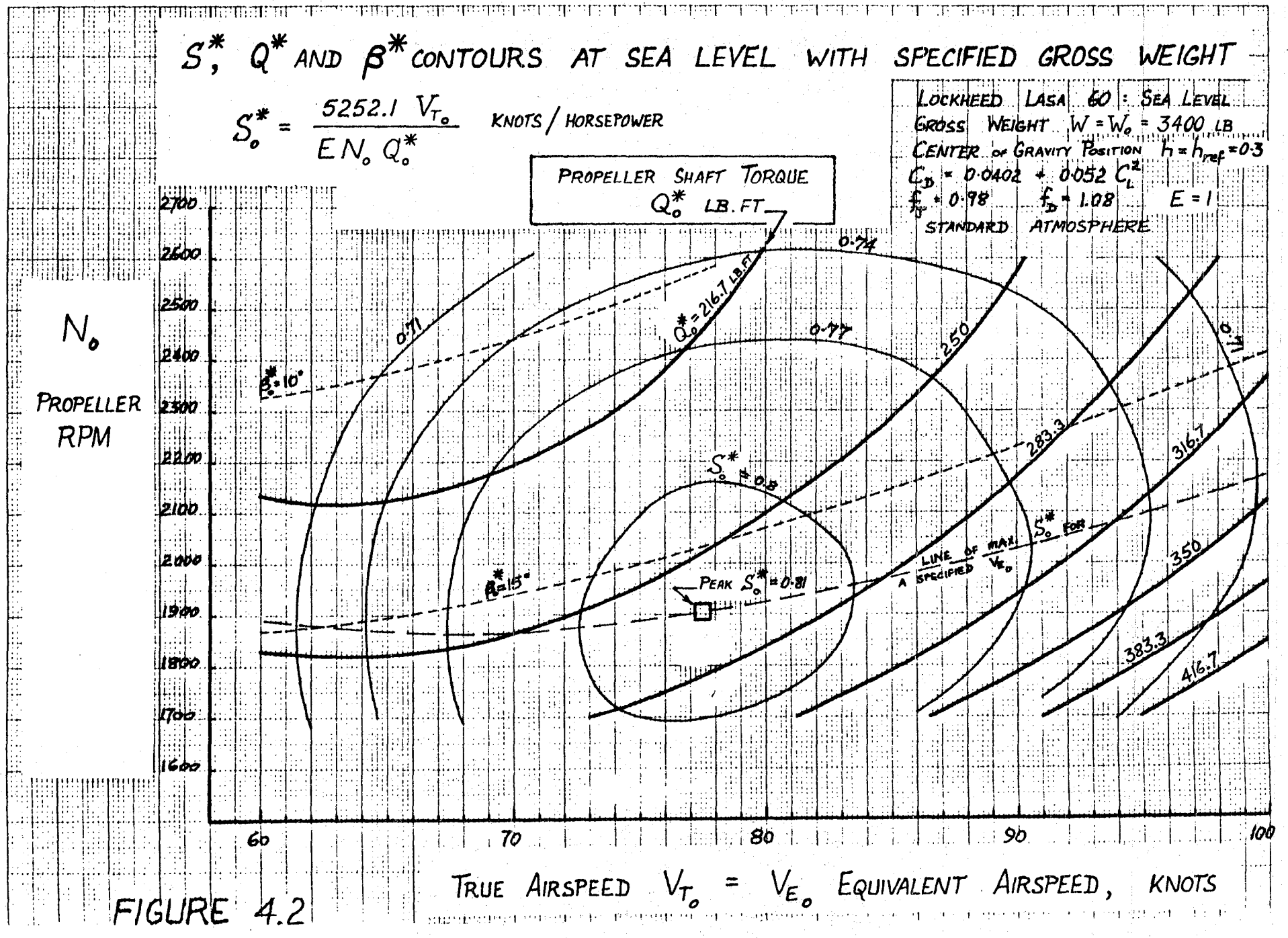
S^*, Q^* AND β^* CONTOURS AT SEA LEVEL WITH SPECIFIED GROSS WEIGHT
$S_o^* = \frac{5252.1\ V_{T_o}}{E N_o Q_o^*}$ KNOTS / HORSEPOWER
LOCKHEED LASA 60 : SEA LEVEL
GROSS WEIGHT $W = W_o = 3400$ LB
CENTER OF GRAVITY POSITION $h = h_{ref} = 0.3$
$C_D = 0.0402 + 0.052\ C_L^2$
$f_D = 0.98$ $f_D = 1.08$ $E = 1$
STANDARD ATMOSPHERE
PROPELLER SHAFT TORQUE Q_o^* LB. FT
N_o PROPELLER RPM
2700
2600
2500
2400
2300
2200
2100
2000
1900
1800
1700
1600
$Q_o^* = 216.7$ LB.FT
0.71
0.74
0.77
250
283.3
316.7
350
383.3
416.7
$\beta^* = 10°$
$\beta^* = 15°$
$S_o^* = 0.8$
PEAK $S_o^* = 0.81$
A LINE OF SPECIFIED MAX S_o^* FOR V_{E_o}
60
70
80
90
100
TRUE AIRSPEED V_{T_o} = V_{E_o} EQUIVALENT AIRSPEED, KNOTS

FIGURE 4.2

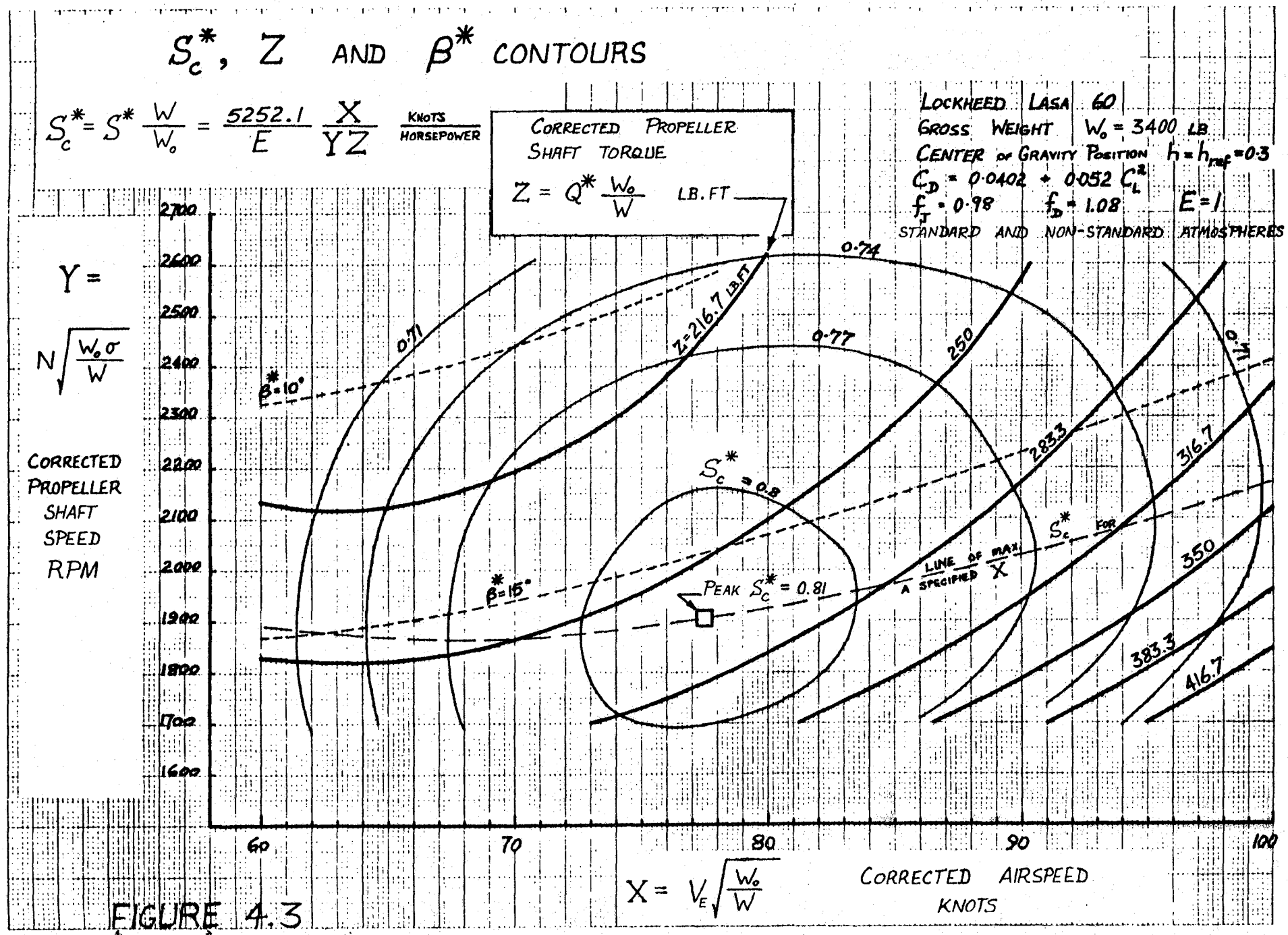
S_c^*, Z AND β^* CONTOURS
$S_c^* = S^* \frac{W}{W_o} = \frac{5252.1}{E} \frac{X}{YZ}$ KNOTS / HORSEPOWER
CORRECTED PROPELLER SHAFT TORQUE
$Z = Q^* \frac{W_o}{W}$ LB. FT
LOCKHEED LASA 60
GROSS WEIGHT W_o = 3400 LB.
CENTER OF GRAVITY POSITION $h = h_{ref} = 0.3$
$C_D = 0.0402 + 0.052\, C_L^2$
$f_T = 0.98$ $f_D = 1.08$ $E = 1$
STANDARD AND NON-STANDARD ATMOSPHERES
$Y = N\sqrt{\frac{W_o \sigma}{W}}$
CORRECTED PROPELLER SHAFT SPEED RPM
2700
2600
2500
2400
2300
2200
2100
2000
1900
1800
1700
1600
0.74
0.71
0.77
Z=216.7 LB.FT
250
283.3
316.7
350
383.3
416.7
$\beta^* = 10°$
$\beta^* = 15°$
$S_c^* = 0.8$
PEAK $S_c^* = 0.81$
LINE OF MAX S_c^* FOR A SPECIFIED X
60
70
80
90
100
$X = V_E\sqrt{\frac{W_o}{W}}$
CORRECTED AIRSPEED KNOTS

FIGURE 4.3

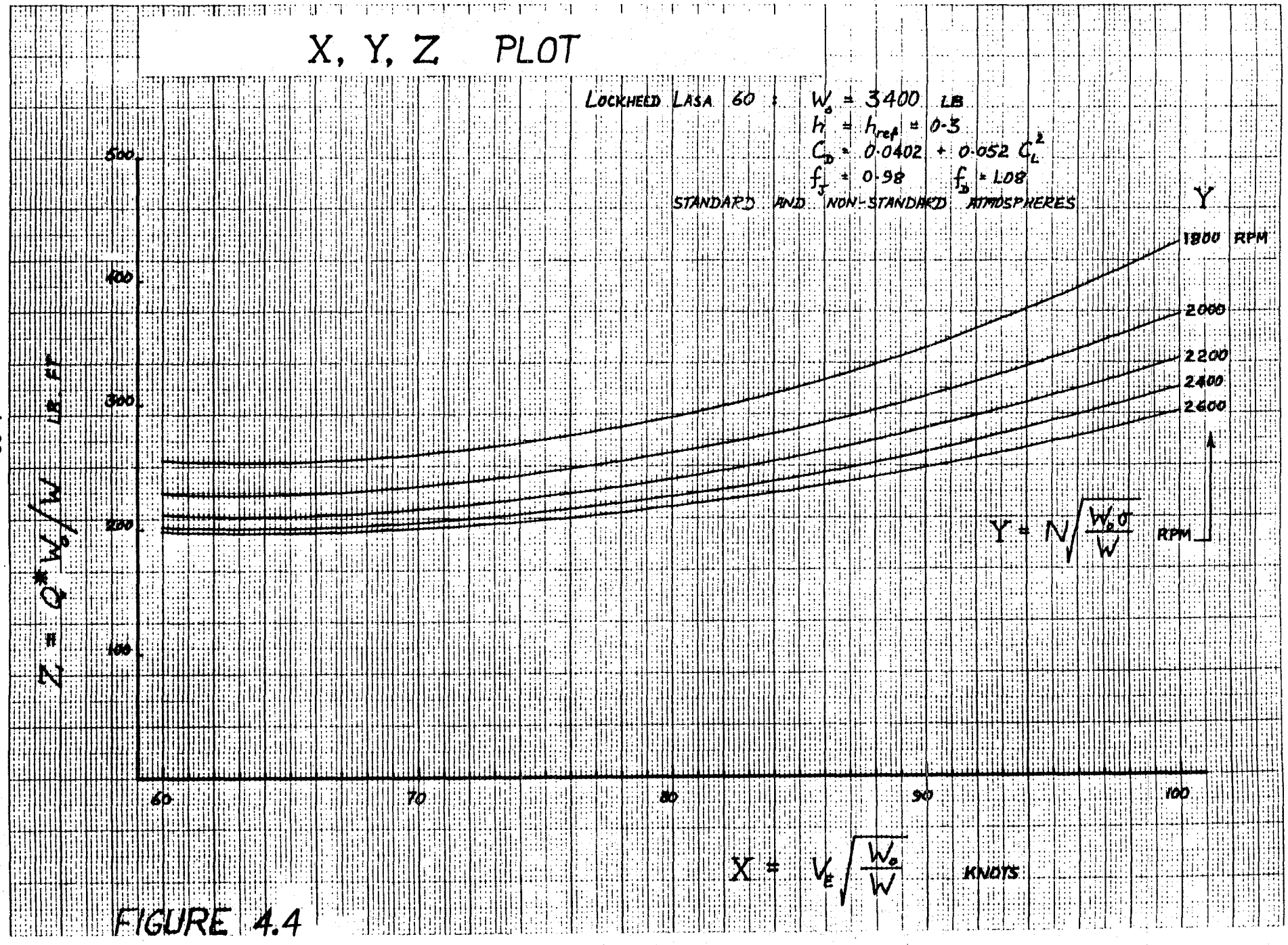
X, Y, Z PLOT
LOCKHEED LASA 60 : W_o = 3400 LB
$h_i = h_{ref}$ = 0·3
C_D = 0·0402 + 0·052 C_L^2
f_J = 0·98 f_D = 1·08
STANDARD AND NON-STANDARD ATMOSPHERES
Y
1800 RPM
2000
2200
2400
2600
$Y = N\sqrt{\frac{W_o\sigma}{W}}$ RPM
500
400
300
200
100
$Z = N/P_M * Q$
60
70
80
90
100
$X = V_E\sqrt{\frac{W_o}{W}}$ KNOTS

FIGURE 4.4

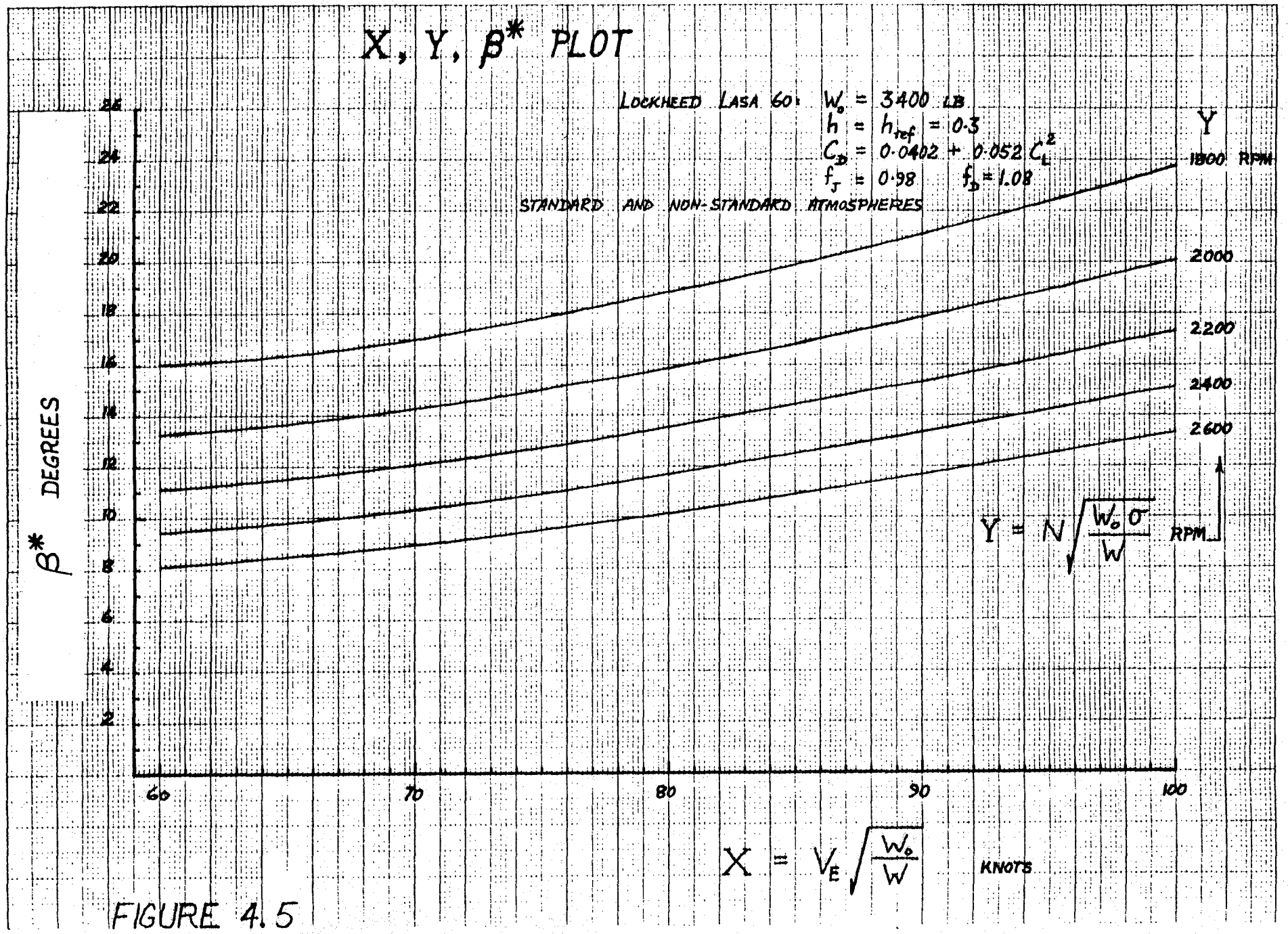
X, Y, β* PLOT
LOCKHEED LASA 60: W_o = 3400 LB
$h = h_{ref}$ = 0.3
C_D = 0.0402 + 0.052 C_L^2
f_J = 0.98 f_D = 1.08
STANDARD AND NON-STANDARD ATMOSPHERES
β* DEGREES
26
24
22
20
18
16
14
12
10
8
6
4
2
60
70
80
90
100
Y
1800 RPM
2000
2200
2400
2600
$Y = N\sqrt{\frac{W_o}{W}\sigma}$ RPM
$X = V_E\sqrt{\frac{W_o}{W}}$ KNOTS

FIGURE 4.5

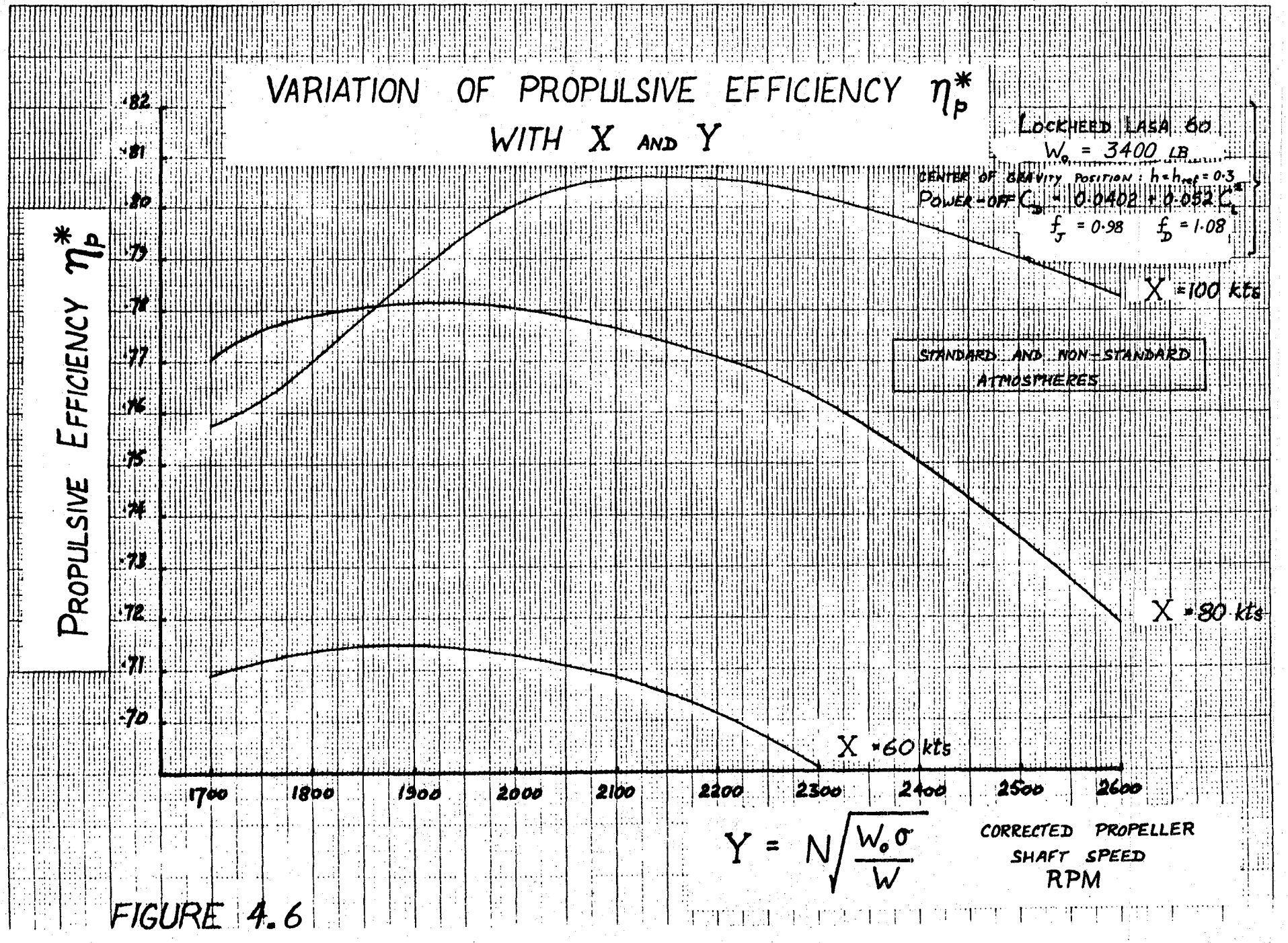
VARIATION OF PROPULSIVE EFFICIENCY η_p^* WITH X AND Y
LOCKHEED LASA 60
W_o = 3400 LB
CENTER OF GRAVITY POSITION : $h = h_{ref} = 0.3$
POWER-OFF $C_D = 0.0402 + 0.052\, C_L^2$
$f_J = 0.98$ $f_D = 1.08$
STANDARD AND NON-STANDARD ATMOSPHERES
X = 100 kts
X = 80 kts
X = 60 kts
PROPULSIVE EFFICIENCY η_p^*
.82
.81
.80
.79
.78
.77
.76
.75
.74
.73
.72
.71
.70
1700
1800
1900
2000
2100
2200
2300
2400
2500
2600
$Y = N\sqrt{\frac{W_o \sigma}{W}}$
CORRECTED PROPELLER SHAFT SPEED RPM

FIGURE 4.6

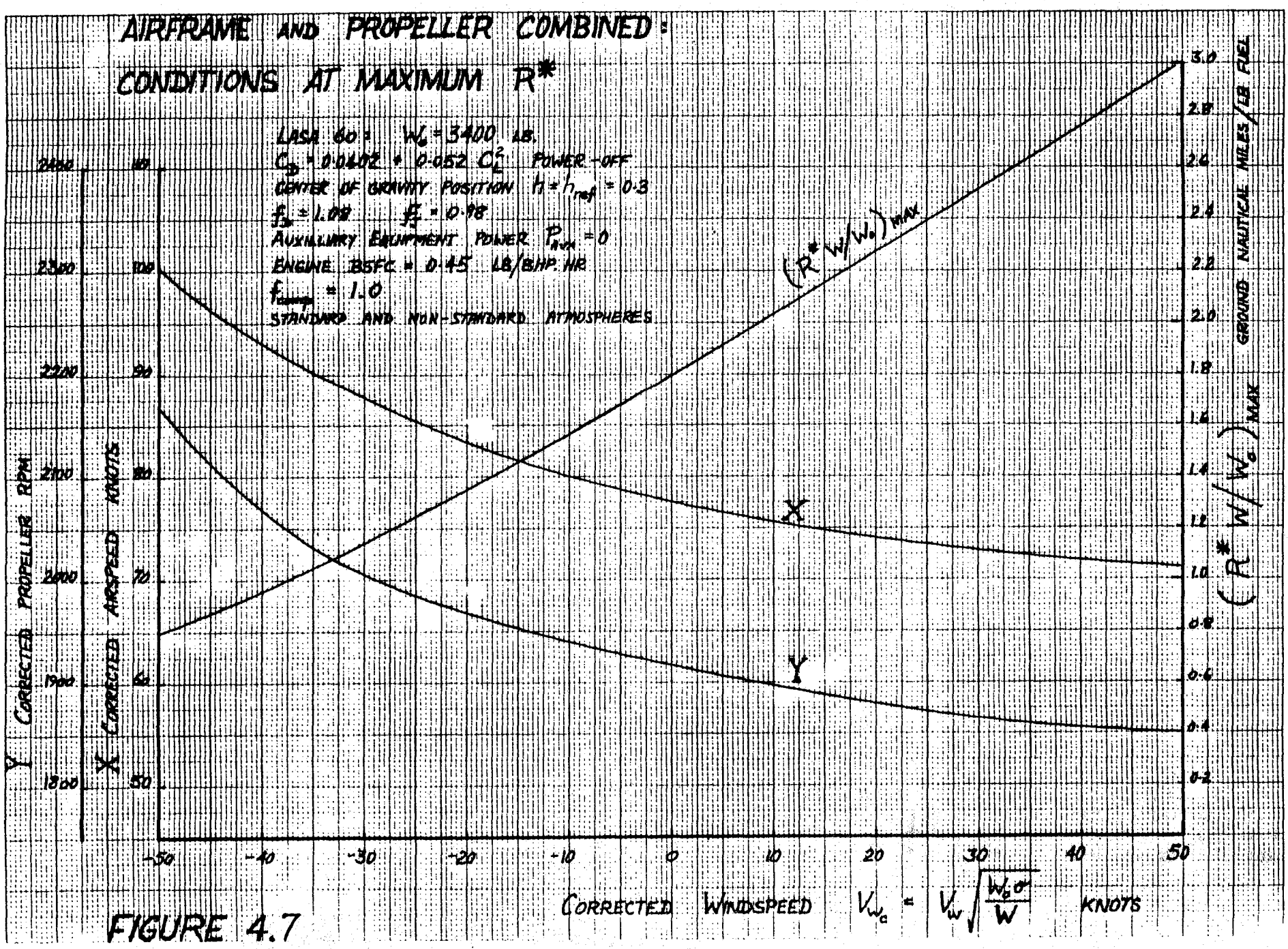
AIRFRAME AND PROPELLER COMBINED:
CONDITIONS AT MAXIMUM R*
LASA 60: W_o = 3400 LB.
$C_D = 0.0402 + 0.052\,C_L^2$ POWER-OFF
CENTER OF GRAVITY POSITION $h = h_{ref} = 0.3$
$f_{Vc} = 1.08$ $f_T = 0.98$
AUXILLIARY EQUIPMENT POWER $P_{a_{ux}} = 0$
ENGINE BSFC = 0.45 LB/BHP HR
$f_{comp} = 1.0$
STANDARD AND NON-STANDARD ATMOSPHERES
Y CORRECTED PROPELLER RPM
X CORRECTED AIRSPEED KNOTS
$(R^* W/W_o)_{MAX}$
GROUND NAUTICAL MILES/LB FUEL
$(R^* W/W_o)_{MAX}$
X
Y
CORRECTED WINDSPEED $V_{W_c} = V_W \sqrt{\frac{W_o \sigma}{W}}$ KNOTS

FIGURE 4.7

APA SUBSYSTEM INPUT - OUTPUT MODEL

STANDARD AND NON-STANDARD ATMOSPHERIC CONDITIONS

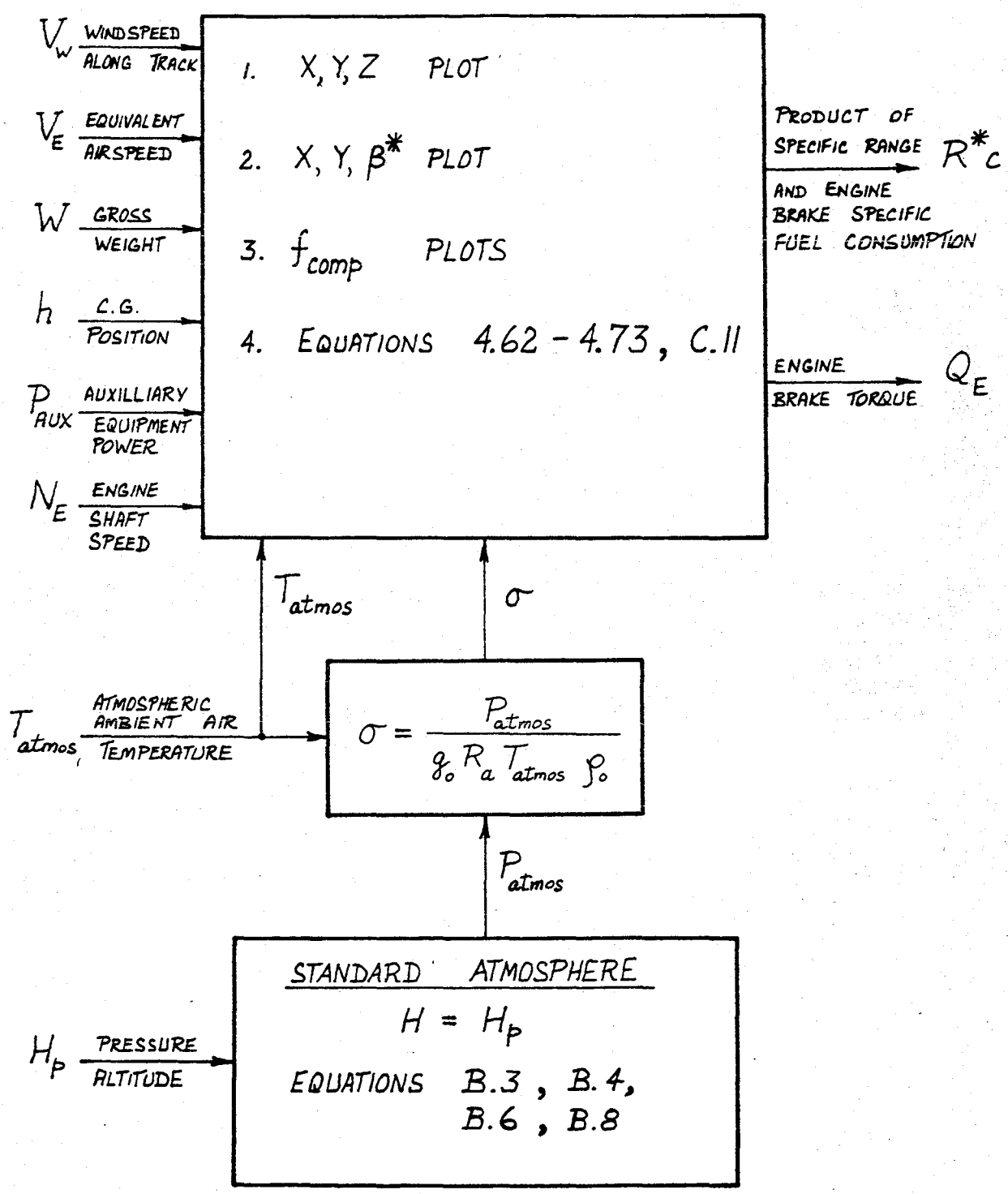

NOTE: THE INPUT T_{atmos} = THE ATMOSPHERIC AMBIENT TEMPERATURE IS REQUIRED FOR THE COMPUTATION OF THE SPEED OF SOUND IN THE ATMOSPHERE DURING THE COMPUTATION OF f_{comp}.

FIGURE 4.8

CHAPTER 5

THE ENGINE-ATMOSPHERE SUBSYSTEM

Table of Contents

Table of Contents

(concluded)

CHAPTER 5

THE ENGINE-ATMOSPHERE SUBSYSTEM

INTRODUCTION

This chapter develops an input-output model for the cruise performance of the engine-atmosphere subsystem. The engine-atmosphere subsystem considered here consists of a naturally aspirated, spark-ignition, inlet port fuel injection, four-stroke piston aero engine; operating in the standard atmosphere or in a non-standard atmosphere.

In this development, the engine is assumed to be of fixed design. We consider only steady state operation of the engine: no attempt is made to develop a dynamic engine model. In addition, no account is taken of engine exhaust emission controls.

The tasks of the engine-atmosphere subsystem input-output model are:

1. To compute the engine control inputs required to minimize the engine Brake Specific Fuel Consumption (BSFC) at any engine operating point demanded by the APA subsystem (Chapter 4).
2. To compute the engine BSFC, c (lbm/BHP.hr). The airplane R* may then be computed from c and the value of R*c (knots/BHP) provided by the APA subsystem input-output model.

The input-output model developed here reflects current General Aviation piston engine technology in all respects but one: that of

ignition timing. All commercially available General Aviation piston engines employ fixed ignition timing. According to Chirivella (16):

> The magnetos are wired to ignite the mixture at a certain fixed advanced timing. This feature is different from the variable timing that automobile engines are provided with. The reason for this resides mostly in simplicity and the fact that the engine regimes in an airplane are not subject to drastic changes during flight. The optimum timing is selected for inhibiting detonation during take-off power situations. No attempt is made later on to vary the timing for cruise power . . . The normal timing varies somewhat from engine to engine, but is on the order of 20° BTDC [before top dead center].

In the pursuit of good fuel economy, the ignition timing incorporated in the input-output model developed here is optimized for maximum brake torque in every engine operating condition. This optimum ignition timing is called Minimum ignition advance for Best Torque (MBT), and is discussed in detail in Appendix E.

The engine-atmosphere subsystem input-output model developed here is referred to as the NEA (Naturally aspirated MBT ignition timing Engine-Atmosphere) subsystem input-output model. This model is developed from computations performed by the Naturally aspirated MBT ignition timing Engine (NMBTE) performance model presented in Appendix E.

The content of the NMBTE performance model is first examined. The performance of current technology, naturally aspirated (fixed ignition timing) General Aviation piston engines is then discussed. We then discuss in detail the performance predictions of the NMBTE performance model, and develop the NEA subsystem input-output model.

Finally, turbocharged spark-ignition piston engines are discussed briefly, and some recommendations offered for the development of a Turbocharged MBT ignition timing Engine-Atmosphere (TEA) subsystem input-output model: this model is not developed in this work.

THE NATURALLY ASPIRATED ENGINE PERFORMANCE MODEL

The naturally aspirated engine performance model used in this work is presented in Appendix E. That model will here be referred to as the Naturally aspirated MBT ignition timing Engine (NMBTE) performance model.

The NMBTE performance model is an analytical-experimental hybrid which computes naturally aspirated piston engine performance in terms of Brake Horsepower (BHP) and Brake Specific Fuel Consumption (BSFC) lbm/BHP.hr. The parameters included in this model are discussed briefly below. Parameters and phenomena which affect engine performance but which have been excluded from this model are also discussed below.

Parameters Included in the NMBTE Performance Model

The parameters included in the NMBTE performance model fall into two groups: design parameters and operational parameters.

Design Parameters:

Design parameters are those fixed by engine design. Since we consider engines of fixed design, these parameters are modelled

as constants. The design parameters included in the NMBTE performance model, and the values given them in the present work, are presented in Table 5.1.

Operational Parameters:

Operational parameters are those under the control of the pilot. Those included in the NMBTE performance model are listed below as inputs to and outputs from the computations of that model:

Inputs:	F	Fuel-dry air mass ratio
	P_m	Inlet manifold absolute pressure, inches Hg
	T_m	Inlet manifold temperature, degrees Kelvin
	P_e	Exhaust absolute back-pressure, inches Hg
	N_E	Engine shaft speed, RPM
Outputs:	$\dot{m}_a$	Air mass flow rate, lbm/hr
	$\dot{m}_f$	Fuel mass flow rate, lbm/hr
	BHP	Brake horsepower, horsepower
	c	Brake specific fuel consumption, lbm/BHP.hr
	Q_E	Brake torque, lb ft.

The quantities F, P_m, T_m, P_e are common to all cylinders. The quantities $\dot{m}_a$ and $\dot{m}_f$ are equally divided between all cylinders.

The NMBTE performance model assumes that:

1. Inlet manifold temperature T_m is equal to the atmospheric ambient air temperature T_s computed from the standard atmosphere model of Appendix B.
2. Exhaust absolute back-pressure P_e is equal to the

atmospheric ambient air absolute pressure P_{atmos} computed from the standard atmosphere model of Appendix B (with appropriate units conversion).

3. The ignition timing is the Minimum ignition advance for Best Torque (MBT) at all times. This ensures the maximum possible brake torque and the minimum possible BSFC for all operating points defined by the above set of inputs.

For computations performed by the NMBTE performance model in this work:

1. The computational scheme is given on pages E-39 through E-43.
2. The fuel metering schedules used are discussed on pages E-38 and E-39, and illustrated in Figure E.18.
3. The Reference Operating Point and the Fuel Schedule Datum Conditions are listed in Table 5.2.
4. The engine delivers maximum continuous BHP at the Reference Operating Point.

Parameters and Phenomena Excluded from the NMBTE Performance Model

The parameters and phenomena excluded from the NMBTE performance model are listed below.

1. Ignition timing τ: The assumption of MBT ignition timing obviates the need to include ignition timing τ explicitly in the NMBTE performance model: the MBT ignition timing τ_o at any operating point is unknown in this model.

Taylor (13) presents some automobile data, here reproduced as Figure 5.1, which shows the effect on Brake Mean Effective Pressure (BMEP) of variations in ignition timing τ from τ_o. According to Taylor (13),

> . . . variations in spark timing, from that for maximum power, have the same percentage effect on brake mep at all loads and speeds. This correlation makes it possible to predict the effect of a given departure from best-power spark advance on both output and fuel economy.

In the light of Figure E.3, however, these data would appear inapplicable to all usable equivalence ratios. It is unclear from Taylor (13) if the data of Figure 5.1 apply to all values of $\{\phi, T_m, P_e, \text{CHT}, h\}$.

With a knowledge of τ_o and the effect on BMEP of variations in τ from τ_o, the performance of fixed ignition timing engines might be easily modelled. Such performance has not been modelled here.

2. Cylinder Head Temperature (CHT): CHT was not required for any performance computations. Monts (23) shows that for fixed ignition timing engines, leanouts at constant inlet manifold pressure and constant RPM result in a maximum CHT at $\phi \simeq 1$ (see Figure 5.4). It is assumed that the same behavior is demonstrated by engines employing MBT ignition timing. Curtiss-Wright (15) state that for their TC18 engine, in which the spark was advanced from 25° BTDC to

30° BTDC for cruise power settings (resulting in improved fuel economy):

> There is one disadvantage to using spark advance; if the mixture is ignited sooner, then the duration of the combustion period is longer; the burning takes place over a longer period of time inside the combustion chamber; the result is more heat generated inside the cylinder and higher cylinder head temperature. So spark advance requires the use of a little more cowl flap to maintain a given cylinder head temperature.

In the NMBTE performance model, it is assumed that CHT remains within operational limits at all times.

3. Exhaust Gas Temperature (EGT): EGT was not required for any performance computations.

With regard to operating limits on EGT, Monts (23) shows that for fixed ignition timing engines, leanouts at constant inlet manifold pressure and constant RPM result in a peak EGT slightly lean of $\phi = 1$ (see Figure 5.4).

When leaning at constant BHP and constant RPM with approximately MBT ignition timing, Chirivella (16) found that for the Lycoming TIO-541-E engine:

> . . . the engine temperatures do not necessarily become higher than those obtained at the best power point if one is able to lean sufficiently to the left of the TIT [Turbine Inlet Temperature] peak.

Curtiss-Wright (15) state that for the TC18 engine, when the spark was advanced from 25° BTDC to 30° BTDC:

> . . . since the burning takes place for a longer period of time, inside the cylinder, the resulting exhaust gas temperatures are lower. This is the main reason for using spark advance. Exhaust gas temperatures are reduced, with resulting benefits to turbine and parts in the exhaust system.

From these observations it is concluded that MBT ignition timing will probably yield acceptably low values of EGT in all ultralean operating conditions. For simplicity in the NMBTE performance model, it is assumed that EGT never exceeds engine operational limits in any operating condition.

4. Detonation: No attempt is made in the NMBTE performance model to either predict the occurrence of detonation or to model its effects on engine performance. The interested reader is referred to Appendix F where these matters are briefly discussed.
5. Non-Uniform Distribution of Air and Fuel to Each Cylinder: Uniform distribution of induction air and fuel flow to all cylinders is assumed in the NMBTE performance model.
6. Atmospheric humidity: The NMBTE performance model assumes that the inducted air is dry.
7. Ram Effects: Inlet manifold temperature changes due to ram are neglected. Similarly, at wide open throttle (WOT), inlet manifold absolute pressure changes due to ram are neglected (clearly at a given inlet manifold absolute pressure at part throttle, ram air pressure need not be considered).

In all WOT operations, the NMBTE performance model considers inlet manifold absolute pressure P_m to be a function of engine shaft speed N_E and atmospheric ambient air absolute pressure P_{atmos} (Appendix B) as follows:

N_E, RPM	(P_m/P_{atmos}) at WOT
2,000	0.969
2,200	0.963
2,400	0.956
2,600	0.950

At WOT, increasing engine shaft speed results in: increasing absolute pressure losses in the inlet manifold, due to friction; and hence decreasing P_m/P_{atmos} (see Ref. 24, p. 19).

8. Inlet Manifold Heat Exchanger Effects: Variations in the temperature of the cooling air surrounding the inlet manifold, from the atmospheric ambient temperature, may significantly affect the inlet manifold air temperature.

> The relatively long length and large diameter of the modern air cooled aircraft engine's intake air manifolding make an excellent heat exchanger. In fact, we find that the inlet port temperature may be more influenced by the temperature of the air surrounding the inlet manifold than it is by the temperature of the consumed air (25).

The complexity involved in modelling this installation effect has been avoided. The inlet manifold temperature T_m is assumed (for simplicity) equal to the atmospheric ambient air temperature T_s (Appendix B) at all times in the NMBTE performance model.

9. Inlet Manifold and Exhaust Manifold Pressure Acoustic Effects: In the NMBTE performance model, P_m (P_e) is taken to be the mean value of the inlet (exhaust) manifold absolute pressure at the inlet (exhaust) valve: variations in $\{P_m, P_e\}$ in time and from cylinder to cylinder, due to inlet and exhaust manifold dynamics, are ignored. The interested reader is referred to Reference 26 for a study of these phenomena.

10. Exhaust Absolute Back-Pressure Variations from Atmospheric Ambient Air Absolute Pressure: The NMBTE performance model sets the exhaust absolute back-pressure P_e equal to the atmospheric ambient air absolute pressure P_{atmos} of Appendix B (with appropriate units conversion): variations in this condition due to exhaust manifold acoustic effects, flight speed, the installation of an exhaust augmentor (24) etc. are ignored.

NATURALLY ASPIRATED ENGINE PERFORMANCE: FIXED IGNITION TIMING

All commercially available General Aviation piston engines employ fixed ignition timing. Before discussing the performance predictions of the NMBTE performance model, it is instructive to consider the performance of these fixed ignition timing engines.

Brake Horsepower

A typical plot of BHP versus inlet Manifold Absolute Pressure

(MAP) for various constant values of engine RPM, is shown in Figure 5.2 (24). This figure was "developed from the performance of Continental O-470-K and -L engines" (24) at standard sea level conditions.

Figure 5.3 (24) shows a typical sea level and altitude performance plot of BHP vs. inlet MAP and RPM. This Figure is (24):

> . . . used to determine the power output of a Continental O-470-M engine at altitude. The chart at the left shows engine output at sea-level standard conditions with no ram air pressure applied to the carburetor intake. The chart at the right shows the effect of altitude and is used in conjunction with the first chart. The points corresponding to engine rpm and manifold pressure are located on both charts. The horsepower indicated on the sea-level chart is transferred to an equivalent point C on the altitude chart. Then a straight line is drawn from the point A to the point C to establish the altitude correction. The intersection of this line with the density altitude line (D in the example) establishes the power output of the engine. The horsepower should be corrected by adding 1 percent for each 6°C . . . temperature decrease below T_s [T_s = standard atmospheric ambient temperature] and subtracting 1 percent for each 6°C temperature increase above T_s.

The fuel-air mass ratio appropriate to each point on the power charts of Figures 5.2 and 5.3 are not given by Bent and McKinley (24).

Leanout Performance

The General Aviation piston engine manufacturers usually present variations in engine power and specific fuel consumption with fuel-air mass ratio, for conditions of fixed throttle position (constant inlet MAP) and constant RPM.

Figure 5.4 (23) shows generalized mixture strength (fuel-air mass ratio) characteristics for General Aviation piston engines with fixed ignition timing. According to Monts (23), Figure 5.4†:

> . . . is a classic fixed-throttle [and fixed RPM] mixture control curve, and it depicts the relation of power (BHP or IHP), specific fuel consumption . . ., cylinder head temperature (CHT), and exhaust gas temperature (EGT) as a function of fuel/air ratio (F/A). Although the data presented here was developed at Teledyne Continental Motors, this same rather precise relationship is valid for all aircraft piston engines regardless of manufacturer. The F/A at which power peaks is called "best power" and the F/A at which specific fuel consumption minimizes is known as "maximum economy". It is obvious from an examination of this mixture control curve that maximum fuel economy occurs at approximately .060 F/A. Therefore, for most efficient operation and maximum energy conservation, all operation should be carried out at this mixture strength, unless limited by other factors.

Figure 5.5 (27) shows generalized data similar to that of Figure 5.4. With regard to Figure 5.5, Ref. 27 states:

> While the absolute values of [BSFC, BHP, CHT, EGT] . . . change with engine power, the relationship shown here is approximately true for operation over the normal flight regime of the engine from 40-100% power. Best power occurs at about 0.076 fuel-air ratio, peak cylinder head temperature at 0.067 which is the stoichiometric (chemically correct) fuel-air ratio, peak exhaust gas temperature at 0.062, and best economy at 25F° lean of peak EGT at a fuel-air ratio in the vicinity of 0.059 . . . While the "lean misfire limit" has been variously defined . . ., it will

---

†The original figure of Ref. 23 does not include the BHP curve shown in Figure 5.4; but treats the IHP curve of Figure 5.4 as both IHP and BHP, and treats the indicated specific fuel consumption curve of Figure 5.4 as both ISFC and BSFC. The modifications to the original figure of Ref. 23, presented here in Figure 5.4, were performed by Mr. F. Monts (28).

be defined here as a point at which the engine operator detects audible roughness in engine operation. This point is characterized by a sudden decrease in EGT and usually occurs between fuel-air ratios of .052 and .042 depending on the engine, ignition timing and fuel system.

A comparison of Figures 5.4 and 5.5 confirms that the relationships therein are not precise in general.

Current practice in General Aviation is to lean at constant inlet MAP and constant RPM (when a constant speed propeller is installed) in cruise. As shown above, the minimum BSFC is obtained at a fuel-air mass ratio of about 0.060 using this leaning technique. However, it is not always practical to lean to this fuel-air mass ratio because of engine temperature limits, detonation limits or other limits (see Ref. 27 and the discussion of Fuel Metering Requirements below). The General Aviation airframe manufacturers recommend leaning procedures which enable the pilot to establish a safe minimum fuel-air mass ratio between "best power" and "maximum economy" (as defined above):

1. In the absence of a fuel flow gauge, fuel pressure gauge or EGT gauge, the mixture is usually leaned until rough running is encountered, and then enrichened to re-establish smooth running.
2. An EGT gauge, fuel flow gauge or fuel pressure gauge permits the fuel-air mass ratio to be established more accurately than in (1) above. The fuel-air mass ratio may be established most precisely using an EGT gauge, by varying the fuel flow rate until the exhaust gas temperature

is a specified increment below peak EGT on the rich or lean side of peak EGT (see Figure 5.4).

The loss in BHP which occurs during leaning at constant inlet MAP and constant RPM is often undesirable. Constant BHP can be maintained during leaning by continuously opening the throttle and thereby increasing inlet MAP. According to Monts (23):

> During the late 1940's and 1950's when the airlines operated piston engine powered aircraft, they were naturally interested in economy of operation and extended service life. To promote both of them, Wright and Pratt & Whitney each published methods for economical cruise operation. Both were based on the use of torque meters (or BMEP gauge) and the mixture strength/power relationship . . . Pratt & Whitney called it the torque drop method of setting cruise mixture . . . Simply stated, the approximate desired power was set and the mixture leaned to peak the torque reading. The torque value was then reduced approximately 9 percent by leaning, thus establishing cruise economy mixture setting. The throttle was then opened to regain the 9 percent torque loss. The Wright method [(15)] . . . was the same except a 10 percent torque drop was used . . . It should be noted that there is no loss in performance from this operation and increased service life resulted.
>
> Although general aviation piston engines are not equipped with torque meters, approximately the same results can be obtained using an EGT gauge . . . [It] is possible to identify mixture strength from relative EGT's. After leaning to the desired mixture strength, the throttle may be opened to regain the power lost in the fixed throttle leaning. [The only measure of power recovery for the GA pilot is Indicated Airspeed.] There seems to be no hesitation about correcting throttle settings to compensate for ambient temperatures, but there seems to be reluctance to move the throttle (increase manifold pressure) to compensate for mixture strength. Obviously, if the operation is at an altitude requiring full throttle for the desired power setting, it will be necessary to suffer the airspeed loss.

Note that such power recovery by opening the throttle is only feasible if:

1. The fuel metering system maintains constant fuel-air mass ratio as the throttle is opened;
2. The absolute value of EGT does not exceed engine limits as the throttle is opened.

With regard to the constancy of fuel-air mass ratio in the TC18 engine as the throttle is opened or closed, Curtiss-Wright (15) states:

> . . . if you set 10% BMEP drop mixture, leave the mixture control where it is and then move the throttle (up and down), the BMEP will change, as will the fuel flow, but the fuel-air ratio will remain about the same. It should be noted that present day carburetors are not quite capable of holding the same fuel-air ratio if the changes in airflow are substantial.

According to Curtiss-Wright (15), the 10% BMEP drop mixture used for cruise power settings with the TC18 engine corresponds to a fuel-air mass ratio of about 0.053, which fuel-air mass ratio was used for cruise in conjunction with a spark advanced 5° from the normal spark timing of 25° BTDC. The leaning procedure used for the TC18 engine in cruise was equivalent to leaning at constant RPM and constant BHP to a fuel-air mass ratio of about 0.053.

Power recovery by opening the throttle during or after leaning in cruise is not common practice at present in General Aviation.

Fuel Metering Requirements

Figure 5.6 (23) shows generalized fuel-air mass ratio requirements

of General Aviation piston engines with fixed ignition timing. At power levels appropriate to idle, taxi and approach: a rich fuel-air mass ratio is required for starting, idling (29) and smooth transient response. In the cruise power range: operation near the "maximum economy" fuel-air mass ratio is possible. At the higher power levels: the fuel-air mass ratio must be increased to permit the development of high power, to cool the engine and to prevent detonation.

It is emphasized that the curve of Figure 5.6 varies from engine to engine. Figure E.16 (23) shows the fuel-air mass ratio metered to the Continental IO-540-N engine by the Beech Single Lever Power Control (23,30): the Desirable Schedule in Figure E.17 is the generalized curve of Figure 5.6.

NATURALLY ASPIRATED ENGINE-ATMOSPHERE SUBSYSTEM PERFORMANCE: MBT IGNITION TIMING

We here develop the Naturally aspirated MBT ignition timing Engine-Atmosphere (NEA) subsystem input-output model. This model is developed using the Naturally aspirated MBT ignition timing Engine (NMBTE) performance model described on pages 5-3 through 5-10.

The discussion in this section proceeds as follows:

1. For the NMBTE performance model
   a) A typical plot of BHP vs. inlet MAP and RPM is presented, and compared with corresponding data for fixed ignition timing engines.

b) The leanout performance predictions are examined, and compared with corresponding generalized leanout data for fixed ignition timing engines.

An indication of the reliability of the NMBTE performance model is obtained by the above comparisons of its performance predictions with the performance of fixed ignition timing engines.

c) For various fuel metering schedules: variations in BSFC, P_m and $\dot{m}_f$ with brake torque, RPM and altitude are presented.

d) Altitude variations of BSFC with various constraints are examined.

e) Corrected quantities are identified.

f) Corrected part-throttle performance plots are developed and presented.

2. The input-output model of the NEA subsystem is presented.

Figures 5.7 - 5.26 were drawn from computations performed using the NMBTE performance model. In these figures, engine operation at wide open throttle is denoted W.O.T.

Brake Horsepower

Figure 5.7 shows the variation of BHP with inlet MAP and RPM at sea level, with fuel metering schedule A, as predicted by the NMBTE performance model. Figure 5.7 is similar to the fixed ignition timing, sea level data of Figures 5.2 and 5.3. Each of these three figures applies to a naturally aspirated engine with a displacement

of 470 cubic inches. Comparing these three (sea level) figures:

1. The rate of change of BHP with inlet MAP at constant RPM is approximately the same.
2. The smaller rate of change of BHP with RPM at constant inlet MAP in Figure 5.7 is attributed to the MBT ignition timing in the latter figure.

Leanout Performance

Constant P_m and Constant BHP Leanouts:

Leanout performance of the NMBTE performance model is here examined under the following conditions:

1. At constant inlet MAP and constant RPM, at sea level
2. At constant BHP and constant RPM, at sea level.

Figure 5.8 shows typical leanout performance under each of these conditions. In Figure 5.8: curves labelled A pertain to leanout at constant inlet MAP = 23 in. Hg and 2300 RPM; and curves labelled B pertain to leanout at constant BHP = 132.55 BHP and 2300 RPM. During the constant inlet MAP leanout A, the minimum BSFC occurred at a fuel-air mass ratio of 0.058 (point 1 on the right hand side of Figure 5.8): at this point the BHP = 132.55 which value was used to perform the constant BHP leanout B.

Consider first the left hand side of Figure 5.8, which shows the variation of BHP during leanout A, and the variation of inlet MAP during leanout B. Peak BHP on curve A, and minimum P_m on curve B, both occur at a fuel-air mass ratio F = 0.080. Each experimental

BHP data point added to Figure 5.8 (denoted □) was obtained from the generalized BHP curve of Figure 5.4 in the following manner:

1. In Figure 5.4, let the best power fuel-air ratio be
   $F_B = 0.078$
2. In Figure 5.4, determine y% = percent best BHP at a fuel-air ratio = x% x F_B
3. In Figure 5.8, let the peak BHP fuel-air ratio be
   $F_p = 0.08$, and the peak BHP be $BHP_p = 157.97$
4. Compute F = x% x F_p
   BHP = y% x BHP_p
   and mark the point (F, BHP) as □ in Figure 5.8.

For $F \leq 0.08$, the BHP curve A and the experimental data points show close agreement. [For the fixed ignition timing data, BHP tends to decrease more rapidly with decreasing F (at ultralean values of F) than the MBT ignition timing model predicts: this is an expected trend.] For $F > 0.08$, the model does not show close agreement with the experimental data: this discrepancy is attributed to the fact that a cubic polynominal in equivalence ratio ϕ was used to represent the indicated thermal efficiency η_i' in the model (see Equation E.41 and Figure E.7). Such representation of η_i' may not be sufficiently accurate over the whole of the usable range of ϕ: a table lookup of η_i' may prove to be more accurate.

Curve B on the left hand side of Figure 5.8 shows the extent to which the throttle must be opened, as the fuel-air mass ratio is decreased below F = 0.08, during the constant BHP leanout.

Consider now the right hand side of Figure 5.8. First: comparing curve A with the generalized (fixed ignition timing) curve of Figure 5.5; we see that on the former curve the fuel-air mass ratio yielding minimum BSFC (point 1) is 0.058, while on the latter curve it is 0.059. On curve A, the minimum BSFC = 0.4631 is 86.4% of the BSFC = 0.5360 obtained at the peak BHP fuel-air mass ratio of 0.08; while in Figure 5.5, the minimum BSFC is approximately 85% of the best power BSFC. Thus for this case of leanout at constant inlet MAP and constant RPM, the variations in both BHP and BSFC predicted by the NMBTE performance model are quite close to those given by the generalized (constant inlet MAP, constant RPM) leanout data for fixed ignition timing engines.

Second: consider the BSFC variation along the constant BHP leanout curve B in Figure 5.8. While the general shape of this curve is similar to that of curve A, the minimum BSFC = 0.4556 (point 2) is lower than the minimum BSFC = 0.4631 on curve A (point 1), and occurs at a lower fuel-air mass ratio = 0.0495 than does point 1. The BSFC decreases by 1.62% along curve B from point 1 to point 2. Consequently, if the mixture is leaned at constant inlet MAP and constant RPM to the nominal "maximum economy" point 1, a further decrease in BSFC of 1.62% is possible with no loss in BHP by leaning along curve B to the true minimum BSFC point 2. In leaning at constant BHP from point 1 to point 2, the inlet MAP must be increased from 23 inches Hg to 26.17 inches Hg. Note that the minimum BSFC point 2 at F = 0.0495 is slightly lean of the peak

of the η_i' curve at F = 0.0514 (ϕ = 0.7667: see Figure E.7).

Consider now a series of leanout pairs similar to the pair on the right hand side of Figure 5.8. At sea level and 2300 RPM, a number of constant inlet MAP leanouts were performed [P_m = 28, 25, 23, 20, 16, 13, 10 inches Hg]. From the point of minimum BSFC (point 1: F_1, $BSFC_1$, BHP_1) each of these leanouts was continued at constant BHP = BHP_1 until the point of minimum BSFC (point 2: F_2, $BSFC_2$, BHP_1) was reached. Figure 5.9 shows for each leanout sequence:

1. F_1 and F_2
2. $\Delta BSFC_{min}\% = 100\ [BSFC_2 - BSFC_1]/BSFC_1$

plotted against percent maximum continuous (mc) BHP = 100 [BHP_1/230]. The increase in inlet MAP from point 1 to point 2 may also be observed in Figure 5.9. As the inlet MAP of point 1 decreases, the value of F_1 increases, reaching the stoichiometric fuel-air mass ratio at $P_m \approx 10$"Hg. In comparison, the value of F_2 is virtually constant at $F_2 \approx 0.0494$. The value of $\Delta BSFC_{min}\%$ decreases as the percent mc BHP decreases.

As discussed previously, the current practice in General Aviation is to lean at constant inlet MAP and constant RPM. Once the "maximum economy" point is reached by this leaning technique, a further decrease in BSFC is possible with no further loss in BHP: Figure 5.9 indicates that for the engine represented therein (at sea level, 2300 RPM) this BSFC decrease is less than 2% for BHP values (at the "maximum economy" point) greater than 50% mc BHP [this is the BHP range in which General Aviation airplanes generally

operate in cruise].

For BHP values (at the "maximum economy" point) less than 50% mc BHP, the decrease in BSFC from point 1 to point 2 is substantial. This BHP range is appropriate to automobiles in constant speed driving conditions. From Figure 5.9, an automobile cruising at say 25% mc BHP would achieve a 4.5% decrease in BSFC if its fuel metering schedule was established on the basis of leanouts at {constant BHP, constant RPM} rather than at {constant inlet MAP, constant RPM}.

F for Minimum BSFC During Constant BHP Leanouts:

Woods (31) discusses the procedures for establishing optimum fuel metering schedules. He shows that fuel-air mass ratio schedules for minimum BSFC must be obtained by leaning at constant BHP (rather than at constant inlet MAP) and constant RPM. This has been confirmed by the NMBTE performance model in the foregoing subsection.† Woods (31) concludes that approximately a 4% decrease in BSFC is achieved, with the Jeep engine at constant RPM, by leaning from point 1 to point 2 in the manner described in the foregoing subsection; and that the true minimum BSFC = $BSFC_2$ occurs at a fuel-air mass ratio $F_2 = 0.9\ F_1$††. [In Figure 5.9, a decrease in BSFC of 4% corresponds to $F_2 \approx 0.78\ F_1$ and to BHP ≈ 27.5% mc BHP].

---

† Woods also shows that an equivalent correct method for obtaining optimum fuel metering schedules is to: "Maximize torque for a constant fuel consumption [fuel mass flow rate] and constant speed" (31).

††Woods (31) does not state the ignition timing corresponding to these results, but from the context of his discussion that timing is assumed to be MBT.

In the present work, we are interested in determining the fuel-air mass ratio schedule yielding the minimum possible BSFC over the operational envelope {BHP, RPM, altitude} of the engine. To determine this schedule, a series of leanouts at {constant BHP, constant RPM, constant altitude} was performed using the NMBTE performance model. The results of these leanouts are shown in Table 5.3.

On the basis of these results it is proposed that, for General Aviation naturally aspirated piston engines employing MBT ignition timing:

> A single value of $F = F_{min}$ will yield minimum BSFC in all steady state operating conditions {BHP, N_E, H} (when F is not constrained by other considerations). In the present work, $F_{min} = 0.05$ is used.[†] The choice of a single value of F_{min} is expected to yield negligable variation in BSFC from the true minimum BSFC at any operating point {BHP, N_E, H} due to the flatness of the (F, BSFC) curve at such an operating point.

It is assumed in the present work that in all steady state operating conditions {BHP, N_E, H} of General Aviation naturally aspirated piston engines employing MBT ignition timing, BSFC increases continuously as F increases from $F_{min} = 0.05$ through $F_{max} = 0.08$ (F_{max} is defined in the next subsection).

[†] cf. Curtiss-Wright TC18 leanout discussed on pp. 5-14 through 5-15.

In the (NMBTE performance model) constant BHP leanouts described above, inlet MAP P_m was found to reach its minimum[†] at F = F_{max} = 0.08 and to increase continuously as F decreased from F_{max} = 0.08[†] through F_{min} = 0.05. In the present work, this same behavior of P_m is assumed to be true of General Aviation naturally aspirated piston engines employing MBT ignition timing.

Note that the value of F_{min} = 0.05 determined above is about 16.7% leaner than the value F = 0.06 currently recognized (23) as offering maximum economy for fixed ignition timing engines. The value F_{min} = 0.05 predicted by the NMBTE performance model may not be the value found to pertain to real engines using MBT ignition timing, since it results from the particular design parameter values used in the NMBTE model. The true importance of these constant BHP leanout results is that the minimum value of BSFC, throughout the engine operational envelope, occurs at essentially a *constant* value of F. On the other hand, the value F_{min} = 0.05 is supported by the fact that: for the leanouts at {constant inlet MAP, constant RPM, sea level} in Figure 5.9, the NMBTE performance model predicts minimum BSFC to occur in the range $0.0565 \leq F \leq 0.059$ for P_m in the range $28 \geq P_m$ inches Hg ≥ 20. This F range is slightly lean of the "maximum economy" value F = 0.06 (23) and F = 0.059 (27) for fixed ignition timing engines.

F for Maximum BHP During Constant P_m Leanouts:

The NMBTE performance model was used to determine the variation in fuel-air mass ratio yielding maximum BHP, during leanouts at

---

[†]Within 0.01 inches Hg.

{constant inlet MAP, constant RPM, constant altitude}, over the operational envelope of the engine. The results of these leanouts are shown in Table 5.4.

On the basis of these results it is proposed that, for General Aviation naturally aspirated piston engines employing MBT ignition timing:

> A single value of $F = F_{max}$ will yield maximum BHP in all steady state operating conditions $\{P_m, N_E, H\}$ (when F is not constrained by other considerations). In the present work, $F_{max} = 0.08$ is used. The choice of a single value of F_{max} is expected to yield negligible variation in BHP from the true maximum BHP at any operating point $\{P_m, N_E, H\}$ due to the flatness of the (F, BHP) curve at such an operating point.

It is assumed in the present work that, in all steady state operating conditions $\{P_m, N_E, H\}$ of General Aviation naturally aspirated piston engines employing MBT ignition timing, BHP decreases continuously as F decreases from $F_{max} = 0.08$ through $F_{min} = 0.05$.

The value of $F_{max} = 0.08$ predicted by the NMBTE performance model may not be the value found to pertain to real engines using MBT ignition timing, since it results from the particular design parameter values used in the NMBTE model. The importance of these constant P_m leanout results is that the maximum value of BHP, throughout the engine operational envelope, occurs at essentially a *constant* value of F. The value $F_{max} = 0.08$ is slightly rich of

the "best power" value F = 0.078 (23) and F = 0.076 (27) for fixed ignition timing engines.

Constant P_m and Constant BHP Leanouts from F_{max}:

Chirivella (16) identifies the "best power point" as a fuel-air mass ratio commonly selected by General Aviation pilots in cruise operations:

> . . . the "best power point" is an engine condition well known to pilots and easy to reach. Furthermore, and in spite of the power settings offered by the manufacturer for airplanes provided with TIT and fuel flow gauges, most pilots do like to operate the engine at such a point because of the safe margin in TIT and/or the absence of engine roughness (16).

We shall therefore examine some typical cases of leanout from the fuel-air mass ratio F_{max} = 0.08, using the NMBTE performance model. These leanouts will provide, for naturally aspirated MBT ignition timing engines, an indication of the BSFC improvements possible relative to the BSFC values obtained using a fuel-air mass ratio typical in current General Aviation practice.

Figure 5.10 shows four leanouts from F_{max} = 0.08: the left half of this figure shows sea level performance at 2450 RPM; and the right half of this figure shows performance at 6000 ft and 2450 RPM.

Consider the left half of Figure 5.10. At the operating point 1 [F = F_{max} = 0.08, P_m = 17.72 inches Hg, BHP = 115 = 50% mc BHP] the BSFC is $BSFC_1$. Two leanouts are shown originating from point 1.

1. Leaning at constant P_m = 17.72 in. Hg, from point 1 to the minimum BSFC = $BSFC_2$ at point 2, yields a decrease in BSFC of 12.15% $BSFC_1$ and a drop in BHP of 16 BHP.
2. Leaning at constant BHP = 115, from point 1 to the minimum BSFC = $BSFC_3$ at point 3, yields a decrease in BSFC of 17.84% $BSFC_1$, and requires the inlet MAP to be increased to 22.93 in. Hg.
3. Operation at point 3 rather than at point 2 yields a decrease in BSFC of 6.48% $BSFC_2$ and an increase in BHP of 16 BHP.

The right half of Figure 5.10 is similar to the left half of the same figure. At point 6, the inlet MAP has been increased to 21.51 inches Hg which is almost the wide open throttle value $P_{m_{WOT}} \simeq 22.9$ inches Hg.

Figure 5.10 clearly shows that significant decreases in BSFC may be achieved by leaning from the "best power" fuel-air mass ratio. The constant BHP leanouts from the "best power" point in Figure 5.10 show a maximum possible decrease in BSFC of about 17.8% of the "best power" BSFC. This result compares well with the experimental results reported by Chirivella (16) for similar leanouts of a turbocharged Lycoming TIO-541-E engine in flight. Chirivella's tabulated results of leaning at constant BHP from the "best power" fuel-air mass ratio, with the ignition timing advanced from the standard setting of 20° BTDC to 30° BTDC, show that BSFC decreases (16):

> . . . from 11.8 up to 20.8% if severe roughness is allowed. The numbers become limited to 17.4% if only incipient roughness is tolerated. If on the other hand the engine is not allowed to operate with any trace of roughness, the best fuel economy [BSFC] improvement is identified as 14.4% at 15,000 ft altitude and 75% rated power.

When leaning from the "best power" fuel-air mass ratio, the advantages of leaning at constant BHP rather than at constant inlet MAP are that:

1. No loss in BHP is suffered
2. A substantially lower minimum BSFC is achieved: about 6% lower in the cases shown in Figure 5.10.

Of course, if WOT is encountered during a constant BHP leanout, the full BSFC advantage of this leaning technique cannot be realized.

Performance with Specified Fuel Metering Schedule

We here examine the manner in which BSFC, inlet MAP and fuel mass flow rate vary with brake torque, RPM and altitude; when fuel is metered to the engine according to the fuel metering schedules A, B and C shown in Figure E.18.

BSFC Performance Maps at Sea Level:

Figures 5.11 - 5.13 show BSFC versus engine brake torque, for constant values of P_m and RPM at sea level; as computed by the NMBTE performance model. Lines of constant percent maximum continuous BHP are superimposed on these figures. Figures 5.11, 5.12, 5.13 correspond to fuel metering schedules A, B, C respectively.

In each of Figures 5.11 - 5.13:

- $19 \leq$ inlet MAP, inches Hg ≤ 29
- $2000 \leq$ RPM ≤ 2600

The following may be observed in Figures 5.11 - 5.13:

1. At constant fuel-air mass ratio
   a) Brake torque increases with increasing P_m, at constant RPM
   b) Brake torque decreases with increasing RPM, at constant P_m
   c) BSFC decreases with increasing P_m, at constant RPM
   d) BSFC increases with increasing RPM, at constant P_m.
2. The diagrams generally move to lower BSFC and lower brake torque ranges, as the fuel metering schedule varies from A to B to C. This is to be expected from the foregoing discussion of leanout performance.

In Figures 5.11 and 5.12, the rising values of BSFC with increasing brake torque (at constant RPM and high BHP) are due to the rising value of F with increasing air mass fraction at high values of the latter.

With fuel metering schedule A (Figure 5.11) at any fixed RPM, minimum BSFC occurs at about 85% maximum continuous BHP. With fuel metering schedule B (Figure 5.12) at any fixed RPM, minimum BSFC occurs at about 64% maximum continuous BHP. With fuel metering schedule C (Figure 5.13) at any fixed RPM, minimum BSFC occurs at WOT: note that fuel metering schedule C meters the fuel-air mass ratio F_{min} to the engine at all times.

Figures 5.14 and 5.15 correspond to Figure 5.11:

- Figure 5.14 shows inlet MAP vs. brake torque for various constant values of RPM; for fuel metering schedule A.

- Figure 5.15 shows fuel mass flow rate vs. brake torque for various constant values of RPM; for fuel metering schedule A.
- All of the information in Figure 5.11 is contained in Figures 5.14 and 5.15. In particular, for any brake torque and RPM in Figure 5.15, the BSFC is computed from Equations E.3 and E.8.

Likewise, Figures 5.16 and 5.17 correspond to Figure 5.12; and Figures 5.18 and 5.19 correspond to Figure 5.13.

BSFC Performance Maps at Altitude:

Figure 5.20 shows BSFC versus engine brake torque, for constant values of P_m and RPM at 6,000 ft altitude; as computed by the NMBTE performance model using fuel metering schedule B. Lines of constant percent maximum continuous BHP are superimposed on this figure.

Figure 5.20 may be compared to its sea level counterpart Figure 5.12. Note that in Figure 5.20: at any fixed RPM, minimum BSFC occurs at about 65% maximum continuous BHP.

Figures 5.21 and 5.22 correspond to Figure 5.20, and may be compared respectively to their sea level counterparts Figures 5.16 and 5.17.

Altitude Variations of BSFC with Constraints

We now examine altitude variations in BSFC when various constraints are imposed upon the engine operation.

Beginning at the operating point

- Sea level
- P_m = 21.56 inches Hg
- RPM = 2100
- BHP = 55% maximum continuous (mc) BHP
- F = 0.067

five constrained altitude variations in BSFC were computed using the NMBTE performance model. The constraints imposed and the results of the computations are shown in Figure 5.23.

The constraints BHP$\sqrt{\sigma}$ = constant and RPM$\sqrt{\sigma}$ = constant were selected for the computations of Figure 5.23 because:

Straight and level steady flight of a fixed-pitch propeller airplane with

- Fixed gross weight
- Fixed center of gravity position
- No propeller compressibility effects

at constant equivalent airspeed (EAS) and at various altitudes requires that BHP$\sqrt{\sigma}$ = constant and RPM$\sqrt{\sigma}$ = constant (see Chapter 4).

In Figure 5.23:

1. Compare curves A and C: the greater values of P_m required for curve C result in greater decreases in BSFC with altitude for curve C than occur for curve A.
2. Compare curves C and B: the greater values of RPM for curve B result in smaller decreases in BSFC with altitude

for curve B than occur for curve C (or curve A). Note that curve B, which corresponds to the fixed-pitch propeller airplane at constant EAS described above, reaches a minimum BSFC at an altitude of about 8,000 ft.

3. Curves C and D are not identical, but are almost indistinguishable and are shown as a single curve. The altitude variations in BSFC for curve D are attributed solely to the altitude variations in inlet manifold temperature and exhaust absolute back-pressure.
4. Compare curves D and E: the increased values of RPM for curve E result in smaller decreases in BSFC with altitude for curve E than occur for curve D.

Figure 5.23 clearly shows the extent to which altitude variations in BSFC depend upon the engine operational constraints. The co-location of curves C and D in Figure 5.23 is further discussed in the next subsection.

Corrected Quantities

In order to formulate a compact engine-atmosphere subsystem input-output model, we do well to make use of corrected quantities; as we did in Chapter 4 in the formulation of the APA subsystem input-output model. We here develop such corrected quantities using the NMBTE performance model.

Corrected Brake Torque:

The co-location of curves C and D in Figure 5.23 stimulated the search for an expression for corrected brake torque in part-throttle operating conditions.

Examination of the computer computations which produced curve D (Figure 5.23) revealed that:

> At constant P_m = 21.56 inches Hg, constant N_E = 2100 RPM, and constant F = 0.067; $BHP\sqrt{\sigma}$ varied from the sea level value BHP_0 by no more than 0.5% of BHP_0, for altitude variations from sea level through 10,000 ft (standard atmosphere).

To check the reality of these computations, the cruise performance charts in the Information Manual for the Cessna 1980 Centurion were examined, and it was found that:

> For the Cessna 1980 Centurion at constant P_m = 22 inches Hg, constant N_E = 2300 RPM and recommended lean mixture; the value of $BHP\sqrt{\sigma}$ at 2000 ft, 4000 ft, 6000 ft and 8000 ft (standard atmosphere) varied from the mean value $\overline{BHP\sqrt{\sigma}}$ by no more than 1% $\overline{BHP\sqrt{\sigma}}$. The value of the fuel-air mass ratio F for the "recommended lean mixture" is unknown to the author.

These data agree with the NMBTE performance model computations for curve D (Figure 5.23).

Extensive computations using the NMBTE performance model were then performed to determine an expression for Corrected Brake Torque in part-throttle operating conditions. These computations revealed that:

Operation of the naturally aspirated MBT ignition timing engine here modelled, in the standard atmosphere, with constant values of

- Inlet MAP P_m, inches Hg
- Engine speed N_E, RPM
- Fuel-air mass ratio F

yields a brake torque Q_E lb ft which is a function of altitude H (ft) only. At sea level, Q_E takes the value Q_{E_0}. The Corrected Brake Torque Q_{E_c} given by

$$Q_{E_c} = Q_E \sigma^n \quad \text{lb ft} \tag{5.1}$$

varies from Q_{E_0} by less than $\pm 1\%$ of Q_{E_0}, for altitudes in the range $0 \leq H \text{ (ft)} \leq 10{,}000$; for constant values of $\{P_m, N_E, F\}$ in the ranges

- $19 \leq P_m$ (inches Hg) $\leq [P_m$ at WOT$]$
- $2000 \leq N_E$ (RPM) ≤ 2600
- $0.05 \leq F \leq 0.08$

where σ = atmospheric air density ratio at altitude H (ft) (Appendix B)

n = Density Index = n(F). The Density Index n is a function of the fuel-air mass ratio F only: this functional relationship is shown in Figure 5.24.

Equation 5.1 is illustrated in Figure 5.25.

It is emphasized that constancy of the corrected brake torque Q_{E_c} with variations in altitude applies only to engine operation at constant inlet MAP. Q_{E_c} is not constant with variations in altitude when the engine is run at wide open throttle at each

altitude, since inlet MAP varies with altitude in this case.

Corrected Air Mass Flow Rate:

Equation E.42 shows the relationship between the air mass flow rates at any two operating points 1 and 2. Consider two operating points, one represented by the subscript 0 and the other by the absence of any subscript: for these two operating points, Equation E.42 becomes

$$\dot{m}_{a_0} = \dot{m}_a \left[\frac{T_m}{T_{m_0}}\right]^{(1-\varepsilon_t)} \left[\frac{P_{m_0}}{P_m}\right]^{(1+\varepsilon_p)} \left[\frac{P_e}{P_{e_0}}\right]^{\varepsilon_p} \left[\frac{N_{E_0}}{N_E}\right] \text{ lbm/hr} \quad (5.2)$$

The following assumptions are now made:

1. The operating point represented by subscript 0 is at sea level in the standard atmosphere (Appendix B), where

   $P_{atmos_0} = P_0$ = ambient atmospheric absolute pressure = 29.92 inches Hg

   $T_{atmos_0} = T_0$ = ambient atmospheric temperature = 288.15 degrees Kelvin.

2. The operating point represented by the absence of a subscript is at any altitude in the standard atmosphere, or in a non-standard atmosphere, where

   P_{atmos} = ambient atmospheric absolute pressure, inches Hg

   T_{atmos} = ambient atmospheric temperature, degrees Kelvin

3. $$\left.\begin{aligned} P_m &= P_{m_0} \\ N_E &= N_{E_0} \end{aligned}\right\} \quad (5.3)$$

4. $$\left.\begin{aligned} \frac{T_m}{T_{m_0}} &\simeq \frac{T_{atmos}}{288.15} \\ \frac{P_e}{P_{e_0}} &\simeq \frac{P_{atmos}}{29.92} \end{aligned}\right\} \qquad (5.4)$$

With these assumptions, Equation 5.2 becomes

$$\dot{m}_{a_0} = \dot{m}_a \left[\frac{T_{atmos}}{288.15}\right]^{(1-\varepsilon_t)} \left[\frac{P_{atmos}}{29.92}\right]^{\varepsilon_p} \quad \text{lbm/hr} \qquad (5.5)$$

We now define the Corrected Air Mass Flow Rate $\dot{m}_{a_c}$ to be

$$\dot{m}_{a_c} \equiv \dot{m}_{a_0} \quad \text{lbm/hr} \qquad (5.6)$$

Substituting this definition in Equation 5.5 yields

$$\dot{m}_{a_c} = \dot{m}_{a_0} = \dot{m}_a \left[\frac{T_{atmos}}{288.15}\right]^{(1-\varepsilon_t)} \left[\frac{P_{atmos}}{29.92}\right]^{\varepsilon_p} \quad \text{lbm/hr} \qquad (5.7)$$

When $\dot{m}_{a_0}$ is known for any conditions $\{P_{m_0}, N_{E_0}\}$, the value of $\dot{m}_a$ in any other operating condition $\{P_m = P_{m_0}, N_E = N_{E_0}, P_{atmos}, T_{atmos}\}$ may be computed using Equation 5.7. Note that Equation 5.7 is independent of the fuel-air mass ratio F metered to the engine.

Corrected Part-Throttle Performance Model of P_m and $\dot{m}_a$

The foregoing discussion of corrected quantities permits the formulation of a corrected part-throttle performance model of P_m and $\dot{m}_a$. Figure 5.26 shows such a model, computed using the NMBTE performance model.

Consider the left half of Figure 5.26, which shows P_m versus Q_{E_c} and N_E: this has been drawn for $F = F_{min} = 0.05$ and standard

atmosphere conditions, for which the density index n = 0.57 (Figure 5.24); and is applicable to all altitudes in the standard atmosphere. The sea level wide open throttle line is shown. At altitudes above sea level, the WOT line moves to lower values of P_m than indicated by this sea level WOT line. The left half of Figure 5.26 was drawn by plotting P_{m_0} versus Q_{E_0} and N_{E_0}, and relabelling the resulting diagram in accordance with Equations 5.1 and 5.3. Diagrams similar to the left half of Figure 5.26 may be drawn for fuel-air mass ratios F = constant $\neq$ 0.05.

Consider the right half of Figure 5.26, which shows P_m versus $\dot{m}_{a_c}$ and N_E: this diagram applies to all fuel-air mass ratios F; and to all altitudes in either the standard atmosphere or any non-standard atmosphere. The sea level wide open throttle line is shown. At pressure altitudes other than sea level, the position of the WOT line varies from the position of this sea level WOT line. The right half of Figure 5.26 was drawn by plotting P_{m_0} versus $\dot{m}_{a_0}$ and N_{E_0}, and relabelling the resulting diagram in accordance with Equations 5.3 and 5.7.

Input-Output Model

We now formulate the input-output model of the Naturally aspirated MBT ignition timing Engine-Atmosphere (NEA) subsystem.

Formulation for the Standard Atmosphere:

The NEA subsystem input-output model is required:

1. To be compatible with the input-output model of the APA subsystem (Chapter 4). This requires that $\{N_E, Q_E, T_{atmos}, P_{atmos}\}$ be inputs to the model (see Figure 4.8). It will be shown that H is also separately required as an input to the NEA subsystem input-output model.†
2. To output the values of $\{P_m, F\}$ required to minimize BSFC at the operating point $\{N_E, Q_E, H\}$. The values of P_m and F are required as control inputs to the engine.
3. To output values of BHP and $\dot{m}_f$ in order that BSFC may be computed. R* may then be computed from this BSFC and the value of R*c provided by the APA subsystem input-output model.
4. To be suitable for airborne microprocessor implementation.

The required inputs and outputs of the NEA subsystem input-output model are:

Inputs:	Q_E	Brake torque, lb ft
	N_E	Engine shaft speed, RPM
	H	Altitude, ft
	T_{atmos}	Atmospheric ambient air temperature, degrees Kelvin
	P_{atmos}	Atmospheric ambient air absolute pressure, inches Hg
Outputs:	P_m	Inlet MAP, inches Hg

†In the standard atmosphere, $T_{atmos} \equiv T_s$ and P_{atmos} are uniquely determined by H in the manner described by Appendix B.

F	Fuel-air mass ratio
$\dot{m}_f$	Fuel mass flow rate, lbm/hr
c	Brake specific fuel consumption, lbm/BHP.hr.

Previous discussion in this chapter (pp. 5-22 through 5-26) has shown that, for naturally aspirated MBT ignition timing engines operating in the standard atmosphere:

1. In all steady state operating conditions $\{Q_E, N_E, H\}$ requiring part-throttle or WOT:
   a) BSFC is minimized by operating the engine at a fuel-air mass ratio $F = F_{min} = 0.05$ (when F is not constrained by other considerations)
   b) BSFC increases continuously as F increases from $F = F_{min} = 0.05$ through $F = F_{max} = 0.08$.
   c) P_m decreases continuously as F is increased from $F = F_{min} = 0.05$ through $F = F_{max} = 0.08$.
2. In all steady state operating conditions $\{P_m, N_E, H\}$:
   a) Q_E increases continuously as F increases from $F = F_{min} = 0.05$ through $F = F_{max} = 0.08$.
   b) Q_E reaches its maximum value at $F = F_{max} = 0.08$.

   [These same results 1(a) through 2(b) are assumed to be true for naturally aspirated MBT ignition timing engines in all operating conditions $\{H_p, T_{atmos}, P_{atmos}\}$ in any non-standard atmosphere.]

The cruise operating condition $\{Q_E, N_E, H\}$ of the engine is

prescribed by the APA subsystem, which subsystem also establishes the value of R*c. In order to maximize R* in every such cruise operating condition of the engine, we would like to operate the engine at the fuel-air mass ratio $F = F_{min}$ at all times in cruise (see 1(a) above). However, it may be impossible for the engine to deliver the required value of Q_E, even at WOT, when $F = F_{min}$. In the latter case, the only way to obtain the required value of Q_E is to increase F above F_{min}: the minimum possible BSFC will then be obtained with a value of F which yields the required value of Q_E at WOT (see 1(b,c) and 2(a) above). In the operating condition $\{N_E, H\}$, the engine delivers maximum brake torque Q_E when operating at WOT and $F = F_{max}$ (see 2(b) above, and Equations E.43, E.57).

In the light of these considerations, we proceed as follows in the formulation of the NEA subsystem input-output model:

1. Fuel-air mass ratios in the range $(F_{min} = 0.05) \leq F \leq (F_{max} = 0.08)$ only are considered.
2. The engine part-throttle performance is modelled at a constant fuel-air mass ratio $F = F_{min} = 0.05$.
3. At fuel-air mass ratios $F > (F_{min} = 0.05)$, the engine WOT performance only is modelled.

The NEA subsystem input-output model consists of:

1. A corrected part-throttle performance plot such as that shown in Figure 5.26.
2. A set of five Wide Open Throttle performance plots such as those shown in Figures 5.27 and 5.28.

3. Equations 5.1 and 5.7.

4. Equations 5.8 - 5.10, following:

Fuel mass flow rate $\dot{m}_f$:

$$\dot{m}_f = F\ \dot{m}_a \qquad \text{lbm/hr} \tag{5.8}$$

Brake horsepower BHP:

$$BHP = \left[\frac{2\pi}{33{,}000}\right] Q_E\ N_E \tag{5.9}$$

Brake Specific Fuel Consumption c:

$$c = \frac{\dot{m}_f}{BHP} \qquad \text{lbm/BHP.hr} \tag{5.10}$$

Figure 5.26 shows the part-throttle performance in terms of the corrected quantities Q_{E_c} and $\dot{m}_{a_c}$. The left half of Figure 5.26 applies to $F = F_{min} = 0.05$ and to the standard atmosphere. The right half of Figure 5.26 applies to all values of F, to the standard atmosphere and to all non-standard atmospheres.

Figure 5.27 shows schematic WOT performance at four values of F in the range $F_{min} \leq F \leq F_{max}$. [The WOT performance is presented at four values of F in order to permit cubic interpolation in Figure 5.29.] Each of the four Figures 5.27 (a-d) shows Q_E as a function of N_E and H at WOT, in the standard atmosphere, for a fixed value of F.

Figure 5.28 is a schematic WOT performance plot of P_m as a function of N_E and H. This figure applies to the standard atmosphere, to all non-standard atmospheres (in non-standard atmospheres, H is read as pressure altitude H_p) and to all values of F.

Note that Figures 5.27 and 5.28 are schematic: they have not

been computed using an accurate WOT performance model. The minimum and maximum values of $N_{E_{WOT}}$ shown in Figures 5.27 and 5.28 represent the RPM limits for continuous operation of the engine.

Schmidt (32) gives a number of formulae for computing the WOT altitude performance (BHP, BSFC) of naturally aspirated aero engines from the WOT performance (BHP, BSFC) of these engines at sea level. WOT performance has not been formulated in terms of Corrected Quantities in the present work and the data storage penalty for this omission is small.

Computational Scheme (Standard Atmosphere):

The use of the NEA subsystem input-output model for computing the set $\{P_m, F, \dot{m}_f\}$ which yields minimum BSFC for any set of inputs $\{Q_E, N_E, H, T_{atmos}, P_{atmos}\}$ is now described. The standard atmosphere is assumed, so that $T_{atmos} \equiv T_s$ (Appendix B).

1. Enter Figure 5.27(a) with $\{N_{E_{WOT}} = N_E, H_{WOT} = H\}$ and determine $Q_{E_{WOT}}$.

   a) If $Q_{E_{WOT}} \geq Q_E$ it is possible to operate the engine with $F = F_{min} = 0.05$, at either part-throttle or WOT. Go to Step 2.

   b) If $Q_{E_{WOT}} < Q_E$ it is not possible to operate the engine with $F = F_{min} = 0.05$. Go to Step 3.

2. $F = F_{min}$:

   a) Compute Q_{E_c} (Equation 5.1).

b) Enter Figure 5.26 with $\{Q_{E_c}, N_E\}$ and determine $\{P_m, \dot{m}_{a_c}\}$.

c) Compute $\dot{m}_a$ (Equation 5.7)

d) Compute $\dot{m}_f = F_{min}\ \dot{m}_a$, lbm/hr.

e) The required quantities $\{P_m, F, \dot{m}_f\}$ have now been evaluated.

f) Compute BSFC (Equations 5.9 and 5.10). Stop.

3. $F > F_{min}$ and WOT:

a) Enter each of Figures 5.27 (a, b, c, d) in turn with $\{Q_{E_{WOT}} = Q_E, N_{E_{WOT}} = N_E\}$ and determine the value of the corresponding wide open throttle altitude H_{WOT}. In Figure 5.27 (a, b, c, d) the value of H_{WOT} is H_1, H_2, H_3, H_4 respectively. Store the four co-ordinate pairs $[(H_i, F_i), i = 1, 2, 3, 4]$ so obtained.

This step is illustrated in Figure 5.27 by the points A, B, C, D each of which corresponds to the same $\{Q_E, N_E\}$.

b) Interpolate between the four co-ordinate pairs $[(H_i, F_i), i = 1, 2, 3, 4]$ to determine the value of F corresponding to the required altitude H. This step is illustrated in Figure 5.29. This value of F yields the required value of Q_E at $\{N_E, H\}$ and WOT. Note that if H exceeds the value of H_{WOT} obtained from Figure 5.27(d) (in which $F = F_{max}$) then the engine is incapable of developing the required value of Q_E at $\{N_E, H\}$.

c) Enter Figure 5.28 with $\{N_{E_{WOT}} = N_E, H_{WOT} = H\}$ and determine the required inlet MAP $P_m = P_{m_{WOT}}$.

d) Enter the right half of Figure 5.26 with $\{P_m, N_E\}$ and determine $\dot{m}_{a_c}$.

e) Compute $\dot{m}_a$ (Equation 5.7).

f) Compute $\dot{m}_f$ (Equation 5.8).

g) The required quantities $\{P_m, F, \dot{m}_f\}$ have now been evaluated. P_m is not required for output since the throttle is wide open.

h) Compute BSFC (Equations 5.9 and 5.10). Stop.

In the above computations, interpolations (linear, parabolic, cubic) may be performed using Lagrange's Interpolation formula (33).

Formulation and Computations (Non-Standard Atmosphere):

In non-standard atmospheric conditions, the operating condition of the engine (as demanded by the APA subsystem) is defined by the set $\{Q_E, N_E, H_p, T_{atmos}, P_{atmos}\}$

where H_p = pressure altitude, ft

T_{atmos} = atmospheric ambient air temperature at H_p, degrees Kelvin

P_{atmos} = atmospheric ambient air absolute pressure at H_p, inches Hg.

The only change in the above Formulation for the Standard Atmosphere required to account for non-standard temperature T_{atmos} at pressure altitude H_p is:

Altitude H must be read as pressure altitude H_p in the text and in Figures 5.27 - 5.29.

The computational scheme listed in the foregoing subsection for the standard atmosphere is retained for non-standard atmospheres, with the following adjustments.

1. H is read as pressure altitude H_p in the text and in Figures 5.27 - 5.29.
2. It is necessary to adjust the value of Q_E required by the APA subsystem, to account for non-standard temperature at H_p, prior to entry into the computational scheme.

Let:

ΔT_{atmos} = [atmospheric ambient temperature (degrees Kelvin) in the non-standard atmosphere at pressure altitude H_p] - [atmospheric ambient temperature (degrees Kelvin) in the standard atmosphere at $H = H_p$] = $T_{atmos} - T_s$

$\left.\frac{\partial Q_E}{\partial T_{atmos}}\right|_{H_p,\ P_m,\ N_E,\ F,\ \tau_o}$ = [rate of change of Q_E with T_{atmos} when $\{H_p, P_m, N_E, F\}$ are invariant: τ_o denotes that MBT ignition timing is maintained during perturbations in T_{atmos}], lb ft/degree Kelvin.

$\left[Q_E\right]_{APA}$ = brake torque (lb ft) required by the APA subsystem in the non-standard atmosphere, and

developed by the engine in the operating condition $\{H_p, T_{atmos}, P_m, N_E, F, \tau_o\}$ in the same non-standard atmosphere.

$\left[Q_E\right]_{NEA}$ = brake torque (lb ft) developed by the engine in the standard atmosphere, in the operating condition $\{H = H_p, P_m, N_E, F, \tau_o\}$

where τ_o denotes MBT ignition timing.

Then,

$$\left[Q_E\right]_{NEA} = \left[Q_E\right]_{APA} - \left.\frac{\partial Q_E}{\partial T_{atmos}}\right|_{H_p,\ P_m,\ N_E,\ F,\ \tau_o} \Delta T_{atmos} + (\text{higher order terms in } \Delta T_{atmos}) \qquad (5.11)$$

We retain only the first two terms on the right hand side of Equation 5.11. The functional dependence of the derivative $\partial Q_E/\partial T_{atmos}\big|_{H_p,\ P_m,\ N_E,\ F,\ \tau_o}$ on the variables $\{H_p, P_m, N_E, F\}$ at τ_o has not been determined in this work. It may be found that sufficient accuracy in the computations is obtained by allocating a constant value to this derivative: if this is not the case, some iteration may have to be incorporated into the computational scheme.

The brake torque $Q_E = \left[Q_E\right]_{NEA}$ is used in the computational scheme when computing Q_{E_c} and when entering Figure 5.27. However, when computing BHP (Equation 5.9) and BSFC (Equation 5.10), the brake torque value used must be $Q_E = \left[Q_E\right]_{APA}$.

3. In computing $Q_{E_c} = Q_E \sigma^n$ for entry into Figure 5.26, the density ratio σ used must be the standard atmosphere value of σ at the altitude $H = H_p$ ft.
4. The non-standard atmosphere values of T_{atmos} and P_{atmos} are used to compute $\dot{m}_a$ (Equation 5.7).

The NEA subsystem input-output model, appropriate to standard and non-standard atmospheric conditions, is presented in block diagram form in Figure 5.30.

Implementation:

The principal hardware items required for implementation of the NEA subsystem input-output model are:

1. An ignition timing regulator providing MBT ignition timing and retarding this ignition timing as necessary to control detonation.
2. A fuel-air mass ratio controller providing F as commanded by the NEA subsystem input-output model. It is desirable that this controller provides a value of F within 1% of any command value of F.
3. Microprocessor.

Items 1 and 2 should be automatic control systems.

The NEA subsystem input-output model is well suited to implementation in an airborne microprocessor for the following reasons:

1. Figures 5.26 - 5.28 require very little memory space for data storage.

2. The required computations are few and simple.

Figures 5.26 - 5.28 must be compiled from flight test data in order that installation effects may be properly accounted for. The data requirements of these figures are self-evident, perhaps with the following exceptions: The flight test data must establish

1. The values of F to be used for the compilation of Figures 5.26 and 5.27.
2. The value of the Density Index n for Figure 5.26.
3. The values of ε_t and ε_p for Figure 5.26.

Flight test data are also required to establish the functional nature of $\partial Q_E/\partial T_{atmos}\Big|_{H_p,\ P_m,\ N_E,\ F,\ \tau_o}$ and to quantify this function for use in the input-output model.

Summary

The performance predictions of the NMBTE performance model have been discussed. The NEA subsystem input-output model has been formulated, and the use of this model for performance computations has been discussed. This input-output model is compatible with the APA subsystem input-output model developed in Chapter 4. The NEA subsystem input-output model is summarized in block diagram form in Figure 5.30.

TURBOCHARGED ENGINES

The turbocharger is a mechanical device, consisting of a rotating turbine and a rotating compressor, which is used in

conjunction with a piston engine. The turbine extracts power from the exhaust gas of the engine, and with this power drives the compressor by means of a rotating shaft. The compressor uses this power to increase the pressure (and temperature) of the engine induction air. A piston engine and turbocharger are shown schematically in Figure 5.31.

The shaft power output of the turbine is often controlled by means of a Waste-Gate, which is used to direct a portion of the engine exhaust gas through the turbine and to discharge the remainder of this exhaust gas directly to the atmosphere. The waste-gate is located in the Exhaust Manifold (the region of the exhaust system between the exhaust valves and the Turbine Inlet). When the waste-gate is closed, all of the engine exhaust gas passes through the turbine; and when the waste-gate is wide open, most of the engine exhaust gas is discharged directly to the atmosphere without passing through the turbine.

A throttle is placed in the engine induction system downstream of the compressor outlet. The portion of the engine induction system between the compressor outlet and the throttle is called the Deck; and the portion of the engine induction system downstream of the throttle is called the Inlet Manifold.

The relationships between the absolute pressures and temperatures of the atmosphere, deck and exhaust manifold are determined by the performance characteristics of the compressor and turbine. In general, however, when $\{H_p, T_{atmos}, N_E, F,$ waste-gate position$\}$

are constants and τ = constant or MBT, opening the throttle increases:

1. Inlet MAP
2. Exhaust manifold absolute pressure (this is the exhaust back-pressure on the engine)
3. Turbocharger shaft rotational speed
4. Deck absolute pressure
5. Deck temperature
6. Inlet manifold temperature.

In general, these same six quantities are increased by closing the waste-gate, when $\{H_p, T_{atmos}, N_E, F$, throttle position$\}$ are constants and τ = constant or MBT.

Therefore both the throttle and the waste-gate may be used to control the BHP and Q_E of the engine, since both influence the inlet MAP. However, an increase in inlet MAP is achieved at the expense of: an increase in inlet manifold temperature (which increases engine temperatures generally, decreases the engine indicated horsepower which decrease contributes to increasing the engine BSFC, and increases the likelihood of detonation); and an increase in engine back-pressure (which decreases volumetric efficiency and increases the engine pumping losses, both of which effects contribute to an increase in engine BSFC).

The performance of turbocharged spark-ignition (SI) piston engines employing MBT ignition timing may be modelled by incorporating a performance model of the turbocharger compressor and turbine in the model of the naturally aspirated engine given in Appendix E.

Such modelling is a necessary prerequisite to the construction of a fuel-efficient input-output performance model of the Turbocharged MBT ignition timing Engine-Atmosphere (TEA) subsystem. The author was able to obtain the compressor performance data for a turbocharger used in General Aviation, but was unable to obtain the corresponding turbine performance data. Consequently, turbocharged SI piston engine performance is not modelled in this work.

The author was also unable to obtain experimental performance data for naturally aspirated and turbocharged SI piston aero engines using MBT ignition timing. In the absence of such data, and in the absence of a turbocharger performance model, no rigorous comparison of naturally aspirated and turbocharged engine performance is presented in this work.

The following remarks concerning turbocharged engine performance and the construction of a TEA subsystem input-output model are offered on the basis of the foregoing sections in this chapter.

Performance Comparison: Naturally Aspirated and Turbocharged Engines

Brake Torque:

The maximum brake torque Q_E of a naturally aspirated engine at any operating point $\{H_p, T_{atmos}, N_E, F\}$ is limited by the maximum available inlet MAP P_m. As altitude increases, the fall in atmospheric ambient air pressure and the resultant fall in maximum $\{P_m, Q_E\}$ for any $\{N_E, F\}$, seriously diminishes the performance [decreased maximum: cruise equivalent airspeed (EAS), rate of

climb (RC), angle of climb (AC)] of an airplane powered by a naturally aspirated engine.

A turbocharger enables the P_m of a given engine at any $\{H_p, T_{atmos}, N_E, F\}$ to be significantly increased (boosted) above the maximum P_m available to that engine with natural aspiration at the same $\{H_p, T_{atmos}, N_E, F\}$. Associated with such increases in P_m are significant increases in Q_E. The airplane performance improvements [increased maximum EAS, RC, AC at any $\{H_p, T_{atmos}, N_E, F\}$] resulting from this increase in Q_E, especially at altitude, has been the historical motivation for turbocharging airplane piston engines.

Brake Specific Fuel Consumption:

On the basis of the discussions of naturally aspirated engines earlier in this chapter, it is assumed here that: in all steady state operating conditions $\{H_p, T_{atmos}, BHP, N_E\}$ of General Aviation turbocharged piston engines employing MBT ignition timing

1. A single value of $F = F_{min}$ will yield minimum BSFC (when F is not constrained by other considerations)
2. BSFC increases continuously as F increases above $F = F_{min}$.

The ability of the turbocharger to boost P_m, above the maximum P_m that would be available to the engine with natural aspiration, has important consequences for the BSFC of turbocharged engines.

Consider an airplane powered by a naturally aspirated engine, and assume that the APA subsystem demands that the engine operates in the condition $\{H_p, T_{atmos}, Q_E, N_E\}$. It is desirable to operate

the engine at $F = F_{min}$ in order to minimize BSFC. If the engine cannot develop the required Q_E at WOT when $F = F_{min}$, the only way the engine can increase the brake torque to the desired value Q_E is to increase F above F_{min}. The maximum brake torque will be developed at $F = F_{max}$ and WOT. Increasing brake torque by mixture enrichment is accompanied by an increase in BSFC. For the naturally aspirated engine, this BSFC increase is an unavoidable penalty for operation at high brake torque: it has been demonstrated (Figure 5.10) that BSFC increases of about 21% may be sustained [at constant $\{H, Q_E, N_E\}$ and MBT ignition timing] by mixture enrichment from $F = F_{min} = 0.05$ to $F = F_{max} = 0.08$.

Now consider an airplane powered by a turbocharged engine, and assume that the APA subsystem demands that the engine operates in the condition $\{H_p, T_{atmos}, Q_E, N_E\}$. It is desirable to operate the engine at $F = F_{min}$ in order to minimize BSFC. The ability of the turbocharged engine to boost inlet MAP to high values means that high brake torque can be developed at $F = F_{min}$. Consequently, the turbocharged engine can operate at $F = F_{min}$ over a greater range of flight conditions than can the naturally aspirated engine, with attendant increases in R*. The feasibility of operating turbocharged engines ultralean up to 75% rated BHP at high inlet MAP has been demonstrated by flight tests (16) of a Lycoming TIO-541-E engine.

Recommendations: TEA Subsystem Input-Output Model

As stated above, the performance of turbocharged SI piston engines employing MBT ignition timing may be modelled by incorporating a performance model of the turbocharger compressor and turbine in the model of the naturally aspirated engine given in Appendix E. Such modelling is a necessary prerequisite to the construction of a fuel-efficient input-output model of the TEA subsystem.

In constructing the TEA subsystem input-output model, attention should be paid to the following:

1. Leanout performance should be examined to determine the fuel-air mass ratio F_{min} yielding minimum BSFC during constant BHP leanouts.
2. The engine should be operated at WOT at all times, and the inlet MAP controlled by
   a) Waste-gate position
   and/or b) Variable geometry turbine nozzle ring (34).
   In this manner, a given inlet MAP can be achieved with a minimum engine back-pressure and a minimum inlet manifold temperature, which conditions contribute to minimizing engine BSFC.
3. The option of installing an aftercooler downstream of the turbocharger compressor should be examined. This device cools the induction air, thereby reducing engine temperatures, increasing indicated horsepower (and hence decreasing BSFC) and decreasing the likelihood of detonation.

SUMMARY

The content of this chapter is summarized briefly below.

1. A performance model of naturally aspirated, spark-ignition, inlet port fuel injection, four-stroke piston aero engines employing MBT ignition timing (the NMBTE performance model) has been presented.
2. The performance of current technology General Aviation piston engines has been discussed.
3. The performance predictions of the NMBTE performance model have been presented and discussed.
   a) The leanout performance predictions of this model indicate that:
      (i) The fuel-air mass ratio yielding maximum BHP in all engine operating conditions $\{P_m, N_E, H\}$ in the standard atmosphere is approximately constant at $F = F_{max} \simeq 0.080$.
      (ii) When leaning from $F = F_{max} = 0.080$ at constant $\{N_E, H\}$, a substantially lower minimum BSFC is obtained when leaning at constant BHP than when leaning at constant inlet MAP. A 6% difference in minimum BSFC for these two leaning techniques has been demonstrated.
      (iii) A decrease in BSFC of approximately 17% is possible when leaning, at constant $\{BHP, N_E, H\}$, from $F = F_{max} = 0.080$ to the fuel-air mass ratio yielding minimum BSFC. $F = F_{max} = 0.080$ is a typical

operating fuel-air mass ratio for General Aviation pilots.

(iv) The fuel-air mass ratio yielding minimum BSFC in all engine operating conditions $\{Q_E, N_E, H\}$ in the standard atmosphere is approximately constant at $F = F_{min} \simeq 0.050$.

b) BSFC performance maps have been examined.

c) The altitude variation of BSFC has been shown to be strongly dependent upon engine operating constraints.

d) Corrected quantities for engine performance have been determined. Part-throttle performance has been presented in terms of these corrected quantities.

4. The NEA subsystem input-output model has been presented, and its use for computing performance in the standard atmosphere and in a non-standard atmosphere described. Implementation of the NEA subsystem input-output model has been discussed: this input-output model is well suited to airborne microprocessor implementation due to its simplicity and minimal storage requirements.

5. Turbocharged engines and their performance have been briefly reviewed. Recommendations for the construction of a TEA subsystem input-output model have been offered; but this input-output model has not been developed in this work.

TABLE 5.1

ENGINE DESIGN PARAMETERS INCLUDED IN
THE NMBTE PERFORMANCE MODEL

Engine displacement	D = 470 cubic inches
Indicated thermal efficiency η_i' cubic (Eq. E.41) (compression ratio ≈ 7:1)	e_o = -0.0046322
	e_1 = 1.063657
	e_2 = -0.9421708
	e_3 = 0.2200205
Reference temperature	T_m' = 305.556 degrees Kelvin

Data for correcting indicated thermal efficiency for inlet manifold temperature (compression ratio ≈ 7:1)

ϕ	$\left.\frac{\partial R}{\partial T_m}\right\|_{S'}$ degree Kelvin $^{-1}$
0.6	-1.44×10^{-4}
0.8	-1.44×10^{-4}
1.0	-2.16×10^{-4}
1.2	-1.08×10^{-4}
1.4	-0.54×10^{-4}

ϕ	R_o
0.7	0.6
0.8	0.73
0.9	0.81
1.0	0.83
1.2	0.83
1.5	0.81

$$\left.\frac{\partial R_1}{\partial T_m}\right|_{S', \tau_o} = -0.0004 \text{ degree Kelvin}^{-1}$$

TABLE 5.1
(concluded)

Lost horsepower data:

Motoring coefficients ($2000 \leq RPM \leq 2600$) taken from Figure E.15.

$a_o = 30.99$

$a_1 = -2.705 \times 10^{-2}$

$a_2 = 1.125 \times 10^{-5}$

Lost horsepower coefficients

$k_x = 1.667$

$C_Z = 2.112 \times 10^{-3}$

$y_o = 0.007$

$k_{yn} = 5.111 \times 10^{-6}$

Volumetric efficiency correction indices

$\varepsilon_t = 0.2$

$\varepsilon_p = 0.1$

TABLE 5.2

REFERENCE OPERATING POINT
AND FUEL SCHEDULE DATUM CONDITIONS
USED IN THE NMBTE PERFORMANCE MODEL

Reference Operating Point	
Inlet manifold absolute pressure	P_{m_1} = 28.42 inches Hg
Inlet manifold temperature	T_{m_1} = 288.15 degrees Kelvin
Exhaust absolute back-pressure	P_{e_1} = 29.92 inches Hg
Fuel-dry air mass ratio	F_1 = 0.084
Brake horsepower	BHP_1 = 230 horsepower
Engine shaft speed	N_{E_1} = 2600 RPM
Fuel Schedule Datum	
Inlet manifold absolute pressure	$P_{m_{fsd}}$ = 28.42 inches Hg
Inlet manifold temperature	$T_{m_{fsd}}$ = 288.15 degrees Kelvin
Exhaust absolute back-pressure	$P_{e_{fsd}}$ = 29.92 inches Hg
Engine shaft speed	$N_{E_{fsd}}$ = 2600 RPM

TABLE 5.3

NMBTE PERFORMANCE MODEL: CONSTANT BHP LEANOUTS

During leanouts at {constant BHP, constant RPM, constant altitude}:

1. Minimum BSFC occurred at a fuel-air mass ratio F in the range

$$0.0485 \leq F \leq 0.0500$$

2. BSFC increased continuously as F increased from the value of F which yielded minimum BSFC through the value F = 0.0935

throughout the operational envelope:

- [45% mc BHP] $\leq$ BHP $\leq$ [BHP at WOT and F = 0.08]
- $2000 \leq N_E$, RPM ≤ 2600
- $0 \leq H$, ft $\leq 10{,}000$ (standard atmosphere)

TABLE 5.4

NMBTE PERFORMANCE MODEL: CONSTANT INLET MAP LEANOUTS

During leanouts at {constant inlet MAP, constant RPM, constant altitude}:

1. Maximum BHP occurred at a fuel-air mass ratio F in the range

   $0.0795 \leq F \leq 0.0805$

2. BHP decreased continuously as F decreased from the value of F which yielded maximum BHP through the value

   $F = 0.0470$

throughout the operational envelope:

- $10 \leq P_m$ inches Hg $\leq$ [P_m inches Hg at WOT]
- $2000 \leq N_E$, RPM ≤ 2600
- $0 \leq H$, ft $\leq 10{,}000$ (standard atmosphere)

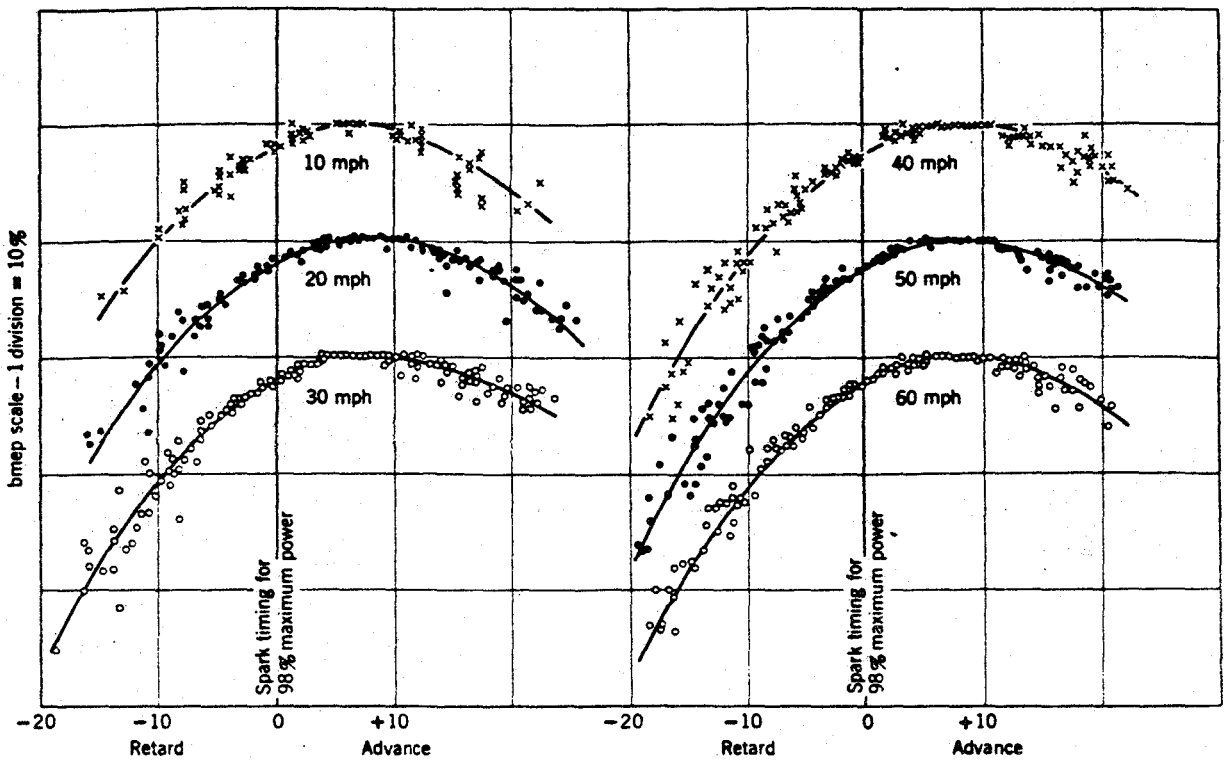

Effect of spark timing on bmep for a number of US passenger-car engines (Barber, ref 12.41)

[FROM TAYLOR (13)]

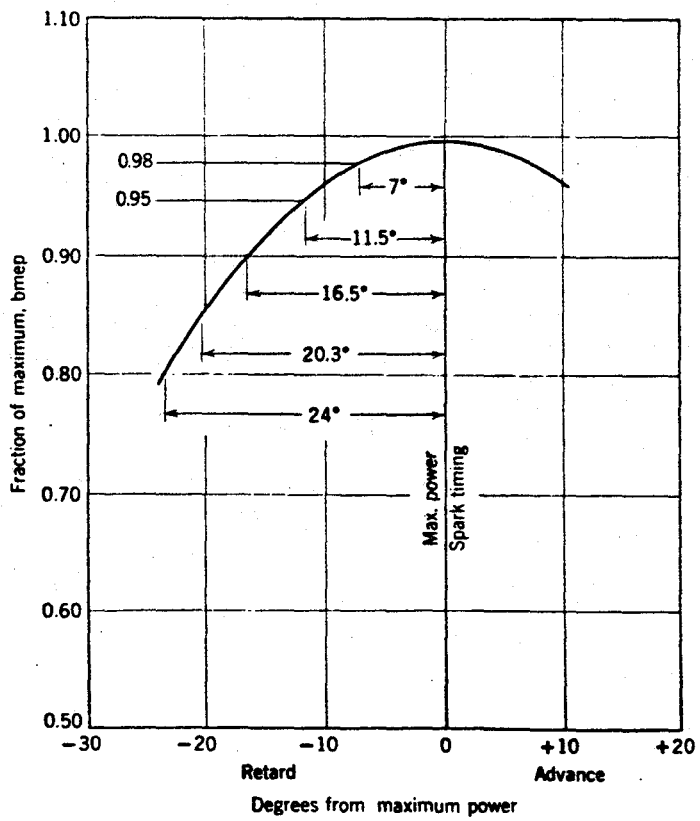

Correlation for all speeds and loads.

[FROM TAYLOR (13)]

FIGURE 5.1 EFFECTS OF IGNITION TIMING ON BRAKE MEAN EFFECTIVE PRESSURE

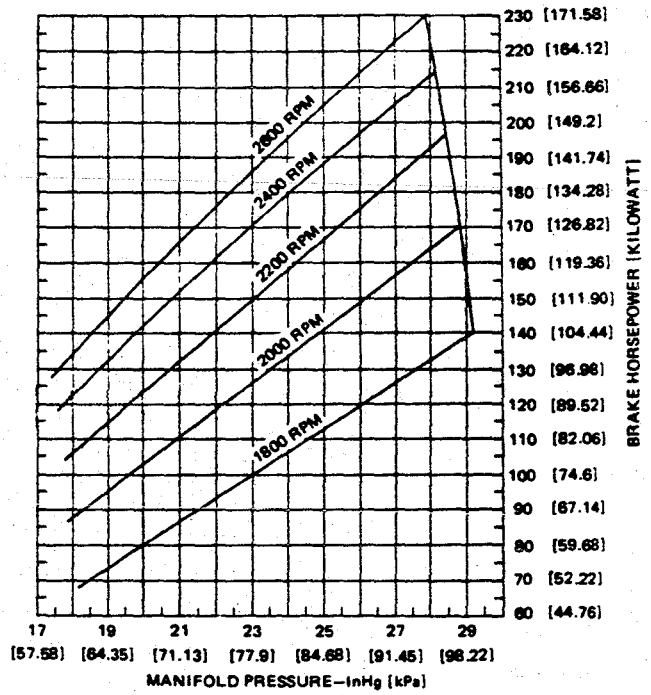

Bhp vs. intake manifold pressure vs. revolutions per minute.

(REF. 24)

FIGURE 5.2

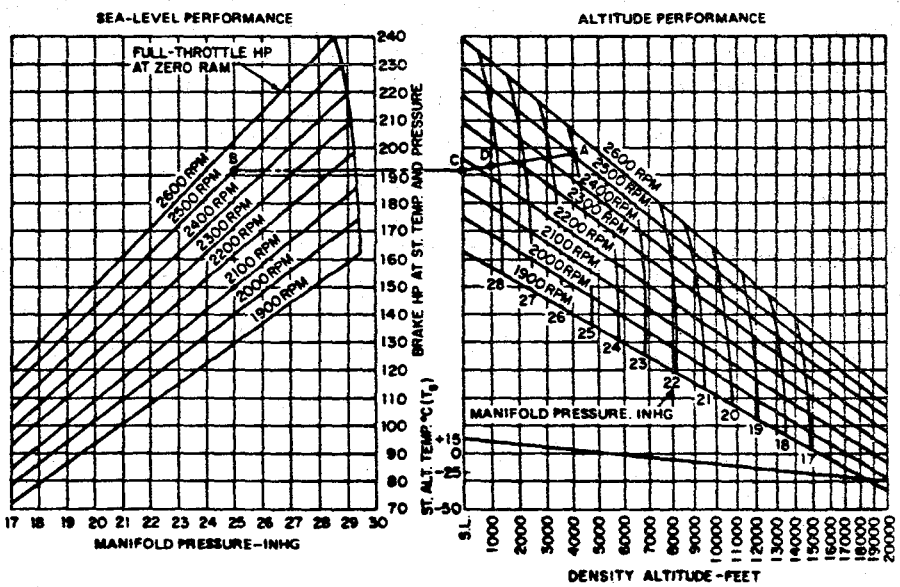

Finding actual horsepower from sea-level and altitude charts.

(REF. 24)

FIGURE 5.3

(REF. 23, FIGURE 1)

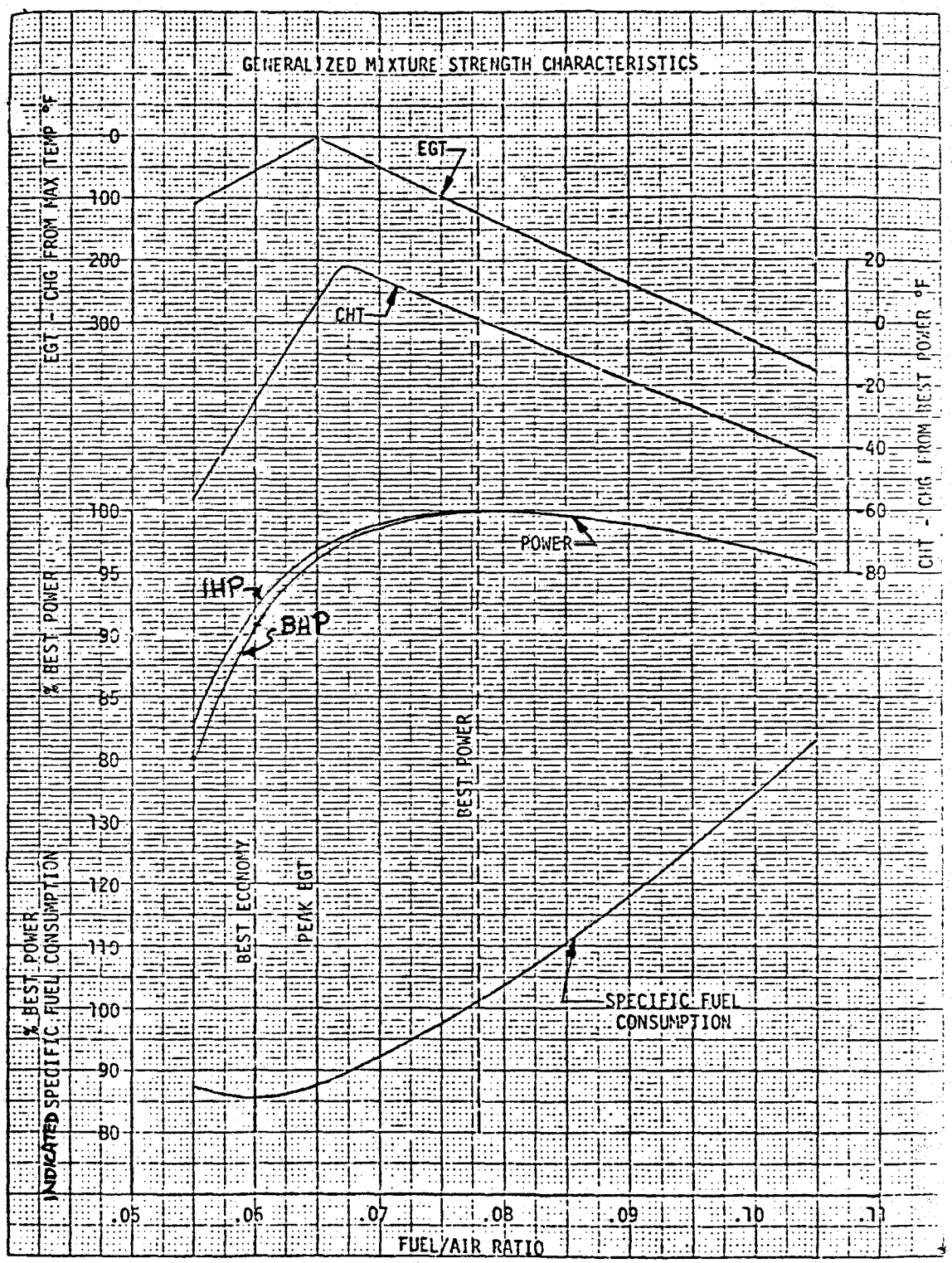

IT IS ASSUMED THAT THESE GENERALIZED MIXTURE STRENGTH CHARACTERISTICS APPLY TO THE FIVE CONDITIONS LISTED IN FIGURE 5.5 .

FIGURE 5.4 GENERALIZED MIXTURE STRENGTH CHARACTERISTICS.

(REF. 27)

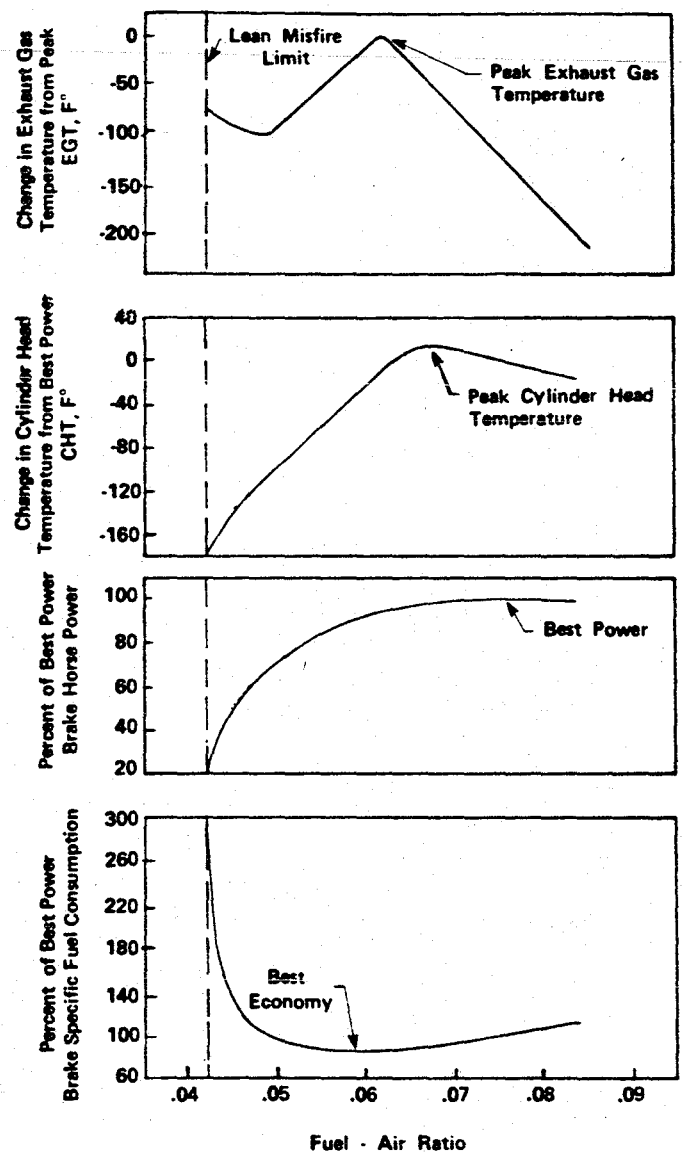

Effect of fuel-air ratio on power, brake specific fuel consumption, cylinder head temperature and exhaust gas temperature at constant engine speed, manifold pressure and spark timing.

THESE GENERALIZED MIXTURE RATIO CURVES APPLY (35) TO:

1. NATURALLY ASPIRATED AND TURBOCHARGED SI PISTON ENGINES.
2. ALL CONSTANT SETS $\{P_m, N_E, H_P, T_{atmos}, \text{humidity}\}$ WITHIN THE NORMAL OPERATING ENVELOPE OF THE ENGINE.
3. FIXED IGNITION TIMING τ.
4. BHP IN THE RANGE 40% - 100% OF MAXIMUM CONTINUOUS BHP.
5. STANDARD AND NON-STANDARD ATMOSPHERIC CONDITIONS.

FIGURE 5.5 GENERALIZED MIXTURE RATIO CURVES.

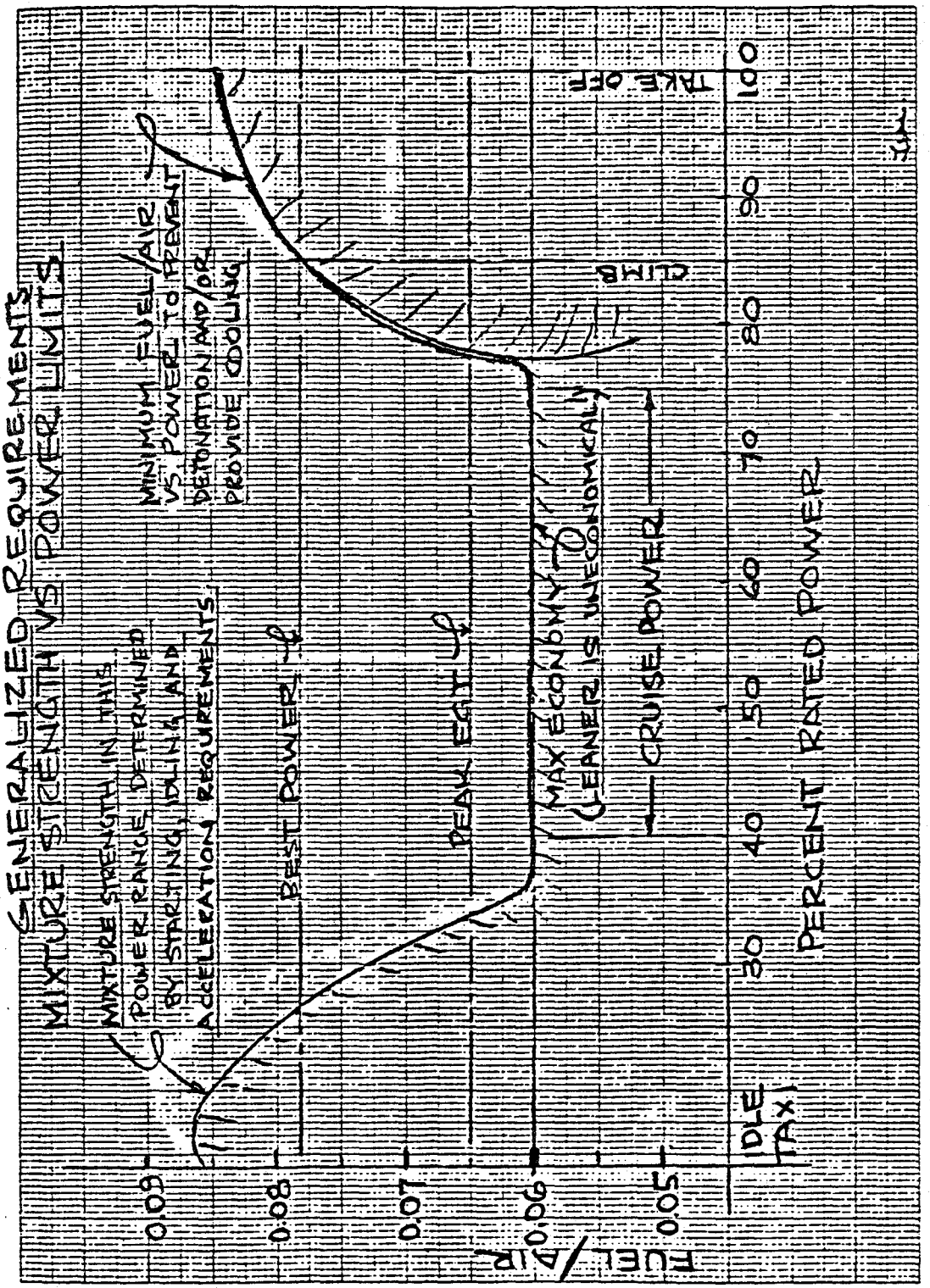

(REF. 23)

FIGURE 5.6

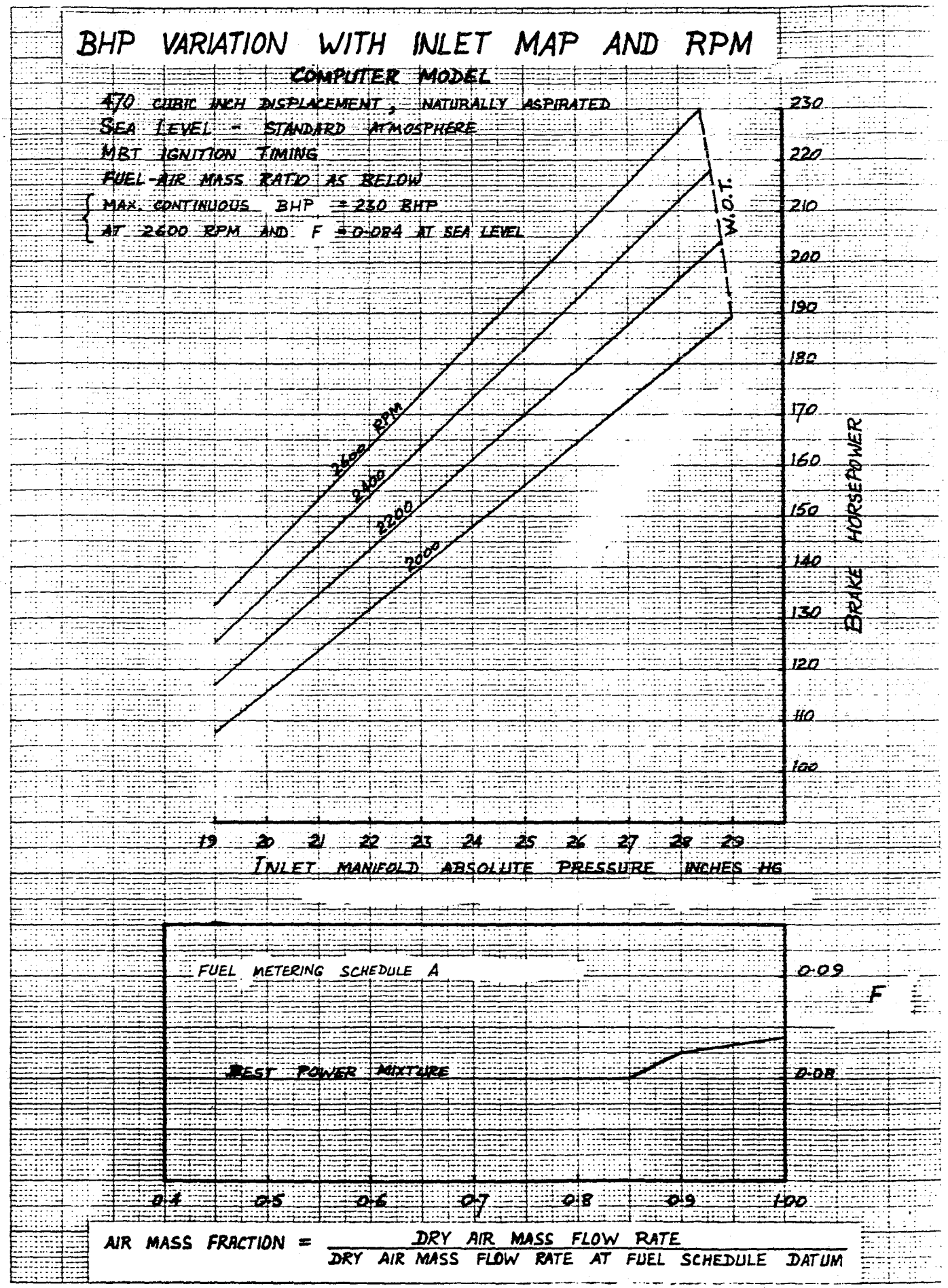
BHP VARIATION WITH INLET MAP AND RPM
COMPUTER MODEL
470 CUBIC INCH DISPLACEMENT, NATURALLY ASPIRATED
SEA LEVEL - STANDARD ATMOSPHERE
MBT IGNITION TIMING
FUEL-AIR MASS RATIO AS BELOW
MAX. CONTINUOUS BHP = 230 BHP
AT 2600 RPM AND F = 0.084 AT SEA LEVEL
M.O.T.
2600 RPM
2400
2200
2000
230
220
210
200
190
180
170
160
150
140
130
120
110
100
BRAKE HORSEPOWER
19
20
21
22
23
24
25
26
27
28
29
INLET MANIFOLD ABSOLUTE PRESSURE INCHES HG
FUEL METERING SCHEDULE A
BEST POWER MIXTURE
0.09
F
0.08
0.4
0.5
0.6
0.7
0.8
0.9
1.00
AIR MASS FRACTION = DRY AIR MASS FLOW RATE / DRY AIR MASS FLOW RATE AT FUEL SCHEDULE DATUM

FIGURE 5.7

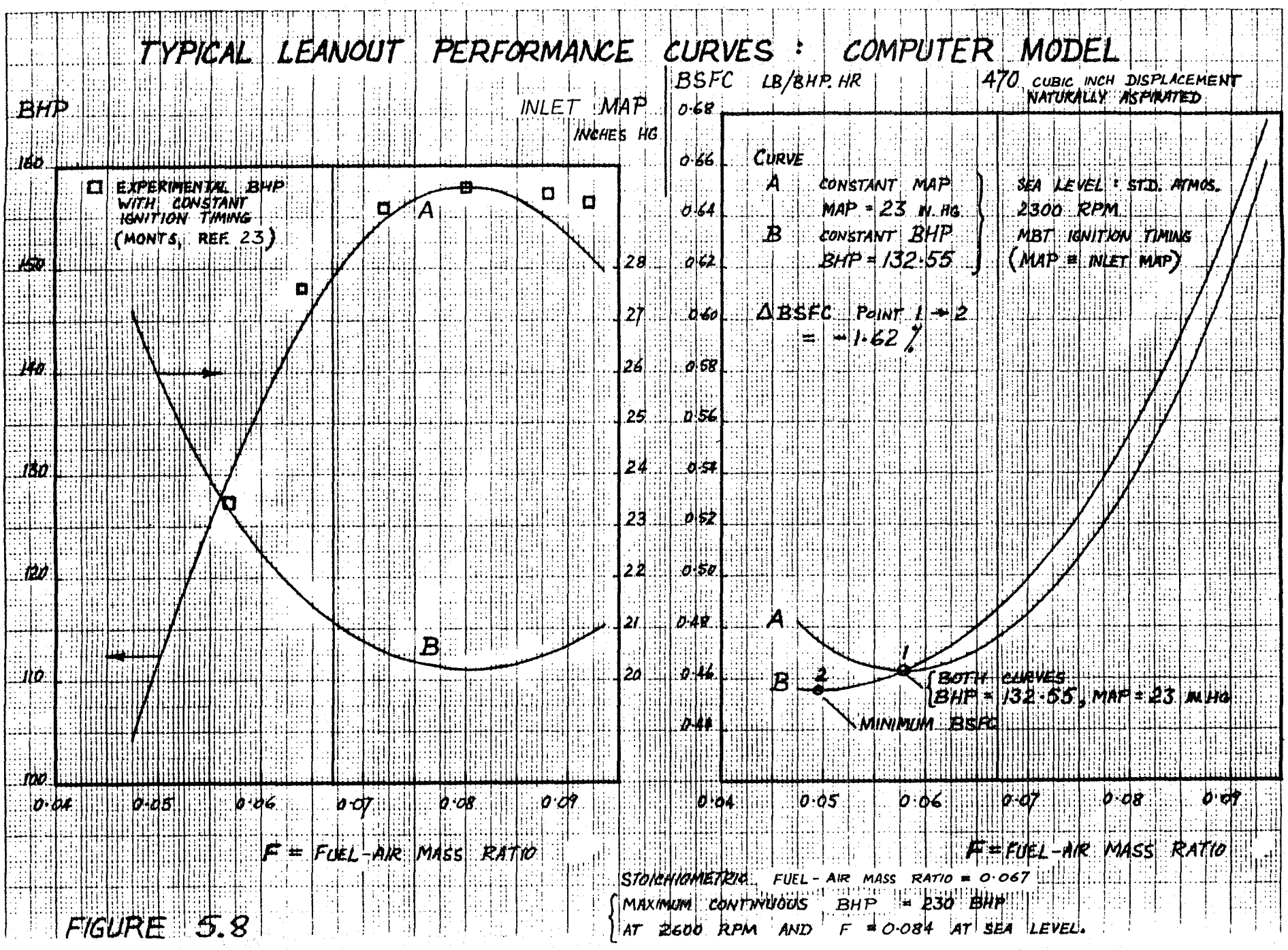
TYPICAL LEANOUT PERFORMANCE CURVES : COMPUTER MODEL
BHP
INLET MAP
INCHES HG
EXPERIMENTAL BHP WITH CONSTANT IGNITION TIMING (MONTS, REF. 23)
A
B
160
150
140
130
120
110
100
28
27
26
25
24
23
22
21
20
0·04
0·05
0·06
0·07
0·08
0·09
F = FUEL-AIR MASS RATIO
BSFC LB/BHP. HR
470 CUBIC INCH DISPLACEMENT NATURALLY ASPIRATED
0·68
0·66
0·64
0·62
0·60
0·58
0·56
0·54
0·52
0·50
0·48
0·46
0·44
CURVE
A CONSTANT MAP MAP = 23 IN. HG
B CONSTANT BHP BHP = 132·55
SEA LEVEL : STD. ATMOS.
2300 RPM
MBT IGNITION TIMING
(MAP = INLET MAP)
ΔBSFC POINT 1 → 2 = → 1·62 %
A
B
1
2
BOTH CURVES BHP = 132·55, MAP = 23 IN. HG
MINIMUM BSFC
0·04
0·05
0·06
0·07
0·08
0·09
F = FUEL-AIR MASS RATIO
STOICHIOMETRIC FUEL-AIR MASS RATIO = 0·067
MAXIMUM CONTINUOUS BHP = 230 BHP AT 2600 RPM AND F = 0·084 AT SEA LEVEL.

FIGURE 5.8

COMPARISON OF MINIMUM BSFC DURING CONSTANT INLET MAP & CONSTANT BHP LEANOUTS

ENGINE MODEL : 470 CUBIC INCH DISPLACEMENT
NATURALLY ASPIRATED
MBT IGNITION TIMING

SEA LEVEL - STANDARD ATMOSPHERE
2300 RPM

MAXIMUM CONTINUOUS BHP = 230
AT 2600 RPM AND F = 0.084
AT SEA LEVEL.

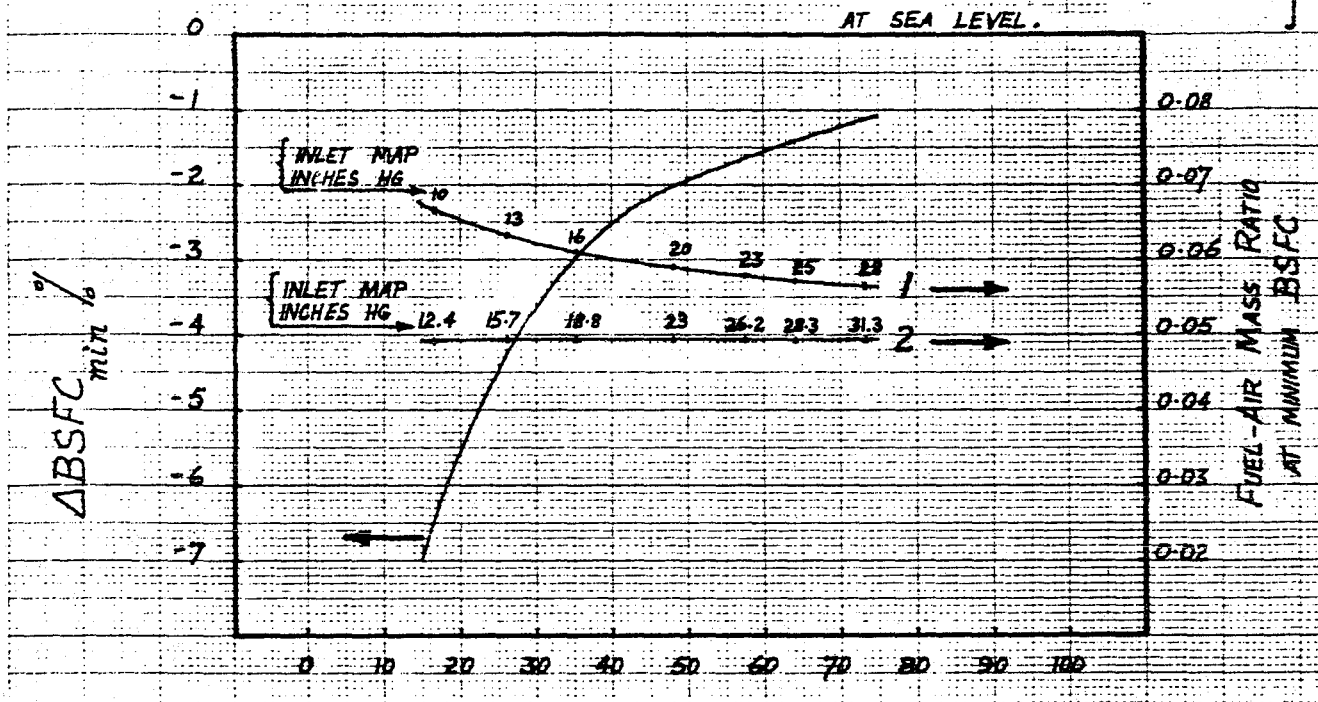

CURVE

1 FUEL-AIR MASS RATIO AT MINIMUM BSFC DURING CONSTANT INLET MAP LEANOUT.

2 FUEL-AIR MASS RATIO AT MINIMUM BSFC DURING CONSTANT BHP LEANOUT.

$$\Delta BSFC_{min}\ \% = \left[\frac{BSFC_2 - BSFC_1}{BSFC_1}\right] \times 100$$

FIGURE 5.9

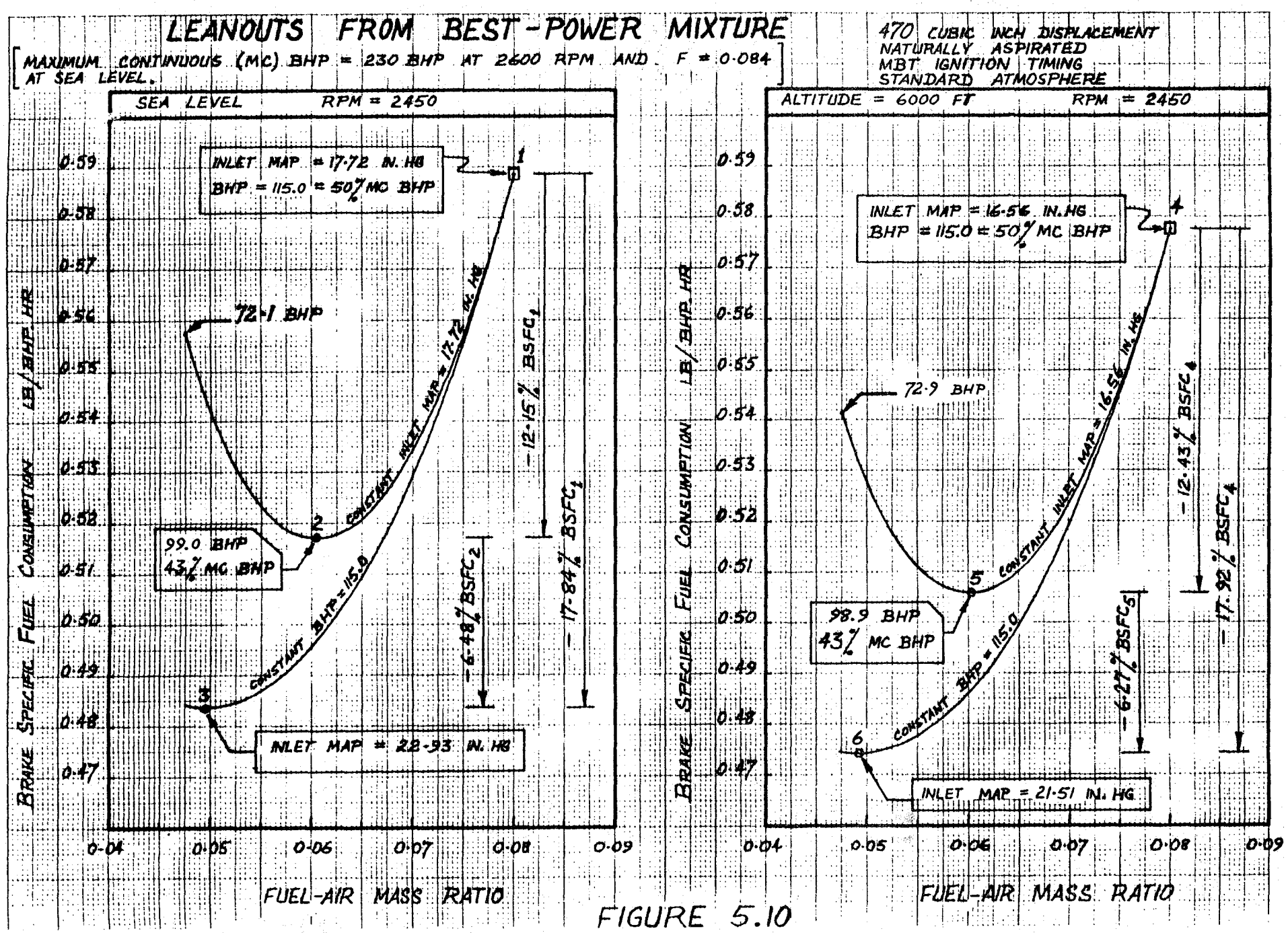
LEANOUTS FROM BEST-POWER MIXTURE
MAXIMUM CONTINUOUS (MC) BHP = 230 BHP AT 2600 RPM AND F = 0.084 AT SEA LEVEL.
470 CUBIC INCH DISPLACEMENT
NATURALLY ASPIRATED
MBT IGNITION TIMING
STANDARD ATMOSPHERE
SEA LEVEL RPM = 2450
ALTITUDE = 6000 FT RPM = 2450
INLET MAP = 17.72 IN. HG
BHP = 115.0 = 50% MC BHP
72.1 BHP
99.0 BHP
43% MC BHP
CONSTANT INLET MAP = 17.72 IN. HG
CONSTANT BHP = 115.0
INLET MAP = 22.93 IN. HG
- 12.15% BSFC1
- 17.84% BSFC1
- 6.48% BSFC2
INLET MAP = 16.56 IN. HG
BHP = 115.0 = 50% MC BHP
72.9 BHP
98.9 BHP
43% MC BHP
CONSTANT INLET MAP = 16.56 IN. HG
CONSTANT BHP = 115.0
INLET MAP = 21.51 IN. HG
- 12.43% BSFC4
- 17.92% BSFC4
- 6.27% BSFC5
BRAKE SPECIFIC FUEL CONSUMPTION LB/BHP HR
0.59
0.58
0.57
0.56
0.55
0.54
0.53
0.52
0.51
0.50
0.49
0.48
0.47
0.04
0.05
0.06
0.07
0.08
0.09
FUEL-AIR MASS RATIO

FIGURE 5.10

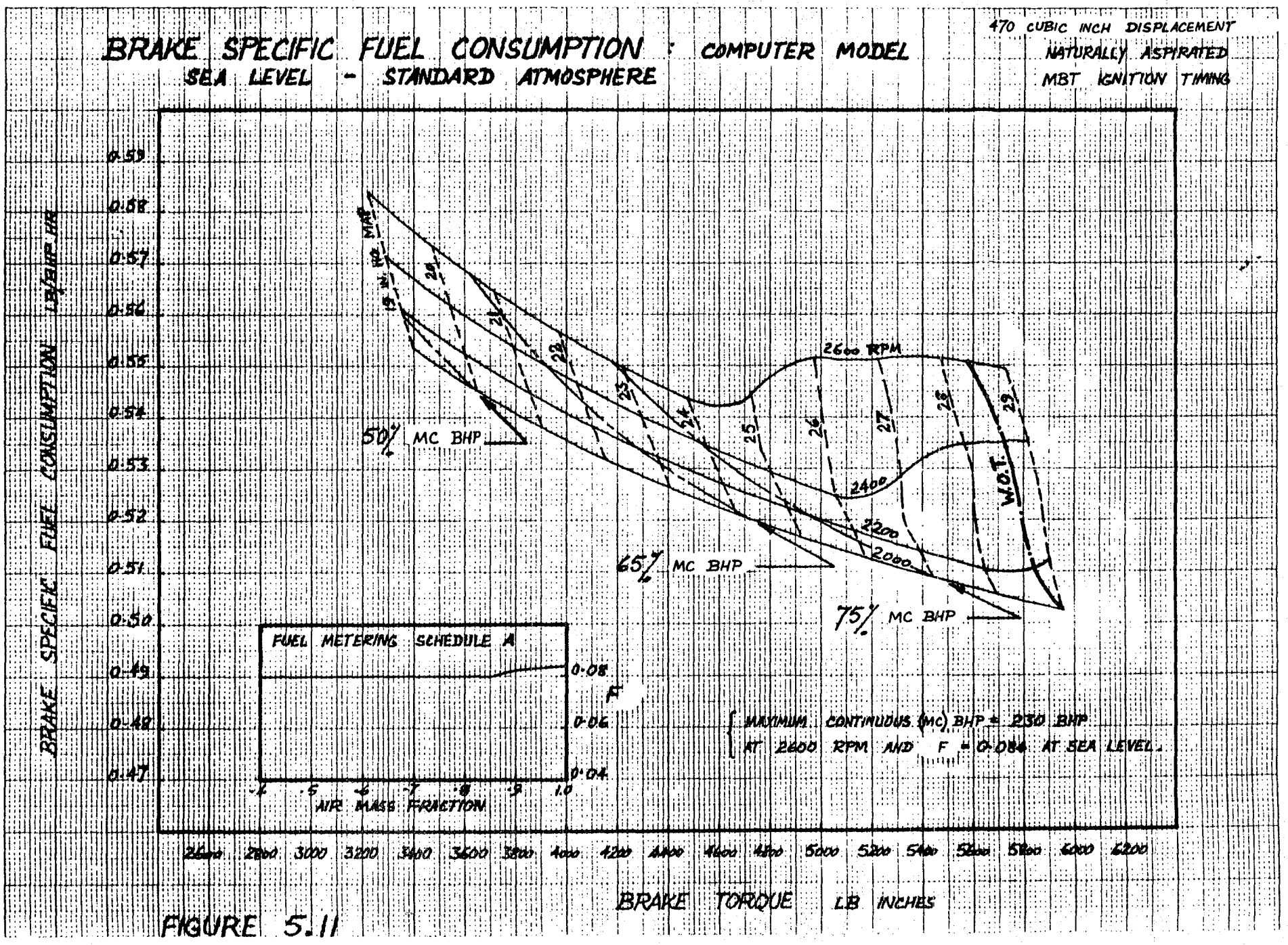
BRAKE SPECIFIC FUEL CONSUMPTION : COMPUTER MODEL
SEA LEVEL - STANDARD ATMOSPHERE
470 CUBIC INCH DISPLACEMENT
NATURALLY ASPIRATED
MBT IGNITION TIMING
BRAKE SPECIFIC FUEL CONSUMPTION LB/BHP HR
0.59
0.58
0.57
0.56
0.55
0.54
0.53
0.52
0.51
0.50
0.49
0.48
0.47
IN. HG MAP
28
26
24
22
50% MC BHP
65% MC BHP
75% MC BHP
2600 RPM
2400
2200
2000
W.O.T.
25
26
27
28
29
FUEL METERING SCHEDULE A
0.08
0.06
0.04
F
.4
.5
.6
.7
.8
.9
1.0
AIR MASS FRACTION
MAXIMUM CONTINUOUS (MC) BHP = 230 BHP
AT 2600 RPM AND F = 0.084 AT SEA LEVEL
2600
2800
3000
3200
3400
3600
3800
4000
4200
4400
4600
4800
5000
5200
5400
5600
5800
6000
6200
BRAKE TORQUE LB INCHES

FIGURE 5.11

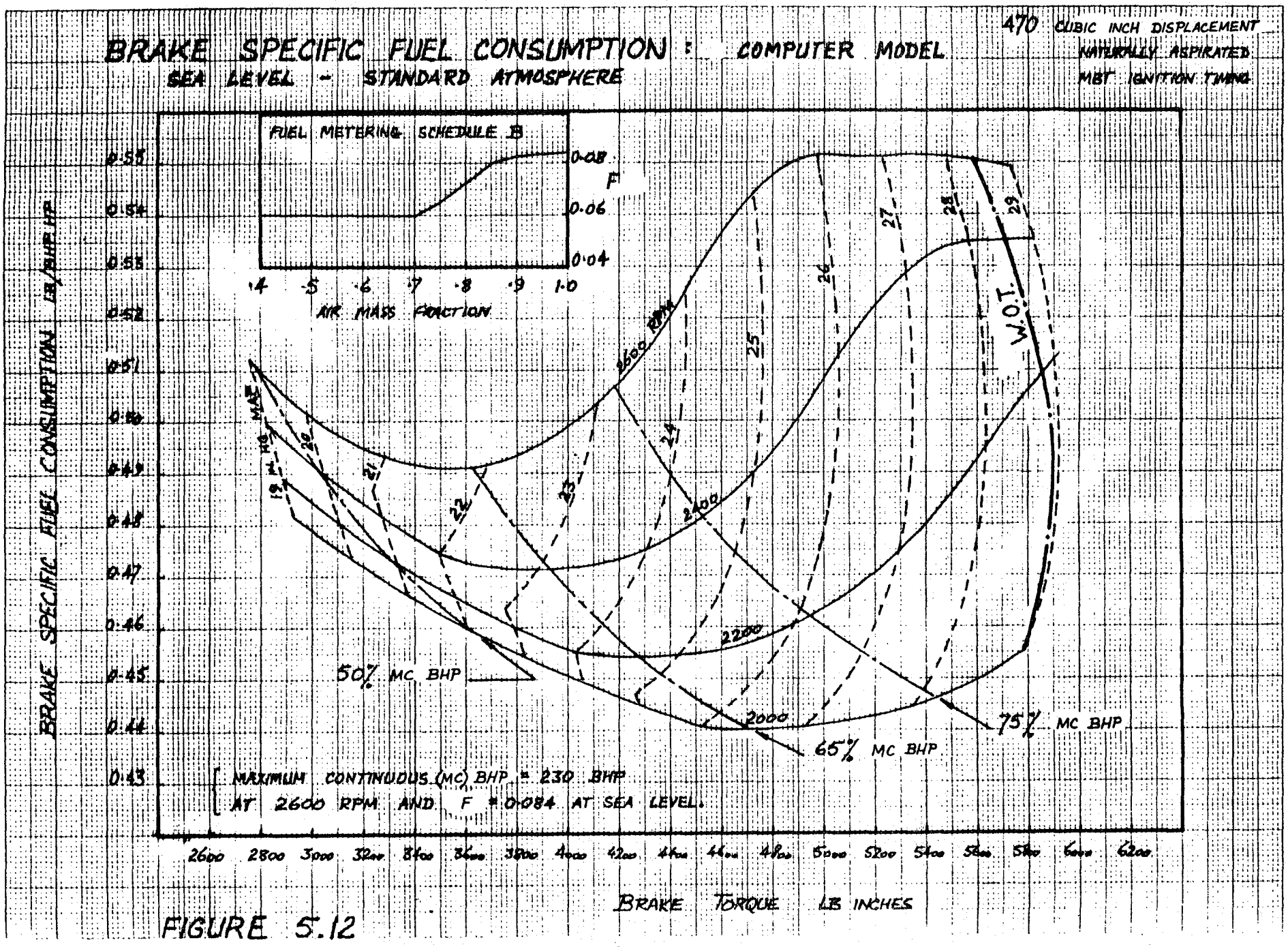
BRAKE SPECIFIC FUEL CONSUMPTION : COMPUTER MODEL
SEA LEVEL - STANDARD ATMOSPHERE
470 CUBIC INCH DISPLACEMENT
NATURALLY ASPIRATED
MBT IGNITION TIMING
FUEL METERING SCHEDULE B
F
0.08
0.06
0.04
.4 .5 .6 .7 .8 .9 1.0
AIR MASS FRACTION
BRAKE SPECIFIC FUEL CONSUMPTION LB/BHP HR
0.55
0.54
0.53
0.52
0.51
0.50
0.49
0.48
0.47
0.46
0.45
0.44
0.43
MAP
19 IN HG
20
21
22
23
24
25
26
27
28
29
1.0 M
2600 RPM
2400
2200
2000
50% MC BHP
65% MC BHP
75% MC BHP
MAXIMUM CONTINUOUS (MC) BHP = 230 BHP
AT 2600 RPM AND F = 0.084 AT SEA LEVEL.
2600 2800 3000 3200 3400 3600 3800 4000 4200 4400 4600 4800 5000 5200 5400 5600 5800 6000 6200
BRAKE TORQUE LB INCHES

FIGURE 5.12

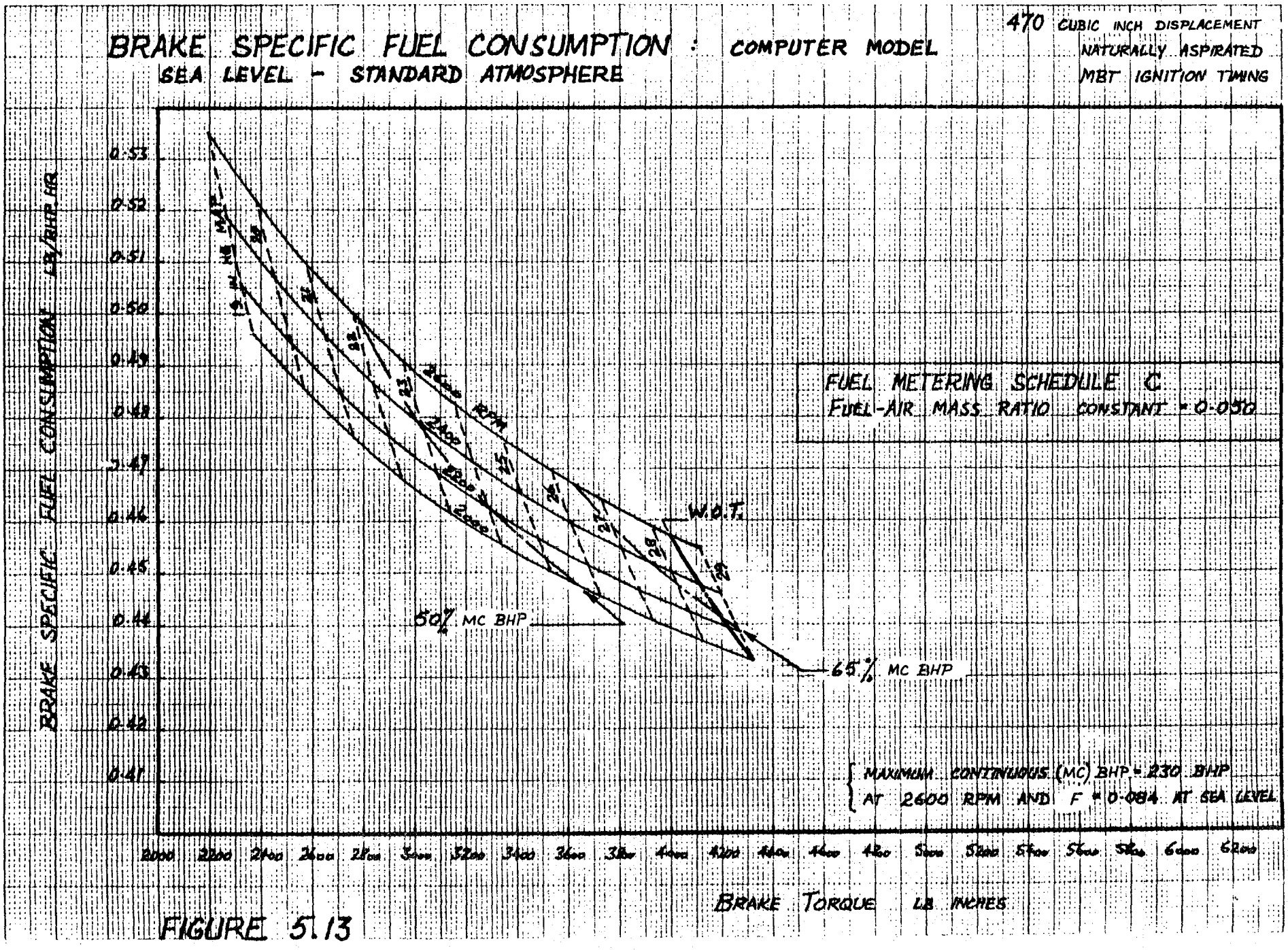
BRAKE SPECIFIC FUEL CONSUMPTION : COMPUTER MODEL
SEA LEVEL - STANDARD ATMOSPHERE
470 CUBIC INCH DISPLACEMENT
NATURALLY ASPIRATED
MBT IGNITION TIMING
FUEL METERING SCHEDULE C
FUEL-AIR MASS RATIO CONSTANT = 0.050
W.O.T.
50% MC BHP
65% MC BHP
MAXIMUM CONTINUOUS (MC) BHP = 230 BHP
AT 2600 RPM AND F = 0.084 AT SEA LEVEL
BRAKE SPECIFIC FUEL CONSUMPTION LB/BHP HR
BRAKE TORQUE LB INCHES
0.53
0.52
0.51
0.50
0.49
0.48
0.47
0.46
0.45
0.44
0.43
0.42
0.41
2000
2200
2400
2600
2800
3000
3200
3400
3600
3800
4000
4200
4400
4600
4800
5000
5200
5400
5600
5800
6000
6200

FIGURE 5.13

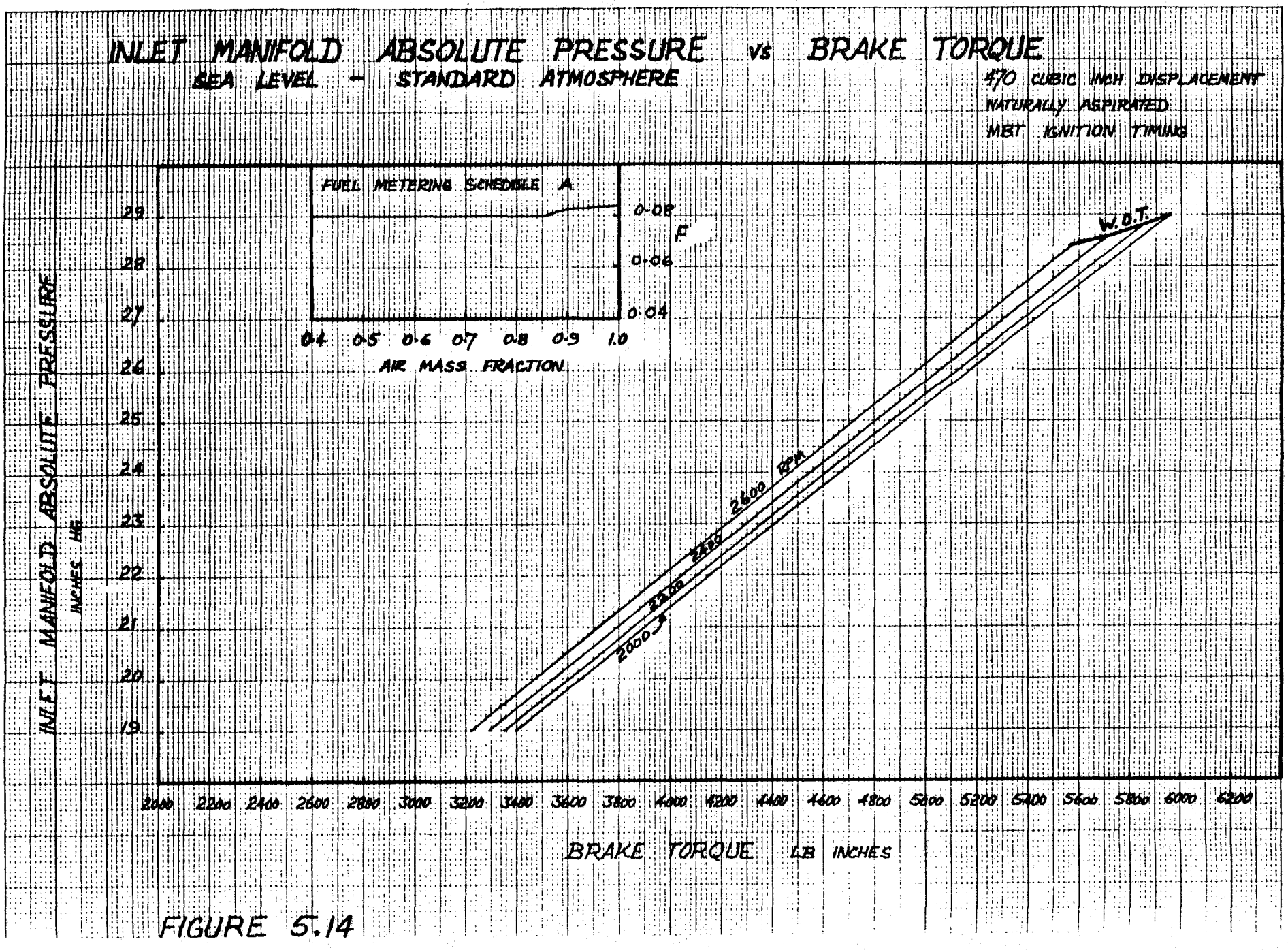
INLET MANIFOLD ABSOLUTE PRESSURE Vs BRAKE TORQUE
SEA LEVEL - STANDARD ATMOSPHERE
470 CUBIC INCH DISPLACEMENT
NATURALLY ASPIRATED
MBT IGNITION TIMING
FUEL METERING SCHEDULE A
0.08
0.06
0.04
F
0.4 0.5 0.6 0.7 0.8 0.9 1.0
AIR MASS FRACTION
W.O.T.
2600 RPM
2400
2200
2000
INLET MANIFOLD ABSOLUTE PRESSURE
INCHES HG
29 28 27 26 25 24 23 22 21 20 19
2000 2200 2400 2600 2800 3000 3200 3400 3600 3800 4000 4200 4400 4600 4800 5000 5200 5400 5600 5800 6000 6200
BRAKE TORQUE LB INCHES

FIGURE 5.14

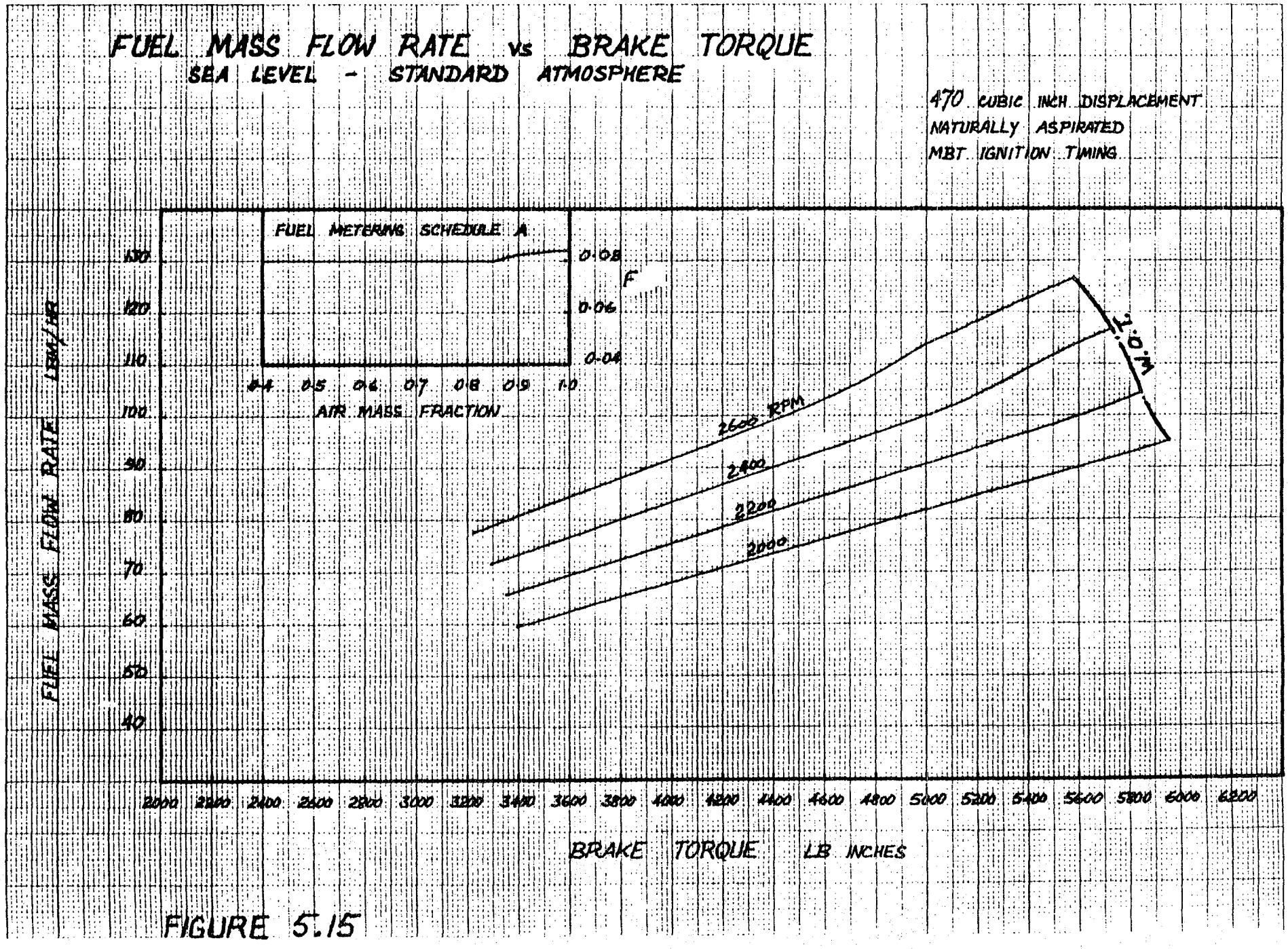
FUEL MASS FLOW RATE Vs BRAKE TORQUE
SEA LEVEL - STANDARD ATMOSPHERE
470 CUBIC INCH DISPLACEMENT
NATURALLY ASPIRATED
MBT IGNITION TIMING
FUEL METERING SCHEDULE A
0.08
0.06
0.04
F
.4 .5 .6 .7 .8 .9 1.0
AIR MASS FRACTION
2600 RPM
2400
2200
2000
2.0 M
FUEL MASS FLOW RATE LBM/HR
130
120
110
100
90
80
70
60
50
40
2000 2200 2400 2600 2800 3000 3200 3400 3600 3800 4000 4200 4400 4600 4800 5000 5200 5400 5600 5800 6000 6200
BRAKE TORQUE LB INCHES

FIGURE 5.15

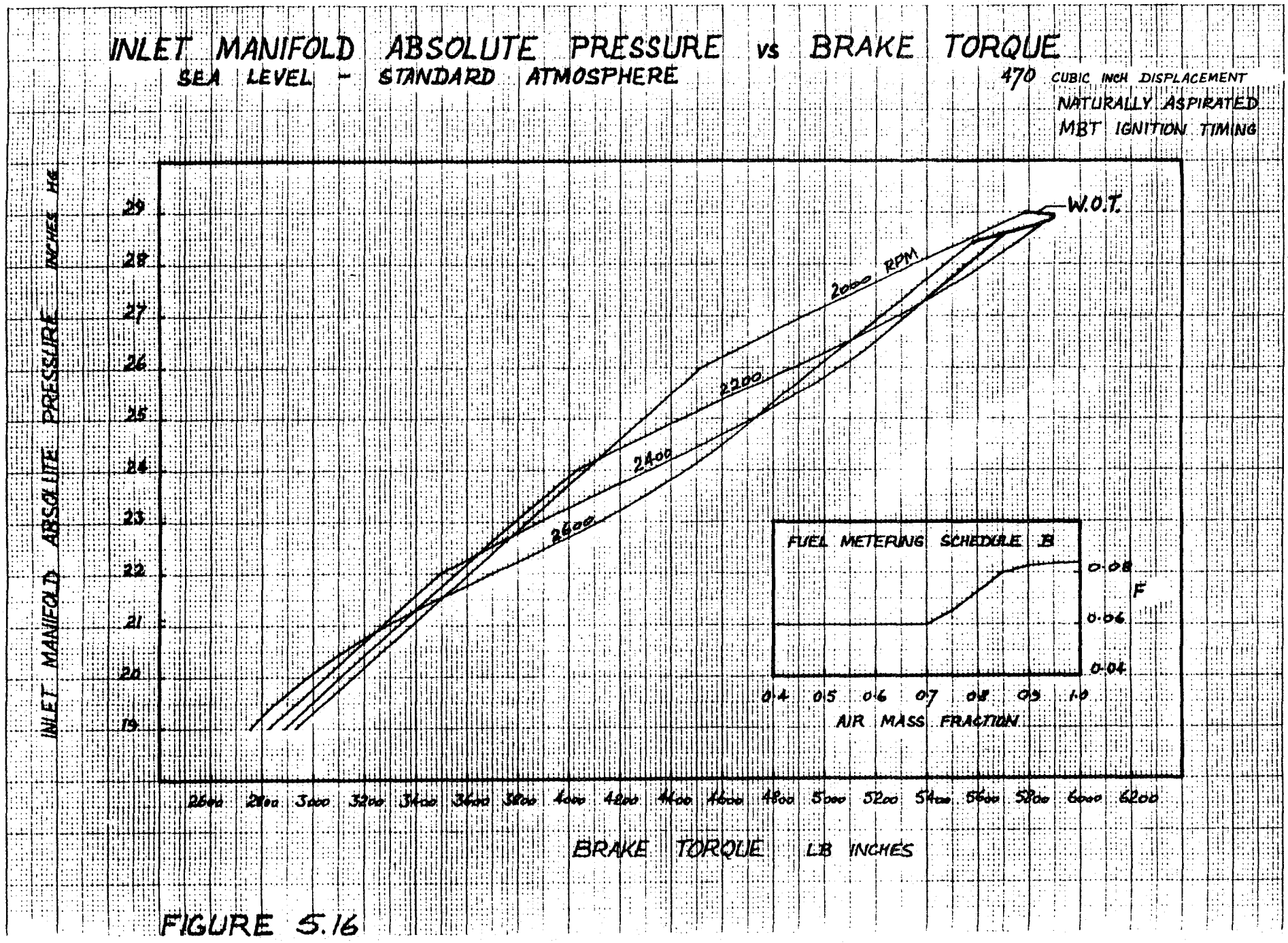
INLET MANIFOLD ABSOLUTE PRESSURE vs BRAKE TORQUE
SEA LEVEL - STANDARD ATMOSPHERE
470 CUBIC INCH DISPLACEMENT
NATURALLY ASPIRATED
MBT IGNITION TIMING
W.O.T.
2000 RPM
2200
2400
2600
INLET MANIFOLD ABSOLUTE PRESSURE INCHES Hg
29
28
27
26
25
24
23
22
21
20
19
FUEL METERING SCHEDULE B
0.08
0.06
0.04
F
0.4 0.5 0.6 0.7 0.8 0.9 1.0
AIR MASS FRACTION
2600 2800 3000 3200 3400 3600 3800 4000 4200 4400 4600 4800 5000 5200 5400 5600 5800 6000 6200
BRAKE TORQUE LB INCHES

FIGURE 5.16

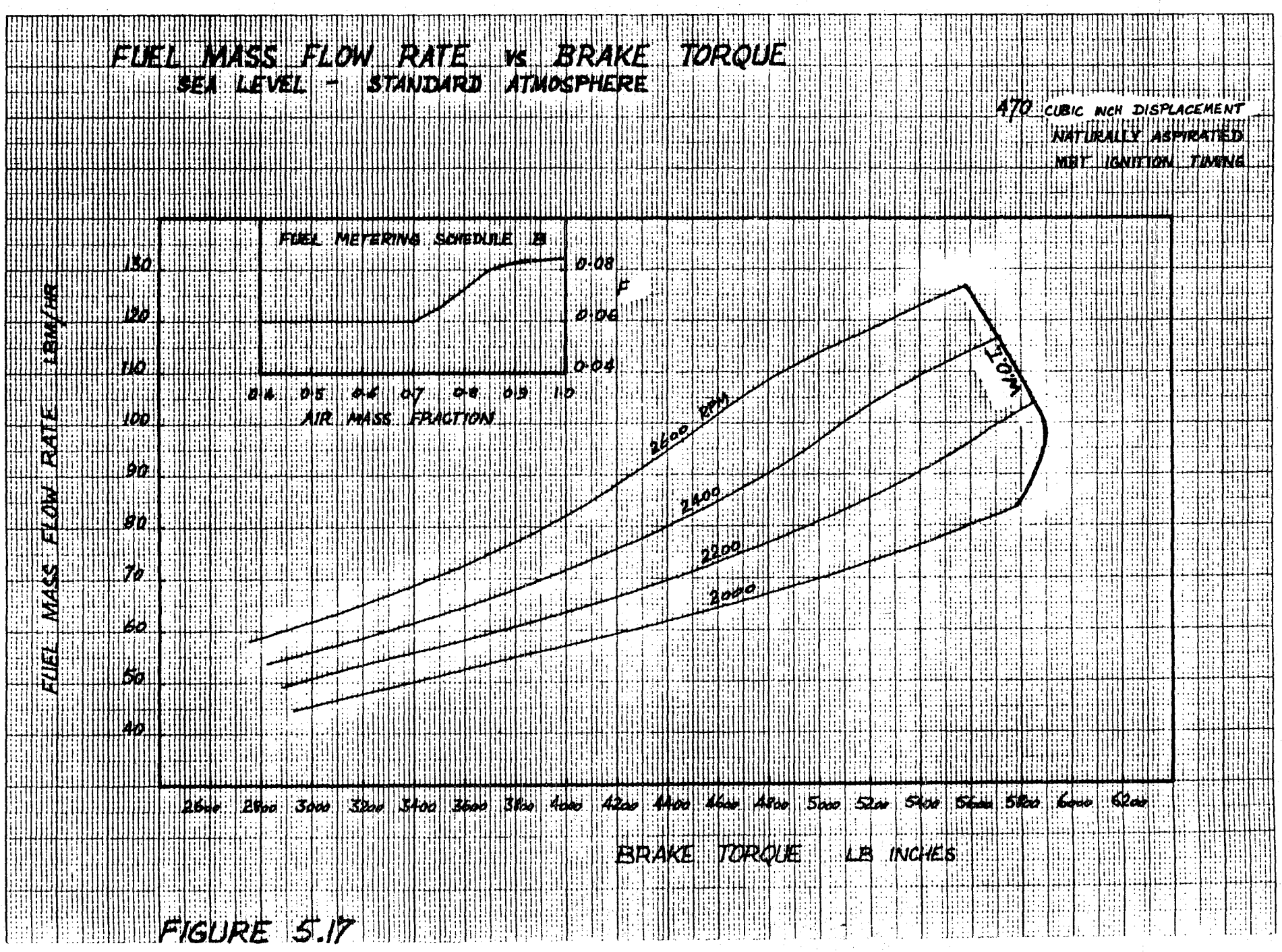
FUEL MASS FLOW RATE vs BRAKE TORQUE
SEA LEVEL - STANDARD ATMOSPHERE
470 CUBIC INCH DISPLACEMENT
NATURALLY ASPIRATED
MBT IGNITION TIMING
FUEL METERING SCHEDULE B
0.08
0.06
0.04
0.4 0.5 0.6 0.7 0.8 0.9 1.0
AIR MASS FRACTION
FUEL MASS FLOW RATE LBM/HR
150
120
110
100
90
80
70
60
50
40
2600 RPM
2400
2200
2000
2600 2800 3000 3200 3400 3600 3800 4000 4200 4400 4600 4800 5000 5200 5400 5600 5800 6000 6200
BRAKE TORQUE LB INCHES

FIGURE 5.17

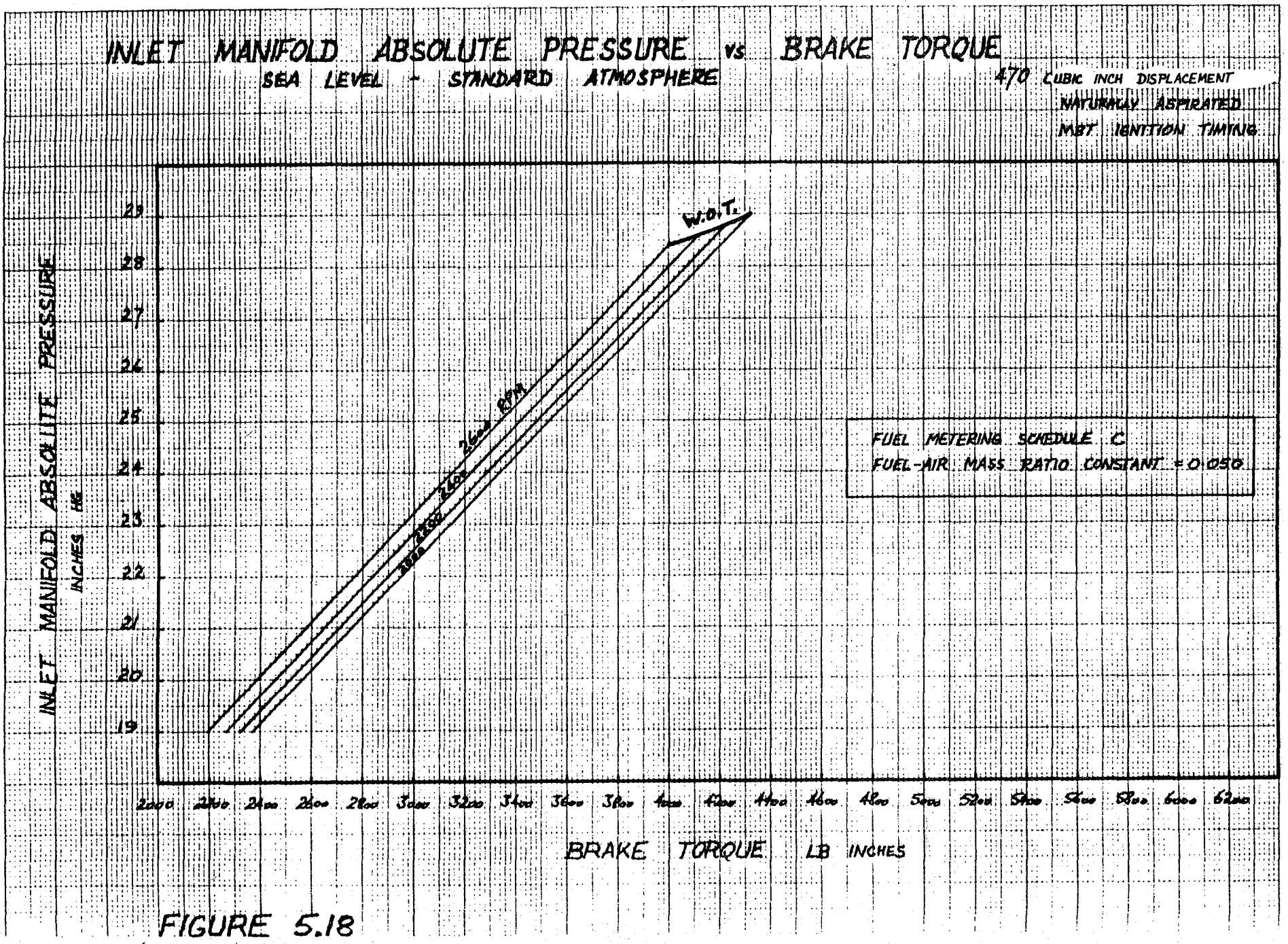
INLET MANIFOLD ABSOLUTE PRESSURE vs BRAKE TORQUE
SEA LEVEL - STANDARD ATMOSPHERE
470 CUBIC INCH DISPLACEMENT
NATURALLY ASPIRATED
MBT IGNITION TIMING
W.O.T.
2600 RPM
2400
2200
2000
1800
FUEL METERING SCHEDULE C
FUEL-AIR MASS RATIO CONSTANT = 0.050
INLET MANIFOLD ABSOLUTE PRESSURE
INCHES HG
29
28
27
26
25
24
23
22
21
20
19
2000
2200
2400
2600
2800
3000
3200
3400
3600
3800
4000
4200
4400
4600
4800
5000
5200
5400
5600
5800
6000
6200
BRAKE TORQUE LB INCHES

FIGURE 5.18

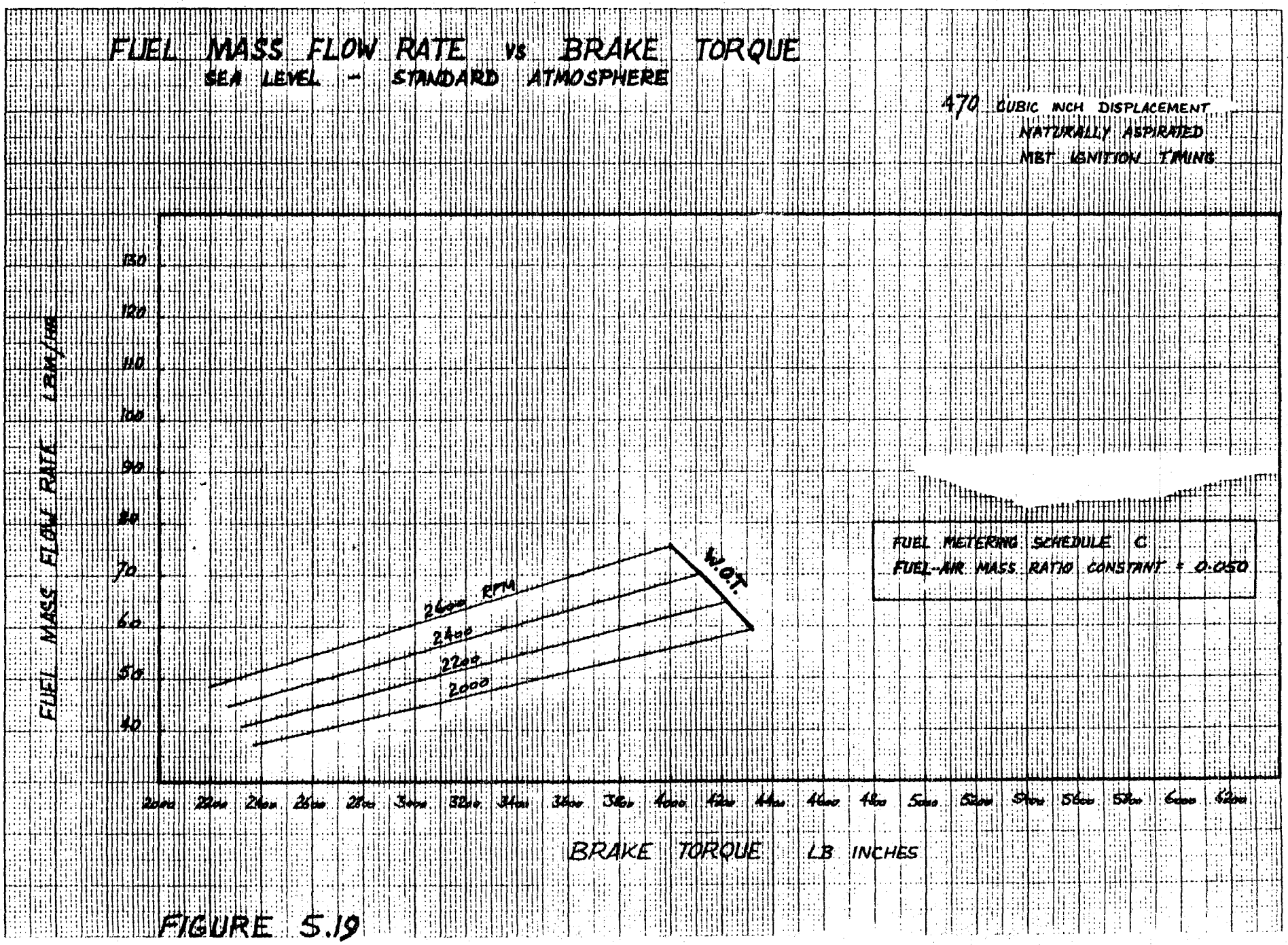
FUEL MASS FLOW RATE Vs BRAKE TORQUE
SEA LEVEL – STANDARD ATMOSPHERE
470 CUBIC INCH DISPLACEMENT
NATURALLY ASPIRATED
MBT IGNITION TIMING
FUEL METERING SCHEDULE C
FUEL-AIR MASS RATIO CONSTANT + 0.050
W.O.T.
2600 RPM
2400
2200
2000
FUEL MASS FLOW RATE LBM/HR
130
120
110
100
90
80
70
60
50
40
BRAKE TORQUE LB INCHES

FIGURE 5.19

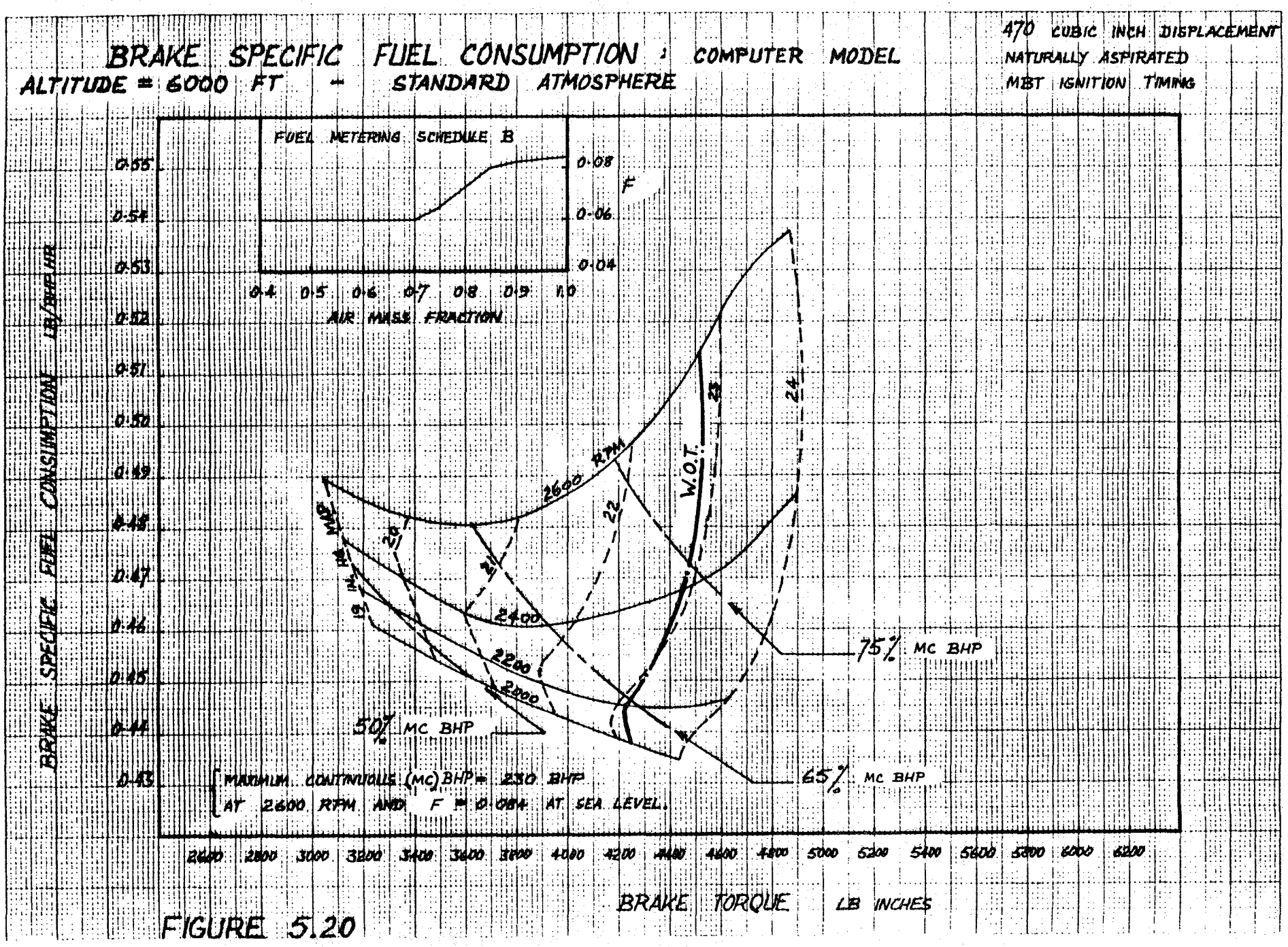
BRAKE SPECIFIC FUEL CONSUMPTION - COMPUTER MODEL
ALTITUDE = 6000 FT - STANDARD ATMOSPHERE
470 CUBIC INCH DISPLACEMENT
NATURALLY ASPIRATED
MBT IGNITION TIMING
FUEL METERING SCHEDULE B
F
AIR MASS FRACTION
BRAKE SPECIFIC FUEL CONSUMPTION LB/BHP HR
BRAKE TORQUE LB INCHES
W.O.T.
2600 RPM
2400
2200
2000
75% MC BHP
65% MC BHP
50% MC BHP
MAXIMUM CONTINUOUS (MC) BHP = 230 BHP
AT 2600 RPM AND F = 0.084 AT SEA LEVEL.

FIGURE 5.20

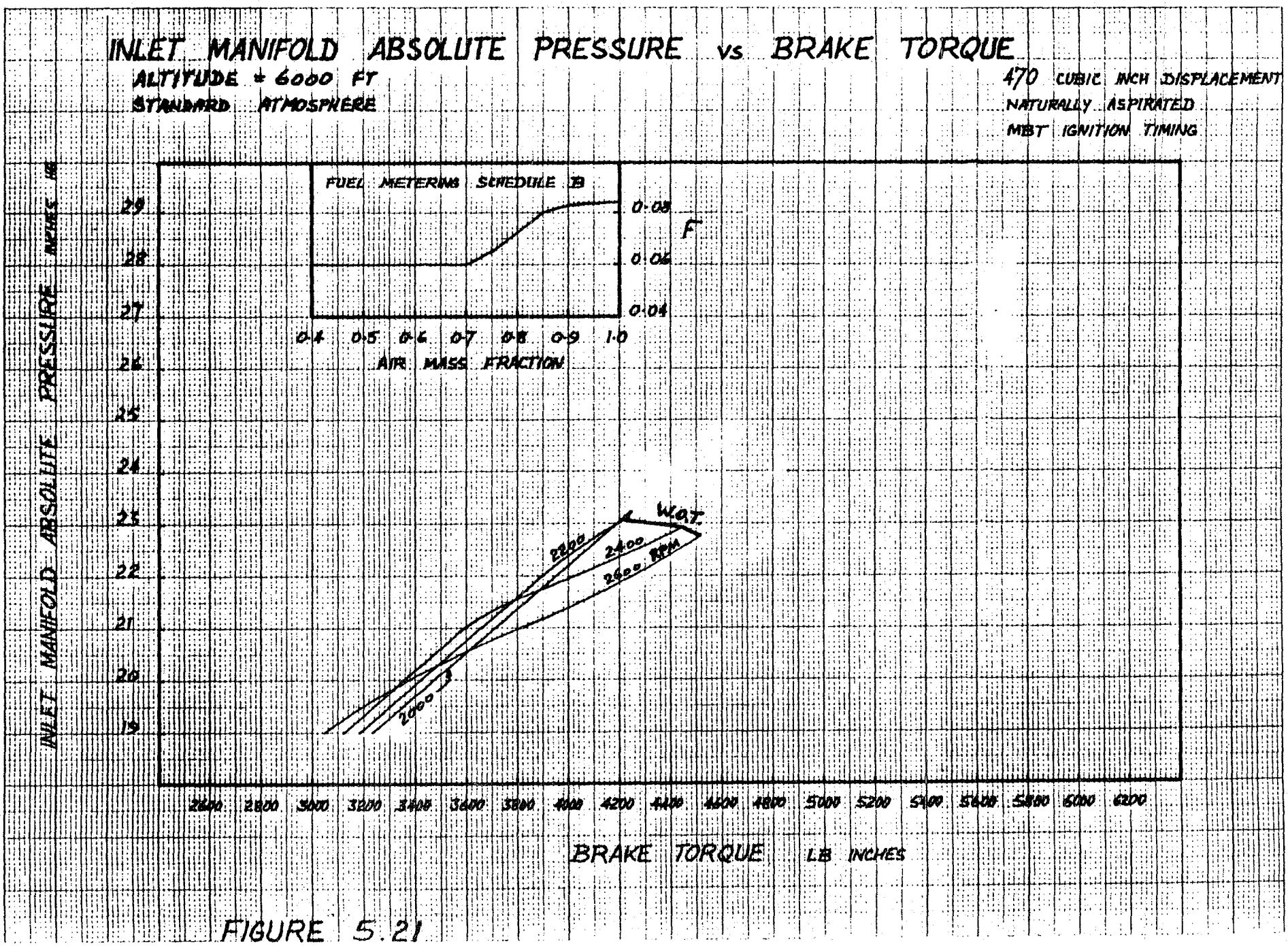
INLET MANIFOLD ABSOLUTE PRESSURE Vs BRAKE TORQUE
ALTITUDE = 6000 FT
STANDARD ATMOSPHERE
470 CUBIC INCH DISPLACEMENT
NATURALLY ASPIRATED
MBT IGNITION TIMING
FUEL METERING SCHEDULE B
0.08
0.06
0.04
F
0.4 0.5 0.6 0.7 0.8 0.9 1.0
AIR MASS FRACTION
INLET MANIFOLD ABSOLUTE PRESSURE INCHES HG
29 28 27 26 25 24 23 22 21 20 19
WOT
2200
2400
2600 RPM
2000
2600 2800 3000 3200 3400 3600 3800 4000 4200 4400 4600 4800 5000 5200 5400 5600 5800 6000 6200
BRAKE TORQUE LB INCHES

FIGURE 5.21

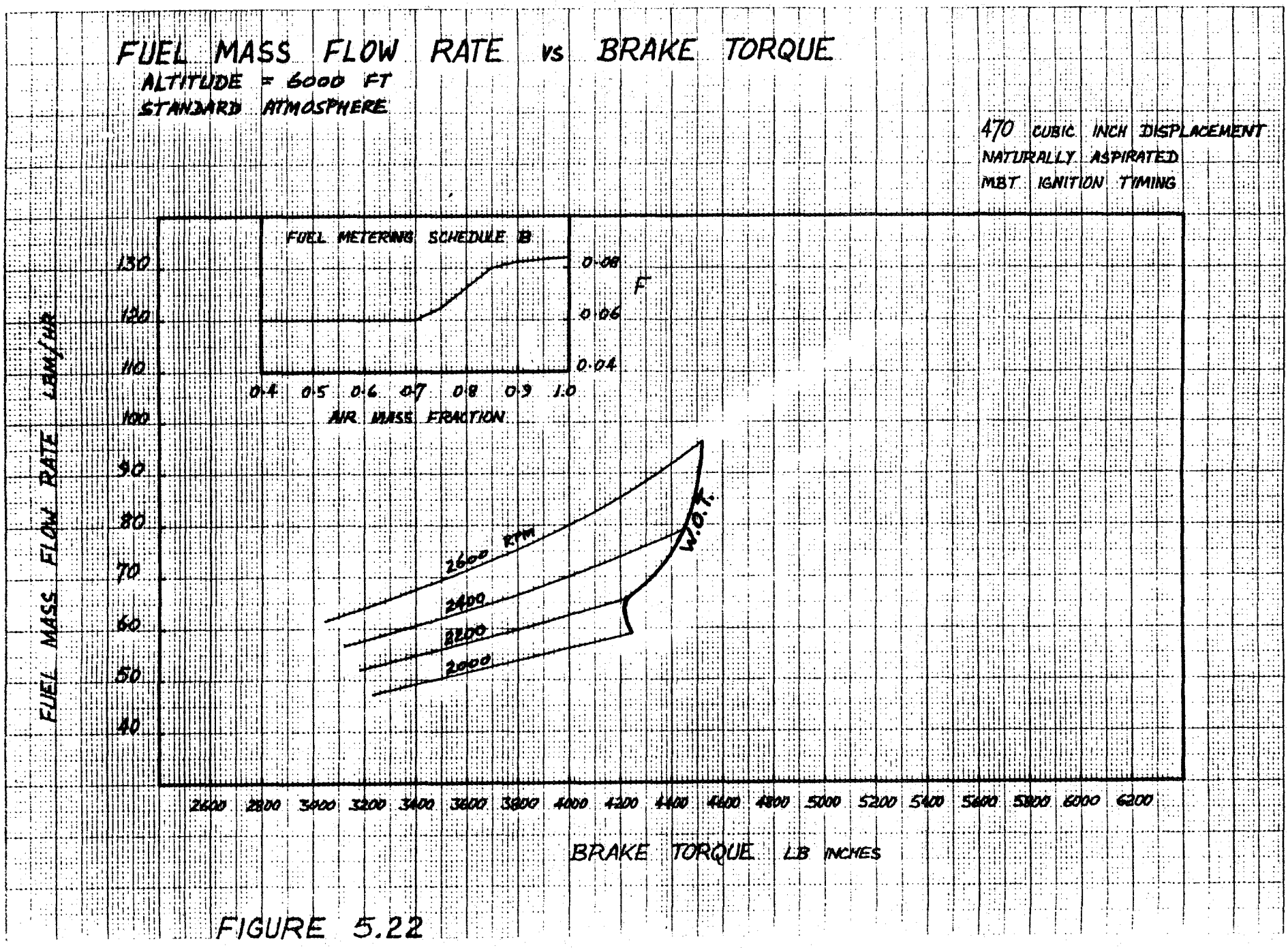

FIGURE 5.22

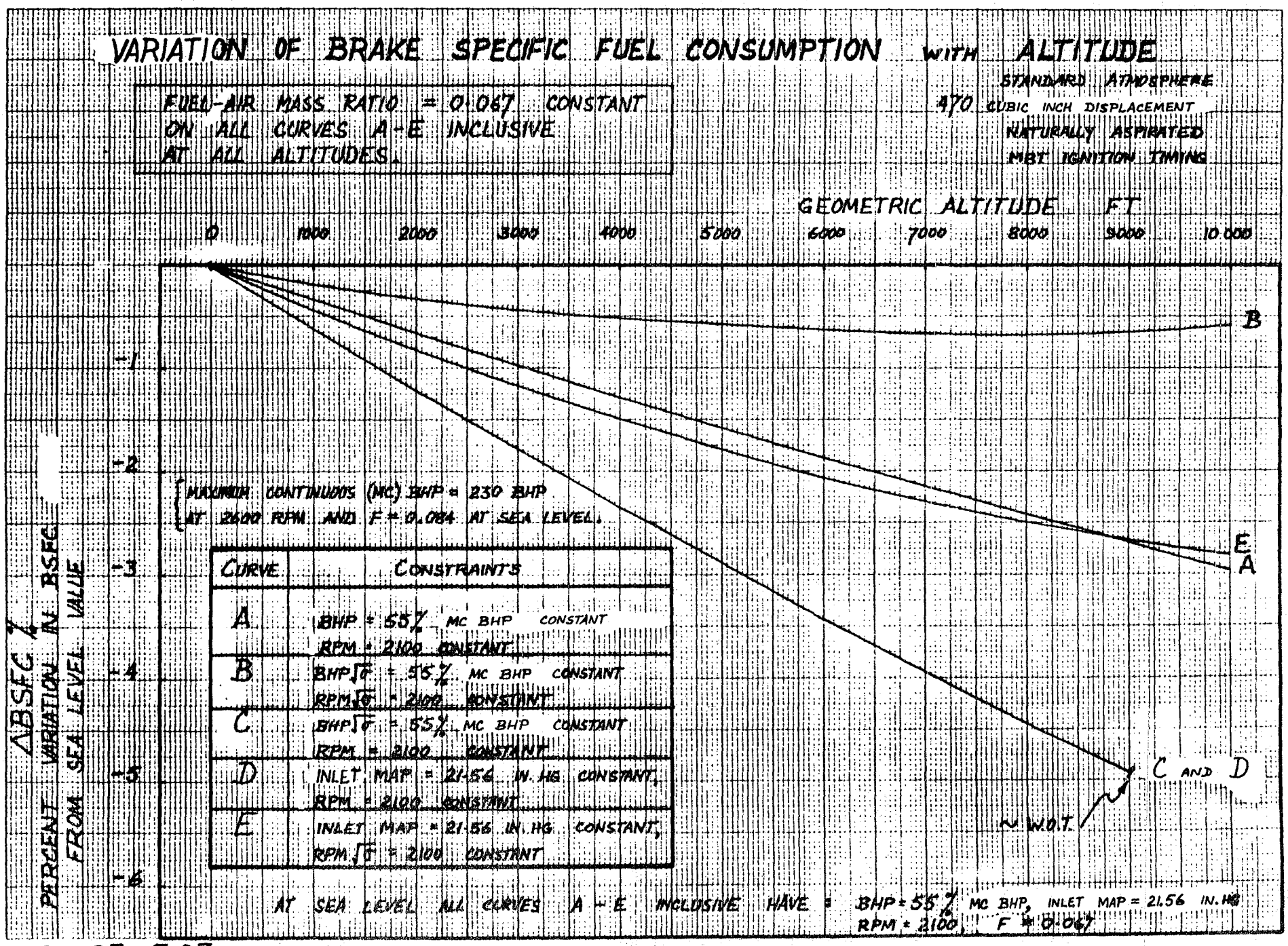
VARIATION OF BRAKE SPECIFIC FUEL CONSUMPTION WITH ALTITUDE
STANDARD ATMOSPHERE
470 CUBIC INCH DISPLACEMENT
NATURALLY ASPIRATED
MBT IGNITION TIMING
FUEL-AIR MASS RATIO = 0.067 CONSTANT ON ALL CURVES A-E INCLUSIVE AT ALL ALTITUDES.
GEOMETRIC ALTITUDE FT
0
1000
2000
3000
4000
5000
6000
7000
8000
9000
10,000
ΔBSFC % PERCENT VARIATION IN BSFC FROM SEA LEVEL VALUE
+1
+2
+3
+4
+5
+6
MAXIMUM CONTINUOUS (MC) BHP = 230 BHP AT 2600 RPM AND F = 0.084 AT SEA LEVEL.
CURVE
CONSTRAINTS
A
BHP = 55% MC BHP CONSTANT
RPM = 2100 CONSTANT
B
BHP√σ = 55% MC BHP CONSTANT
RPM√σ = 2100 CONSTANT
C
BHP√σ = 55% MC BHP CONSTANT
RPM = 2100 CONSTANT
D
INLET MAP = 21.56 IN. HG CONSTANT,
RPM = 2100 CONSTANT
E
INLET MAP = 21.56 IN. HG CONSTANT,
RPM√σ = 2100 CONSTANT
B
E
A
C AND D
~ W.O.T.
AT SEA LEVEL ALL CURVES A - E INCLUSIVE HAVE = BHP = 55% MC BHP, INLET MAP = 21.56 IN. HG
RPM = 2100, F = 0.067

FIGURE 5.23

DENSITY INDEX vs FUEL/AIR MASS RATIO

470 CUBIC INCH DISPLACEMENT
NATURALLY ASPIRATED ENGINE
MBT IGNITION TIMING
STANDARD ATMOSPHERE

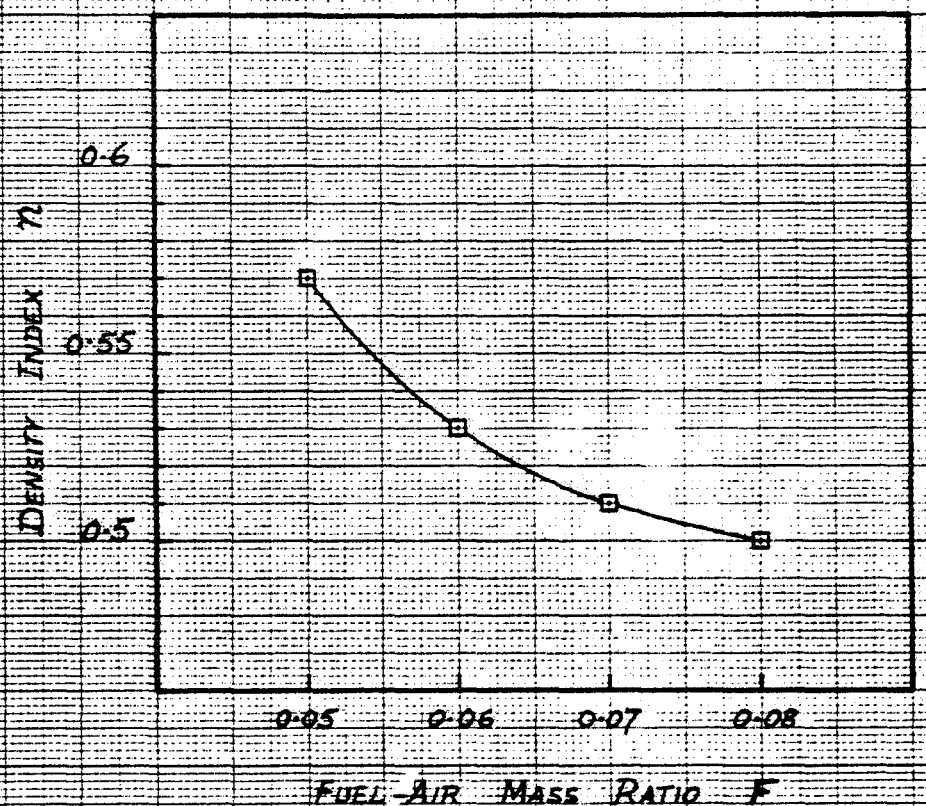

THE DENSITY INDEX n IS USED TO COMPUTE THE CORRECTED BRAKE TORQUE $Q_{E_c} = Q_E \sigma^n$ LB FT

$\sigma = \rho/\rho_0$ = ATMOSPHERIC AIR DENSITY RATIO

ρ = ATMOSPHERIC AIR DENSITY AT ALTITUDE H FT, SLUGS/CUBIC FT

ρ_0 = ATMOSPHERIC AIR DENSITY AT SEA LEVEL, SLUGS/CUBIC FT.

FIGURE 5.24

SCHEMATIC : VARIATION OF Q_E AND Q_{E_c} WITH ALTITUDE

STANDARD ATMOSPHERE
NATURALLY ASPIRATED
MBT IGNITION TIMING

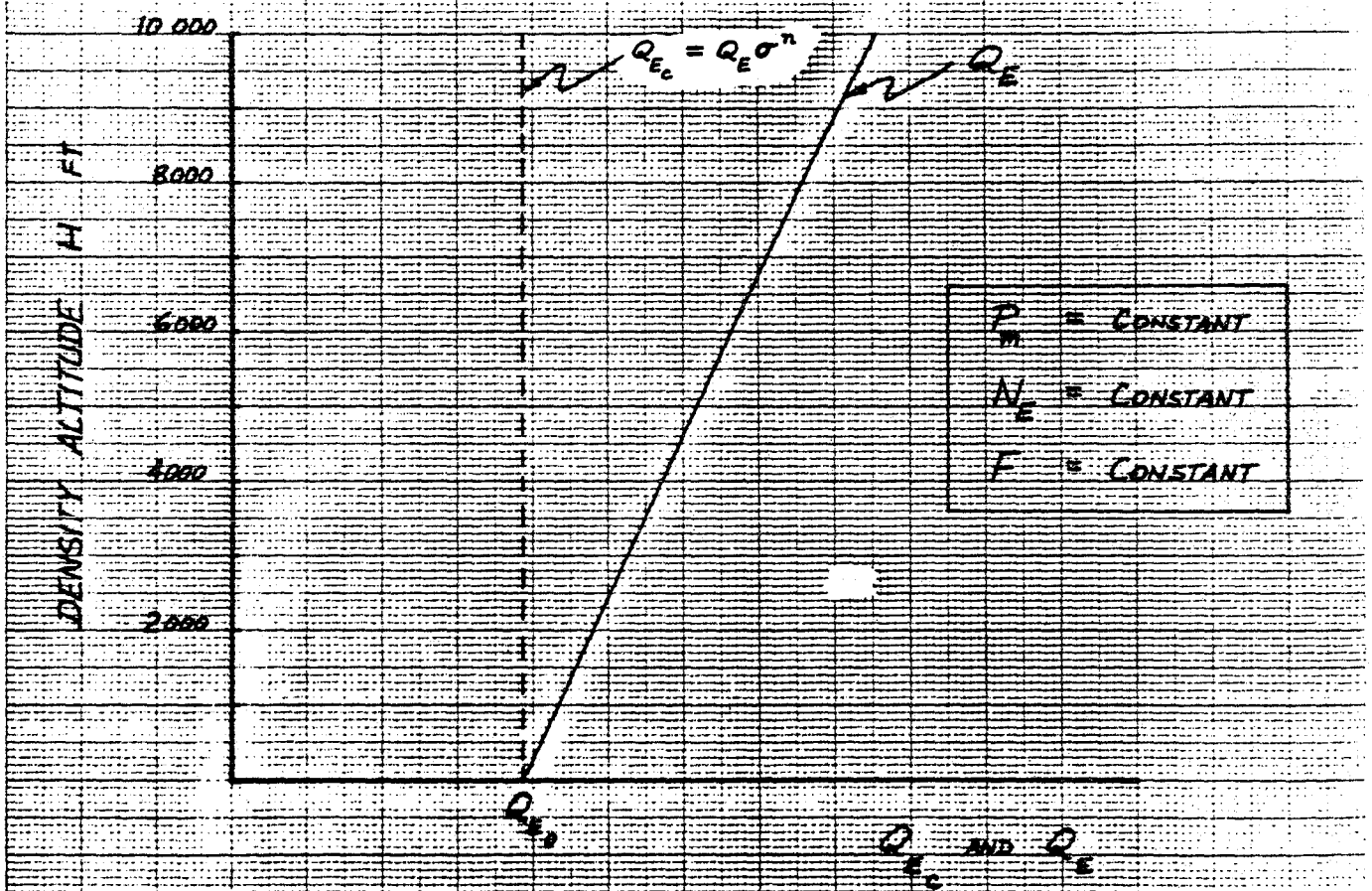

FIGURE 5.25

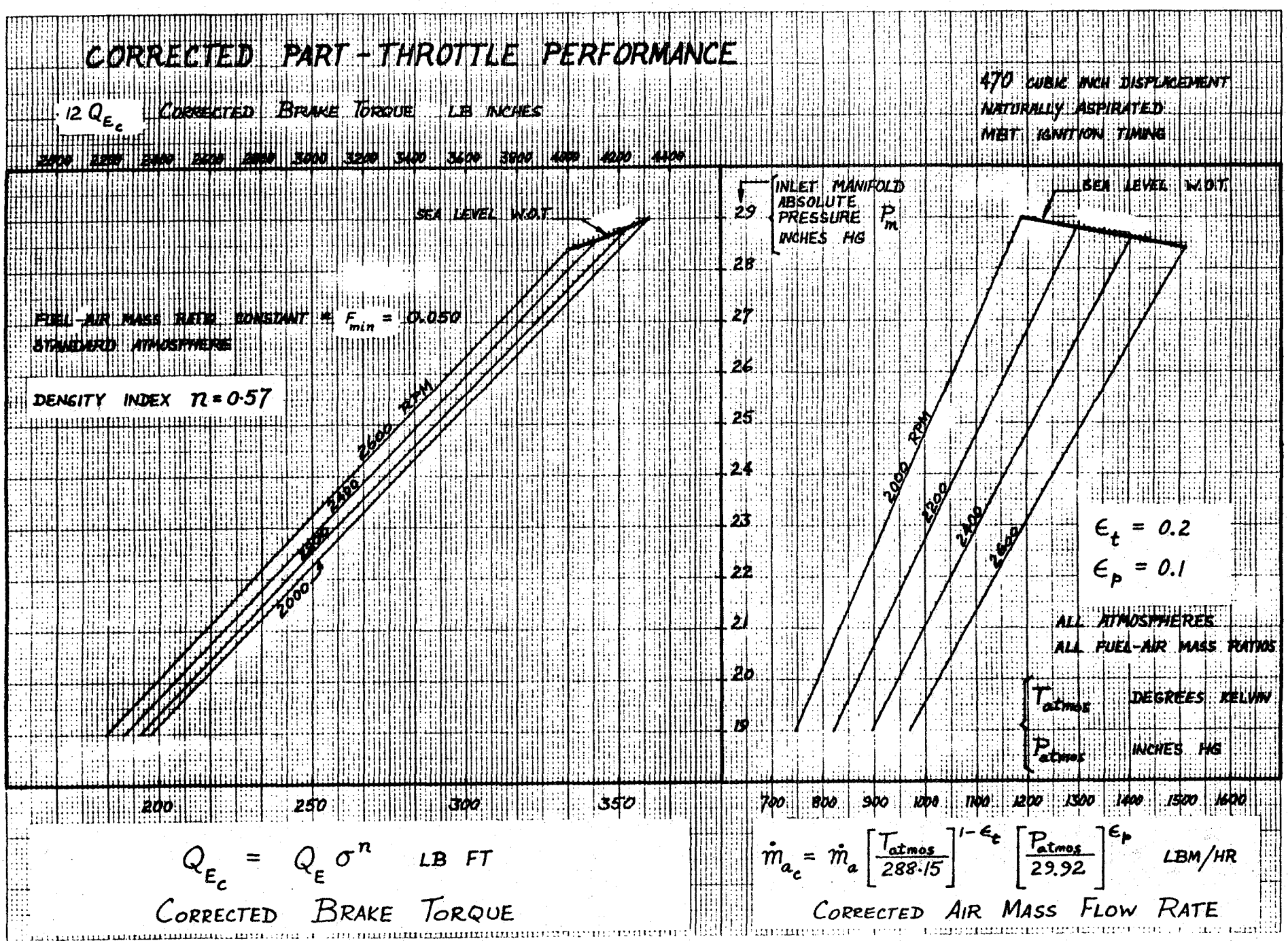
CORRECTED PART - THROTTLE PERFORMANCE
470 CUBIC INCH DISPLACEMENT
NATURALLY ASPIRATED
MBT IGNITION TIMING
12 Q_{E_c}
CORRECTED BRAKE TORQUE LB INCHES
2400 2600 2800 3000 3200 3400 3600 3800 4000 4200 4400
SEA LEVEL W.O.T.
INLET MANIFOLD ABSOLUTE PRESSURE P_m INCHES HG
29
28
27
26
25
24
23
22
21
20
19
FUEL-AIR MASS RATIO CONSTANT = F_{min} = 0.050
STANDARD ATMOSPHERE
DENSITY INDEX n = 0.57
2600 RPM
2400
2200
2000
1800
SEA LEVEL W.O.T.
2000 RPM
2200
2400
2600
ϵ_t = 0.2
ϵ_p = 0.1
ALL ATMOSPHERES
ALL FUEL-AIR MASS RATIOS
T_{atmos} DEGREES KELVIN
P_{atmos} INCHES HG
200 250 300 350
700 800 900 1000 1100 1200 1300 1400 1500 1600
$Q_{E_c} = Q_E \sigma^n$ LB FT
CORRECTED BRAKE TORQUE
$\dot{m}_{a_c} = \dot{m}_a \left[\frac{T_{atmos}}{288.15}\right]^{1-\epsilon_t} \left[\frac{P_{atmos}}{29.92}\right]^{\epsilon_p}$ LBM/HR
CORRECTED AIR MASS FLOW RATE

FIGURE 5.26

FIGURES 5.27 - 5.29 : NATURALLY ASPIRATED ENGINE WITH MBT IGNITION TIMING.

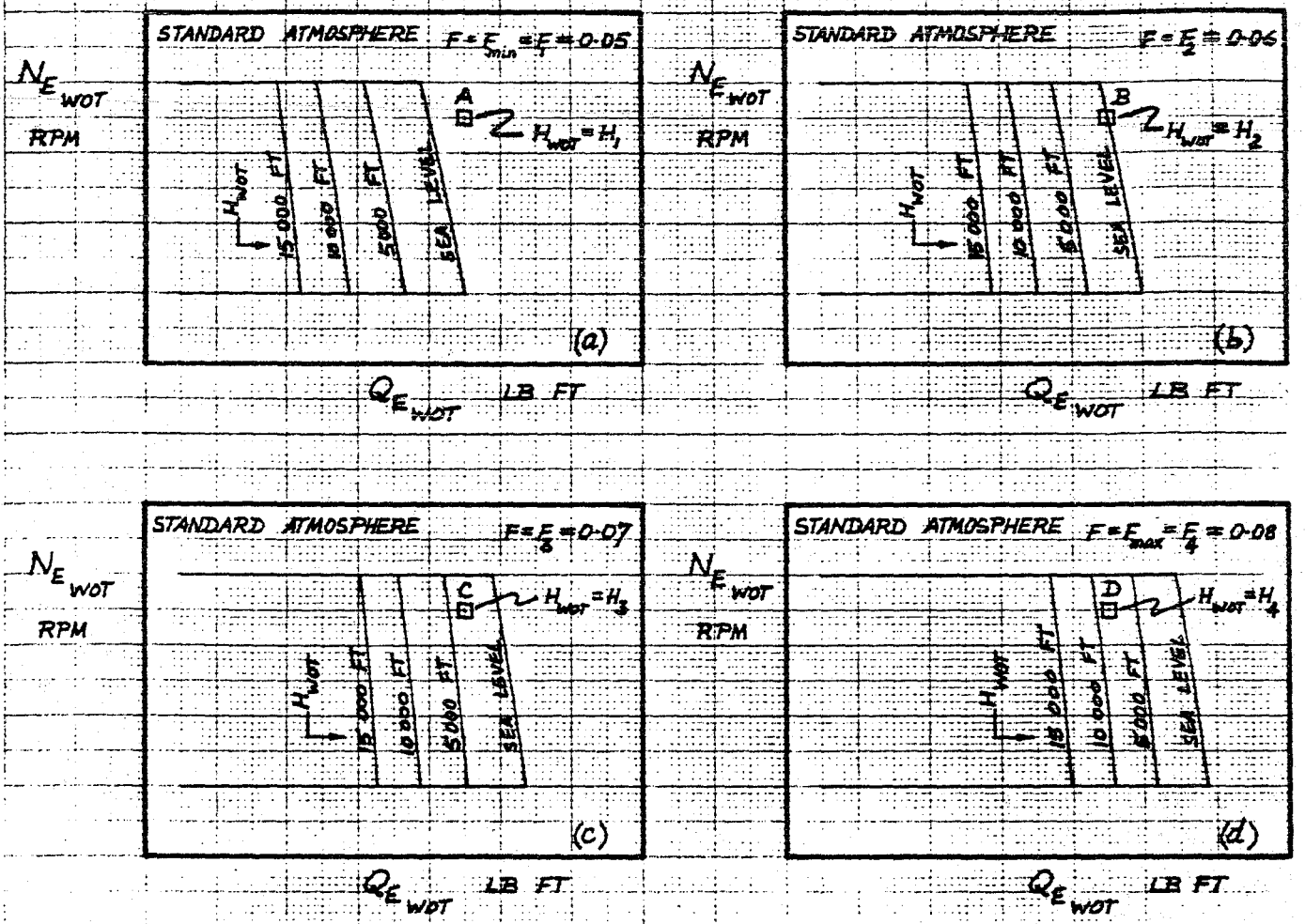

FIGURE 5.27 WIDE OPEN THROTTLE PERFORMANCE : ENGINE SHAFT SPEED $N_{E_{WOT}}$ VS ENGINE BRAKE TORQUE $Q_{E_{WOT}}$

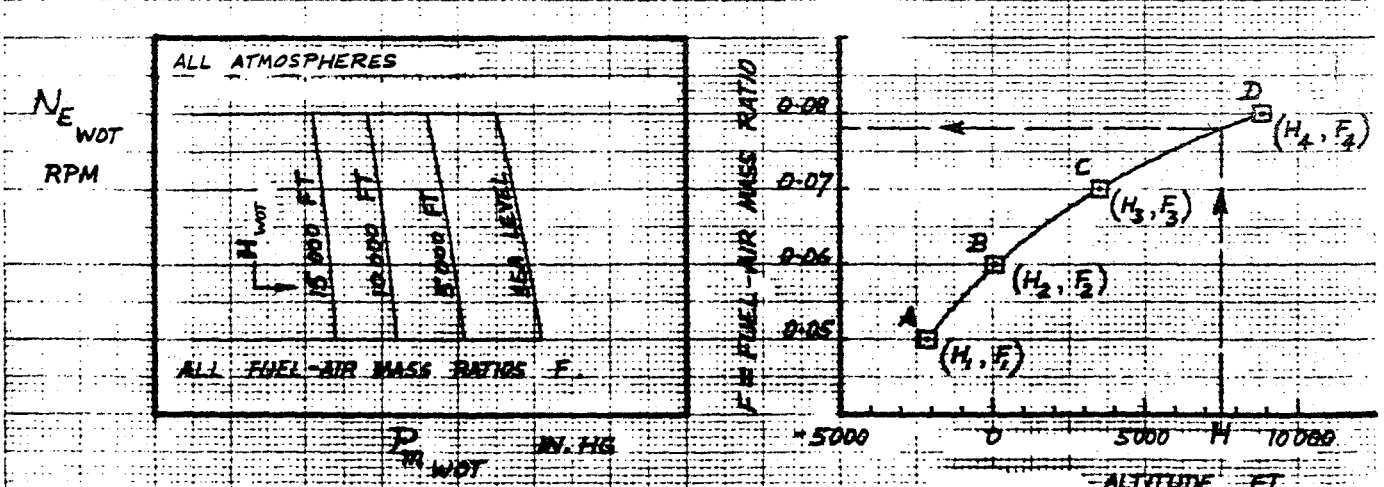

FIGURE 5.28 WIDE OPEN THROTTLE PERFORMANCE : ENGINE SHAFT SPEED $N_{E_{WOT}}$ VS INLET MAP $P_{m_{WOT}}$

FIGURE 5.29 DETERMINATION OF REQUIRED FUEL-AIR MASS RATIO AT WIDE OPEN THROTTLE

NEA SUBSYSTEM INPUT-OUTPUT MODEL

STANDARD AND NON-STANDARD ATMOSPHERIC CONDITIONS

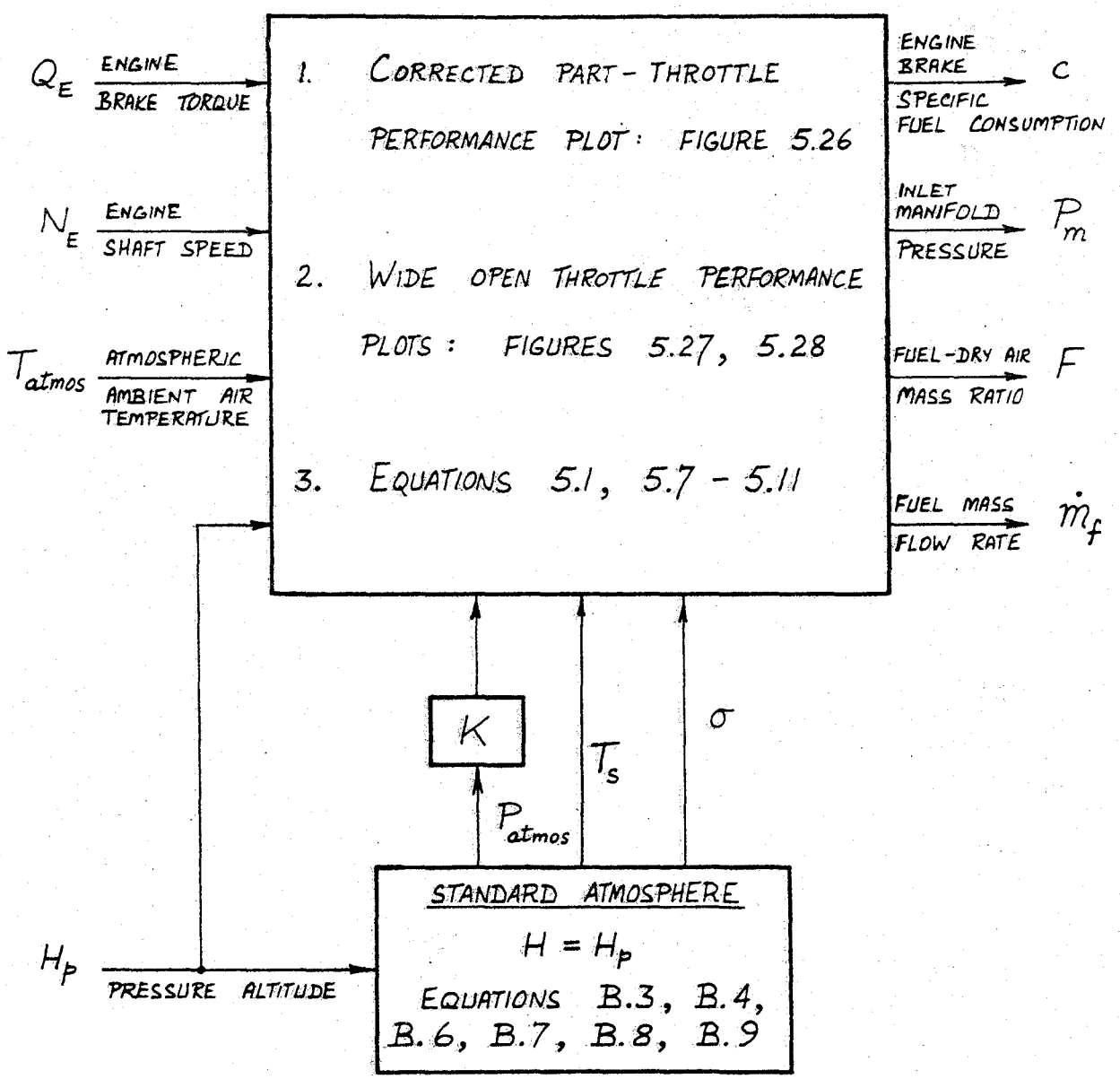

NOTE:
1. IGNITION TIMING OPTIMIZED FOR MAXIMUM Q_E.
2. ENGINE BRAKE SPECIFIC FUEL CONSUMPTION c CONSTRAINED TO A MINIMUM COMMENSURATE WITH THE INPUTS.
3. $K = 29.92 / 2116.22$ = CONVERSION FACTOR: LB/FT^2 TO INCHES HG.

FIGURE 5.30

SCHEMATIC : TURBOCHARGED PISTON ENGINE

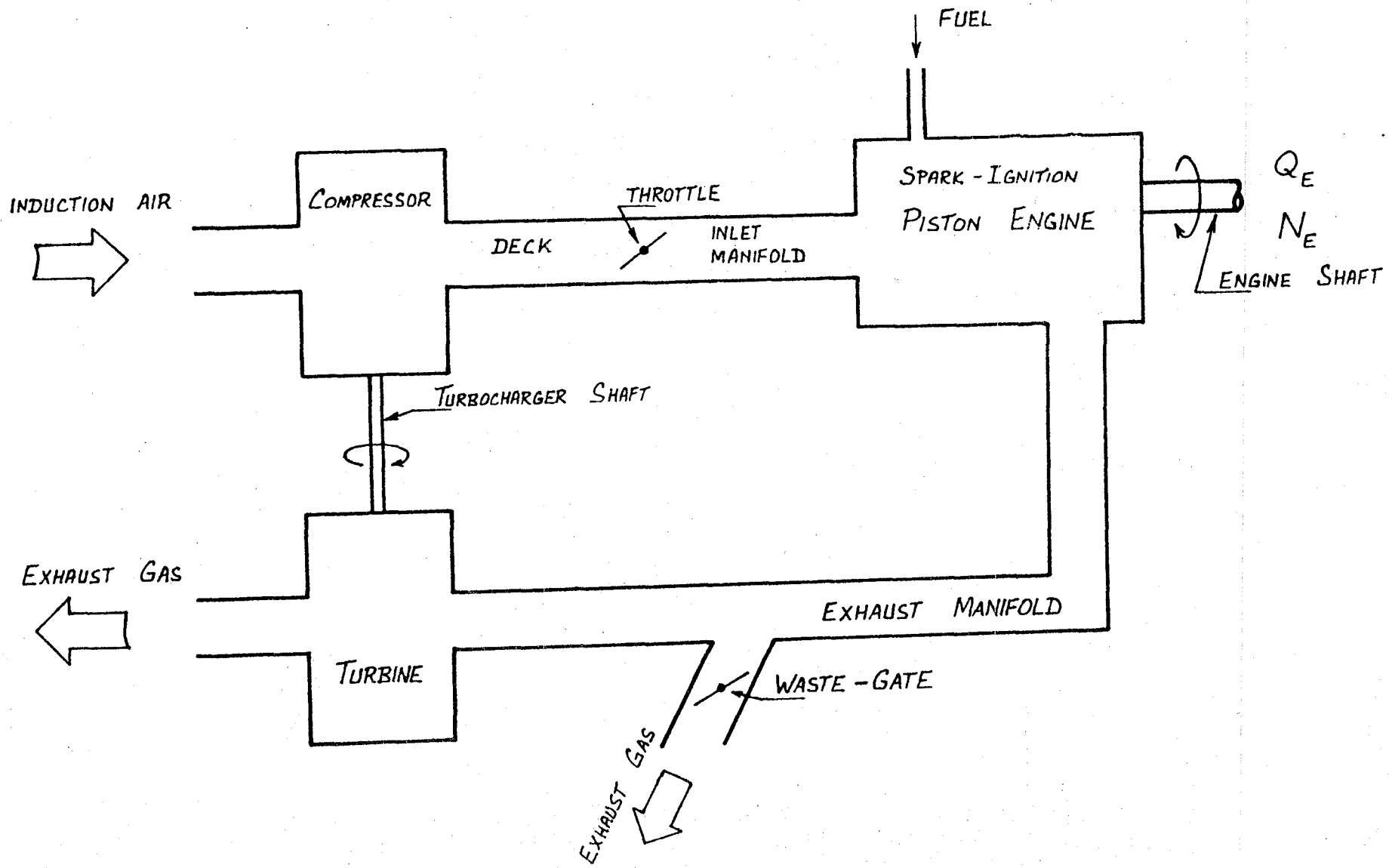

FIGURE 5.31

CHAPTER 6

THE AIRPLANE-ATMOSPHERE SYSTEM

Table of Contents

CHAPTER 6

THE AIRPLANE-ATMOSPHERE SYSTEM

INTRODUCTION

This chapter integrates the APA and NEA subsystem input-output models (developed in Chapters 3 through 5) to form a cruise performance model of the airplane-atmosphere system. The latter model is referred to as the Integrated Subsystem Cruise Performance Model (ISCPM).

First: the ISCPM is formulated. Second: the implementation of the ISCPM, and the use of the ISCPM for performance computations and optimizations is discussed. Third: engine control requirements of the ISCPM are discussed. Fourth: the potential increases in R* offered by the ISCPM, relative to current General Aviation practice, are examined. Finally: the ISCPM is compared with the Pilot Operating Handbook Cruise Performance Model developed in Chapter 2.

THE INTEGRATED SUBSYSTEM CRUISE PERFORMANCE MODEL

Formulation

The APA subsystem input-output model has been summarized in the block diagram of Figure 4.8. Likewise, the NEA subsystem input-output model has been summarized in the block diagram of Figure 5.30. These two block diagrams are combined in Figure 6.1.

The ISCPM is the set of relationships which determines the outputs

$$S_{out} = \{ R^*, P_m, F, \dot{m}_f \}$$

of Figure 6.1 in terms of the inputs

$$S_{in} = \{ V_w, V_E, W, h, P_{AUX}, N_E, T_{atmos}, H_p \}$$

of Figure 6.1. The ISCPM yields the point performance of the complete airplane in cruise, in the standard atmosphere or in any non-standard atmosphere; when the engine is operating at the minimum possible BSFC commensurate with S_{in}.

Implementation

It is proposed that the ISCPM forms the core of an airborne microprocessor computational package. Computational software contained in this package, but extra to the ISCPM core, is referred to here as the Peripheral Computational Package (PCP).

The ISCPM:

For a discussion of implementation of the ISCPM: the reader is referred to pages 4-22 and 5-47 for a discussion of the implementation of the APA and NEA subsystem input-output models.

The Peripheral Computational Package:

The function of the PCP is to perform computations other than those which may be performed directly by the ISCPM. The ISCPM can only perform point performance computations. The PCP might be designed to perform tasks such as:

1. Use the ISCPM to compute the airplane operating point which maximizes R* with or without contraints
2. Use the ISCPM and an APA subsystem climb-descent input-output model, together with navigation data, to compute trajectories which minimize trip time or M_f with or without constraints.

In performing these tasks, the PCP must provide the inputs $\{V_w, V_E, W, h, P_{AUX}, N_E, T_{atmos}, H_p\}$ to the ISCPM. These inputs are obtained by the PCP either from sensors, from direct pilot input, or as computational outputs of the PCP itself (see following subsection). The outputs of the PCP may be used in the aircraft: to drive displays (including appropriate fuel management displays); or as command inputs to automatic control systems.

The "architecture" of the PCP is task-dependent and is not addressed here.

Computations Using the ISCPM

The point performance computation which may be performed directly by the ISCPM is:

I. Computation of the set $S_{out} = \{R^*, P_m, F, \dot{m}_f\}$ for any given set $S_{in} = \{V_w, V_E, W, h, P_{AUX}, N_E, T_{atmos}, H_p\}$.

A PCP may be designed to facilitate other computations. Following is a list of the computations which may be performed by the PCP/ISCPM to maximize R* with or without constraints:

II. Computation of the set $\{P_m, F, \dot{m}_f, N_E\}$ yielding maximum R* and computation of this R*, for any given set $\{V_w, V_E, W, h, P_{AUX}, T_{atmos}, H_p\}$. This requires that

computation I be performed for a number of values of N_E: the value of N_E yielding maximum R* is determined by interpolation; and computation I is then performed using this value of N_E.

III. Computation of the set $\{P_m, F, \dot{m}_f, V_E, N_E\}$ yielding maximum R* and computation of this R*, for any given set $\{V_w, W, h, P_{AUX}, T_{atmos}, H_p\}$. This requires that computation I be performed for a number of sets $\{V_E, N_E\}$: the values of $\{V_E, N_E\}$ yielding maximum R* are determined by interpolation; and computation I is then performed using these values of $\{V_E, N_E\}$.

IV. Computation of the set $\{P_m, F, \dot{m}_f, V_E, N_E, H_p\}$ yielding maximum R* and computation of this R*, for any given set {W, h, P_{AUX}, vertical profile of atmospheric conditions (H_p, T_{atmos}, V_w)}. This requires that computation I be performed for a number of sets $\{V_E, N_E, H_p\}$: the values of $\{V_E, N_E, H_p\}$ yielding maximum R* are determined by interpolation; and computation I is then performed using these values of $\{V_E, N_E, H_p\}$.

For a given airplane and atmosphere, computation IV constitutes an unconstrained optimization of R*.

Engine Control

Formulation of the airplane-atmosphere system cruise performance model in the manner shown in Figure 6.1 facilitates optimizing

(maximizing) R* under various constraints. From the above discussion and Chapters 4 and 5, it is clear that such optimizations require that:

1. The pilot or the airborne microprocessor system be able to allocate values to $\{N_E, P_m, F\}$ independently.
2. The engine ignition timing τ be maintained at the MBT value τ_o, the spark being retarded as necessary to control detonation. MBT ignition timing τ_o has been functionally described by Equation E.33.

These requirements preclude controlling the engine with a "single power lever" in which $\{N_E, P_m, F, \tau\}$ are prescheduled. Such a "single power lever" has been advocated by Chirivella (16). The ISCPM requires that the engine be controlled with independent:

1. Throttle
2. Engine speed controller (propeller governor)
3. Ignition timing regulator (see p. 5-47)
4. Fuel-air mass ratio controller (see p. 5-47).

Items 3 and 4 probably should be feedback control systems.

Increases in R* Relative to Current Practice

Implementation of the ISCPM in any General Aviation airplane offers significant increases in R* relative to R* achieved when operating that airplane in accordance with current GA practice. The following discussion is based on Chapters 3 through 5.

1. Choice of $\{V_E, N\}$ for actual gross weight and altitude:

Consider the LASA 60 performance in Figure 4.3: S_c^* might reasonably be expected to increase from 0.71 to 0.75 in typical fuel-conscious operations, and from 0.71 to 0.81 in extreme cases. Hence the ISCPM is estimated to offer S_c^* increases of

Typical S_c^* increase = 6%

Maximum S_c^* increase = 14%.

An accurate knowledge of the gross weight then permits an estimate of the corresponding R* increases. We assume that the ISCPM has an accurate value of the gross weight; that the gross weight varies from the take-off gross weight by an average of -100 lb in 3,000 lb = -3%; and that the pilot currently uses the take-off gross weight for performance computations. The ISCPM therefore offers R* increases of

Typical R* increase = 9%

Maximum R* increase = 17%.

2. Choice of altitude to maximize effect of wind:

In currently choosing cruise altitude, the pilot is assumed to fail to take advantage of an extra five knots tailwind component available at some other altitude. The ISCPM is assumed to have the correct altitude profile of wind V_w. Assuming a typical true airspeed of 110 knots, and a minimum true airspeed of 90 knots, the ISCPM offers R* increases of

Typical R* increase = 4.5%

Maximum R* increase = 5.5%.

3. Center of gravity position, auxiliary equipment power and propeller compressibility:

   It is assumed (conservatively) that the ISCPM offers no R* advantage due to an accurate knowledge of the airplane center of gravity position $\overline{hc}$, auxiliary equipment power P_{AUX}, or propeller compressibility effects reflected in variations in the value of f_{comp} from unity.

4. Engine brake specific fuel consumption:

   From Figure 5.10, the maximum possible BSFC improvement when leaning from best power mixture with MBT ignition timing is about 17%. On the basis of Figures E.3-E.5 it is assumed that operation with given {BHP, N_E, H_p, T_{atmos}} at best power mixture and with MBT ignition timing yields about the same BSFC as achieved by operating at the same {BHP, N_E, H_p, T_{atmos}} at best power mixture with a fixed ignition timing τ typical of the values of τ used in current GA practice. GA pilots typically operate their engines at the best power mixture. Hence, the maximum possible BSFC improvement offered by the ISCPM over currently achieved BSFC is about 17%. However, due to the fact that BHP decreases significantly during leanout at wide open throttle with the result that the engine cannot always be leaned to the fuel-air mass ratio yielding

minimum BSFC, the maximum BSFC improvement offered by the ISCPM is taken to be 10%. This yields a maximum increase in R* of 11%.

It has not been possible to compare the minimum BSFC achieved with the ISCPM with the minimum BSFC achieved when current fixed ignition timing engines are leaned in accordance with the manufacturer's recommendations. It is assumed here that this comparison results in a typical decrease in BSFC of 5% when using the ISCPM: this yields a 5% increase in R*.

Hence the ISCPM is assumed to offer R* increases of

Minimum R* increase = 5%

Maximum R* increase = 11%.

The total percentage increase in R* offered by the ISCPM relative to R* achieved in current practice is $\Delta R^*\%$ which is obtained from the above as follows:

$$\text{Typical } \Delta R^*\% = [(1.09 \times 1.045 \times 1.05) - 1] \times 100\% \text{ to } [(1.09 \times 1.045 \times 1.11) - 1] \times 100\%$$

$$= 20\% \text{ to } 26\%$$

$$\text{Maximum } \Delta R^*\% = [(1.17 \times 1.055 \times 1.11) - 1] \times 100\%$$

$$= 37\%.$$

These figures are taken to apply to all GA airplanes powered by naturally aspirated SI piston engines. The savings are perceived as significant. Implementation of a cruise performance model similar to the ISCPM, in GA airplanes powered by

turbocharged SI piston engines, is expected to result in values of $\Delta R^*\%$ which substantially exceed these figures. (The turbocharged engine can operate at the fuel-air mass ratio offering minimum BSFC over a greater range of flight conditions than can the naturally aspirated engine.)

COMPARISON OF THE ISCPM WITH THE POH CRUISE PERFORMANCE MODEL

The Pilot Operating Handbook Cruise Performance Model (POHCPM) has been developed in Chapter 2. The advantages of the ISCPM over the POHCPM are:

1. The ISCPM permits cruise performance to be computed for all values of {W, h, H_p, atmospheric conditions}. The POHCPM must interpolate between cruise performance specified for certain values of {W, h, H_p, atmospheric conditions}: in some cases, cruise performance data appropriate to only one value of one or more of {W, h, atmospheric conditions} are available in the POH.
2. The ISCPM permits true optimization of R*, with the engine operating at the minimum possible BSFC at all times. The POHCPM permits optimization of R* subject to the operational recommendations {P_m, RPM, $\dot{m}_f$} of the manufacturer, and with fixed ignition timing.
3. The ISCPM commands F which is established automatically by the fuel-air mass ratio controller. This precludes the fuel-inefficient operation which results from poorly executed manual leaning. The POHCPM requires manual leaning.

Consequently, the ISCPM is considered superior to the POHCPM as a tool for maximizing R*.

The ISCPM and the POHCPM have one problem in common: both utilize calibrated cruise performance data appropriate to the airplane. However, the performance of new airplanes of the same type and model is not precisely the same; and the performance of a given airplane varies throughout its life, reflecting variations in the condition of the airframe, propeller and engine. Therefore, the cruise performance predictions of the ISCPM and the POHCPM must be expected always to vary from the actual airplane performance. The author has not addressed this issue, but it is one which will require study if calibrated cruise performance models are to be introduced into General Aviation.

INTEGRATED SUBSYSTEM CRUISE PERFORMANCE MODEL : ISCPM

STANDARD AND NON-STANDARD ATMOSPHERIC CONDITIONS

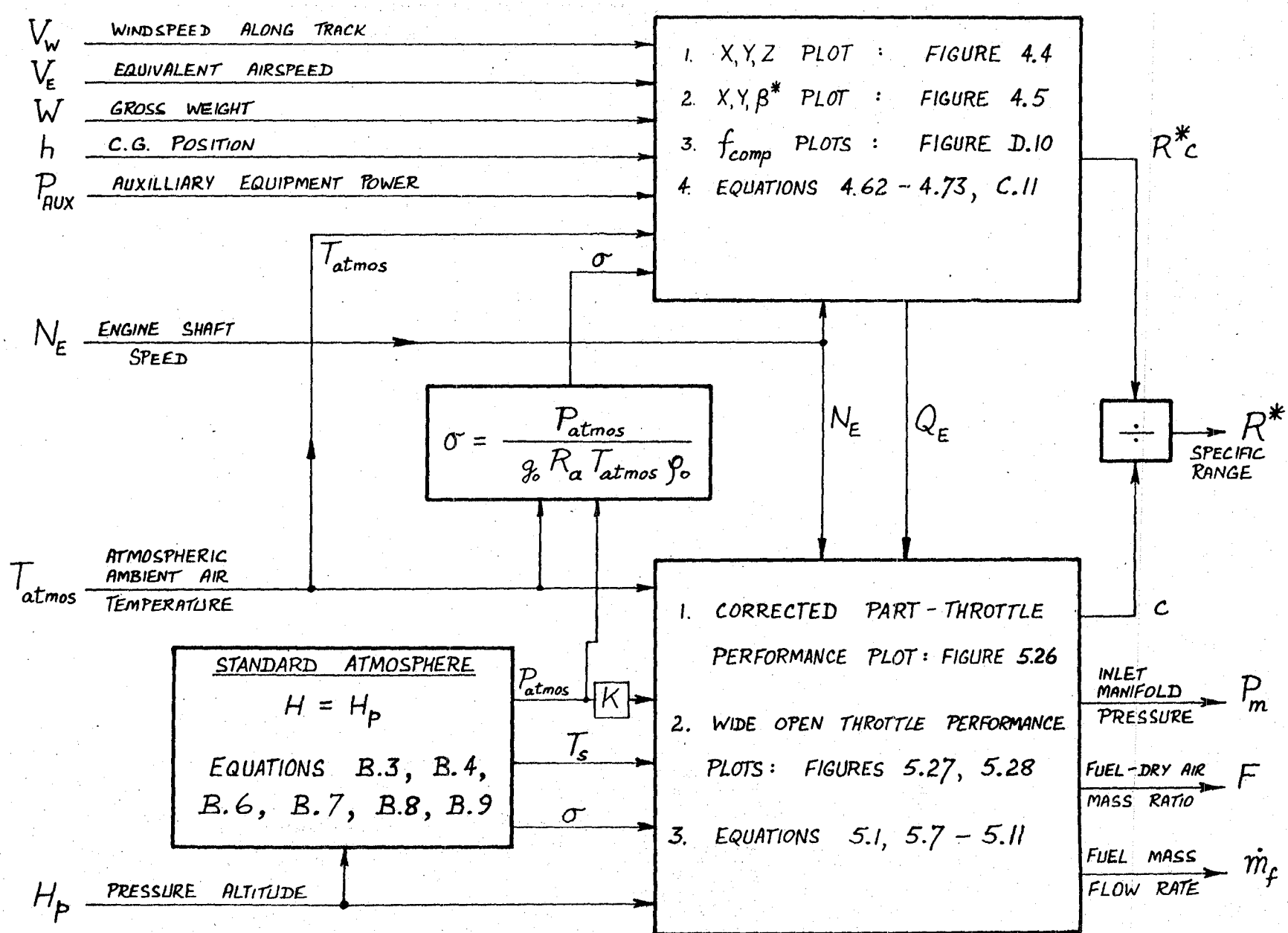

NOTE : $K = 29.92 / 2116.22$ = CONVERSION FACTOR : LB/FT^2 TO INCHES HG.

FIGURE 6.1

CHAPTER 7

CONCLUSIONS AND RECOMMENDATIONS

Table of Contents

CHAPTER 7

CONCLUSIONS AND RECOMMENDATIONS

CONCLUSIONS

1. Variations in Specific Range over the cruise envelopes of General Aviation (GA) airplanes are sufficiently large to warrant the development of a methodology for performing cruise fuel-use optimization computations.
2. Currently available Pilot Operating Handbook (POH) cruise performance data are not suitable for developing such a methodology because, in general, these data are appropriate to constrained airplane operation. POH cruise data typically apply to constrained values of
   a) Gross weight
   b) Center of gravity position
   c) Pressure altitude and atmospheric conditions
   d) Engine inlet manifold pressure
   e) Engine rotational speed
   f) Engine fuel-air mass ratio
   g) Engine ignition timing.

   A methodology for cruise fuel-use optimization requires performance data which cover the operating range of these items (a-f), and which correspond to optimized engine ignition timing.
3. The abovementioned deficiencies of POH data are overcome by the new cruise performance model developed in Chapters

3 through 6. The POH data deficiencies are overcome by this model as follows:

a) Cruise performance data are presented in terms of novel Corrected Quantities which incorporate variations in gross weight, atmospheric density ratio, and atmospheric ambient temperature and pressure in such a way as to generalize a specific airplane's performance for all values of gross weight, pressure altitude, atmospheric conditions, engine inlet manifold pressure and engine rotational speed.

b) The model incorporates a simple formulation of the effects of airplane longitudinal center of gravity position on cruise performance.

c) The model incorporates data for the useful range of engine fuel-air mass ratio.

d) The model assumes optimized engine ignition timing.

4. The new cruise performance model yields the outputs {specific range, inlet manifold pressure, fuel-air mass ratio, and fuel mass flow rate} corresponding to any given values of the inputs {geocentric true windspeed along track, equivalent airspeed, gross weight, longitudinal center of gravity position, auxiliary equipment power, engine rotational speed, pressure altitude, and atmospheric ambient temperature}, when the engine is operating at the minimum possible brake specific fuel consumption commensurate with the inputs.

This cruise performance model appears suitable for airborne microprocessor implementation.

5. The new model may be used to compute the airplane operating point which maximizes specific range, with or without constraints. A methodology for performing these computations has been presented. In combination with a climb/descent model for the airframe-propeller-atmosphere subsystem, the new model might be used to compute trajectories which minimize trip time or trip total fuel consumption, with or without constraints. Implementation of the new model shall contribute to achieving the efficiency and safety objectives discussed in Chapter 1.

6. It is concluded that, for GA airplanes powered by naturally aspirated spark-ignition piston engines: implementation of the new cruise performance model developed herein will yield

   a) Typical increases in specific range of 20% to 26%

   b) Maximum increases in specific range of 37%

   above the values of specific range currently achieved by such airplanes. Implementation of a cruise performance model similar to this model, in GA airplanes powered by turbocharged spark-ignition piston engines, is expected to yield specific range increases (above the specific range values currently achieved by such airplanes) which substantially exceed these figures.

RECOMMENDATIONS

1. The new cruise performance model developed in this work, for GA airplanes powered by naturally aspirated piston engines employing optimized ignition timing, should be subjected to experimental verification.
2. In order to implement the new cruise performance model in GA airplanes, development of the following hardware items may usefully be pursued:
   a) A microprocessor system capable of performing specific range optimization computations based on the methodology presented in this work
   b) An ignition timing regulator
   c) A fuel-air mass ratio controller.

   These hardware items may be incorporated into an airplane cruise computation/control system. This system should be evaluated in an engine test cell and in flight.
3. The cruise performance model developed herein should be extended to GA airplanes powered by turbocharged SI piston engines. Then, for this extended model, recommendation 2 should be pursued.
4. The question of the accuracy of the cruise performance model over the life of the airplane should be studied. Such a study should consider the sensitivity of the airplane performance to degradation of its subsystems (airframe, propeller, engine); and the feasibility of collecting

flight data, using standard GA airplane instrumentation, to recalibrate the model (if necessary) periodically throughout the life of the airplane.

5. The cruise performance models for naturally aspirated and turbocharged piston engine GA airplanes should be extended to include climb/descent. The resulting models should be used to study the minimization of trip total fuel consumption.

APPENDIX A

FUNDAMENTALS OF THE POINT ECONOMY FUNCTION

Table of Contents

APPENDIX A

FUNDAMENTALS OF THE POINT ECONOMY FUNCTION

INTRODUCTION

The airplane Point Economy Function, denoted by R*, is a scalar quantity with the units: ground distance travelled per unit mass of fuel burned. The units of R* used in this work are ground nautical miles per lbm.[†] R* is the integrand in the Breguet range formula (3).

In this study, only straight and level steady flight is considered.

The fundamental expression for R* is:

$$R^* = \frac{\text{Groundspeed}}{\text{Fuel mass flow rate}}$$

$$= \frac{V_G}{\dot{m}_{f_t}} \qquad \text{ground nautical miles/lbm} \tag{A.1}$$

where

V_G = Groundspeed, knots

$\dot{m}_{f_t}$ = Total fuel mass flow rate to all engines, lbm/hr

Groundspeed

The navigation wind triangle is shown in Figure A.1. The achieved groundspeed is:

$$V_G = V_T \cos \delta + V_w$$

[†] The exception is Chapter 2, where statute miles are used as the distance unit, when that unit is used in POH data.

where

V_T = Airplane true airspeed, knots

V_w = Geocentric true windspeed along track, knots

$V_w > 0$ for tailwinds

$V_w < 0$ for headwinds

δ = Angle of drift, degrees.

In General Aviation, δ is typically 10 degrees or less, in which case the cosine of δ is approximately unity. This study adopts the simplification

$$V_G = V_T + V_w \tag{A.2}$$

Fuel Mass Flow Rate and Brake Horsepower

The total fuel mass flow rate to all engines, $\dot{m}_{f_t}$ is:

$$\dot{m}_{f_t} = E\dot{m}_f = E\ P_E c \qquad \text{lbm/hr} \tag{A.3}$$

where

E = Number of engines, each driving one propeller

$\dot{m}_f$ = Fuel mass flow rate per engine, lbm/hr

P_E = Brake horsepower (BHP) per engine

c = Engine Brake Specific Fuel Consumption (BSFC), lbm/BHP.hr.

When an engine is tested by the manufacturer, the published brake horsepower and the associated BSFC apply with the following typical Primary Equipment operating:

A. Primary Equipment:

- Magnetos

- Mechanical fuel pump
- Oil pump
- Starter drive train (portion)
- Tachometer.

When the engine is installed in an airplane, some Secondary Equipment is also driven by the engine shaft. This typically includes:

B. Secondary Equipment:

- Generator or alternator
- Propeller governor pump
- Vacuum pump
- Hydraulic system pump
- Air conditioning system (if any).

The motive power delivered by the hydraulic system to drive the undercarriage and perhaps flaps, is an intermittant power which is ignored here. The other items of secondary equipment draw power continuously.

The primary and secondary equipment are collectively referred to as Standard Equipment.

In this work, P_E (Equation A.3) is the brake horsepower that each engine delivers after power to drive the Standard Equipment has been drawn from the engine shaft. This is illustrated in Figure A.2. The torque Q_E (lb ft) associated with P_E is referred to as Brake Torque: Q_E is given by Equation E.3.

Auxiliary Equipment Power

It is sometimes desirable to determine the effect on R* of adding some extra item of mechanical, hydraulic or electrical equipment to the aircraft, which draws motive power from the engine.

Such items are referred to as Auxiliary Equipment, and the Auxiliary Equipment Power consumed per engine is denoted P_{AUX} horsepower. From Figure A.2,

$$P_{AUX} = P_E - P_S \tag{A.4}$$

where

P_S = shaft horsepower (SHP) delivered to the propeller.

The shaft specific fuel consumption c' lbm/SHP.hr is defined by

$$\dot{m}_{f_t} = E\ P_S\ c' \tag{A.5}$$

Substitution of this result in Equation A.3 yields

$$P_{AUX} = P_E\left[1 - \frac{c}{c'}\right] \tag{A.5a}$$

P_S and c' may be determined experimentally with the aid of a torquemeter mounted between the engine shaft flange and the propeller hub. When c' is determined in this manner, and c defined equal to c', then P_{AUX} is defined to be zero.

EQUIVALENT QUANTITIES

The most common example of an Equivalent Quantity in airplane work is the Equivalent Airspeed (EAS) defined by

$$V_E = V_T \sqrt{\sigma} \tag{A.6}$$

where

V_E = Airplane equivalent airspeed, knots

V_T = Airplane true airspeed, knots

σ = Atmospheric air density ratio (Appendix B: standard or non-standard atmosphere).

By analogy with the EAS, four other Equivalent Quantities are used in this work. These are:

$V_w \sqrt{\sigma}$	Equivalent windspeed, knots
$P_R \sqrt{\sigma}$	Airframe equivalent power required, horsepower
$P_{AUX} \sqrt{\sigma}$	Equivalent auxiliary equipment power, horsepower
$N \sqrt{\sigma}$	Equivalent propeller shaft speed, RPM

where

P_R = Airframe power required (power-off), horsepower (Appendix C)

N = Propeller shaft speed, RPM.

EXPRESSIONS FOR THE POINT ECONOMY FUNCTION

Combining Equations A.1 - A.4 yields

$$R^* = \frac{V_T + V_w}{\dot{m}_{f_t}} \tag{A.7}$$

$$= \frac{V_T + V_w}{E\ P_E\ c} \tag{A.8}$$

$$= \frac{V_T + V_w}{E(P_S + P_{AUX})\ c} \tag{A.9}$$

In straight and level steady flight, P_S is expressed (Appendix D) as

$$P_S = \frac{P_R}{E\eta_p} \tag{D.29}$$

where η_p = propulsive efficiency.

Equation A.9 may therefore be written

$$R^* = \frac{V_T + V_w}{\left[\frac{P_R}{\eta_p} + E\ P_{AUX}\right] c} \tag{A.10}$$

In terms of the various Equivalent Quantities, the following expressions apply:

$$R^* = \frac{V_E + V_w \sqrt{\sigma}}{\dot{m}_{f_t} \sqrt{\sigma}} \tag{A.11}$$

$$= \left[1 + \frac{V_w \sqrt{\sigma}}{V_E}\right] \frac{V_E}{(P_R \sqrt{\sigma} + E\ \eta_p\ P_{AUX} \sqrt{\sigma})} \frac{\eta_p}{c} \tag{A.12}$$

The airframe power required (Appendix C) is

$$P_R = 6080.2\ D_{OFF}\ V_T/(550 \times 3600) \text{ horsepower}$$

$$= D_{OFF}\ V_T/325.65 \qquad \text{horsepower} \tag{A.13}$$

where D_{OFF} = airframe drag force (power-off), lbf (Appendix C).

For those cases where P_{AUX} is zero, we therefore have:

$$R^* = 325.65 \frac{(V_T + V_w)}{V_T} \frac{L}{D_{OFF}} \frac{1}{W} \frac{\eta_p}{c} \tag{A.14}$$

$$= 325.65 \left[1 + \frac{V_w \sqrt{\sigma}}{V_E}\right] \frac{L}{D_{OFF}} \frac{1}{W} \frac{\eta_p}{c} \tag{A.15}$$

where

W = airplane gross weight, lbf

L = airplane lift force = W, lbf.

THE NAVIGATION WIND-TRIANGLE

V_T AIRPLANE TRUE AIRSPEED

V_{WIND} TRUE WINDSPEED

V_{WX} TRUE WINDSPEED COMPONENT ACROSS TRACK

V_W TRUE WINDSPEED COMPONENT ALONG TRACK.
FOR A TAILWIND COMPONENT V_W IS POSITIVE
FOR A HEADWIND COMPONENT V_W IS NEGATIVE

δ DRIFT ANGLE

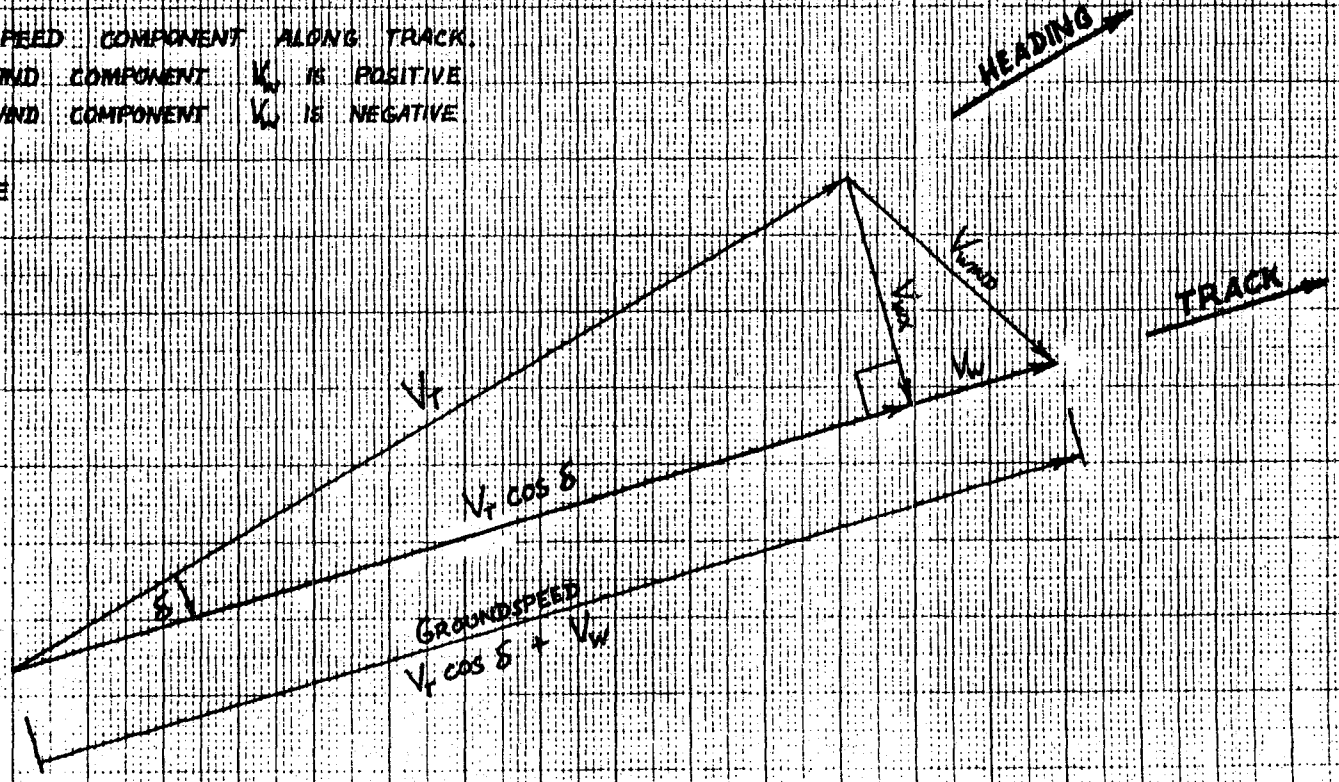

FIGURE A.1

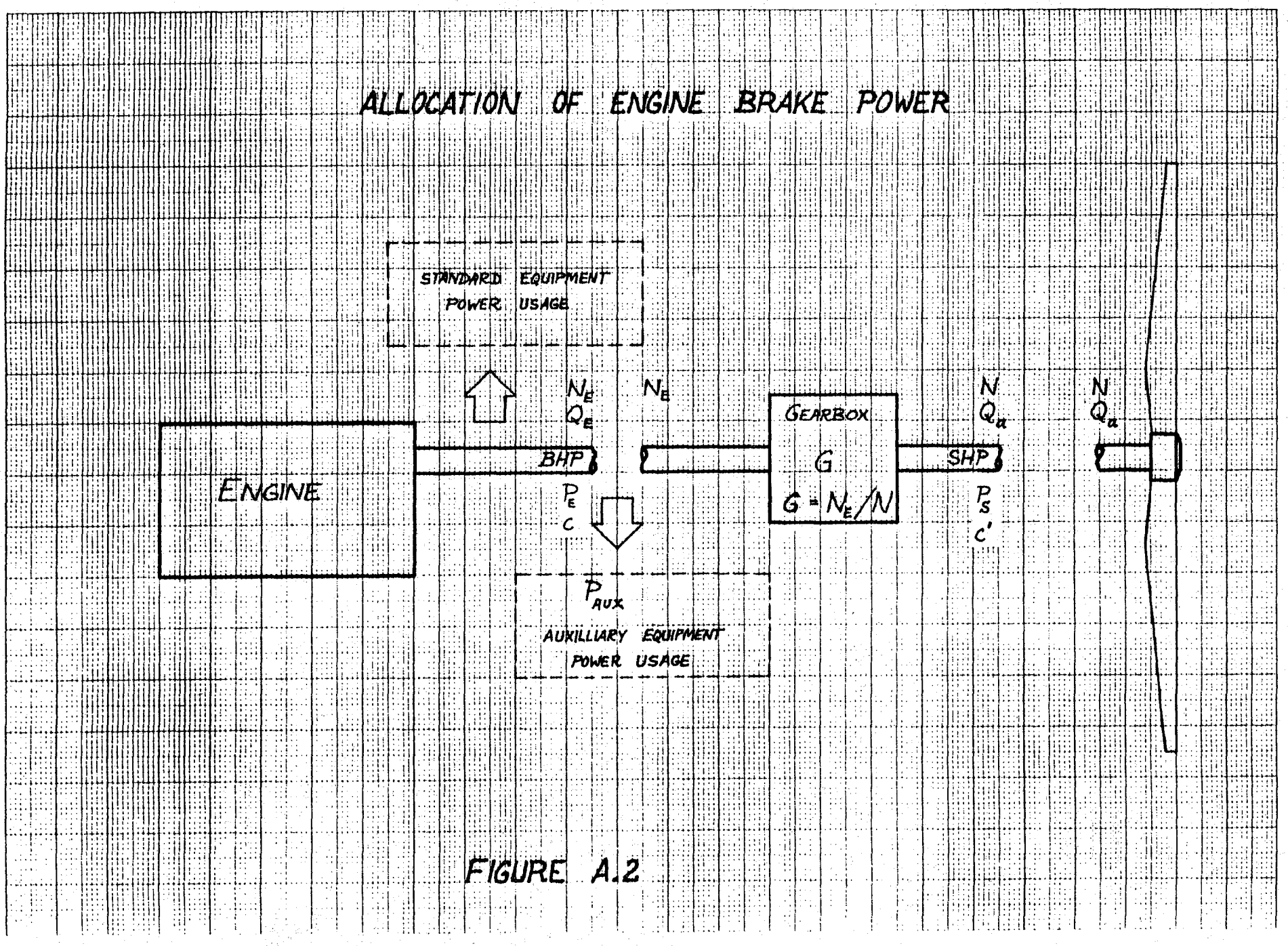
ALLOCATION OF ENGINE BRAKE POWER
STANDARD EQUIPMENT
POWER USAGE
N_E
Q_E
N_E
GEARBOX
G
$G = N_E/N$
N
Q_a
N
Q_a
ENGINE
BHP
SHP
P_E
C
P_S
C'
P_{AUX}
AUXILLIARY EQUIPMENT
POWER USAGE

FIGURE A.2

APPENDIX B

THE STANDARD AND NON-STANDARD ATMOSPHERE MODELS

Table of Contents

APPENDIX B

THE STANDARD AND NON-STANDARD ATMOSPHERE MODELS

THE STANDARD ATMOSPHERE MODEL

The standard atmosphere model used in this work yields the characteristics of the U.S. Standard Atmosphere, 1962 in the troposphere (18). Zero humidity is assumed throughout the Standard Atmosphere in the present work.

Nomenclature

The notation used for this atmospheric model is as follows:

P_0	Sea level ambient absolute pressure	lbf/ft^2
T_0	Sea level ambient temperature	degrees Kelvin
ρ_0	Sea level density	$slugs/ft^3$
g_0	Sea level gravitational acceleration	ft/sec^2
R_a	Gas constant for dry air	ft.lbf/lbm. degree Kelvin
H	Geometric altitude above sea level (= density altitude)	ft
P_{atmos}	Ambient absolute pressure at altitude H	lbf/ft^2
$T_{atmos} \equiv T_s$	Ambient temperature at altitude H	degrees Kelvin
ρ	Density at altitude H	$slugs/ft^3$
δ	Pressure ratio P_{atmos}/P_0 at altitude H	
θ	Temperature ratio T_s/T_0 at altitude H	
σ	Density ratio ρ/ρ_0 at altitude H	

Sea Level Conditions

$P_0 = 2116.22$ lbf/ft^2

$T_0 = 288.15$ degrees Kelvin

$$\rho_0 = 0.076474/g_0 \qquad \text{slugs/ft}^3$$

$$g_0 = 32.1741 \qquad \text{ft/sec}^2$$

The perfect gas law states

$$P_{atmos} = \rho g_0 R_a T_s \tag{B.1}$$

Application of this law to the conditions at sea level yields

$$R_a = 96.03474 \quad \text{ft.lbf/lbm.degree Kelvin} \tag{B.2}$$

Altitude Conditions

The temperature lapse rate is virtually linear with geometric altitude, such that

$$\theta = 1 - L\,H \tag{B.3}$$

The value of L yielding the correct value of θ (18) at H = 10,000 ft is

$$L = 6.87239 \times 10^{-6} \tag{B.4}$$

The value of L in Equation B.4 is used here, in conjunction with Equation B.3, to compute θ at altitude H.

The pressure ratio δ is given (7) by

$$\delta = \theta^{1/LT_0R_a} \tag{B.5}$$

Substituting Equations B.2 and B.4 in Equation B.5 yields

$$\delta = \theta^{5.2583}$$

However, using the value of θ (computed by Equations B.3 and B.4) at H = 10,000 ft, in conjunction with the value of δ (18) at H = 10,000 ft, yields:

$$\delta = \theta^{5.25581} \tag{B.6}$$

Equation B.6 is used here, in conjunction with Equations B.3 and B.4, to compute δ at altitude H.

Having computed θ and δ at altitude H,

$$T_s = T_0\theta \tag{B.7}$$

$$P_{atmos} = P_0\delta \tag{B.8}$$

The density ρ at altitude H is then computed using Equation B.1.

The density ratio σ at altitude H is computed from

$$\sigma = \frac{\rho}{\rho_0} = \frac{\delta}{\theta} \tag{B.9}$$

THE NON-STANDARD ATMOSPHERE MODEL

Zero humidity is assumed throughout every non-standard atmosphere in this work.

Nomenclature

H_p	Pressure altitude	ft
P_{atmos}	Ambient absolute pressure at pressure altitude H_p	lbf/ft^2
T_{atmos}	Ambient temperature at pressure altitude H_p	degrees Kelvin
ρ	Density at pressure altitude H_p	$slugs/ft^3$
σ	Density ratio ρ/ρ_0 at pressure altitude H_p, where ρ_0 is the sea level density ($slugs/ft^3$) in the Standard Atmosphere.	

The pressure altitude H_p (ft) at any point $\{P_{atmos}, T_{atmos}\}$, in any non-standard atmosphere, is defined to be equal to the altitude H (ft) which corresponds to P_{atmos} in the Standard Atmosphere. An atmosphere is Non-Standard when T_{atmos} at H_p is not equal to the ambient temperature T_s in the Standard Atmosphere at $H = H_p$.

Density and Density Ratio

The density ρ at $\{H_p, P_{atmos}, T_{atmos}\}$ is computed using the perfect gas law:

$$\rho = \frac{P_{atmos}}{g_0 R_a T_{atmos}} \qquad \text{slugs/ft}^3 \tag{B.10}$$

The density ratio σ at $\{H_p, P_{atmos}, T_{atmos}\}$ is then

$$\sigma = \frac{\rho}{\rho_0} = \frac{P_{atmos}}{g_0 R_a T_{atmos} \rho_0} \tag{B.11}$$

where ρ_0 is the sea level density (slugs/ft^3) in the Standard Atmosphere.

APPENDIX C

THE AIRFRAME PERFORMANCE MODEL

Table of Contents

APPENDIX C

THE AIRFRAME PERFORMANCE MODEL

INTRODUCTION

The airframe contributes to the value of the Point Economy Function R* in that it determines the quantity of thrust work required to propel the airplane per unit of ground distance travelled. Only straight and level steady flight is here considered. The items of modelling interest are the airframe aerodynamic drag and the airframe power required.

In this appendix, the well known equations for airframe drag and power required are presented. In addition, an expression for the airframe drag coefficient, in both power-off and power-on flight, is developed. The latter expression quantifies the influence of airframe geometry, aerodynamic characteristics, center of gravity position and power-effects on the airframe drag coefficient.

AIRFRAME DRAG AND POWER REQUIRED

The power-off airframe drag is given by

$$D_{OFF} = C_D \frac{1}{2} \rho V^2 S \qquad (C.1)$$

$$= C_D \frac{1}{2} \rho_0 V_e^2 S \qquad (C.2)$$

where

D_{OFF} = power-off airframe drag, lbf

C_D = power-off drag coefficient

ρ = atmospheric air density, slugs/ft^3

ρ_0 = standard sea level value of ρ, slugs/ft^3 (Appendix B)

V = true airspeed, ft/sec

V_e = equivalent airspeed = $V\sqrt{\sigma}$, ft/sec

σ = atmospheric density ratio = ρ/ρ_0

S = airframe reference area = wing area, ft^2

The airframe power required (power-off) P_R is given by

$$\left.\begin{aligned} P_R &= D_{OFF}\ V/550 \\ &= D_{OFF}\ V_e/550\ \sqrt{\sigma} \end{aligned}\right\} \text{ horsepower} \qquad (C.3)$$

The airframe equivalent power required, as defined in Appendix A, is therefore

$$\left.\begin{aligned} P_R\ \sqrt{\sigma} &= D_{OFF}\ V_e/550 \\ &= C_D\ \tfrac{1}{2}\rho_0\ V_e^3\ S/550 \end{aligned}\right\} \text{ horsepower} \qquad (C.4)$$

Equations C.1 - C.4 describe the power-off flight condition. The equations for power-on drag D_{ON}, power required $P_{R_{ON}}$ and equivalent power required $P_{R_{ON}}\ \sqrt{\sigma}$ are identical to Equations C.1 - C.4 except that the power-on drag coefficient $C_{D_{ON}}$ replaces C_D. That is,

$$D_{ON} = C_{D_{ON}}\ \tfrac{1}{2}\ \rho\ V^2\ S \qquad (C.5)$$

$$= C_{D_{ON}}\ \tfrac{1}{2}\ \rho_0\ V_e^2\ S \qquad (C.6)$$

$$\left.\begin{aligned} P_{R_{ON}} &= D_{ON}\ V/550 \\ &= D_{ON}\ V_e/550\ \sqrt{\sigma} \end{aligned}\right\} \text{ horsepower} \qquad (C.7)$$

$$\left.\begin{aligned} P_{R_{ON}} \sqrt{\sigma} &= D_{ON} V_e/550 \\ &= C_{D_{ON}} \frac{1}{2} \rho_0 V_e^3 S/550 \end{aligned}\right\} \text{ horsepower} \qquad (C.8)$$

The drag coefficients C_D and $C_{D_{ON}}$ may, in general, be expressed as cubic polynomials in terms of the lift coefficient C_L:

$$C_D = C_{D_0} + k_1 C_L + k_2 C_L^2 + k_3 C_L^3 \qquad (C.9)$$

$$C_{D_{ON}} = C_{D_0}' + k_1' C_L + k_2' C_L^2 + k_3' C_L^3 \qquad (C.10)$$

The lift coefficient C_L is defined by,

$$\left.\begin{aligned} L = W &= C_L \frac{1}{2} \rho V^2 S \\ &= C_L \frac{1}{2} \rho_0 V_e^2 S \end{aligned}\right\} \qquad (C.11)$$

where

L = airplane lift force, lbf

W = airplane gross weight, lbf.

The quantities C_{D_0}, C_{D_0}', k_i, k_i' (i = 1,2,3) are discussed below.

Plots of C_D versus C_L and $C_{D_{ON}}$ versus C_L, as described by Equations C.9 and C.10, are referred to as the airframe power-off drag polar and the airframe power-on drag polar respectively.

THE AIRFRAME DRAG POLAR

The following discussion develops an expression for the airframe

power-off drag polar in terms of the airframe geometry, aerodynamic characteristics and center of gravity (c.g.) position. By suitable adjustment of the values of certain parameters in that expression, the airframe power-on drag polar is obtained.

A specified airframe geometry is assumed, with the exception of the tailplane geometry. In particular, this discussion pertains to a specified geometry of the undercarriage, high lift devices, cowl flaps and other variable geometry devices. The airplane is assumed to be trimmed by varying the tailplane geometry.

The airplane is assumed to be laterally symmetric about its longitudinal centerline, with respect to geometry and mass distribution. Therefore only longitudinal variations in c.g. position are considered. The airplane geometry is shown in Figure C.1.

Power-Off Flight

The following definitions apply (36):

b_w = wing span, ft

b_t = tailplane span $\leq b_w$, ft

c = local wing chord, ft

$\bar{c}$ = mean aerodynamic chord of the wing, ft. $\bar{c}$ is defined by

$$\bar{c} = \frac{2}{S}\int_0^{b_w/2} c^2\, dy \qquad \text{feet}$$

C_L = lift coefficient of complete airplane

C_{L_w} = lift coefficient of airplane less tailplane

C_{L_t} = lift coefficient of tailplane

C_m = pitching moment coefficient of complete airplane, about the airplane c.g.

C_{m_o} = pitching moment coefficient of the airplane less tailplane, about the aerodynamic center C of the airplane less tailplane

$h\bar{c}$ = distance of the airplane center of gravity aft of the leading edge of the mean aerodynamic chord of the wing, ft

$h_o\bar{c}$ = distance of the aerodynamic center C of the airplane less tailplane aft of the leading edge of the mean aerodynamic chord of the wing, ft

ℓ = tail arm = distance of the tailplane aerodynamic center aft of the aerodynamic center C of the airplane less tailplane, ft

L = lift of complete airplane = gross weight W, lbf

L_w = lift of airplane less tailplane, lbf

L_t = lift of tailplane, lbf

M = pitching moment of complete airplane about the airplane c.g., ft lbf

M_c = pitching moment of aerodynamic forces for the airplane less tailplane about the aerodynamic center C of the airplane less tailplane, ft lbf

S = wing area, ft^2

S_t = tailplane area, ft^2

$\bar{V}$ = tail volume ratio = $S_t\ell/S\bar{c}$

η_t = tailplane efficiency = $q_t/q = \frac{1}{2}\rho V_t^2/\frac{1}{2}\rho V^2$ = (dynamic pressure at tailplane)/(freestream dynamic pressure).

We have (36, 37):

$$L = C_L \frac{1}{2}\rho V^2 S$$

$$L_w = C_{L_w} \frac{1}{2}\rho V^2 S$$

$$L_t = C_{L_t} \frac{1}{2}\rho V^2 \eta_t S_t$$

$$M = C_m \frac{1}{2}\rho V^2 S \bar{c}$$

$$M_c = C_{m_o} \frac{1}{2}\rho V^2 S \bar{c}$$

$$C_m = C_{m_o} + C_{L_w}(h-h_o) - C_{L_t}\frac{S_t}{S}\left[\frac{\ell}{\bar{c}} - (h-h_o)\right]\eta_t \qquad (C.12)$$

Also,

$$L = L_w + L_t$$

$$C_L = C_{L_w} + C_{L_t}\frac{S_t}{S}\eta_t \qquad (C.13)$$

Therefore from Equations C.12 and C.13,

$$C_m = C_{m_o} + C_L(h-h_o) - C_{L_t}\bar{V}\eta_t \qquad (C.14)$$

In trimmed straight and level steady flight $C_m = 0$, so that from Equation C.14,

$$C_{L_t} = [C_{m_o} + C_L(h-h_o)]/\bar{V}\eta_t \qquad (C.15)$$

Also from Equation C.13,

$$C_{L_w} = C_L - C_{L_t} \frac{S_t}{S} \eta_t$$

$$= C_L \left[1 - \frac{\bar{c}}{\ell} (h-h_o)\right] - \frac{\bar{c}}{\ell} C_{m_o} \qquad (C.16)$$

Consider the power-off airplane drag. The following definitions apply:

A_w = aspect ratio of wing

A_t = aspect ratio of tailplane

C_D = airplane power-off drag coefficient

$C_{D_{pw}}$ = power-off parasite drag coefficient of airplane less tailplane

$C_{D_{pmw}}$ = lift-independent part of $C_{D_{pw}}$

$C_{D_{pt}}$ = power-off parasite drag coefficient of tailplane

$C_{D_{pmt}}$ = lift-independent part of $C_{D_{pt}}$

C_{D_i} = airplane power-off induced drag coefficient

D_{OFF} = airplane power-off drag, lbf

D_{pw} = power-off parasite drag of airplane less tailplane, lbf

D_{pt} = power-off parasite drag of tailplane, including fuselage/tailplane interference drag, lbf

D_i = airplane power-off induced drag, lbf.

We have,

$$D_{OFF} = C_D \frac{1}{2} \rho V^2 S$$

$$D_{pw} = C_{D_{pw}} \frac{1}{2} \rho V^2 S$$

$$D_{pt} = C_{D_{pt}} \frac{1}{2} \rho V^2 S_t \eta_t$$

$$D_i = C_{D_i} \frac{1}{2} \rho V^2 S$$

$$D_{OFF} = D_{pw} + D_{pt} + D_i$$

$$C_D = C_{D_{pw}} + C_{D_{pt}} \frac{S_t}{S} \eta_t + C_{D_i} \tag{C.17}$$

The parasite drag coefficients $C_{D_{pw}}$ and $C_{D_{pt}}$ may be written (9, 38):

$$C_{D_{pw}} = C_{D_{pmw}} + K_w (C_{L_w} - \xi_w)^2 \tag{C.18}$$

$$C_{D_{pt}} = C_{D_{pmt}} + K_t (C_{L_t} - \xi_t)^2 \tag{C.19}$$

where

$C_{D_{pmw}}$, $C_{D_{pmt}}$, K_w, K_t, ξ_w and ξ_t

are constants. The quantities ξ_w and ξ_t are included to account for non-symmetric wing and tailplane sections respectively. In order to trim the airplane in level flight, the lift of the tailplane is established at the required value (Equation C.15) by deflecting the elevator and/or trim tab, or by changing the incidence of the (all-moving) tailplane. For the small tailplane geometry changes so involved, the quantities $C_{D_{pmt}}$ and K_t are assumed to retain constant values.

Laitone (20) demonstrates the use of the equation for the induced drag of a biplane, as it applies to computations of the induced drag of a monoplane wing and tailplane. In the case of a monoplane with an elliptically loaded wing and tailplane in potential flow, the biplane induced drag equation (9, 20) yields

$$D_i = \frac{1}{\frac{1}{2}\rho V^2 \pi}\left[\frac{L_w^2}{b_w^2} + \frac{2\sigma_{wt} L_w L_t}{b_w b_t} + \frac{L_t^2}{b_t^2}\right] \qquad (C.20)$$

where

σ_{wt} = a coefficient dependent upon the span ratio b_t/b_w and the gap g (the vertical distance between the two wings), but independent of the stagger distance (the horizontal distance between the two wings) with potential flow.

By invoking Munk's equivalence theorem for stagger (9), Laitone (20) shows that the mutual interference between the wing and tailplane (the middle term of Equation C.20) can be computed with the tailplane at infinity downstream of the wing ($\ell \to \infty$), with a gap g equal to that of the actual airplane.† In addition, Laitone gives the following expression for σ_{wt}:

$$\sigma_{wt}\left[\frac{b_w}{b_t}\right] \simeq 1 - \frac{2g}{b_w}\left[1 + \left(\frac{2g}{b_w}\right)^2\right]^{-1/2} \qquad (C.21)$$

†This procedure is adopted here. The mutual interference is computed for the tailplane placed at infinity downstream of its actual position on the airplane, with the wing wake assumed to be a flat vortex sheet extending to infinity downstream of the aerodynamic center C of the airplane less tailplane. The mutual interference is then adjusted for rollup of the flat vortex sheet into a horseshoe vortex (9).

This equation yields the value of σ_{wt} appropriate to a tailplane operating in conjunction with an elliptically loaded wing. The wing wake is assumed to extend back to infinity, from the elliptically loaded wing, as a flat vortex sheet. Laitone (20) states that the value of σ_{wt} given by Equation C.21 is accurate within 7% for $b_t/b_w = 0.6$, within 2% for $b_t/b_w = 0.3$, and within 1% for $b_t/b_w \leq 0.25$. Referring to Figure C.2, we may write

$$g = \left| [g_o + \ell \tan (\alpha_w - i_w)] \cos (\alpha_w - i_w) \right| \qquad (C.22)$$

where α_w = angle of attack of the zero-lift line of the airplane less tailplane to the freestream velocity vector, radians

g_o = vertical distance of tailplane below wing when $\alpha_w = i_w$, ft.

Note that g is always positive; g_o is positive (negative) when the tailplane lies below (above) the wing. The angle of attack α of the zero-lift line of an untwisted wing to the freestream velocity vector is given by (9):

$$\alpha = C_{L_w} \left[\frac{1}{a_{o_w}} + \frac{(1 + \tau_w)}{\pi A_w} \right] \quad \text{radians} \qquad (C.23)$$

where

a_{o_w} = wing section lift curve slope, radian^{-1}

τ_w = correction factor for wing spanwise loading. Figure C.3 (9) shows typical values of $\tau_w = \tau$ for untwisted wings of rectangular planform.

The angle α_w in Equation C.22 is here computed from Equation C.23 with $\alpha_w = \alpha$.

The biplane Equation C.20 applies to two wings operating in an airstream with a dynamic pressure $q = \frac{1}{2}\rho V^2$. When the wing operates in an airstream with dynamic pressure q, and the tailplane operates in one with dynamic pressure $\eta_t q$, then Equation C.20 becomes

$$D_i = \frac{1}{\frac{1}{2}\rho V^2 \pi}\left[\frac{L_w^2}{b_w^2} + \frac{2\sigma_{wt} L_w L_t}{b_w b_t \sqrt{\eta_t}} + \frac{L_t^2}{b_t^2 \eta_t}\right] \qquad (C.24)$$

In coefficient form, Equation C.24 is,

$$C_{D_i} = \frac{C_{L_w}^2}{\pi A_w} + \frac{\sigma_{wt} b_w}{b_t}\frac{2C_{L_w} C_{L_t}}{\pi A_w}\frac{S_t}{S}\sqrt{\eta_t} + \frac{C_{L_t}^2}{\pi A_t}\frac{S_t}{S}\eta_t \qquad (C.25)$$

When the wing and tailplane are not elliptically loaded, and allowing the wing wake to roll up into a horseshoe vortex (9), Equation C.25 becomes:

$$C_{D_i} = \frac{C_{L_w}^2 (1+\delta_w)}{\pi A_w} + \frac{\sigma_{wt} b_w}{b_t}\frac{2C_{L_w} C_{L_t}}{\pi A_w e_t}\frac{S_t}{S}\sqrt{\eta_t} + \frac{C_{L_t}^2 (1+\delta_t)}{\pi A_t}\frac{S_t}{S}\eta_t \qquad (C.26)$$

where

δ_w, δ_t = induced drag correction factors for spanwise loading of the wing and tailplane respectively. Figure C.3 (9) shows typical values of $\delta_w = \delta$ or $\delta_t = \delta$ for untwisted wings of rectangular planform.

Also

$$e_t = \varepsilon'/\varepsilon = 2/(\varepsilon/\varepsilon_o) \tag{C.27}$$

where

ε = wing wake downwash angle at downstream infinity (measured on the wing longitudinal centerline), due to a wing with lift coefficient C_{L_w} and any load distribution, and having a horseshoe vortex wake, radians

$\varepsilon' = 2\varepsilon_o$ = wing wake downwash angle at downstream infinity (measured on the wing longitudinal centerline), due to an elliptically loaded wing with lift coefficient C_{L_w} and a flat vortex-sheet wake, radians

$\varepsilon_o = C_{L_w}/\pi A_w$ = downwash angle at the center of pressure of an elliptically loaded wing with lift coefficient C_{L_w}, radians.

Values of $\varepsilon/\varepsilon_o$, for an elliptically loaded wing and for a rectangular wing with various aspect ratios, are given by Glauert (9, pg. 168).

The quantity σ_{wt} in Equations C.21 and C.26 is assumed here to be invariant with the lift distribution of the wing, and to be the same for a horseshoe vortex wake as it is for a flat vortex sheet wake.

In the foregoing discussion, the wing downwash has received very simple treatment. However the calculation of wing downwash is, in general, very complex; this matter is discussed in detail by Spreiter and Sacks (39).

Substitution of Equations C.18, C.19 and C.26 into Equation C.17 yields:

$$\left.\begin{aligned} C_D = {} & C_{D_{pm}} + K_w \xi_w^2 + K_t \xi_t^2 \frac{S_t}{S} \eta_t \\ & - C_{L_w} (2K_w \xi_w) - C_{L_t} (2K_t \xi_t) \frac{S_t}{S} \eta_t \\ & + \frac{\sigma_{wt} b_w}{b_t} \frac{2 C_{L_w} C_{L_t}}{\pi A_w e_t} \frac{S_t}{S} \sqrt{\eta_t} \\ & + C_{L_w}^2 \left[K_w + \frac{1+\delta_w}{\pi A_w} \right] + C_{L_t}^2 \left[K_t + \frac{1+\delta_t}{\pi A_t} \right] \frac{S_t}{S} \eta_t \end{aligned}\right\} \qquad (C.28)$$

where

$$C_{D_{pm}} = C_{D_{pmw}} + C_{D_{pmt}} \frac{S_t}{S} \eta_t$$

Substituting Equations C.15 and C.16 into Equation C.28 then yields:

$$\left.\begin{aligned} C_D = {} & C_{D_{pm}} + \left(\frac{\bar{c}}{\ell} C_{m_o}\right)^2 \left[K_w + \frac{1+\delta_w}{\pi A_w} \right] + C_{m_o}^2 \left[K_t + \frac{1+\delta_t}{\pi A_t} \right] \frac{S_t}{S \bar{V}^2} \eta_t \\ & + 2 \frac{\bar{c}}{\ell} C_{m_o} \xi_w K_w + \xi_w^2 K_w - 2 C_{m_o} \xi_t K_t \frac{\bar{c}}{\ell} \\ & + \xi_t^2 K_t \frac{S_t}{S} \eta_t - \frac{\sigma_{wt} b_w}{b_t} \frac{2 C_{m_o}^2}{\pi A_w e_t \sqrt{\eta_t}} \left(\frac{\bar{c}}{\ell}\right)^2 \end{aligned}\right\}$$

(this equation is continued on the next page)

$$+ C_L \left\{ 2C_{m_o}(h-h_o)\left[K_t + \frac{1+\delta_t}{\pi A_t}\right]\frac{S_t}{S\bar{V}^2\eta_t} \right.$$

$$- 2C_{m_o}\frac{\bar{c}}{\ell}\left[1 - \frac{\bar{c}}{\ell}(h-h_o)\right]\left[K_w + \frac{1+\delta_w}{\pi A_w}\right]$$

$$- 2\left[1 - \frac{\bar{c}}{\ell}(h-h_o)\right]\xi_w K_w - 2(h-h_o)\,\xi_t K_t \frac{\bar{c}}{\ell}$$

$$\left. + \frac{\sigma_{wt} b_w}{b_t}\frac{2(\bar{c}/\ell)}{\pi A_w e_t \sqrt{\eta_t}}\left[C_{m_o} - 2\frac{\bar{c}}{\ell}C_{m_o}(h-h_o)\right] \right\}$$

$$+ C_L^2 \left\{ \left[1 - \frac{\bar{c}}{\ell}(h-h_o)\right]^2\left[K_w + \frac{1+\delta_w}{\pi A_w}\right] \right.$$

$$+ (h-h_o)^2\left[K_t + \frac{1+\delta_t}{\pi A_t}\right]\frac{S_t}{S\bar{V}^2\eta_t}$$

$$\left. + \frac{\sigma_{wt} b_w}{b_t}\frac{2(\bar{c}/\ell)}{\pi A_w e_t \sqrt{\eta_t}}\left[1 - \frac{\bar{c}}{\ell}(h-h_o)\right](h-h_o) \right\} \qquad \text{(C.29)}$$

Equation C.29 may be expressed as

$$C_D = \kappa_0 + \kappa_1 C_L + \kappa_2 C_L^2 \qquad \text{(C.30)}$$

The coefficients κ_0, κ_1 and κ_2 are dependent upon C_L inasmuch as $\sigma_{wt} b_w / b_t$ is dependent on C_L (see Equations C.21, C.22, C.23 and C.16)†.

†Also, $C_{D_{pw}}$ and $C_{D_{pt}}$ (Equations C.18 and C.19) might be written more accurately as cubic polynomials in C_{L_w} and C_{L_t} respectively.

Consequently the curve given by Equation C.30 may be represented by a least squares cubic fit of the form

$$C_D = C_{D_0} + k_1 C_L + k_2 C_L^2 + k_3 C_L^3 \qquad (C.9)$$

as previously written. Equation C.9 describes the airframe power-off drag polar.

Power-On Flight

In powered flight, the following parameters may have values different from those pertaining to power-off flight at the same C_L[†]:

1. $C_{D_{pm}}$
2. C_{m_o}
3. a_{o_w} with corresponding values of δ_w, τ_w and e_t
4. η_t
5. i_w

Substitution of these power-on values in Equation C.29 gives the power-on drag polar,

$$C_{D_{ON}} = \kappa_0' + \kappa_1' C_L + \kappa_2' C_L^2 \qquad (C.31)$$

A least squares cubic fit of Equation C.31 then yields the coefficients of Equation C.10. The relationship between C_D and $C_{D_{ON}}$ may be determined from a comparison of Equations C.30 and C.31 or Equations C.9 and C.10.

[†]We assume that the thrust vector passes horizontally through the airplane c.g. so that the foregoing lift and pitching moment equations are unaffected by the application of power. (This is not always the case.)

Of particular interest in the present study is the influence of c.g. position on the power-on drag polar. As shown by the foregoing analysis, variations in longitudinal c.g. position necessitate changes in the tailplane and wing lift forces (Equations C.15 and C.16) so as to trim the airplane. These lift variations result in variations in both lift-dependent parasite drag and induced drag (Equations C.18, C.19 and C.26). These drag variations in turn cause changes in the coefficients κ_0', κ_1' and κ_2' in Equation C.31. Such changes in drag, due to longitudinal movement of the c.g., are referred to as "trim drag." Associated changes in the airplane power-on drag polar result in changes in the airplane power-on lift/drag ratio, which affects the value of R*.

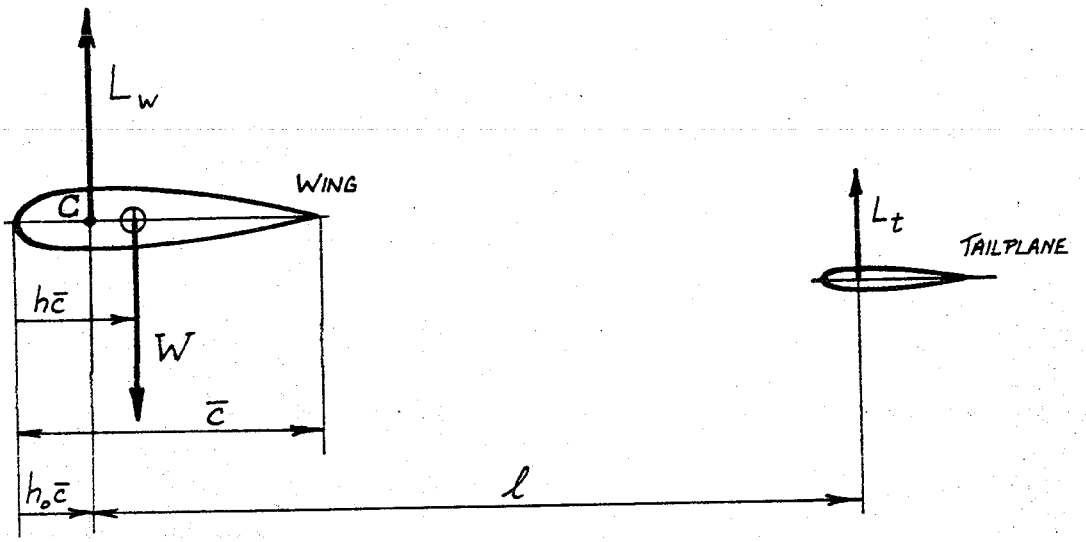

(REFERENCE 36, p. 50)

FIGURE C.1 AIRPLANE GEOMETRY

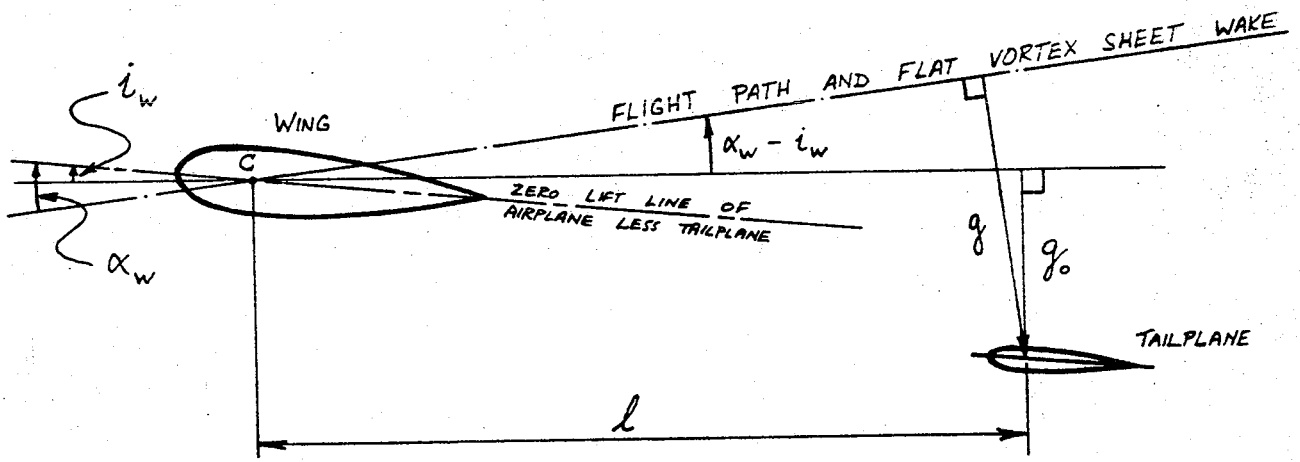

FIGURE C.2 WING - TAILPLANE GAP

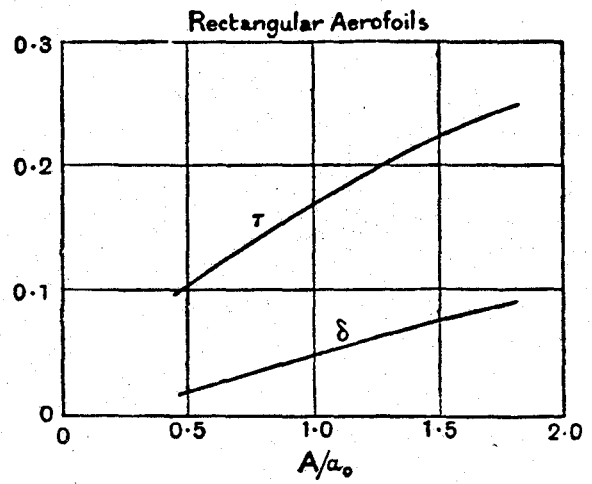

Fig. 85.

A = ASPECT RATIO OF WING

a_o = WING SECTION LIFT CURVE SLOPE (2-DIMENSIONAL FLOW), PER RADIAN.

τ = CORRECTION FACTOR FOR WING SPANWISE LOADING EFFECTS ON WING ANGLE OF ATTACK.

δ = CORRECTION FACTOR FOR WING SPANWISE LOADING EFFECTS ON WING INDUCED DRAG COEFFICIENT.

(REFERENCE 9, p. 147)

FIGURE C.3 AERODYNAMIC CHARACTERISTICS OF UNTWISTED WINGS WITH RECTANGULAR PLANFORM.

APPENDIX D

THE PROPELLER PERFORMANCE MODEL

Table of Contents

APPENDIX D

THE PROPELLER PERFORMANCE MODEL

INTRODUCTION

This Appendix presents a method for modelling the performance of a propeller operating in the presence of an airframe (installed propeller), and the propulsive efficiency of the propeller-airframe combination; in terms of the performance of the propeller operating in isolation from any body (free propeller). Compressible flow effects on performance are modelled as a correction factor which adjusts efficiency and torque computed under the assumption of incompressible flow.

Specification of the performance of a propeller-body combination in terms of the free propeller performance facilitates computation of the former performance when only free propeller performance data are available.

The discussion is appropriate to fixed pitch propellers (those made in one piece, and ground-adjustable propellers) and to variable pitch propellers (controllable pitch and constant speed propellers). These various propeller types are described by Bent and McKinley (24).

The geometry and performance of the McCauley C33/90M-4 constant speed free propeller are presented and discussed at the conclusion of this Appendix.

THE FREE PROPELLER

Performance Characteristics

Dimensional analysis shows that the thrust developed by any free propeller, having a specific blade shape and number of blades, may be expressed by the functional relation

$$T = (\rho n^2 d^4)\ f_T[J,\ \beta,\ R_N,\ M] \tag{D.1}$$

Similarly, the shaft torque required to turn the propeller may be expressed by the functional relation

$$Q = (\rho n^2 d^5)\ f_Q[J,\ \beta,\ R_N,\ M] \tag{D.2}$$

where T = Thrust of the free propeller, lb

Q = Shaft torque of the free propeller, lb ft

ρ = Density of the air, slugs/ft^3

n = Propeller rotation rate, revolutions/second

d = Propeller diameter, ft

J = Advance ratio = V/nd

β = Representative blade angle, degrees

R_N = Reynolds number = $V_N \ell_N/\nu$

M = Representative Mach number

V = Free stream airspeed parallel to propeller shaft axis, ft/sec

ν = Kinematic viscosity of air, ft^2/sec.

The performance of all geometrically similar propellers is characterized by the same function f_T and the same function f_Q.

In this work unless otherwise stated, the blade angle β is the angle between the plane of rotation of the propeller and the

flat face of the blade, at a radius of 0.75R (where R = d/2 is the propeller tip radius, ft).

The definition of the Reynolds number requires the use of a representative speed v_N (ft/sec) and length ℓ_N (ft). Since the airflow over the elements of a propeller blade varies greatly from the hub to the tip, a number of choices for these quantities is available. Glauert (1) defines

$v_N = \pi nd$, ft/sec

$\ell_N = d/2$, ft

as useful quantities for evaluating R_N.

A useful representative Mach number is the helical tip Mach number M_T given by

$$M_T = \frac{V_{TIP}}{a} = \frac{[V^2 + \pi^2 n^2 d^2]^{\frac{1}{2}}}{a} \qquad (D.3)$$

where V_{TIP} = Helical tip speed, ft/sec

a = Speed of sound in air, ft/sec.

The dimensional quantities on both sides of Equations D.1 and D.2 are combined to give the non-dimensional thrust and torque coefficients:

$$C_T = \frac{T}{\rho n^2 d^4} \qquad (D.4)$$

$$C_Q = \frac{Q}{\rho n^2 d^5} \qquad (D.5)$$

Using Equations D.4 and D.5 and substituting M_T for M, the functional relations D.1 and D.2 become

$$C_T = f_T[J, \beta, R_N, M_T] \tag{D.6}$$

$$C_Q = f_Q[J, \beta, R_N, M_T] \tag{D.7}$$

General aviation airplane propellers operate at values of the Reynolds number R_N (as defined above) of approximately 10^7. For values of $R_N < 10^7$, the thrust and torque coefficients can show a strong dependence on R_N. However, according to Glauert (1), for $R_N > 10^7$, "important changes of the propeller characteristics . . . are improbable. . . ." Consequently, full scale propeller characteristics, such as those used in the present work, are treated as being independent of Reynolds number.

As a result of their performance-invariance with Reynolds number, we have, for full-scale airplane propellers:

$$C_T = f_T[J, \beta, M_T] \tag{D.8}$$

$$C_Q = f_Q[J, \beta, M_T] \tag{D.9}$$

The power P (ft lb/sec) needed to drive the propeller is the product of the torque and the shaft speed; and a non-dimensional power coefficient C_P is defined by

$$C_P = \frac{P}{\rho n^3 d^5} = 2\pi C_Q \tag{D.10}$$

The efficiency of the propeller is defined by

$$\eta = \frac{TV}{P} = \frac{C_T J}{C_P} \tag{D.11}$$

For some purposes it is convenient to use propeller characteristics other than C_T, C_Q, C_P and η. It is sometimes convenient to use the forward speed V instead of nd in defining non-dimensional coefficients. By multiplying both C_T and C_Q by $1/J^2$ we obtain

$$T_c = \frac{C_T}{J^2} = \frac{T}{\rho V^2 d^2} \tag{D.12}$$

and $$Q_c = \frac{C_Q}{J^2} = \frac{Q}{\rho V^2 d^3} \tag{D.13}$$

In the design of propellers, use is often made of the non-dimensional Speed-Power coefficient C_S defined by

$$C_S = \frac{J}{C_P^{1/5}} = V \left[\frac{\rho}{Pn^2}\right]^{\frac{1}{5}} \tag{D.14}$$

Since C_S does not contain the propeller diameter as a factor, it is useful for determining the optimum diameter propeller of any family of geometrically similar propellers, for specific operating conditions of the airplane and the engine (4, 7, 8, 10).

Polar diagrams, consisting of plots of C_P/J^2 versus C_T/J^2 are used in various forms for airplane performance analysis (4), including range computation. Kerber (2) makes use of a plot of T_c versus J for estimating propeller performance by the Lesley-Reid Method. A scaled plot of T_c versus J^2 is presented by Von Mises (4) who discusses its usefulness in determining the optimum diameter propeller of any family, given values of the thrust, altitude, airspeed and engine revolutions.

In this work, use is made of the Speed-Thrust coefficient C_R defined by

$$C_R = \frac{J}{\sqrt{C_T}} = \frac{1}{\sqrt{T_c}} \tag{D.15}$$

plotted against J^2.

Performance Characteristics: Incompressible Aerodynamics

The functional dependence of C_T and C_Q on the helical tip Mach number M_T (Equations D.8 and D.9) is important only when the value of M_T exceeds some critical value. For subcritical helical tip Mach numbers, the propeller flow field is essentially incompressible; then this dependence on M_T may be ignored; and we may write:

$$C_T^i = \frac{T^i}{\rho n^2 d^4} = f_T^i[J, \beta] \tag{D.16}$$

$$C_Q^i = \frac{Q^i}{\rho n^2 d^5} = f_Q^i[J, \beta] \tag{D.17}$$

$$C_P^i = \frac{P^i}{\rho n^3 d^5} = 2\pi C_Q^i \tag{D.18}$$

$$\eta^i = \frac{T^i V}{P^i} = \frac{C_T^i J}{C_P^i} \tag{D.19}$$

$$T_c^i = \frac{T^i}{\rho V^2 d^2} = \frac{C_T^i}{J^2} \tag{D.20}$$

$$Q_c^i = \frac{Q^i}{\rho V^2 d^3} = \frac{C_Q^i}{J^2} \tag{D.21}$$

$$C_S^i = V\left[\frac{\rho}{P^i n^2}\right]^{1/5} = \frac{J}{(C_P^i)^{1/5}} \tag{D.22}$$

$$C_R^i = \frac{Vd}{\sqrt{T^i/\rho}} = \frac{J}{\sqrt{C_T^i}} \qquad (D.23)$$

where the superscript i denotes incompressible aerodynamics.

At the end of this Appendix, the McCauley C33/90M-4 constant speed propeller is described; its free performance as computed by McCauley (using incompressible aerodynamics) tabulated (Table D.1); and the assumptions underlying those computations listed. Figure D.1 depicts the geometry of this propeller; Figures D.2-D.4 are plots of the data in Table D.1 showing C_T^i, C_P^i and η^i plotted against J for fixed values of β; and Figures D.5-D.7 show plots of C_S^i and C_R^i computed from Table D.1. The McCauley C33/90M-4 constant speed propeller is installed on the Lockheed LASA 60 airplane owned by Princeton University.

Performance Characteristics: Compressible Aerodynamics

As the helical tip Mach number increases toward unity, the propeller blade airfoil characteristics are affected by the onset of compressibility. When this occurs, the functional dependence of C_T and C_Q on M_T (Equations D.8 and D.9) must be considered.

For fixed values of J and β: C_T is observed to increase slightly above C_T^i and then to decrease, while C_P rises above C_P^i at first slowly and then more rapidly; as the helical tip Mach number increases toward unity (40). Glauert (1), considering the effects of compressibility on the blade airfoil characteristics, states:

> At comparatively low speeds the lift and drag coefficients both increase, and in consequence the torque coefficient of the propeller also increases, while the thrust

> coefficient remains sensibly constant since the increases of the lift and drag coefficients produce opposite effects on the thrust of the propeller. This conclusion has been confirmed by flight tests [British A.R.C. R. and M. 1173, 1928] which showed no change of the thrust coefficient and an increase of the torque coefficient. At higher speeds the thrust coefficient would decrease owing to the decrease of the lift coefficient . . .

The helical tipspeed (Mach number) at which C_T begins to fall and C_p to rapidly rise is called the Critical Helical Tipspeed (Mach Number). Helical tip Mach numbers less (greater) than the critical value are referred to as subcritical (supercritical).

When the helical tip Mach number is supercritical, propeller performance may be characterized, at a constant value of M_T, by variations of C_T and C_Q with J and β (plots of such performance have the same form as those appropriate to incompressible aerodynamics). When these performance characteristics are available for a number of values of M_T, the performance in any operating condition may be obtained by interpolation. This method of performance estimation requires a large quantity of data.

In the present work, propeller performance in all operating conditions is computed from the performance appropriate to incompressible aerodynamics, the effects of compressibility on the efficiency and thrust coefficient being accounted for by the use of Compressibility Correction Factors f_{comp} and f'_{comp} as follows:

$$\eta(J, \beta, M_T) = \eta^i(J, \beta)\, f_{comp}(J, \beta, M_T)$$

$$C_T(J, \beta, M_T) = C_T^i(J, \beta)\ f'_{comp}(J, \beta, M_T).$$

General Aviation airplane propellers are assumed to operate with helical tip Mach numbers not greatly in excess of the critical value. Noting the quote from Glauert above (pp. D-7 and D.8) we therefore set $f'_{comp} = 1$. Consequently,

$$C_T(J, \beta, M_T) = C_T^i(J, \beta) \tag{D.24}$$

$$\eta(J, \beta, M_T) = \eta^i(J, \beta)\ f_{comp}(J, \beta, M_T) \tag{D.25}$$

$$C_Q(J, \beta, M_T) = C_Q^i(J, \beta)/f_{comp}(J, \beta, M_T) \tag{D.26}$$

Before computer technology significantly impacted the propeller industry, a common method for computing f_{comp} was included in the "Hamilton Standard Method of Propeller Performance Calculation," 1941 (21). That method is based upon the correction curves of Fred Weick (10).

The Hamilton Standard Method uses an effective helical tip-speed V_{TIP_E} defined as

$$V_{TIP_E} = V_{TIP}\ f_c\ f_h\ f_\alpha$$

where $f_c = \frac{\text{speed of sound at sea level, } a_{SL}}{\text{speed of sound at altitude, } a}$

f_h = correction factor for blade thickness ratio at 0.75 tip radius

f_α = correction factor for blade angle of attack

$\therefore \quad V_{TIP_E} = (M_T\ f_h\ f_\alpha)\ a_{SL}$

For a given propeller, f_h is a constant, so that V_{TIP_E} is a function only of M_T and blade angle of attack distribution. The value of f_α is computed from the ratio J/J_m, where J is the actual advance ratio, and J_m is the advance ratio yielding maximum efficiency at the operating value of C_S. The value of f_{comp} is determined by entering a plot of f_{comp} versus V_{TIP_E} with the values of V_{TIP_E} and J_m (this plot is reproduced here in Figure D.8).

This method of computing f_{comp} is not accurate for four reasons:

1. The correction curves used (Figure D.8), taken directly from Weick (10), were computed from propeller experimental performance data by an only approximate method (10).
2. These correction curves are entered with a value for J_m, which is not a measure of a single performance item at the operating condition of the propeller.
3. The value of f_α is computed in an indirect manner.
4. The thickness ratio correction f_h is approximate. In discussing this correction, Hamilton Standard (21) state: "Since this correction factor is really a function of some thickness factor integrated along the blade, one

would expect a correction based on the three-quarter station to be only approximate."

A more accurate method for computing f_{comp} for a particular propeller is required. Such a method has not been determined here. In the present work, it is assumed that:

1. f_{comp} (J, β, M_T), for a given free propeller, may be represented by a number of plots here referred to as f_{comp} Plots.
2. The free propeller f_{comp} plots are assumed to be applicable to the same propeller installed on an airframe, with the provision that: J and M_T are computed using the reduced forward speed $f_J V$ (see the following discussion of the Installed Propeller).

A number of items that should be considered in a detailed study of f_{comp} are briefly discussed in Chapter 4 (pp. 4-20 and 4-21).

Values of f_{comp} for some typical flight conditions of the Lockheed LASA 60 airplane, computed using the Hamilton Standard Method (21), are given in Chapter 4.

THE INSTALLED PROPELLER

Free propeller performance characteristics do not directly specify the performance of the same propeller installed on an airframe. The installed propeller operates in the presence of the airframe body (fuselage, lifting surfaces, undercarriage) and ". . . an important mutual interference [arises]: the flow around the body modifies the conditions under which the propeller operates, and the flow generated by the propeller augments the drag of the body. This mutual interference may be complicated also by the proximity of the wings of the airplane, whose lift is modified by the slipstream of the propeller" (Glauert, 1).

The following definitions are adopted:

D_{OFF} = power-off airframe drag (Appendix C), lb

D_{ON} = power-on airframe drag (Appendix C), lb

$D = D_{OFF}/E$, lb

$D_a = D_{ON}/E$ = "apparent drag" (Glauert, 1), lb

E = number of engines, each driving one propeller

T = free propeller thrust (tension in the propeller shaft), lb

T_a = installed propeller thrust (tension in the propeller shaft) called "apparent thrust" (Glauert, 1), lb

T_p = propulsive thrust: the apparent thrust less the increase in drag of the body due to the action of the propeller, lb.

$$T_p = T_a - (D_a - D) \tag{D.27}$$

T_p is that thrust available to overcome the power-off drag of the airplane, and to enable the airplane to climb or maneuver.

Q = free propeller shaft torque, lb ft

Q_a = installed propeller shaft torque, called "apparent torque" (Glauert, 1), lb ft

P = free propeller shaft power, ft lb/sec = $2\pi nQ$

P_a = installed propeller shaft power, ft lb/sec = $2\pi nQ_a$.

The superscript i is added to propeller performance quantities to denote incompressible aerodynamics, while the absence of a superscript denotes compressible aerodynamics.

The performance of a particular propeller-body combination is expressed by equations identical to Equations D.1-D.26 defining free propeller performance, with the following alterations (10, 40, 41):

1. $T_p^{(i)}$ replaces $T^{(i)}$
2. $Q_a^{(i)}$ replaces $Q^{(i)}$
3. $P_a^{(i)}$ replaces $P^{(i)}$
4. $\eta_p^{(i)}$ (propulsive efficiency) replaces $\eta^{(i)}$
5. $f_{T_p}^{(i)}$ replaces $f_T^{(i)}$
6. $f_{Q_a}^{(i)}$ replaces $f_Q^{(i)}$

and V is the airplane true airspeed (ft/sec).

The propulsive efficiency $\eta_p^{(i)}$ is given by

$$\eta_p^{(i)} = \frac{T_p^{(i)} V}{P_a^{(i)}} = \frac{T_p^{(i)} V}{2\pi n Q_a^{(i)}} \qquad (D.28)$$

In straight and level steady flight, $T_p^{(i)} = D$ so that the propulsive efficiency is

$$\eta_p^{(i)} = \frac{DV}{P_a^{(i)}}$$

$$= \frac{D_{OFF} V}{EP_a^{(i)}}$$

$$= \frac{P_R}{EP_a^{(i)}/550} = \frac{P_R}{EP_S} \qquad (D.29)$$

where P_R = airframe power required (power-off), horsepower

= $D_{OFF} V/550$ horsepower (Appendix C)

P_S = engine shaft horsepower

= $P_a^{(i)}/550$ horsepower (Appendix A).

The performance of the propeller-body combination is not always available. The next two subsections address the computation of such performance from the performance characteristics of the free propeller.

Computation of Installed Propeller Performance from Free Propeller Performance

Tractor propellers (those mounted in front of the body) and pusher propellers (those mounted behind the body) operate in a flow which is different from the free stream. "The body does not have the effect of a change of velocity which is uniform throughout

the entire plane of the propeller disc. With bodies of ordinary shape, having their longitudinal center lines in the neighborhood of the propeller shaft axis, the velocity of the air with respect to the body is reduced very greatly at the center but practically none out as far as the propeller tips" (10). The drag of the fuselage, wings and undercarriage influence this flow field while in general[†] the tail surfaces have a negligible effect on it.

Glauert (1) discusses the evaluation of apparent propeller thrust and torque for a propeller operating in such a non-uniform flow field. For a freestream velocity V and a body present, Glauert represents the axial velocity in the plane of the propeller (propeller absent) as V(1 - h) where h is a function of radial position on the blade. The thrust and torque of each annular element of the propeller are calculated "as if it [the annular element] were operating in a stream of velocity V(1 - h). Integration along the blades then gives the apparent thrust T_a and the apparent torque Q_a" (Glauert, 1). More generally, h is a function of both the radial position on the blade and the blade azimuth. The body also causes each blade element to experience a tangential and a radial velocity component. Glauert ignores the small perturbations in tangential and radial velocity caused by the body. In relation to the axial velocity he states: "Although in detailed calculations it is necessary to use values of the parameter h which vary along the blade of the propeller, for many purposes it is sufficiently accurate to use a suitable average effective value of h for the whole propeller. The

[†]With tractor propeller(s).

estimation of the behavior of the propeller as modified by the interference of the body then follows quite simply from the characteristics of the undisturbed propeller . . . The apparent thrust and torque of the propeller in the presence of the body and at the advance-diameter ratio J are determined as the free thrust and torque of the propeller at the lower advance-diameter ratio (1 - h)J and at the same rate of rotation" (1).

For the installed propeller, the advance ratio J is defined as for Equation D.1,

$$J = \frac{V}{nd}$$

where V = airplane true airspeed, ft/sec.

In addition, we define f_J, the propeller J-factor, to be

$$f_J = 1 - h, \text{ h constant} \tag{D.30}$$

and the apparent advance ratio (the advance ratio seen by the installed propeller) J_a as

$$J_a = f_J J = f_J V/nd \tag{D.31}$$

The installed propeller characteristics are then written:

$$T_a^{(i)}(J) = T^{(i)}(f_J J) = T^{(i)}(J_a) \tag{D.32}$$

$$Q_a^{(i)}(J) = Q^{(i)}(f_J J) = Q^{(i)}(J_a) \tag{D.33}$$

The installed performance coefficients are

$$C_{T_a}^{(i)} = \frac{T_a^{(i)}}{\rho n^2 d^4} \tag{D.34}$$

$$C_{Q_a}^{(i)} = \frac{Q_a^{(i)}}{\rho n^2 d^5} \tag{D.35}$$

$$C_{P_a}^{(i)} = \frac{P_a^{(i)}}{\rho n^3 d^5} = \frac{2\pi n Q_a^{(i)}}{\rho n^3 d^5} = 2\pi C_{Q_a}^{(i)} \tag{D.36}$$

and the installed propeller efficiency is

$$\eta_a^{(i)} = \frac{T_a^{(i)} (f_J V)}{2\pi n Q_a^{(i)}} = \frac{C_{T_a}^{(i)} J_a}{C_{P_a}^{(i)}} \tag{D.37}$$

The use of free propeller characteristics (incompressible) for the computation of installed characteristics (incompressible) is summarized in Table D.2.

Installed performance at any $\{J, \beta, M_T\}$ may be computed by:

1. Assuming a value for f_J and using the free propeller characteristics (incompressible) in the manner described in Table D.2.
2. Computing the compressibility correction factor f_{comp} (see the above discussion of compressibility effects on free propeller performance).
3. Computing the thrust, installed efficiency and propeller shaft torque from:

$$C_{T_a} = C_{T_a}^i$$

$$C_{Q_a} = C_{Q_a}^i / f_{comp}$$

$$T_a = T_a^i \tag{D.38}$$

$$\eta_a = \eta_a^i \, f_{comp} \tag{D.39}$$

$$Q_a = Q_a^i / f_{comp} \tag{D.40}$$

The operation of a propeller on an airplane results in the propeller axis being skewed to the airstream at all values but one of the wing angle of attack, and consequently at all values but one of the equivalent airspeed, for a given airplane weight and center of gravity position. Wind tunnel tests "have shown that the effect of this inclination of the axis is to increase the thrust and torque of the propeller" (Glauert, 1). In the same Reference Glauert also concludes however "that the thrust and torque of a propeller are not altered by a small velocity of sideslip or angle of yaw." He quotes experimental results indicating noticeable increases in the torque coefficient at sideslip angles of 10 degrees, and rapid increases of the torque coefficient with further increases in sideslip angle. Weick (10) states that "in actual flight the propeller axis assumes angles as high as 10 or 12 deg. with respect to the flight path. Full-scale tests in the 20-ft. Propeller Research Tunnel of the N.A.C.A. have shown, however, that the propeller characteristics are practically unaffected within that range" (see also Reference 21). Consequently in this work, installed propeller characteristics are considered invariant with airplane angle of attack.

The influence of the wing circulation on the thrust and torque coefficients, in effectively skewing the propeller shaft to the flow, is neglected in the same manner that the effects of airplane attitude are neglected. Any perturbation in propeller axial velocity caused by wing circulation is included in the value of f_J.

Dommasch (8) states that the presence of the wing may improve the propulsive efficiency of a single rotation propeller "by removing some of the rotation of the wake." Removing the wake rotation effects a change in the induced velocity field of the propeller; and such changes from free-propeller operation are grossly accounted for here in the value of f_J.

For a specific airframe-propeller combination, the value of f_J is here considered to be invariant with flight condition. The magnitude of f_J is dependent upon the airplane geometry.

Influence of the Slipstream on the Body

In general, the presence of the slipstream in trimmed powered flight causes changes in the values of the following variables from the values they take in trimmed power-off flight at the same value of the lift coefficient C_L (see Appendix C):

1. $C_{D_{pm}}$
2. C_{m_o}
3. a_{o_w} with corresponding values of δ_w, τ_w and e_t
4. η_t
5. i_w

The drag coefficient of the body in trimmed powered flight therefore

differs from that pertaining to trimmed power-off flight at the same C_L.

In determining the effect of the slipstream on drag, we first consider the lift-independent drag alone. The variations in lift-independent drag due to power here considered correspond to changes in $C_{D_{pm}}$ and η_t (the term $\xi_t^2 K_t S_t \eta_t / S$ in κ_0 only) in Equation C.29. These variations are (Glauert, 1):

"(1) The increase of body drag due to the increased velocity in the slipstream.

(2) The mutual reaction between the body and propeller due to the pressure gradient in the slipstream.

(3) The shielding of the nose of the body or the inclusion of the boss of the propeller inside the body."

The drag of the body with propeller absent may be written:

$$D = D_0 + D_i \tag{D.41}$$

where $D = D_{OFF}/E$, lb

D_0 = (the entire lift-dependent drag, plus the lift-independent drag of those parts of the airplane outside the region to be influenced by the slipstream when the propellers are running)/E, lb

D_i = (the lift-independent drag of those parts of the airplane inside the region to be influenced by the slipstream when the propellers are running)/E, lb.

When the propellers are running, the lift-independent drag of those parts of the body within each slipstream is altered to D_{ia} and we may write

$$D_a = D_0 + D_{ia} \tag{D.42}$$

Glauert (1), in considering those parts of the body totally immersed in the slipstream, shows that the apparent drag D_{ia} may be written:

$$D_{ia} = D_i \left[A + B \frac{T_a}{\pi R^2 \rho V^2} \right] \tag{D.43}$$

where $A \simeq 1$, and B is a constant dependent upon the airplane geometry. Glauert (1) shows that the value of A is, in general, approximately unity, especially in those cases where the free propeller thrust has been evaluated from blade forces alone (has not included the drag of the boss) which is true in the present work. In addition, he indicates that the value of B may vary with the propeller advance ratio, but he neither includes such an effect in his analysis nor discusses the magnitude of the variation. Consequently any such variation of B will be ignored here (see also Reference 21). From Equation D.27, the propulsive thrust is

$$T_p = T_a - (D_a - D)$$

From Equations D.41 and D.42,

$$T_p = T_a - (D_{ia} - D_i) \tag{D.44}$$

Substituting Equation D.43 in Equation D.44 yields

$$T_p = T_a \left[1 - \frac{BD_i}{\pi R^2 \rho V^2} \right]$$

and since D_i is a lift-independent drag, it may be expressed as a constant multiple of the dynamic pressure $\rho V^2/2$. Consequently,

$$T_p = T_a(1 - \varepsilon)$$

where ε is a small constant. Defining the slipstream interference factor f_D as

$$f_D = \frac{1}{1 - \varepsilon} = \text{constant}$$

we then have

$$T_a = f_D T_p \tag{D.45a}$$

It is assumed that the above argument applies equally to compressible and incompressible propeller aerodynamics, and that f_D retains the same value in both cases. Then

$$T_a^i = f_D T_p^i \tag{D.45b}$$

In straight and level steady flight the propulsive thrust $T_p^i = T_p = D$ and hence

$$T_a^{(i)} = D_a = f_D D$$

$$= f_D D_{OFF}/E$$

and hence

$$ET_a^{(i)} = D_{ON} = f_D D_{OFF} \tag{D.46}$$

Equation D.46, in which f_D is constant, was derived from a consideration of power effects on lift-independent drag alone. It is shown in Chapter 3 that the effects of power on the drag, in addition to those effects considered in the formulation of Equation D.46, are small for the LASA 60 airplane. The additional effects, arising from variations in items 2-5 (p. D-19) due to power, are taken to be small for GA airplanes in general. In this work, all power effects on drag are subsumed into f_D. While f_D is not strictly constant with variations in power, it is assumed

to be constant in Equation D.46.

Equations D.30-D.46 are applicable to both tractor and pusher propeller installations. The magnitudes of f_J and f_D are dependent upon the airplane geometry.

Propulsive Efficiency

From Equations D.37, D.45 and D.28,

$$\eta_a^{(i)} = \frac{T_a^{(i)}(f_J V)}{2\pi n Q_a^{(i)}}$$

$$= \frac{(f_D T_p^{(i)})(f_J V)}{2\pi n Q_a^{(i)}}$$

$$= f_D f_J \eta_p^{(i)} \qquad \text{(D.47)}$$

$$\therefore \quad \eta_p^i = \frac{\eta_a^i}{f_D f_J} \qquad \text{(D.48)}$$

Substituting Equation D.39 in Equation D.47 yields

$$\eta_p = \frac{\eta_a^i f_{comp}}{f_D f_J}$$

$$= \eta_p^i f_{comp} \qquad \text{(D.49)}$$

The foregoing discussion has established the fact, expressed by Equations D.48 and D.49, that the propulsive efficiency for any set $\{J, \beta, M_T\}$ may be expressed in terms of:

1. The installed propeller efficiency η_a^i computed using incompressible aerodynamics for the set $\{J_a, \beta\}$: the computation of η_a^i has been discussed.
2. The propeller-body interference factors f_D and f_J.

3. The compressibility correction factor f_{comp}.

The operation of the installed propeller in straight steady flight is subject to the following constraints:

I. The propeller and airframe move with the same forward speed.

II. The propeller shaft torque is a constant multiple (the transmission gear ratio G) of the engine shaft torque.†

III. The propeller shaft speed is a constant multiple (the inverse of the transmission gear ratio G) of the engine shaft speed.

In straight steady level flight, the following force constraint must also be satisfied:

IV. The sum of the thrusts $ET_a^{(i)}$ from all propellers is equal to the power-on airframe drag $f_D D_{OFF}$ (Equation D.46).

The above four constraints apply to the operation of propellers with fixed or variable pitch. All fixed pitch propellers operate with the additional and final constraint:

V. The blade angle β is invariant.

We now seek an understanding of the functional nature of η_a^i subject to the constraints I and IV. This is achieved through a study of the Speed-Thrust Coefficient C_R^i. Presentation of propeller performance in terms of C_R^i is an extension of the method of analysis presented by Pye (12) and Kerber [The Lesley-Reid Method] (2) for the performance analysis of fixed pitch propellers.

†After auxiliary equipment power P_{AUX} has been removed from the engine shaft: see Figure A.2.

The Speed-Thrust Coefficient:

Consider the problem of determining the propeller speed n revolutions/second and blade angle β which maximize the efficiency of a given free propeller, under the constraints of a prescribed forward speed, air density and thrust. Assume that compressibility effects are absent.

This computation is facilitated by plotting a propeller parameter that incorporates all of the known quantities (V, ρ, T^i, d) versus a second propeller parameter containing the unknown n, for fixed values of blade angle β and efficiency η^i. Two such parameters are respectively T_c^i and J. The computation proceeds by calculating the value of T_c^i from the given quantities, and picking off the T_c^i:J plot that value of J which corresponds to maximum efficiency at the fixed value of T_c^i. The blade angle required is readily determined at the resulting $\{T_c^i, J\}$ point. The required value of n is then calculated from the value of J.

The task of interpolation on such a plot is made easier by plotting

$$\bar{C}_R^i = \frac{J}{\sqrt{C_T^i}} = \frac{1}{\sqrt{T_c^i}} \tag{D.50}$$

$$= \frac{Vd}{\sqrt{T^i/\rho}} \tag{D.51}$$

versus J^2 for fixed values of β and η^i. The quantity C_R^i is here defined as the propeller Speed-Thrust Coefficient. The plot of C_R^i:J^2 for the McCauley C33/90M-4 constant speed free propeller is presented in Figure D.6. Plotted in this manner, the lines of

constant blade angle β are almost straight and equally spaced. The dotted contour lines of constant efficiency clearly define a three-dimensional surface, an efficiency ridge. The line of maximum efficiency running up this ridge indicates the maximum efficiency achievable for any value of C_R^i; and the corresponding value of J^2 provides the propeller speed n necessary to achieve that efficiency when V and d are known. In Figure D.7 C_R^i is plotted against 1/J which is essentially a scale of n revolutions/second for any fixed values of V and d: the efficiency ridge is again clear. For any fixed value of the blade angle β, the efficiency η^i is seen to remain almost constant at the higher values of C_R^i.

Now consider an airplane in straight and level steady flight, with E propellers each providing identical thrust. Then, for each propeller,

$$C_{R_a}^i = \frac{J_a}{\sqrt{C_{T_a}^i}} = \frac{f_J V d}{\sqrt{T_a^i/\rho}} \tag{D.52}$$

where V is the airplane true airspeed, ft/sec (constraint I). Invoking Equation D.46 for T_a^i (constraint IV) and Equation C.1 for D_{OFF},

$$C_{R_a}^i = \sqrt{\frac{2f_J^2 E d^2}{f_D C_D S}} \tag{D.53}$$

For a given airplane, the only variable on the right hand side of Equation D.53 is the airframe power-off drag coefficient C_D, which is a function only of V_E, W and h (Appendix C) where

V_E = equivalent airspeed, knots

W = gross weight, lb

h = center of gravity position.

For any value of C_D, the right hand side of Equation D.53 may be computed (values of $C^i_{R_a}$ so computed for the LASA 60 airplane are plotted in Figure D.9). Entering the free propeller C^i_R:J^2 plot with this computed value of $C^i_{R_a}$ gives the variation of $\{\eta^i_a, \beta\}$ with J^2_a, and the values of $\{J_a, \beta\}$ yielding maximum η^i_a are obtained.

Now

$$J_a = \frac{f_J V}{nd} = \frac{101.34\ f_J V_E}{N\sqrt{\sigma} d} \tag{D.54}$$

where $N = 60n$ = propeller revolutions/minute

σ = atmospheric density ratio† (Appendix B).

For a given airframe and propeller in straight and level steady flight, the $C^i_{R_a}$:J^2_a plot (such as Figure D.6) therefore represents a three-dimensional surface, whose height η^i_a is

$$\eta^i_a = \eta^i_a[V_E, W, h, N, \sigma] \tag{D.55}$$

and upon which lines of constant β are inscribed.

For a given airframe and propeller in straight and level steady flight, the $C^i_{R_a}$:J^2_a plot, the f_{comp} plots and Equations D.48 and D.49 together define:

$$\eta_p = \eta_p[V_E, W, h, N, \sigma, M_T] \tag{D.56}$$

This is a complete definition of η_p.

---

†Standard and non-standard atmospheric conditions.

Propeller Shaft Torque

Since the airframe power required P_R is a function only of $\{V_E, W, h, \sigma\}$ (Appendix C and Chapter 3), we have from Equations D.29, D.48 and D.55:

$$P_a^i = 2\pi n Q_a^i = P_a^i[V_E, W, h, N, \sigma]$$

Hence the propeller shaft torque Q_a^i is:

$$Q_a^i = Q_a^i[V_E, W, h, N, \sigma] \qquad (D.57)$$

For a given airframe and propeller in straight and level steady flight, the $C_{R_a}^i : J_a^2$ plot, the $C_{P_a}^i : J_a$ plot and Equation D.36 together define the function in Equation D.57. This is a complete definition of Q_a^i.

Similarly, from Equations D.29 and D.56:

$$P_a = 2\pi n Q_a = P_a[V_E, W, h, N, \sigma, M_T]$$

Hence the propeller shaft torque Q_a is:

$$Q_a = Q_a[V_E, W, h, N, \sigma, M_T] \qquad (D.58)$$

For a given airframe and propeller in straight and level steady flight, the $C_{R_a}^i : J_a^2$ plot, the $C_{P_a}^i : J_a$ plot, the f_{comp} plots, and Equations D.36 and D.40 together define the function in Equation D.58. This is a complete definition of Q_a.

Q_a and N are used in the computation of the engine shaft torque and rotational speed respectively (constraints II and III).

Propeller Blade Angle

For a given airframe and propeller in straight and level

steady flight, the lines of constant β in the $C_{R_a}^i : J_a^2$ plot define the functional relation

$$\beta = \beta[V_E, W, h, N, \sigma] \tag{D.59}$$

Equation D.59 displays no M_T dependence by virtue of Equations D.38 and D.52.

PERFORMANCE MODEL

For a given set $\{V_E, W, h, N, \sigma, M_T\}$ the propulsive efficiency η_p, the propeller shaft torque Q_a and the propeller blade angle β are computed in this work as follows:

1. Assume values for f_J and f_D
2. Compute $C_{R_a}^i$ - Equation D.53
3. Compute J_a - Equation D.31
4. Compute $C_{T_a}^i$ - Equation D.52
5. Compute β - Figure D.6
6. Compute $C_{P_a}^i$ - Figure D.3
7. Compute η_a^i - Equation D.37
8. Compute η_p^i - Equation D.48
9. Compute P_a^i - Equation D.36
10. Compute $Q_a^i = P_a^i/2\pi n$

Finally, the effects of compressibility are included:

11. Compute f_{comp} - See page D-11
12. Compute η_p - Equation D.49
13. Compute Q_a - Equation D.40

The computation of β (Step 5) could be performed using Figure D.2 with the available values of $C_{T_a}^i$ and J_a. The advantages of using the Speed-Thrust Coefficient Figure D.6 are:

1. It affords physical insight into the variation of η_a^i in $\{V_E, W, h, N, \sigma\}$ space,
2. It identifies the trajectory of maximum η_a^i in $\{V_E, W, h, N, \sigma\}$ space.

CHARACTERISTICS OF THE McCAULEY C33/90M-4 CONSTANT SPEED FREE PROPELLER

Geometry

The geometric data of Figure D.1 were provided by the McCauley Accessory Division of the Cessna Aircraft Company (Drawing Number 90M). The modified RAF.6 section used is described by Weick (10).

Performance: Incompressible Aerodynamics

The performance characteristics of the McCauley C33/90M-4 constant speed free propeller (provided by McCauley) are presented in Table D.1. The power coefficient C_P^i, efficiency η^i, and thrust coefficient C_T^i are given for a range of advance ratios J from zero through 0.9, for various values of the blade angle β degrees.

The data were computed using a Goldstein-Lock analysis (1, 8). McCauley was not able to provide any supporting test data. The following should be noted with regard to the computations:

1. The propeller was assumed to operate in a free stream of uniform velocity. No account was taken of the presence

of a body in determining the inflow velocity or the wake structure. The free stream velocity was parallel to the propeller shaft axis.

2. Radial integration was performed between 20% and 100% of the propeller tip radius R. In this manner the presence of the spinner was recognized, although no account was taken of its effect on the inflow velocity field.
3. Zero drag is attributed to the radial stations inboard of 0.2R.
4. The analysis used experimental two-dimensional lift and drag coefficient data from early NACA tests of modified RAF.6 airfoil sections with various thickness to chord ratios (similar data are given by Weick, 10). These data were taken for a Reynolds number of 1.0×10^6, based on airfoil chord as the length measure.
5. The thickness and chord distributions of the C33/90M-4 propeller blade were properly represented in the analysis.
6. For those inboard stations where the blade sections deviate from the modified RAF.6 (0.2R-0.35R), the section was assumed to be a modified RAF.6 section with the correct thickness and chord.
7. No account was taken of compressibility effects.
8. The blade angle β is measured between the plane of rotation and the flat face of the blade, at a radius of 0.75R. Although the computations assume rigid propeller

blades, the performance figures may be used for a flexible propeller when β is considered to be the blade angle in operation (5, 10).

The performance characteristics in Table D.1 are plotted in Figures D.2-D.4.

TABLE D.1

PERFORMANCE CHARACTERISTICS OF C33/90M-4 TYPE PROPELLER

J	β	C_P^i	η^i	C_T^i
0	10	.0245		.0807
0	12	.0308		.0928
0	14	.0373		.1009
0	16	.0441		.1062
0	18	.0525		.1058
0	20	.0629		.1033
0	22	.0719		.1009
0	24	.0771		.0998
0	26	.0785		.0995
0	28	.0787		.0995
.1	10	.0244	.2953	.0721
.1	12	.0309	.2748	.0849
.1	14	.0382	.2551	.0974
.1	16	.0454	.2310	.1049
.1	18	.0526	.2045	.1076
.1	20	.0622	.1695	.1054
.1	22	.0729	.1402	.1022
.1	24	.0806	.1241	.1000
.1	26	.0837	.1187	.0994
.1	28	.0839	.1184	.0993
.2	10	.0235	.5164	.0607
.2	12	.0303	.4875	.0739
.2	14	.0379	.4579	.0868
.2	16	.0464	.4300	.0998
.2	18	.0546	.4004	.1093
.2	20	.0620	.3527	.1093
.2	22	.0727	.2890	.1051
.2	24	.0831	.2439	.1013
.2	26	.0895	.2223	.0995
.2	28	.0912	.2173	.0991
.3	10	.0212	.6696	.0473
.3	12	.0282	.6453	.0607
.3	14	.0362	.6132	.0740
.3	16	.0452	.5808	.0875
.3	18	.0548	.5501	.1005
.3	20	.0641	.5188	.1109
.3	22	.0725	.4667	.1128
.3	24	.0833	.3790	.1052
.3	26	.0931	.3259	.1011
.3	28	.0986	.3021	.0993

TABLE D.1
(continued)

PERFORMANCE CHARACTERISTICS OF C33/90M-4 TYPE PROPELLER

J	β	C_{P-}^{i}	η^{i}	C_{T}^{i}
.4	10	.0170	.7519	.0320
.4	12	.0244	.7542	.0460
.4	14	.0328	.7293	.0598
.4	16	.0422	.6973	.0736
.4	18	.0524	.6648	.0871
.4	20	.0633	.6334	.1002
.4	22	.0741	.5976	.1107
.4	24	.0836	.5487	.1147
.4	26	.0938	.4548	.1067
.4	28	.1031	.3944	.1017
.5	10	.0112	.6911	.0155
.5	12	.0185	.8053	.0298
.5	14	.0272	.8102	.0441
.5	16	.0372	.7864	.0585
.5	18	.0480	.7551	.0725
.5	20	.0595	.7227	.0860
.5	22	.0723	.6866	.0993
.5	24	.0843	.6517	.1099
.5	26	.0944	.6096	.1151
.5	28	.1049	.5221	.1095
.6	14	.0198	.8396	.0277
.6	16	.0300	.8490	.0424
.6	18	.0414	.8261	.0570
.6	20	.0536	.7949	.0710
.6	22	.0670	.7568	.0845
.6	24	.0814	.7219	.0979
.6	26	.0944	.6933	.1091
.6	28	.1048	.6584	.1150
.6	30	.1160	.5741	.1110
.6	32	.1241	.5061	.1047
.7	18	.0326	.8751	.0408
.7	20	.0455	.8529	.0554
.7	22	.0596	.8144	.0693
.7	24	.0746	.7777	.0829
.7	26	.0903	.7501	.0968
.7	28	.1042	.7281	.1084
.7	30	.1156	.6954	.1148
.7	32	.1274	.6145	.1118
.7	34	.1357	.5499	.1066
.7	36	.1414	.5027	.1015

TABLE D.1
(concluded)

PERFORMANCE CHARACTERISTICS OF C33/90M-4 TYPE PROPELLER

J	β	C_p^i	η^i	C_T^i
.8	22	.0500	.8596	.0537
.8	24	.0659	.8240	.0679
.8	26	.0821	.7961	.0817
.8	28	.0990	.7755	.0960
.8	30	.1143	.7553	.1079
.8	32	.1269	.7233	.1147
.8	34	.1393	.6459	.1125
.8	36	.1479	.5843	.1080
.8	38	.1541	.5394	.1039
.8	40	.1540	.5264	.1013
.9	24	.0549	.8579	.0523
.9	26	.0721	.8343	.0668
.9	28	.0896	.8154	.0812
.9	30	.1080	.7959	.0955
.9	32	.1250	.7763	.1078
.9	34	.1388	.7441	.1148
.9	36	.1517	.6701	.1129
.9	38	.1607	.6113	.1092
.9	40	.1670	.5691	.1056
.9	42	.1672	.5538	.1029

TABLE D.2

DETERMINATION OF INSTALLED PROPELLER CHARACTERISTICS FROM FREE PROPELLER CHARACTERISTICS IN THE ABSENCE OF COMPRESSIBILITY EFFECTS

Each free propeller chart with coordinates (x, y, β) may be used directly to determine the characteristics of any geometrically similar propeller installed on an airplane (when scale effects due to Reynolds number variation are negligible), by reading the coordinates (x, y, β) as (x_a, y_a, β) defined below.

Free Propeller Characteristics		Installed Propeller Characteristics	
x	y	x_a	y_a
$J = \frac{V}{nd}$	$C_T^i = T^i/\rho n^2 d^4$	$J_a = \frac{f_J V}{nd}$	$C_{T_a}^i = T_a^i/\rho n^2 d^4$
J	$C_Q^i = Q^i/\rho n^2 d^5$	J_a	$C_{Q_a}^i = Q_a^i/\rho n^2 d^5$
J	$C_P^i = P^i/\rho n^3 d^5$	J_a	$C_{P_a}^i = P_a^i/\rho n^3 d^5$
J	$\eta^i = C_T^i J/C_P^i$	J_a	$\eta_a^i = C_{T_a}^i J_a/C_{P_a}^i$
J	$T_c^i = T^i/\rho V^2 d^2$	J_a	$T_{c_a}^i = T_a^i/\rho f_J^2 V^2 d^2$
J	$Q_c^i = Q^i/\rho V^2 d^3$	J_a	$Q_{c_a}^i = Q_a^i/\rho f_J^2 V^2 d^3$
J	$C_S^i = V[\rho/P^i n^2]^{1/5}$	J_a	$C_{S_a}^i = f_J V[\rho/P_a^i n^2]^{1/5}$
J	$C_R^i = Vd/\sqrt{T^i/\rho}$	J_a	$C_{R_a}^i = f_J Vd/\sqrt{T_a^i/\rho}$

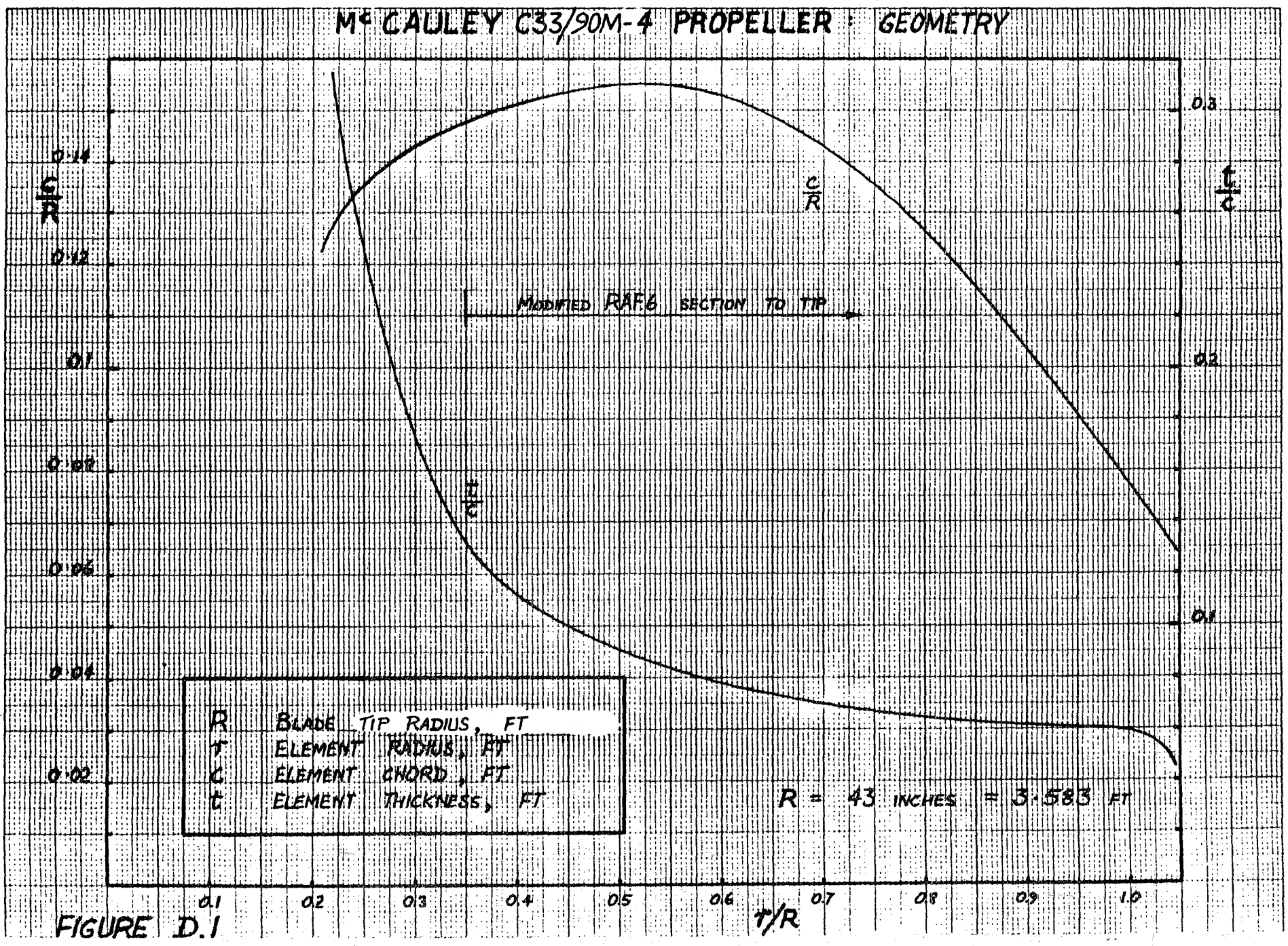
Mc CAULEY C33/90M-4 PROPELLER GEOMETRY
c/R
t/c
t/R
MODIFIED RAF6 SECTION TO TIP
0.14
0.12
0.1
0.08
0.06
0.04
0.02
0.3
0.2
0.1
0.1
0.2
0.3
0.4
0.5
0.6
0.7
0.8
0.9
1.0
r/R
R BLADE TIP RADIUS, FT
r ELEMENT RADIUS, FT
C ELEMENT CHORD, FT
t ELEMENT THICKNESS, FT
R = 43 INCHES = 3.583 FT

FIGURE D.1

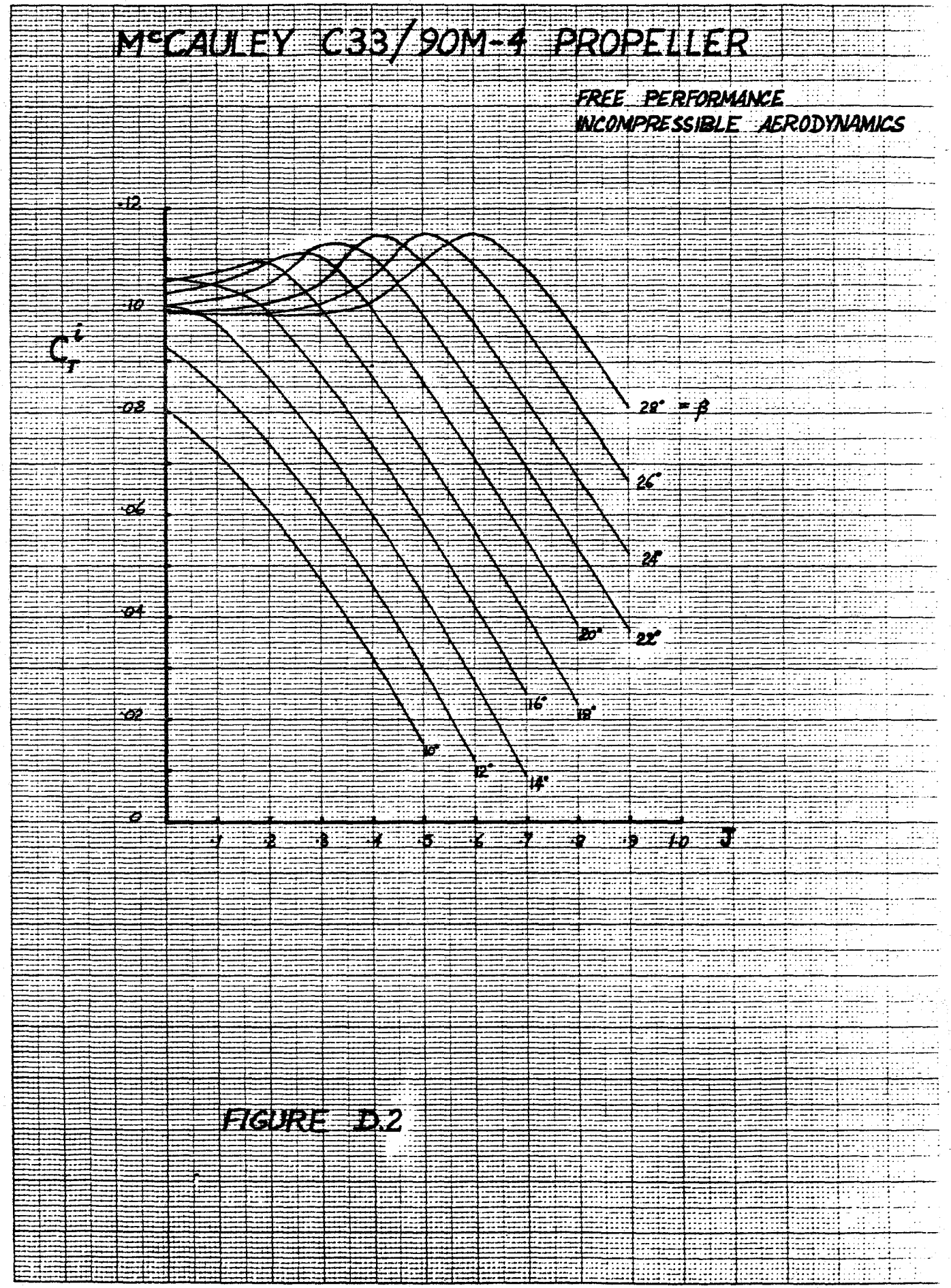

FIGURE D.2

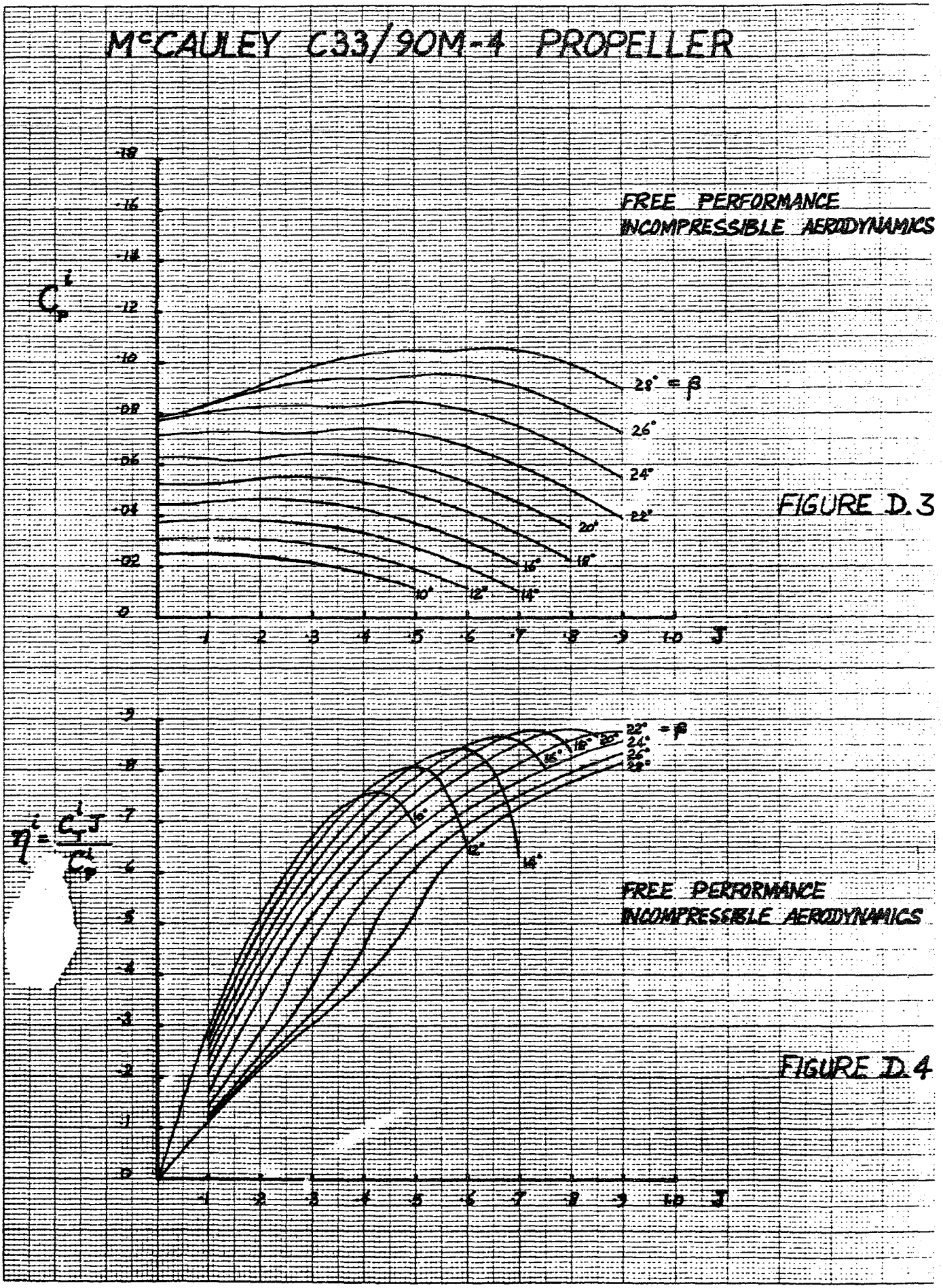

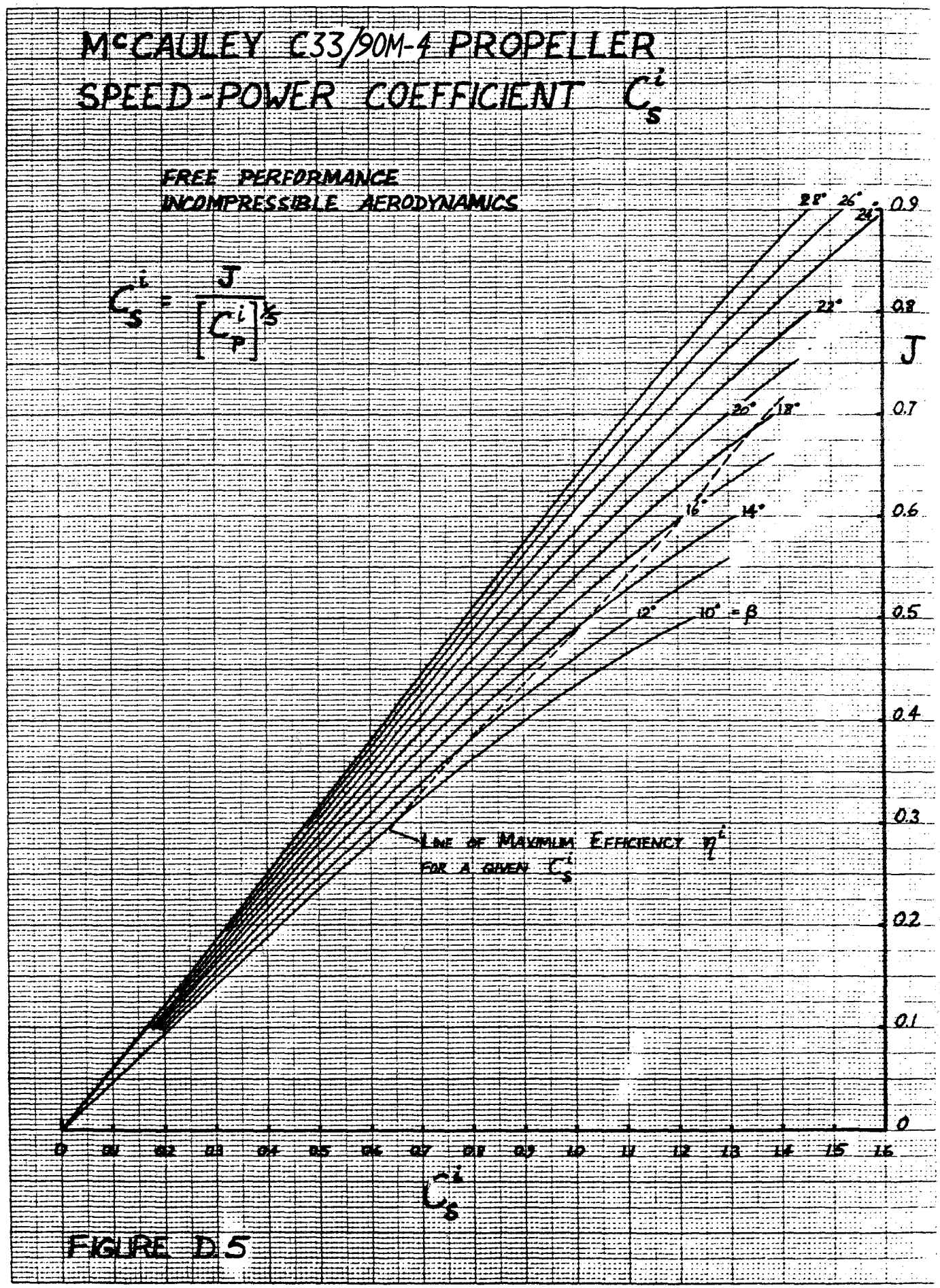

FIGURE D.5

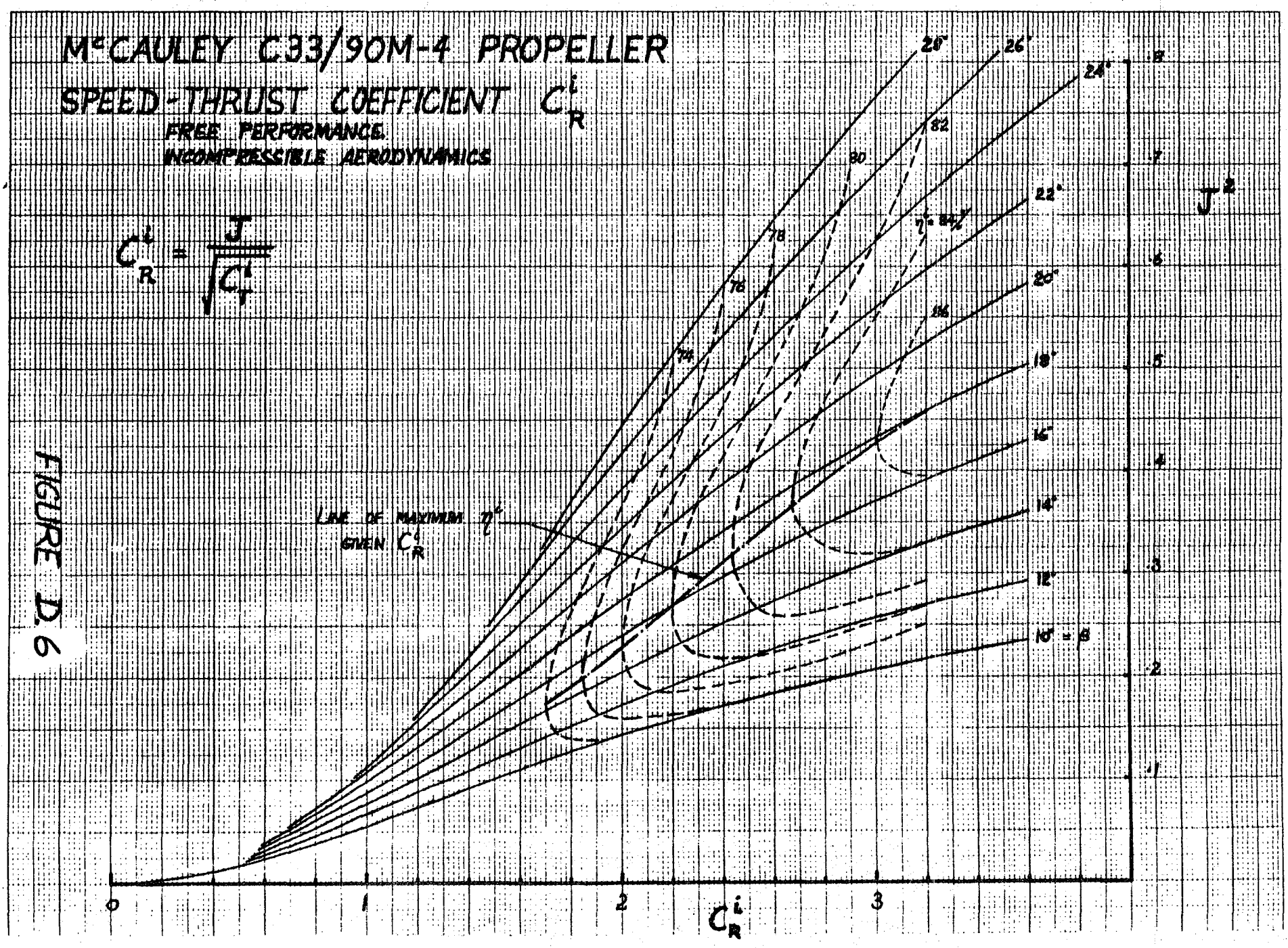
McCAULEY C33/90M-4 PROPELLER
SPEED-THRUST COEFFICIENT C_R^i
FREE PERFORMANCE
INCOMPRESSIBLE AERODYNAMICS
$C_R^i = \frac{J}{\sqrt{C_T^i}}$
LINE OF MAXIMUM η^i GIVEN C_R^i
$\eta^i = 84\%$
26°
24°
22°
20°
18°
16°
14°
12°
10° = β
82
80
78
76
74
86
J
C_R^i
0
1
2
3
.8
.7
.6
.5
.4
.3
.2
.1

FIGURE D.6

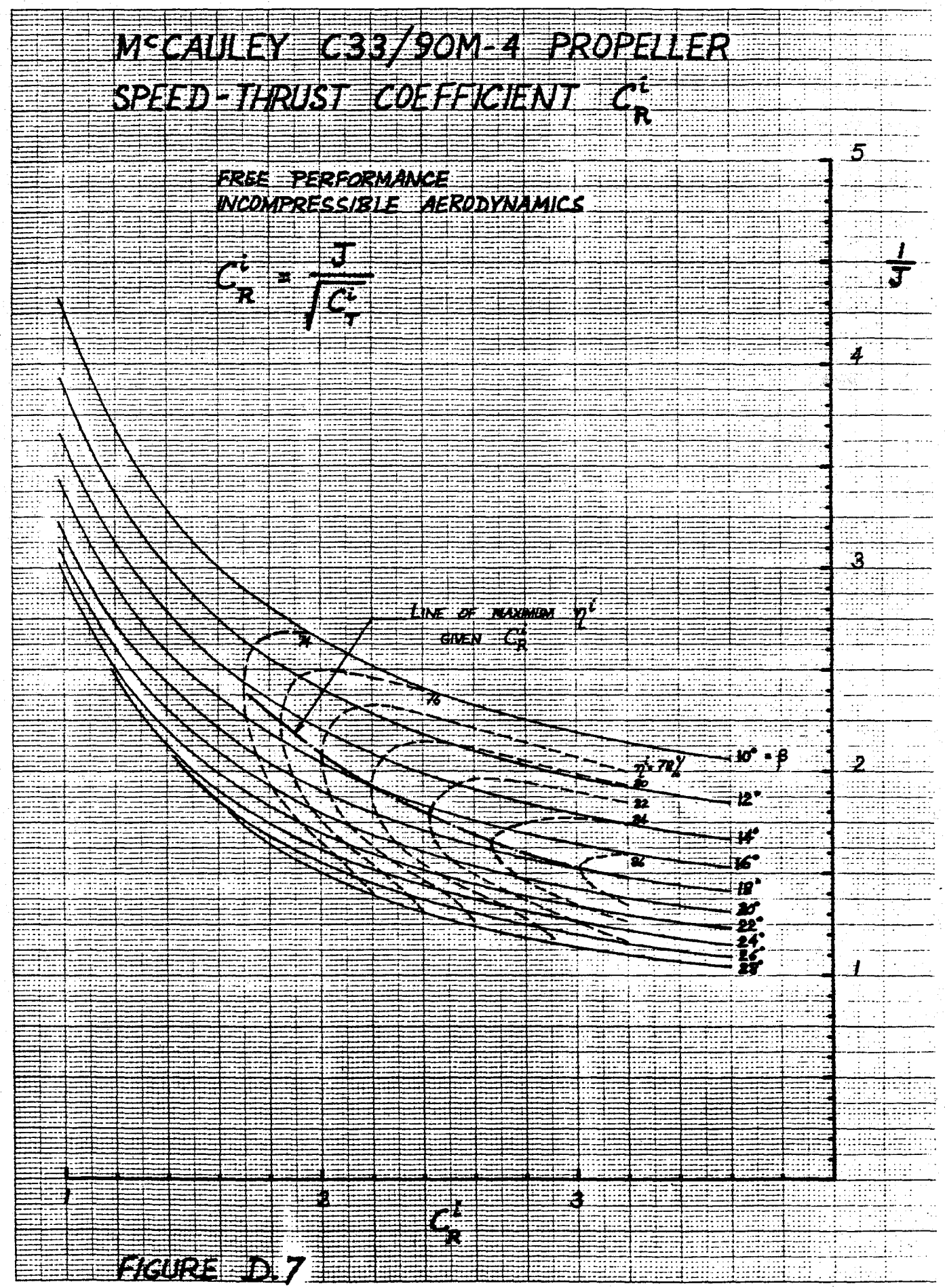

FIGURE D.7

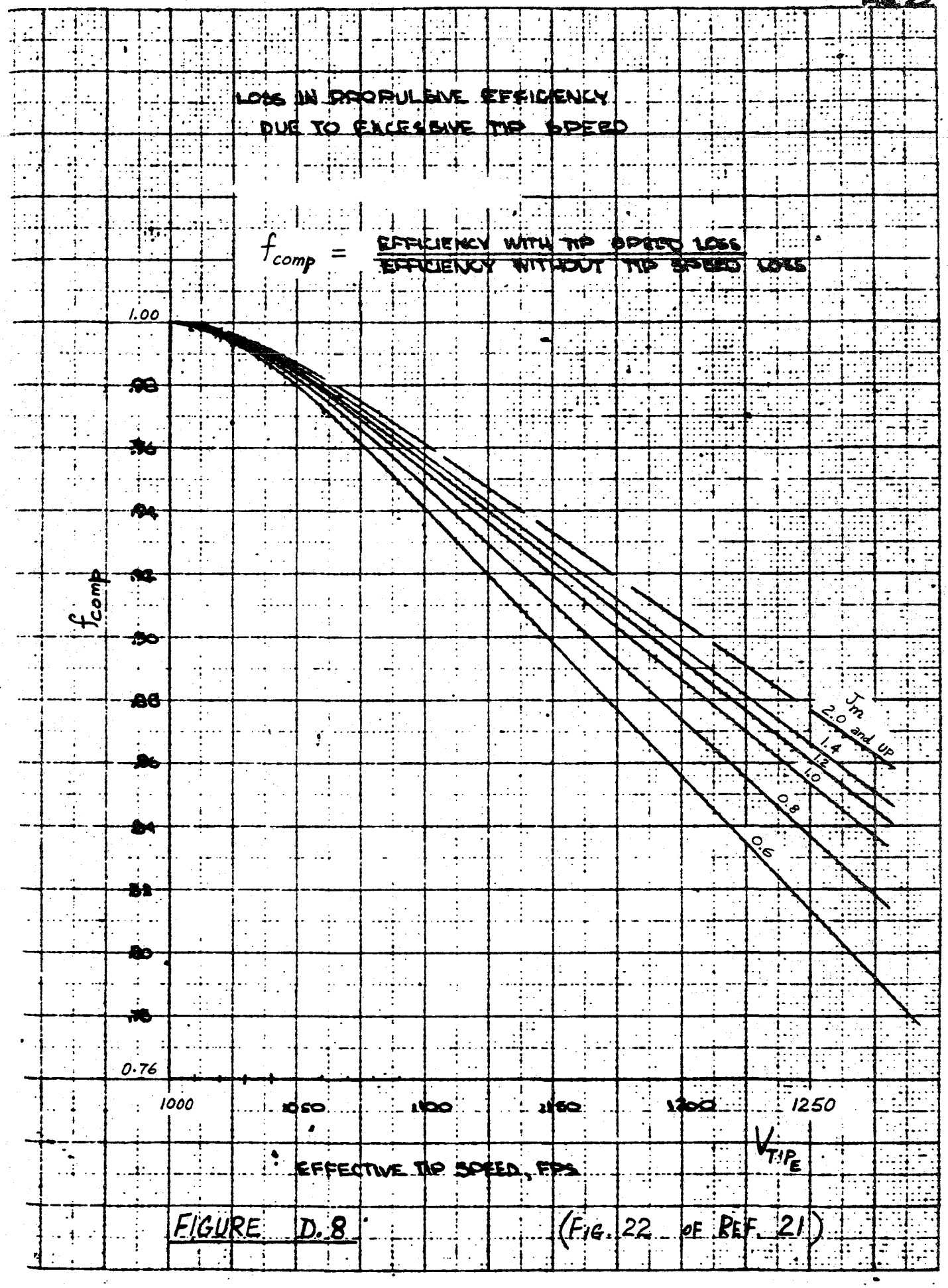

FIGURE D.8 (FIG. 22 OF REF. 21)

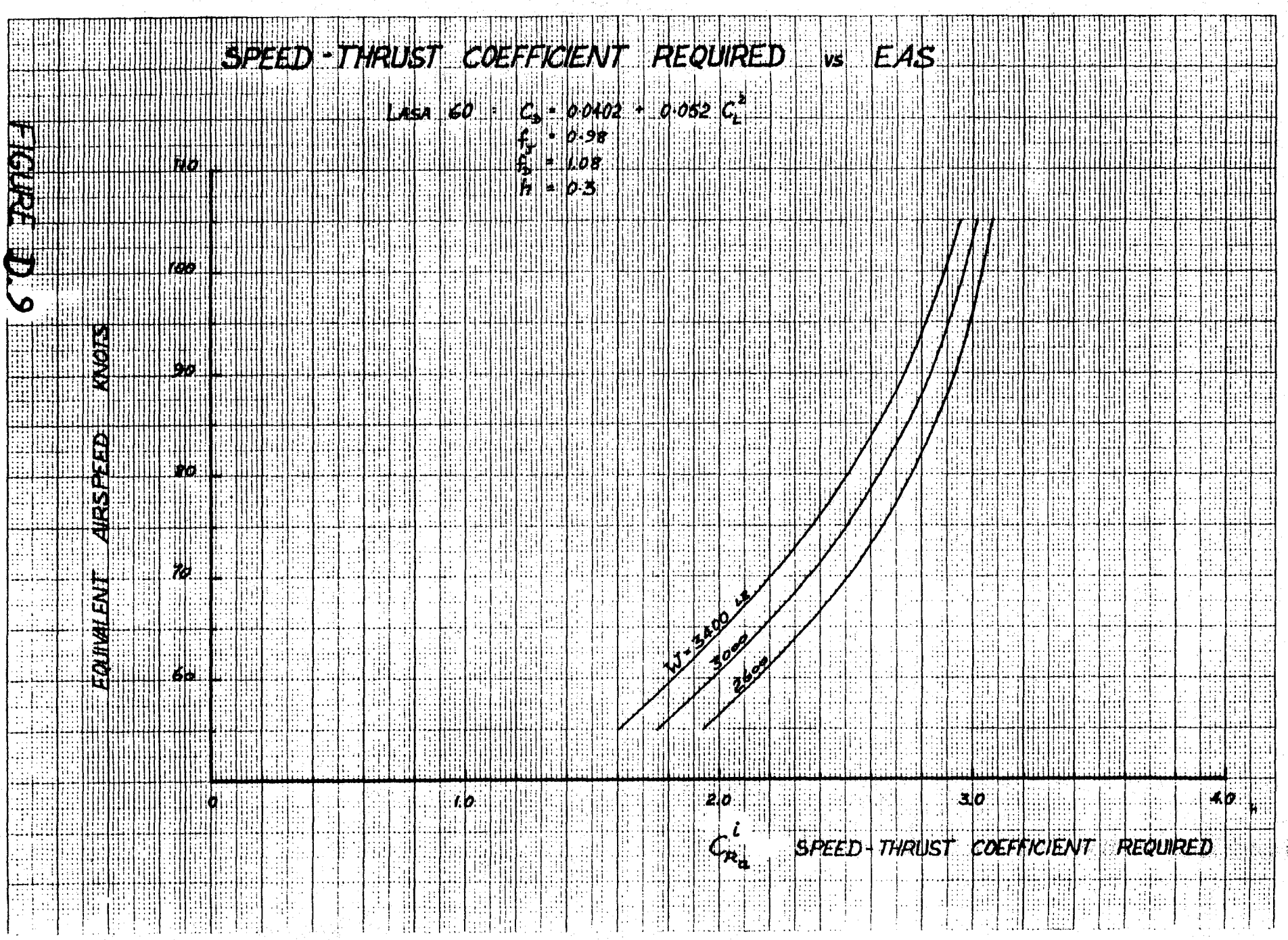
SPEED - THRUST COEFFICIENT REQUIRED vs EAS
LASA 60 : C_D = 0.0402 + 0.052 C_L^2
f_w = 0.98
f_h = 1.08
h = 0.3
EQUIVALENT AIRSPEED KNOTS
110
100
90
80
70
60
W = 3400 LB
3000
2600
0
1.0
2.0
3.0
4.0
$C_{R_a}^i$
SPEED - THRUST COEFFICIENT REQUIRED

FIGURE D.9

APPENDIX E

THE NATURALLY ASPIRATED ENGINE PERFORMANCE MODEL

Table of Contents

Table of Contents
(concluded)

APPENDIX E

THE NATURALLY ASPIRATED ENGINE PERFORMANCE MODEL

INTRODUCTION

This Appendix presents a method for the computation of the performance of naturally aspirated, spark-ignition, fuel injection, 4-stroke reciprocating internal combustion engines, measured in terms of Brake Horsepower and Brake Specific Fuel Consumption. The method involves:

1. Computation of Indicated Horsepower at the required operating point, from
   a) The indicated horsepower developed at a reference operating point.
   b) Scaling functions of the operational parameters.
2. Computation of the Lost Horsepower at the required operating point.

Uniform distribution of induction air and fuel flow to all cylinders is assumed, a condition closely approached by an engine with a well designed induction system and a fuel injection system. This discussion pertains to well designed engines utilizing inlet port fuel injection systems. The difficulties of modelling the effects of non-uniform induction air distribution due to bad inlet manifold design, or non-uniform fuel distribution associated with

carbureted engines, are avoided.

The engine is assumed to operate with all cylinder heads at a common uniform temperature. Similarly, a uniform inlet manifold temperature is assumed between the throttle butterfly and the inlet valves.

All computations pertain to a dry atmosphere. For details on the effects of humidity on engine performance, refer to Taylor (13).

Basic Definitions

The macroscopic gas processes which determine the work output of any spark-ignition, 4-stroke reciprocating internal combustion engine may be characterized by a pressure-volume (pV) cycle diagram. Such a diagram, typical of a naturally aspirated aircraft engine, is shown in Figure E.1, which represents the processes in one cylinder.

Following Obert (29) the Indicated work of each cycle is defined as area (A+C) of Figure E.1, while the Pumping Work is defined as area (B+C). The indicated work is the energy delivered to the piston by the gases in the cylinder during each cycle; while the pumping work is the work done per cycle by the piston in expelling burnt gases from the cylinder and drawing in a fresh charge.

The Indicated Horsepower (IHP) of the engine is the rate at which indicated work is done on all the pistons of the engine.

The Pumping Horsepower (PHP) is the rate at which pumping work is done by all the engine pistons.

Associated with the gas processes of Figure E.1, but not shown therein, is the work done by the entire engine in overcoming mechanical friction. The horsepower required for this is denoted by MHP (Mechanical

friction Horsepower).

The horsepower consumed by pumping and mechanical friction is not available as useful power at the engine shaft, and therefore is referred to herein as Lost Horsepower (LHP):

$$LHP = PHP + MHP \tag{E.1}$$

The horsepower available for useful work at the engine shaft is Brake Horsepower (BHP):

$$P_E = BHP = IHP - LHP \tag{E.2}$$

$$= \left(\frac{2\pi}{33{,}000}\right) Q_E \cdot N_E \tag{E.3}$$

where Q_E = engine brake torque (lb ft)

N_E = engine shaft speed (revolutions/minute)

Mean effective pressure (MEP) is work done per unit time, divided by engine power-stroke displacement per unit time (13). Hence, brake mean effective pressure is (29):

$$BMEP = 458.33\ (BHP)/DN_E \quad lb/in^2 \tag{E.4}$$

where D = total engine displacement (cubic ft). Similarly, indicated mean effective pressure is:

$$IMEP = 458.33\ (IHP)/DN_E \quad lb/in^2 \tag{E.5}$$

and the lost mean effective pressure is:

$$LMEP = IMEP - BMEP$$

$$= 458.33\ (LHP)/DN_E \quad lb/in^2 \tag{E.6}$$

The fuel economy of a reciprocating internal combustion engine is usually measured by its Indicated Specific Fuel Consumption (ISFC) or its Brake Specific Fuel Consumption (BSFC). If the fuel mass flow rate into the engine is $\dot{m}_f$ lbm/hr then:

$$ISFC = \frac{\dot{m}_f}{IHP} \quad lbm/IHP \cdot hr \tag{E.7}$$

$$BSFC = \frac{\dot{m}_f}{BHP} \quad lbm/BHP \cdot hr \tag{E.8}$$

Consequently,

$$\frac{1}{BSFC} = \frac{1}{ISFC} - \frac{LHP}{\dot{m}_f} \tag{E.9}$$

Design Parameters and Operational Parameters

Many parameters, both design and operational, determine the quantities IHP, LHP and hence BHP, ISFC and BSFC. Full treatment of these parameters may be found in References 11-14, 29.

Design parameters are those fixed by engine design such as: engine geometry, compression ratio, valve timing , gasoline octane rating , fuel metering system, air induction system, exhaust system, bearing design and so on. In the present study the design parameters are considered quantities not under our control.

Operational parameters characterize the environment and mode of operation of the engine. These are:

1.	Fuel-dry air mass ratio	F
2.	Ignition timing	τ
3.	Inlet manifold absolute pressure	P_m
4.	Inlet manifold temperature	T_m
5.	Cylinder head temperature	CHT
6.	Exhaust back-pressure	P_e
7.	Exhaust gas temperature	T_e
8.	Engine shaft speed	N_E

9. Engine brake torque Q_E

10. Atmospheric mass ratio water vapour/dry air h

These apply to both naturally aspirated and turbocharged engine types. Each operational parameter is here considered to be measurable during the operation of the engine; and with the exception of atmospheric humidity, each is considered to be controllable (its steady state value may be set within a finite range). However, the operational parameters are not independently controllable, so that only a limited number of them may be prescribed at any one time. The means available for controlling the operational parameters are:

a) Fuel flow lever

b) Variable spark-advance system

c) Throttle

d) Induction air heater (and after-cooler in the case of turbocharged engines)

e) Engine cowl flaps

f) Turbine waste-gate and nozzle geometry, in the case of turbocharged engines

g) Propeller governor

h) Flight altitude

The operational parameters primarily influenced by each of these controls are indicated in Table E.1.

The discussion following addresses the computation of engine performance, and its variation with changes in the operational parameters 1-10, with the exception of atmospheric humidity.

INDICATED HORSEPOWER

The well known expression for indicated horsepower is written (13):

$$IHP = KJ\ \dot{m}_f\ Q_c\ \eta_i \qquad (E.10)$$

$$= KJ\ \dot{m}_a\ F\ Q_c\ \eta_i \qquad (E.11)$$

where K = constant = 1/550 × 3600 hp.hr/ft.lb

J = mechanical equivalent of heat = 777.98 ft.lb/Btu

$\dot{m}_f$ = fuel mass flow rate , lbm/hr

$\dot{m}_a$ = dry air mass flow rate, lbm/hr

F = fuel-dry air mass ratio = $\dot{m}_f/\dot{m}_a$

Q_c = heat of combustion per unit mass fuel, Btu/lbm

η_i = indicated thermal efficiency

Aviation gasoline is here taken to have the properties (13):

C_8H_{17}	Chemical composition
$M_f = 113$	Molecular weight
$F_c = 0.067$	Stoichiometric fuel-dry air mass ratio
$Q_c = 19{,}020$	Lower heat of combustion, Btu/lbm

Using Equation E.11 we may write, for a change in operating conditions from point 1 to point 2:

$$IHP_2 = IHP_1 \left[\frac{\dot{m}_{a_2}}{\dot{m}_{a_1}}\right]\left[\frac{F_2}{F_1}\right]\left[\frac{\eta_{i_2}}{\eta_{i_1}}\right] \qquad (E.12)$$

Air Mass Flow Rate

The total induction mass flow rate (denoted $\dot{m}_i$ lbm/hr) through the engine consists of a mixture of dry air, fuel and water vapour.

This induction mixture flow rate is conveniently expressed in terms of the volumetric efficiency of the engine (13):

$$\dot{m}_i = 60\ \eta_v\ N_E D\ \rho_i/2 \quad \text{lbm/hr} \tag{E.13}$$

where η_v = volumetric efficiency based on inlet manifold density

N_E = engine shaft speed, revolutions/minute

D = total displacement volume of the engine, cu ft

ρ_i = density of mixture at the inlet port, lbm/cu ft

Defined in this way, "the volumetric efficiency measures the pumping performance of the cylinder and valves alone" (13). This definition is the most convenient measure of pumping performance in turbocharged engines, and is retained for use with naturally aspirated engines.

Letting ρ_m be the mass of dry air per unit volume of fresh mixture at the inlet port, (and since $\dot{m}_a/\rho_m = \dot{m}_i/\rho_i$) we have the dry air mass flow rate $\dot{m}_a$ as:

$$\dot{m}_a = 60\ \eta_v\ N_E D\ \rho_m/2 \quad \text{lbm/hr} \tag{E.14}$$

Hence the variation in dry air mass flow rate from operating condition 1 to 2 is:

$$\frac{\dot{m}_{a_2}}{\dot{m}_{a_1}} = \left[\frac{\eta_{v_2}}{\eta_{v_1}}\right]\left[\frac{N_{E_2}}{N_{E_1}}\right]\left[\frac{\rho_{m_2}}{\rho_{m_1}}\right] \tag{E.15}$$

Inlet Air Density

The inlet manifold density of dry air is expressed (13) as:

$$\rho_m = \frac{P_m}{R_a T_m}\left[\frac{1}{1 + F\left(\frac{M_a}{M_f}\right) + h\left(\frac{M_a}{M_w}\right)}\right] \quad \text{lbm/ft}^3 \tag{E.16}$$

In this work, where engines using inlet port fuel injection are studied, we may take (13):

P_m = inlet manifold absolute pressure, lb/ft^2

T_m = inlet manifold absolute temperature, degrees Kelvin

R_a = gas constant for dry air

= 96.03474 ft lb/lbm.degree Kelvin

M_a = molecular weight of dry air

= 28.96408

M_w = molecular weight of water

= 18.016 (Ref. 42)

h = mass ratio of water vapour to dry air where P_m and T_m are measured.

The values of R_a and M_a have been computed from the sea level values of pressure, temperature and density in the standard atmosphere (see Appendix B).

The contribution of F in Equation E.16 is here ignored since fuel evaporation is by no means complete during the induction process with inlet port fuel injection. In addition, humidity is not considered as a variable in this study: all computations pertain to a dry atmosphere. Consequently, Equation E.16 is here used in the form:

$$\rho_m = \frac{P_m}{R_a T_m} \quad lbm/ft^3 \tag{E.17}$$

and the variation in inlet manifold dry air density from operating condition 1 to 2 is:

$$\frac{\rho_{m_2}}{\rho_{m_1}} = \frac{P_{m_2}}{P_{m_1}} \cdot \frac{T_{m_1}}{T_{m_2}} \tag{E.18}$$

Volumetric Efficiency

The volumetric efficiency (based on inlet manifold conditions as defined by Equation E.14) may be expressed by the functional relationship:

$$\eta_v = \eta_v[N_E, \text{CHT}, T_m, P_m, P_e, \phi] \qquad \text{(E.19)}$$

where N_E = engine shaft speed

CHT = cylinder head temperature

T_m = inlet manifold absolute temperature

P_m = inlet manifold absolute pressure

P_e = exhaust absolute back-pressure

ϕ = equivalence ratio, defined as:

$$\phi = \frac{\text{fuel-air mass ratio of fresh mixture}}{\text{stoichiometric fuel-air mass ratio}}$$

$$= F/F_c \qquad \text{(E.20)}$$

All engine design ratios have been omitted from Equation E.19 since they are not variables. We seek an expression for the variation of η_v when the operational parameters in Equation E.19 are varied from condition 1 to condition 2.

Taylor (13) writes the functional relation for volumetric efficiency in the form of non-dimensional groups. He has (with some rearrangement):

$$\eta_v = f_1[Z, \frac{P_m}{P_e}, R_N, \frac{T_m C_p}{FQ_c}, \frac{T_c C_p}{FQ_c}, F, R_1, \ldots R_n] \qquad \text{(E.21)}$$

where Z = inlet valve Mach Index, defined in terms of piston speed and speed of sound in the inlet manifold

R_N = Reynolds Index based on the speed of sound in the

inlet manifold

C_p = specific heat of fresh mixture at constant pressure

T_c = coolant temperature (for liquid-cooled engines), here taken to be cylinder head temperature

$R_1, \ldots R_n$ = engine design ratios.

Taylor (13) shows that:

a) η_v is a unique function of Mach Index Z for a given engine (Z is defined by Equation E.44). For the reasonably small variations in piston speed and inlet manifold temperature encountered herein, with variation of operating condition for a given engine, the functional dependence of η_v on Z is ignored.

b) η_v is a non-linear function of P_e/P_m, dependent on the value of Z. Variations of η_v with back-pressure are reflected in variations of Brake and Indicated horsepower.

Lycoming (25) states: "Many tests have been made, including some at Lycoming, which show that the weight air consumed, and therefore the IHP developed at constant mixture strength, is inversely proportional to the exhaust back pressure raised to the one tenth power." Pye (12) states: "The effect of a change of the exhaust back pressure upon the BHP of an engine will depend a good deal upon the speed and the valve timing; and the magnitude of the effect will be different according to whether the back pressure is above or below that in the inlet manifold."

In the present work, the functional dependence of volumetric efficiency on engine pressure ratio P_m/P_e is taken to be

$$\frac{\eta_{v_2}}{\eta_{v_1}} = \left[\frac{P_{m_2}}{P_{e_2}}\right]^{\varepsilon_p} \left[\frac{P_{e_1}}{P_{m_1}}\right]^{\varepsilon_p} \qquad \text{(E.22a)}$$

and $\varepsilon_p = 0.1$ is used as a typical value.

c) The effect of Reynolds Index R_N on volumetric efficiency is negligible.

d) Volumetric efficiency varies almost in direct proportion to $T_m^{0.5}$.

Lycoming (25) have found that, for Lycoming naturally aspirated aircraft engines employing inlet port fuel injection, the indicated horsepower and the air mass flow rate are both proportional to $1/T^{0.8}$, at sea level (and at altitudes above sea level - Reference 43) where T is the fuel injection system airbox inlet absolute temperature (the airbox houses the air throttle butterfly).

In the present work involving naturally aspirated inlet port fuel injection engines, we modify this Lycoming result and write

$$\dot{m}_a \propto \frac{1}{T_m^{(1-\varepsilon_t)}}$$

where T_m is the inlet manifold absolute temperature. Comparing this expression with Equation E.14 yields

$$\eta_v \propto T_m^{\varepsilon_t}$$

so that

$$\frac{\eta_{v_2}}{\eta_{v_1}} = \left[\frac{T_{m_2}}{T_{m_1}}\right]^{\varepsilon_t} \qquad \text{(E.22b)}$$

This variation accounts for

i) The effect of fuel evaporation on the mixture temperature at inlet valve closing

ii) Heat transfer to the mixture from the engine: from the inlet port, inlet valve and cylinder walls while the inlet valve is open.

In accordance with the findings of Lycoming, $\varepsilon_t = 0.2$ is used in this work as a typical value; and this value is here taken to be invariant with flight altitude.

e) Coolant temperature change (in liquid-cooled engines) has a small effect on volumetric efficiency over a range of 610±50°R. The variation is expressed as

$$\frac{\eta_{v_2}}{\eta_{v_1}} = \frac{T_{c_1} + 2000}{T_{c_2} + 2000}$$

(coolant temperatures T_{c_1} and T_{c_2} in degrees Rankine) about a nominal operating point $T_{c_1} = 610°R$. The corresponding nominal operating point cylinder head temperature (CHT) would be greater than 610°R, and a 1°R variation in coolant temperature would correspond to a larger variation in CHT.

With air-cooled engines, the temperature of the cooling air affects the CHT which in turn affects volumetric efficiency

(as here defined) by heat transfer from the inlet port, inlet valve and cylinder walls. This effect is accounted for with normal levels of CHT and changing T_m by the factor in Equation E.22b. Variations in CHT itself are here considered to have no effect on that factor, nor to vary volumetric efficiency when T_m is fixed. It is recognized that large departures in CHT from normal values will almost certainly violate these two assumptions.

f) Fuel-air ratio affects the temperature drop of the inducted mixture due to fuel evaporation. The effect of fuel evaporation on volumetric efficiency, included in (d) above, is here considered to be invariant with fuel-air ratio.

Considering items (a)-(f) above together, the change in volumetric efficiency (for engines employing inlet port fuel injection) from operating point 1 to 2 is expressed:

$$\frac{\eta_{v_2}}{\eta_{v_1}} = \left[\frac{T_{m_2}}{T_{m_1}}\right]^{\varepsilon_t} \left[\frac{P_{m_2}}{P_{e_2}}\right]^{\varepsilon_p} \left[\frac{P_{e_1}}{P_{m_1}}\right]^{\varepsilon_p} \qquad \text{(E.23)}$$

Fuel-Air Ratio

Equation E.12 shows that the variation in IHP from condition 1 to 2 is in direct proportion to the variation in fuel-air ratio, for constant dry air mass flow rate and constant indicated thermal efficiency. Note that

$$\frac{F_2}{F_1} = \frac{\phi_2}{\phi_1} \qquad \text{(E.24)}$$

where ϕ = equivalence ratio.

In General Aviation piston engines, fuel is metered to the engine for three purposes:

1. To provide a combustible mixture for the development of power.
2. To aid in cooling the engine, especially at high power levels.
3. To ensure detonation-free operation.

The fuel-air ratio appropriate to the various regions of engine operation is discussed under the heading Fuel Metering Schedule below.

Indicated Thermal Efficiency

The indicated thermal efficiency measures the efficiency of conversion to indicated work of the total heat energy available in the fuel burned. The total available heat energy per unit mass of fuel is Q_c, the lower heat of combustion (13).

Comparison of Equations E.7 and E.10 shows the relationship between indicated thermal efficiency and indicated specific fuel consumption,

$$\eta_i = \frac{1}{KJQ_c(ISFC)} \qquad (E.25)$$

The indicated thermal efficiency of a spark ignition reciprocating internal combustion engine can never exceed the ideal efficiency of the 'constant-volume air cycle' for which

$$\eta = 1 - (\frac{1}{r})^{\gamma-1} \qquad (E.26)$$

where r = the compression ratio of the cycle

γ = the ratio of specific heats for air, considered as a perfect gas.

While useful in establishing an upper bound for efficiency, the constant

volume air cycle does not consider the phenomenon of combustion. The idealized cycle which does consider combustion is the 'constant volume fuel-air cycle' whose indicated efficiency is somewhat lower than that of Equation E.26 because (13) of:

1. Variations in specific heats of the gases
2. Progressive and incomplete oxidation of the fuel to CO_2 and H_2O.

Real four-stroke spark ignition engines demonstrate indicated thermal efficiencies below those computed for their equivalent constant volume fuel-air cycles which "represent the limit which can be approached by spark-ignition engines" (13). Departures from this limit, according to Taylor (13) may be attributed to:

1. Leakage - blow-by, usually insignificant
2. Incomplete combustion - failure to reach theoretical chemical equilibrium before the exhaust valve opens.
3. Progressive burning - finite flame speed.
4. Time losses - the loss of work done on the pistons due to piston motion during combustion.
5. Heat losses - losses of heat energy to the piston, cylinder head and cylinder walls during the compression and expansion strokes.
6. Exhaust losses - due to opening the exhaust valve before bottom dead center. This loss is seen as a roundoff in the pV cycle diagram during the blowdown process.

As a consequence of these considerations, the following functional relation may be written for the indicated thermal efficiency of a given

engine burning a particular type of fuel:

$$\eta_i = f_2[\phi, \tau, N_E, P_m, P_e, T_m, CHT, h] \qquad (E.27)$$

where τ = ignition timing: the number of crank angle degrees before top dead center (BTDC) at which the spark (ignition event) occurs.

In Equation E.27 the compression ratio and engine geometry (including valve timing and number of ignition points per cylinder) have been omitted since they are here considered to be constants, as are mixture homogeneity and the condition of the spark. In addition, the residual exhaust gas fraction is accounted for by ϕ, P_m, P_e and T_m.

Since indicated work is obtained directly from the pV cycle diagram, the indicated thermal efficiency may be obtained from the pV cycle diagram and a knowledge of the fuel mass burned during the cycle. The contribution to η_i of each of the arguments of f_2 in Equation E.27 might well be described in terms of its effect on the pV diagram. It is more convenient however, to consider an equivalent plot of cylinder pressure versus crank angle for this purpose.

Figure E.2 shows a typical trace of cylinder pressure versus crank angle for the compression and power strokes. The magnitude of the indicated work is determined by:

(a) The magnitude of δ, the location of the pressure peak in crank angle degrees after top dead center (ATDC)

(b) The magnitude P_δ of the peak cylinder pressure

(c) The shape of the pressure versus crank angle curve

of Figure E.2, which together determine the area (A+C) of Figure E.1.

We are concerned with maximizing indicated thermal efficiency, and therefore with maximizing the sum contribution of (a)-(c) to indicated work for a given mass of fuel burned. Maximizing indicated thermal efficiency contributes to minimizing BSFC (Equations E.25 and E.9).

It is well known that for wide variations in the operating conditions of any spark-ignition internal combustion engine, maximum torque is obtained when the pressure peak P_δ falls within a very small neighborhood of $\delta=\delta_o$ (a constant) crank angle degrees ATDC. Pye (11) determines a single angle $\delta=\delta_o = 12^o$ ATDC for the engines in his discussion; Curtiss Wright (15) claim $\delta_o \simeq 15^o$ ATDC for their Turbo Compound TC18 engine; and Powell (44) found $\delta_o \simeq 15.7^o$ ATDC a good mean value for his work with a CFR engine†. Since variation of the location of P_δ cannot significantly affect the Lost Horsepower, it is apparent that indicated work and hence indicated thermal efficiency are both maximized by so positioning the pressure peak.

Consider the operational parameters which determine the location δ of the pressure peak P_δ.

Following the ignition event, there is a delay interval during which no appreciable rise in cylinder pressure occurs due to combustion. The delay interval is characterized by a time period T_d and a change in crank angle θ_d. Following the delay interval is the pressure rise interval, during which the cylinder pressure rises to its peak value. The pressure rise interval is characterized by a time period T_p and a change in crank angle θ_p. The following functional relations may be written from Pye(11) and Taylor (13):

---

†This fact stimulated the successful attempt by Powell (44) to use cylinder pressure peak position feedback in the closed-loop control of ignition timing for minimum brake specific fuel consumption.

$$T_d = f_3(\phi) \tag{E.28}$$

$$\theta_d = f_4(N_E, \phi) \tag{E.29}$$

$$\theta_p = f_5(\phi, T_\tau, P_\tau, f, h) \tag{E.30}$$

where T_τ is the mixture temperature at the ignition event.

P_τ is the mixture pressure at the ignition event.

f is the residual exhaust gas fraction.

Pye(11) shows that T_d is not sensitive to changes in T_τ and P_τ; also T_d was found to be virtually independent of engine speed N_E, but dependent on ϕ. Consequently θ_d varies approximately in direct proportion to N_E, and varies with ϕ. The pressure rise time T_p decreases with increasing flame speed, which in turn increases with turbulence level and hence with engine speed. As a result, θ_p is virtually independent of N_E for fixed values of ϕ, T_τ, P_τ, f and h. The flame speed is strongly dependent on ϕ and T_τ (29); it is also dependent on f(11) and h(13, 44).

Consequently the crank angle interval between the ignition event and the peak of the cylinder pressure is, from Figure E.2 and Equations E.29, and E.30:

$$\tau + \delta = \theta_d + \theta_p = f_6(\phi, N_E, P_m, P_e, T_m, CHT, h) \tag{E.31}$$

where, for a given engine: T_τ and P_τ have been assumed to be determined by P_m, T_m, CHT and h; and the residual gas fraction f of the charge by ϕ, P_m, P_e and T_m.

Rearranging,

$$\delta = f_6(\phi, N_E, P_m, P_e, T_m, CHT, h) - \tau \tag{E.32}$$

For maximum η_i we have $\delta \simeq \delta_o$ a constant, for variations in the engine operating conditions: in particular for variations in the arguments of the function f_6 of Equation E.32. Constancy of δ under these conditions can only be achieved through variation of ignition timing τ. The value of $\tau = \tau_o$ which establishes maximum torque and hence maximum η_i in any

operating condition is called Minimum ignition advance for Best Torque (MBT). Considering any variation in δ about δ_o at MBT to be itself dependent only on the arguments of f_6, we may express the MBT ignition timing τ_o as

$$\tau_o = f_7(\phi, N_E, P_m, P_e, T_m, CHT, h) \qquad (E.33)$$

"Generally, the purpose of using a spark timing other than that for best power is either to control detonation or to make it unnecessary to re-adjust the spark as a function of engine operating conditions" (Taylor 13). Detonation is discussed in Appendix F. The use of fixed ignition timing is the current practice in General Aviation piston engines.

Variation of η_i with each of the arguments of f_2 in Equation E.27 is now considered.

Equivalence Ratio and Ignition Timing:

These two arguments are considered together because of their powerful interaction in determining η_i. Figure E.3 (45) depicts the performance of a naturally aspirated Volkswagon automobile engine tested under the conditions:

1. Constant RPM
2. Constant fuel flow rate $\dot{m}_f$
3. Air-fuel ratio and hence torque varied by throttling. Hence P_m is not constant.

No indication is given by Reference 45 of the variation of P_e, T_m, CHT and h in Figure E.3. The parameter λ is the inverse of

equivalence ratio ϕ ($\lambda < 1$ is a mixture richer than stoichiometric, $\lambda > 1$ is a mixture leaner than stoichiometric). Variation of BMEP (which is proportional to engine shaft torque) and BSFC are shown along lines of constant ignition timing τ. For mixtures richer than stoichiometric, BSFC and torque show a very weak dependence on ignition timing; for mixtures leaner than stoichiometric they show a marked dependence on ignition timing. MBT timing establishes the upper boundary of the BMEP curves, and the lower boundary of the BSFC curves. With MBT timing, BSFC falls continuously as the mixture is leaned, reaching a minimum around $\lambda = 1.3$ ($\phi = 0.77$). No indication of the onset of rough running is given on the curves of Figure E.3.

Figure E.4 (16) depicts similar data taken with a Lycoming TIO-541-E (turbocharged) aircraft engine, in flight at constant BHP and constant RPM; rough running regions are indicated. For these data, P_m and CHT vary as shown; while variations in P_e, T_m and h are not presented in Ref. 16. These data show a decrease in BSFC of about 18% from $\phi = 1$ to $\phi = 0.75$, along the lower envelope of the curves. Since 35^o spark advance was not established to be MBT (16), a further decrease in BSFC may indeed have been possible with ignition timing advanced beyond 35^o BTDC.

Figure E.5 (16) depicts similar data taken with a Lycoming TIO-541-E (turbocharged) aircraft engine, in flight at constant inlet manifold pressure and constant RPM; rough running regions are indicated. For these data, BHP and CHT vary as shown; while variations in P_e, T_m and h are not presented in Ref. 16.

Figures E.3-E.5 show similar trends in BSFC with variations in ϕ and ignition timing. These data suggest that, for a fixed set $\{N_E$, ($\dot{m}_f$ or BHP or P_m), P_e, T_m, CHT, h$\}$:

1. Lowest BSFC is obtained with $\phi < 1$ and MBT ignition timing
2. For constant $\phi > 1$: BSFC is not sensitive to ignition timing so that a wide range of ignition timings is essentially MBT.
3. For constant $\phi < 1$: departure from MBT can result in large increases in BSFC.

The BSFC curves of Figures E.3-E.5 show brake performance and therefore reflect variations in pumping losses and mechanical friction. If the pumping and mechanical friction losses were removed from these data, and the brake performance thereby reduced to indicated performance, one would expect curves for ISFC similar in form to these BSFC curves. Since η_i is inversely proportional to ISFC (Equation E.25), we expect (for a given engine) a variation of η_i with ϕ and ignition timing similar to that shown in Figure E.6, for constant values of $\{N_E$, ($\dot{m}_f$ or BHP or P_m), P_e, T_m, CHT, h$\}$. The envelope of these curves corresponds to MBT ignition timing. MBT ignition timing becomes progressively more advanced as ϕ decreases.

Throughout the following discussion, and in keeping with Equation E.27, indicated thermal efficiency will be considered to be a function of P_m rather than $\dot{m}_f$ or BHP. The following notation is defined:

η_i' = indicated thermal efficiency for an equivalence ratio ϕ, a set $S' = \{N_E', P_m', P_e', T_m', CHT', h'\}$, and MBT ignition timing τ_o'. A curve such as that shown in Figure E.7 (suitably adjusted for compression ratio and engine geometry) is appropriate to every General Aviation piston engine. Note that η_i' is a simple function of equivalance ratio ϕ.

η_o' = equivalent constant volume fuel-air cycle indicated efficiency corresponding to ϕ and S'.

η_i = indicated thermal efficiency corresponding to equivalence ratio ϕ, a set $S = \{N_E, P_m, P_e, T_m, CHT, h\}$, and ignition timing τ. $S \neq S'$.

η_o = equivalent constant volume fuel-air cycle indicated efficiency corresponding to ϕ and S.

Variation of the operating conditions from the set S' to the set S, and in the ignition timing, results in:

$$\eta_i = \eta_i' + \left.\frac{\partial \eta_i}{\partial N_E}\right|_{S';\phi} dN_E + \left.\frac{\partial \eta_i}{\partial P_m}\right|_{S',\phi} dP_m + \left.\frac{\partial \eta_i}{\partial P_e}\right|_{S',\phi} dP_e$$

$$+ \left.\frac{\partial \eta_i}{\partial T_m}\right|_{S',\phi} dT_m + \left.\frac{\partial \eta_i}{\partial (CHT)}\right|_{S',\phi} d(CHT) + \left.\frac{\partial \eta_i}{\partial h}\right|_{S',\phi} dh$$

$$+ \left.\frac{\partial \eta_i}{\partial \tau}\right|_{S',\phi} d\tau + (\text{higher order terms}) \qquad (E.34)$$

where $dN_E = N_E - N_E'$ etc., and the partial derivatives are evaluated for the conditions (S',ϕ).

When MBT ignition timing is employed, the constraint Equation E.33 applies. Considering this constraint in conjunction with Equation E.34 (and neglecting terms higher than first order therein) we may write:

$$\eta_i = \eta_i' + \left.\frac{\partial \eta_i}{\partial N_E}\right|_{S',\phi,\tau_o} dN_E + \left.\frac{\partial \eta_i}{\partial P_m}\right|_{S',\phi,\tau_o} dP_m + \left.\frac{\partial \eta_i}{\partial P_e}\right|_{S',\phi,\tau_o} dP_e + \left.\frac{\partial \eta_i}{\partial T_m}\right|_{S',\phi,\tau_o} dT_m$$

$$+ \left.\frac{\partial \eta_i}{\partial (CHT)}\right|_{S',\phi,\tau_o} d(CHT) + \left.\frac{\partial \eta_i}{\partial h}\right|_{S',\phi,\tau_o} dh \qquad \text{(E.35)}$$

where the subscript τ_o is used to indicate that MBT ignition timing is maintained during each perturbation.

Following is a discussion of each of the perturbation terms on the right of Equation E.35.

Engine Shaft Speed:

Figure E.8 shows some data from References 11 and 13 on the effects of engine speed on η_i. In both cases fuel-air ratio was constant and MBT timing was used.† According to Pye (11): "an increase or decrease of speed as much as 20 per cent. above or below the normal speed of an engine will have a very small effect on efficiency". The variation in η_i which does occur with change of speed is the result of the collective contributions of:

†The use of MBT ignition timing is implied rather than explicitly stated by Pye(11).

(a) Decreased heat loss to piston, cylinder walls and cylinder head during combustion and expansion, due to decreasing time for heat transfer as speed increases,

(b) Increased rate of heat transfer to piston, cylinder walls and cylinder head, due to increased scouring action of the gases (turbulence) over the metal surfaces as speed increases,

(c) Varying effect of the fixed valve timing with speed changes.

The speed variations encountered in General Aviation piston engines in cruise are typically $\overline{N}_E \pm 300$ RPM, with $\overline{N}_E$ in the range 2200-2600 RPM. The percentage speed variations are therefore within 15% of the midrange value $\overline{N}_E$.

In this study therefore, variations of indicated thermal efficiency η_i with changes in engine speed are ignored when MBT timing is employed: $\left.\frac{\partial \eta_i}{\partial N_E}\right|_{S',\phi,\tau_o} = 0$ is assumed.

Inlet Manifold Pressure and Exhaust Back-Pressure:

Figure E.9(a) shows data from Reference 13 on the effect of inlet pressure $p_1 \simeq P_m$ on indicated thermal efficiency of fuel-air cycles, for various valuesof equivalence ratio $F_R = \phi$ (fuel 1-octene) and inlet temperature $T_1 \simeq T_m$. Over the range $0.5 < p_1 < 2.0$ atmospheres, there is negligible variation in indicated thermal efficiency. These figures are supported for a real

cycle by Taylor (13, page 131) wherein varying P_m from 28 to 20 inches Hg absolute, with MBT, altered η_i from 0.292 to 0.304[†].

As an engine is throttled, there is a progressive rise in the proportion of residual exhaust gas which mixes with the fresh charge during each cycle. This dilution decreases the flame speed and with fixed ignition advance, results in a dramatic fall in indicated thermal efficiency: see curve 'a' of Figure E.9(b) taken from Pye(11)[††]. According to Pye (11): "...the only way of avoiding the fall of efficiency when a homogeneous mixture is throttled is the provision of adequate ignition advance". With MBT ignition timing, curve 'b' (wherein ignition timing is progressively advanced as the throttle is closed) of Figure E.9(b) first rises slightly (as does the quoted data for the real cycle of Taylor (13)) and then drops back to its full load value. However, the variation from a constant value of η_i with throttling at MBT is slight.

The quantity of residual exhaust gas in the cylinder is influenced not only by P_m, but also by the exhaust back-pressure P_e(13). MBT ignition advance nullifies the influence of P_e on η_i, as was the case with P_m(13).

Consequently in this study, variations of indicated thermal efficiency η_i with changes of inlet manifold pressure and exhaust

---

[†]These figures were obtained on a CFR engine , 3 1/4 x 4 1/2 inch: compression ratio 6:1, P_e = 30 in. Hga, T_m = 150°F, N_E = 1200 rpm, ϕ = 1.13.

[††]It is assumed that equivalence ratio is constant in Figure E.9(b), a fact not stated by Pye(11).

back-pressure are assumed negligible, when MBT ignition timing is employed: $\left.\frac{\partial \eta_i}{\partial P_m}\right|_{S',\phi,\tau_o} = \left.\frac{\partial \eta_i}{\partial P_e}\right|_{S',\phi,\tau_o} = 0$ is assumed.

Cylinder Head Temperature:

Discussing a typical heat balance for an engine of compression ratio 5:1, Pye(11) states: "The important thing to grasp about the relationship between I.H.P. and heat loss to the cylinder walls is ... that even if it were possible to run an engine under truly adiabatic conditions in which this loss to the cylinder walls was entirely suppressed, that would only mean an increase in the heat to I.H.P. of some 4 per cent. of the total." The majority of heat lost to the cylinder walls cannot be converted to indicated work even in this ideal case.

We therefore consider that variations in Cylinder Head Temperature resulting from changes in heat flow rate from the burned gases are not indicative of significant variations in indicated thermal efficiency.

As a result of these considerations, this study assumes that indicated thermal efficiency shows no direct dependence on cylinder head temperature:

$$\frac{\partial \eta_i}{\partial (\overline{CHT})} = \left.\frac{\partial \eta_i}{\partial (\overline{CHT})}\right|_{S',\phi,\tau_o} = 0 \text{ is assumed.}$$

In some installations, cylinder head temperature influences inlet manifold temperature T_m and thereby indirectly influences indicated thermal efficiency. The effect of inlet manifold temperature T_m on indicated thermal efficiency is discussed below.

Humidity:

The effect of humidity on indicated thermal efficiency is discussed by Taylor (13). In this study, humidity is not considered to be a variable: all computations pertain to a dry atmosphere. Hence $h' = dh = 0$.

Inlet Manifold Temperature:

As a result of the above discussion, Equation E.35 is contracted to

$$\eta_i = \eta_i' + \left.\frac{\partial \eta_i}{\partial T_m}\right|_{S',\phi,\tau_o} dT_m \qquad \text{(E.36)}$$

The author was unable to obtain data showing the explicit variation of η_i with T_m, as required by the derivative in Equation E.36. The following means was therefore adopted for computing variations of η_i with T_m.

Let

$$\left.\begin{aligned} R &= \eta_o/\eta_o' \\ R_o &= \eta_i'/\eta_o' \\ R_1 &= \eta_i/\eta_o \end{aligned}\right\} \qquad \text{(E.37)}$$

Figure E.10(a) taken from Taylor (13) shows the variation of R = (constant volume fuel-air cycle indicated efficiency)/(constant volume fuel-air cycle indicated efficiency for $T_1 = T'_m = 700\ R^o$) with inlet temperature $T_1 = T_m$. The curves are drawn for various values of $F_R = \phi$ (fuel 1-octene) and inlet pressures $p_1 = P_m$ (atmospheres). Indicated efficiency is apparently most sensitive to inlet temperature T_m with fuel-air ratios near stoichiometric, and with low manifold pressures. It is assumed in this work that Figure E.10(a) is typical of General Aviation piston engines, and that it is typical for all temperatures T'_m. That is,

$$R = R(\phi,P_m,T_m) = 1 + \left.\frac{\partial R(\phi,P_m,T_m)}{\partial T_m}\right|_{S'} dT_m \qquad (E.38)$$

where

$$\left.\frac{\partial R(\phi,P_m,T_m)}{\partial T_m}\right|_{S'} = \left\{ \left[\frac{\partial}{\partial T_1} \left[\frac{\eta}{\eta_{T_1 = 700}} \right] \right]_{\substack{\phi = F_R \\ P'_m = p_1 = 1 \text{ atmos.} \\ T_1 = 700\ R^o}} \right\}$$

FIGURE E.10(a)

$$dT_m = T_m - T'_m$$

The small influence of p_1 on R is ignored.

Figures E.10(b-e), also from Taylor (13), show typical variations of (indicated thermal efficiency)/(indicated efficiency of the equivalent constant volume fuel-air cycle) with compression ratio r, exhaust pressure p_e/inlet pressure p_i, equivalence ratio F/F_c, and inlet temperature T_i (MBT ignition timing is assumed throughout). Comparing the present notation with that shown in these figures:

Present Notation: $P_e = p_e$: Figures E.10(b-e)

$P_m = p_i$

$\phi = F/F_c$

$T_m = T_i$

$\eta_i = \eta$

$\eta_o = \eta_o$

For a given compression ratio engine, it is apparent that the effects of P_e/P_m are negligible, and that the effects of ϕ and T_m are independent. Hence:

$$R_1 = R_1(\phi,T_m) = \frac{\eta_i}{\eta_o} = R_o(\phi,T_m)\Big|_{S',\tau_o} + \frac{\partial R_1(\phi,T_m)}{\partial T_m}\Big|_{S;\tau_o} dT_m \qquad (E.39)$$

where $R_o = R_o(\phi,T_m)\Big|_{S',\tau_o}$ is given by Figure E.10(d)

$\dfrac{\partial R_1(\phi,T_m)}{\partial T_m}\Big|_{S',\tau_o}$ is the slope of Figure E.10(e)

$dT_m = T_m - T'_m$

$T'_m = 550^o$ Rankine in Figure E.10(d)

It is assumed in this work that Figures E.10(b-e) are typical of General Aviation piston engines.

Now

$$\frac{\eta_i}{\eta'_i} = \frac{\eta_i}{\eta_o}\,\frac{\eta_o}{\eta'_o}\,\frac{\eta'_o}{\eta'_i}$$

$$= \frac{R_1\,R}{R_o}$$

Therefore

$$\eta_i = \eta_i' \left[\frac{R_1 R}{R_o} \right] \qquad \text{(E.40)}$$

Equation E.40 is used in this work in the computation of η_i for MBT ignition timing. For these computations:

1. η_i' is represented by a cubic equation

$$\eta_i'(\phi) = e_o + e_1\phi + e_2\phi^2 + e_3\phi^3 \qquad \text{(E.41)}$$

where the coefficients e_o, e_1, e_2, e_3 are constants (see Figure E.7)

2. $T_m' = 550^o$ Rankine $= 305.556^o$ Kelvin
3. $dT_m = T_m - T_m'$
4. Figures E.10 (a,d,e) and Equations E.38 and E.39 supply the bracketed quantities on the right hand side of Equation E.40.

Figure E.11 shows a typical variation of the quantity $R_1 R/R_o$ (Equation E.40) with T_m, computed from the data of Figure E.10.

Summary of Effects on Indicated Thermal Efficiency:

Indicated thermal efficiency η_i has been shown to be a function of $\{\phi,\tau,N_E,P_m,P_e,T_m,CHT,h\}$.

MBT ignition timing maximizes η_i for all sets $\{\phi,N_E,P_m,P_e,T_m,CHT,h\}$. Maximizing η_i contributes to minimizing BSFC. In this study MBT

ignition timing is assumed for all modes of engine operation. This assumption reduces η_i to a function of ϕ and T_m, given by Equations E.40 and E.41.

The contributions of ϕ, τ and P_m to η_i (Equation E.34) are shown schematically in Figure E.12. The variations of η_i with ϕ in the vertical plane A correspond to Figure E.6; while the variations of η_i in the plane B (constant ϕ) are postulated on the basis of Figure E.9. It is postulated that similar figures will be obtained when ΔP_m is replaced by either ΔN_E, ΔP_e, ΔT_m, ΔCHT or Δh in Figure E.12, noting that $\partial \eta_i / \partial T_m \Big|_{S', \phi, \tau_o} \neq 0$.

Summary of Indicated Horsepower Variations

Combining Equations E.15, E.18 and E.23, the variation of air mass flow rate from operating point 1 to operating point 2 is:

$$\dot{m}_{a_2} = \dot{m}_{a_1} \left[\frac{T_{m_1}}{T_{m_2}}\right]^{(1-\varepsilon_t)} \left[\frac{P_{m_2}}{P_{m_1}}\right]^{(1+\varepsilon_p)} \left[\frac{P_{e_1}}{P_{e_2}}\right]^{\varepsilon_p} \left[\frac{N_{E_2}}{N_{E_1}}\right] \quad \text{(E.42)}$$

Then, from Equations E.12, E.24 and E.42, the variation of indicated horsepower from operating point 1 to operating point 2 is:

$$IHP_2 = IHP_1 \left[\frac{\phi_2}{\phi_1}\right] \left[\frac{\eta_{i_2}}{\eta_{i_1}}\right] \left[\frac{T_{m_1}}{T_{m_2}}\right]^{(1-\varepsilon_t)} \left[\frac{P_{m_2}}{P_{m_1}}\right]^{(1+\varepsilon_p)} \left[\frac{P_{e_1}}{P_{e_2}}\right]^{\varepsilon_p} \left[\frac{N_{E_2}}{N_{E_1}}\right]$$

(E.43)

where η_{i_1} and η_{i_2} are separately computed from Equation E.40.

LOST HORSEPOWER

The lost mean effective pressure and hence the lost horsepower are determined by the energy required for pumping, plus that required to overcome mechanical friction.

Pumping Losses

Losses of mean effective pressure due to pumping occur at inlet and exhaust valves. Taylor (13) has for the inlet valve:

$$\frac{MEP_i}{P_m} = f_i \left[Z, \frac{P_e}{P_m} \right] \tag{E.44}$$

for a given engine, where MEP_i is the mean inlet pressure during the inlet stroke, and Z is the inlet valve Mach Index defined as:

$$Z = \left[\frac{b}{d}\right]^2 \frac{s}{C_i a} \quad \text{(non-dimensional)}$$

$$= \frac{\ell (b/d)^2}{30\, C_i \sqrt{g\gamma R_m}} \cdot \frac{N_E}{\sqrt{T_m}}$$

$$= C_Z \frac{N_E}{\sqrt{T_m}} \tag{E.45}$$

where b = cylinder bore, ft

d = inlet valve diameter, ft

ℓ = piston stroke, ft

s = mean piston speed = $2\ell N_E/60$, ft/sec

C_i = mean inlet flow coefficient

a = speed of sound at the inlet valve, ft/sec

g = gravitational acceleration, ft/sec^2

γ = ratio of specific heats for the inducted fuel-air mixture

R_m = inducted mixture gas constant, $ft.lb/lbm.^oK$

$\simeq R_a$ = gas constant for dry air (Equation E.16)

$C_Z \simeq$ constant

Figure E.13(a) from Taylor (13) shows a typical relationship represented by Equation E.44. The effect of P_e/P_m is negligible ($P_m \equiv p_i$, $P_e \equiv p_e$). Linearizing this curve gives the expression:

$$MEP_i = P_m(1 - k_m Z), \qquad k_m > 0 \tag{E.46}$$

We expect an expression similar to Equation E.44 for the exhaust valve. Taylor (13), instead of defining an exhaust valve Mach Index Z_e, expresses the exhaust MEP in terms of the inlet valve Mach Index:

$$\frac{MEP_e}{P_e} = f_e\left[Z, \frac{P_e}{P_m}, F\right] \tag{E.47}$$

for a given engine. The temperature and pressure at exhaust valve opening, which are "chiefly dependent on the volumetric efficiency, the fuel-air ratio, and the compression ratio" (13) have been characterized by Z, P_e/P_m, F (and compression ratio, which is here not included for an engine of fixed design). "In spark-ignition engines, variations in fuel-air ratio are generally within the range in which

the effect on pumping losses is small" (13). The effect of varying F on the exhaust gas temperature, and hence on the speed of sound at the exhaust valve, is thus taken to be small. In the previous discussion of volumetric efficiency, it was determined that the effect of P_m/P_e on η_v was small for the engines here discussed. Hence it is expected that the effect of P_e/P_m in Equation E.47 would also be small for these engines. Consequently we may write

$$\frac{MEP_e}{P_e} = f_e\,[Z] \qquad \text{(E.48)}$$

where the exhaust valve flow characteristics are expressed approximately by the inlet valve characteristics.

Figure E.13(b) from Taylor (13) shows a typical relationship represented by Equation E.48 for an engine in which the effect of P_e/P_m is not negligible: these curves have $P_e \leq P_m$. Taking the form of these curves to be general, we may linearize Equation E.48 to:

$$MEP_e = P_e(1 + k_e Z), \qquad k_e > 0 \qquad \text{(E.49)}$$

for application to General Aviation piston engines.

Combining Equations E.46 and E.49, the total lost mean effective pressure due to pumping is:

$$\begin{aligned} PMEP &= MEP_e - MEP_i \\ &= P_e(1 + k_e Z) - P_m(1 - k_m Z) \end{aligned} \qquad \text{(E.50)}$$

From Equation E.50 it is clear that:

(a) Increasing inlet manifold pressure P_m decreases pumping losses,

(b) Increasing exhaust back-pressure P_e increases pumping losses,

(c) Increasing engine speed increases both inlet and exhaust pumping losses.

Mechanical Friction

The discussion by Taylor (13) permits the approximate representation of lost mean effective pressure due to mechanical friction:

$$MMEP = (N_E+m_o)\ (m_1 + m_2 \cdot IMEP) + m_3 \qquad (E.51)$$

Total Lost Mean Effective Pressure and Lost Horsepower

Combining Equations E.50 and E.51, the total lost mean effective pressure is

$$\begin{aligned} LMEP &= PMEP + MMEP \\ &= P_e(1 + k_eZ) - P_m(1 - k_mZ) \\ &\quad + (N_E+m_o)\ (m_1+m_2 \cdot IMEP) + m_3 \end{aligned} \qquad (E.52)$$

and substituting for Z from Equation E.45,

$$LMEP = P_e\left(1+k_eC_Z \frac{N_E}{\sqrt{T_m}}\right) - P_m\left(1-k_mC_Z \frac{N_E}{\sqrt{T_m}}\right)$$

$$+ (N_E+m_o)\ (m_1+m_2 \cdot IMEP) + m_3 \qquad (E.53)$$

The lost horsepower is then:

$$LHP = (LMEP)\ DN_E/458.33 \qquad (E.54)$$

for LMEP (lb/in^2), D(ft^3), N_E(RPM).

Lost Horsepower Based on the Motoring Test

Taylor (13) states: "The mechanical friction mep of an engine can be measured by measuring indicated and pumping mep with an indicator and the bmep by means of a dynamometer...Friction measurements by means of indicator diagrams are rare, and in most cases the basic data must come from the results of motoring tests...It has been shown that motoring-test results are a reasonably accurate measure of mechanical-plus-pumping friction when imep is in the range of 100 psi and, in the case of four-stroke engines, when p_e/p_i is nearly 1.0. Thus in estimating friction for supercharged or throttled engines, in which these conditions do not hold, suitable correction factors must be applied to motoring-test data."

In the absence of data taken with the engine firing, it is not possible to evaluate the constants in Equation E.53. An equivalent expression for the lost horsepower, based upon motoring-test data, is obtained as follows.

Taylor (13) shows that a reasonable estimate of LMEP for a firing engine is:

$$LMEP = LMEP_o + x\ (P_e - P_m) + y\ (IMEP - 100) \qquad (E.55)$$

where $LMEP_o$ is the result of a motoring test (with P_e and P_m near one atmosphere). All pressures in Equation E.55 have units of lb/in^2.

Values for x and y are given in Figure E.14(13), from which it is apparent that:

$$\left.\begin{aligned} x &= 1 - k_x Z \\ y &= y_o + k_{ys} s = y_o + k_{yn} N_E \end{aligned}\right\} \qquad \text{(E.56)}$$

where

k_x = constant > 0

y_o = constant > 0

$k_{yn} = 2\, k_{ys}\, \ell/60$ = constant > 0

The lost horsepower of the firing engine is then:

$$\begin{aligned} LHP &= (LMEP)\, DN_E/458.33 \\ &= LHP_o + DN_E\, [x(P_e - P_m) + y\,(IMEP-100)]/458.33 \\ &= LHP_o + DN_E\, [(1-k_x Z)\,(P_e-P_m) + (y_o + k_{yn} N_E)(IMEP-100)]/458.33 \\ &= LHP_o + DN_E\, [(1-k_x C_Z \frac{N_E}{\sqrt{T_m}})\,(P_e-P_m) + (y_o + k_{yn} N_E) \\ &\qquad (IMEP-100)]/458.33 \end{aligned} \qquad \text{(E.57)}$$

where LHP_o = the lost horsepower obtained during the motoring test, with $P_e \simeq P_m \simeq 1$ atmosphere.

$= (LMEP_o)\, DN_E/458.33$ horsepower

LMEP, P_e, P_m and IMEP have the units lb/in^2.

The motoring horsepower LHP_o may be represented by a quadratic algebraic equation in engine speed N_E(RPM):

$$LHP_o = a_o + a_1 N_E + a_2 N_E^2 \qquad \text{(E.58)}$$

where the coefficients a_o, a_1, a_2 are constants. Representative motoring horsepower data for General Aviation aircraft piston engines are shown in Figure E.15 (28).

Equations E.57 and E.58 are used in this work to determine the Lost Horsepower in all operating conditions.

FUEL METERING SCHEDULE

Fuel metering requirements for spark ignition reciprocating internal combustion engines are discussed by Obert(29). Figure E.16 taken from Reference 15 shows the fuel-air ratio used by the Curtiss-Wright TC18 Turbo Compound Engine.

A rich fuel-air ratio ($\phi>1$) is required during idling, decreasing to a lean fuel-air ratio ($\phi<1$) requirement for medium-power operation. The fuel-air ratio must be enrichened again at high power levels.

Figure E.17 (from Reference 23) shows the mixture schedule used by the Beech Single Lever Power Control system. While the previous Figure E.16 carries air mass flow rate along the abscissa, Figure E.17 shows an abscissa of percent rated power. Since air mass flow rate is related to IHP by Equation E.11, these two representations are essentially equivalent.

While a constant lean fuel-air ratio is appropriate during cruise below about 75% rated power, richer mixtures are necessary at higher powers for three reasons:

1. Full power can only be developed with a rich mixture. "Best Power Mixture" at wide open throttle (indeed, at any constant air mass flow rate) is a fuel-air ratio of approximately 0.08, $\phi = 1.2$ (11, 23), with MBT timing.
2. Excess fuel is required to provide cooling for the engine.
3. A rich mixture is required to avoid detonation (see Appendix F).

For studies of engine performance in this work, the fuel-air schedules shown in Figure E.18 are used. The abscissa scale is the mass fraction of dry air consumed at some specified Fuel Schedule Datum condition (see below). Schedule A represents cruise operation near best power mixture, enrichening to a fuel-air ratio of 0.084 (ϕ = 1.25) at maximum air mass fraction (cf. Figure E.17). Schedule B differs from Schedule A at low values of the air mass fraction, representing the Desirable Schedule of Figure E.17; while Schedule C gives a constant lean fuel-air ratio in all operating conditions.

Humidity will affect metered fuel-air ratio in a manner determined by the installation. Humidity is not considered in this study.

COMPUTATION OF NATURALLY ASPIRATED ENGINE PERFORMANCE

The procedure used here to compute the performance of a naturally aspirated engine at a prescribed operating point requires the specification of certain engine characteristics; a Reference Operating Point Condition; and a Fuel Schedule Datum Condition.

Required Engine Characteristics

The following characteristics must be specified for the computation of engine performance:

1. Engine displacement, cu ft D

2. Fuel metering schedule — $F(x)$

   F = fuel/dry air mass ratio

   $x = \frac{\text{(dry air mass flow rate)}}{\text{(dry air mass flow rate at the Fuel Schedule Datum)}}$

3. Coefficients of the cubic Equation E.41 — e_o, e_1, e_2, e_3

4. Manifold temperature pertaining to Equation E.41 — T'_m

5. $\left.\frac{\partial R}{\partial T_m}\right|_{S'}$ versus ϕ (Equation E.38)

6. R_o versus ϕ (Equation E.39)

7. $\frac{\partial R_1}{\partial T_m}$ (Equation E.39)

8. Motoring coefficients (Equation E.58) — a_o, a_1, a_2

9. Lost horsepower coefficients (Equation E.57) — k_x, C_z

   y_o, k_{yn}

10. Volumetric efficiency correction indices (Equation E.23) — ε_t, ε_p

Reference Operating Point

The performance of the engine at the Reference Operating Point (denoted by subscript 1) is completely defined by the above characteristics and the following set of mutually consistent operating parameters:

1.	Inlet manifold absolute pressure	P_{m_1}	inches Hg
2.	Inlet manifold temperature	T_{m_1}	deg. K
3.	Exhaust absolute back-pressure	P_{e_1}	inches Hg
4.	Fuel/dry air mass ratio	F_1	
5.	Brake horsepower	BHP_1	horsepower
6.	Engine shaft speed	N_{E_1}	RPM

When values for these parameters have been specified, the remainder of the engine performance at the Reference Operating Point may be computed as follows:

1.	LHP_1	-	Equations E.57, E.58	Iteration on IMEP
2.	IHP_1, $IMEP_1$	-	Equations E.2, E.5	
3.	η_{i_1}	-	Equations E.40, E.41	
4.	$\dot{m}_{f_1}$	-	Equation E.10	
5.	$\dot{m}_{a_1} = \dot{m}_{f_1} / F_1$			
6.	ρ_{m_1}	-	Equation E.17	
7.	η_{v_1}	-	Equation E.14	

Fuel Schedule Datum

The Fuel Schedule Datum condition (denoted by subscript fsd) is nominally Wide Open Throttle at maximum continuous RPM at sea level; but it can be any other desired condition.

The dry air mass flow rate corresponding to this condition may be computed from a knowledge of the engine performance at the Reference Operating Point, and the following set of parameters:

1.	Inlet manifold absolute pressure	$P_{m_{fsd}}$	inches Hg
2.	Inlet manifold temperature	$T_{m_{fsd}}$	deg. K
3.	Exhaust absolute back-pressure	$P_{e_{fsd}}$	inches Hg
4.	Engine shaft speed	$N_{E_{fsd}}$	RPM

When values for these parameters have been specified, the corresponding dry air mass flow rate may be computed as follows:

1. F_{fsd} - Fuel Metering Schedule F(x) at x = 1
2. $\rho_{m_{fsd}}$ - Equation E.17
3. $\eta_{v_{fsd}}$ - Equation E.23 (using the Reference Operating Point value η_{v_1})
4. $\dot{m}_{a_{fsd}}$ - Equation E.14

General Operating Point

Utilizing the computed performance at the Reference Operating Point and the Fuel Schedule Datum, the performance of the engine at any other operating point (denoted by subscript 2) may be computed by specifying the set:

1.	Inlet manifold absolute pressure	P_{m_2}	inches Hg
2.	Inlet manifold temperature	T_{m_2}	deg. K.
3.	Exhaust absolute back-pressure	P_{e_2}	inches Hg
4.	Engine shaft speed	N_{E_2}	RPM

The computation of the performance proceeds as follows:

1. ρ_{m_2} - Equation E.17
2. η_{v_2} - Equation E.23 (using the Reference Operating Point value η_{v_1})
3. $\dot{m}_{a_2}$ - Equation E.14
4. $x = \dot{m}_{a_2}/\dot{m}_{a_{fsd}}$
5. F_2 - Fuel Metering Schedule F(x)

6. ϕ_2 - Equation E.20

7. $\dot{m}_{f_2} = F_2 \dot{m}_{a_2}$

8. η_{i_2} - Equations E.40, E.41

9. IHP_2 - Equation E.10

10. $IMEP_2$ - Equation E.5

11. LHP_2 - Equations E.57, E.58

12. BHP_2 - Equation E.2

13. $BSFC_2$ - Equation E.8

14. Torque Q_{E_2} - Equation E.3

* * * * * * * * * * * * * * * * * *

TABLE E.1

PRIMARY INFLUENCE OF CONTROLS

ON ENGINE OPERATIONAL PARAMETERS

Engine Oper'l Param.	Fuel Flow Lever	Variable Spark-Advance System	Throttle	Induction Air Heater and/or After-Cooler	Cowl Flaps	Turbine Waste-Gate & Nozzle Geometry Control	Propeller Governor	Flight Altitude
F	X							
τ		X						
P_m			X			X		
T_m				X		X		X
CHT	X	X	X	X	X			
P_e						X		X
T_e	X	X	X				X	
N_E							X	
Q_E	X	X	X			X		
h								X

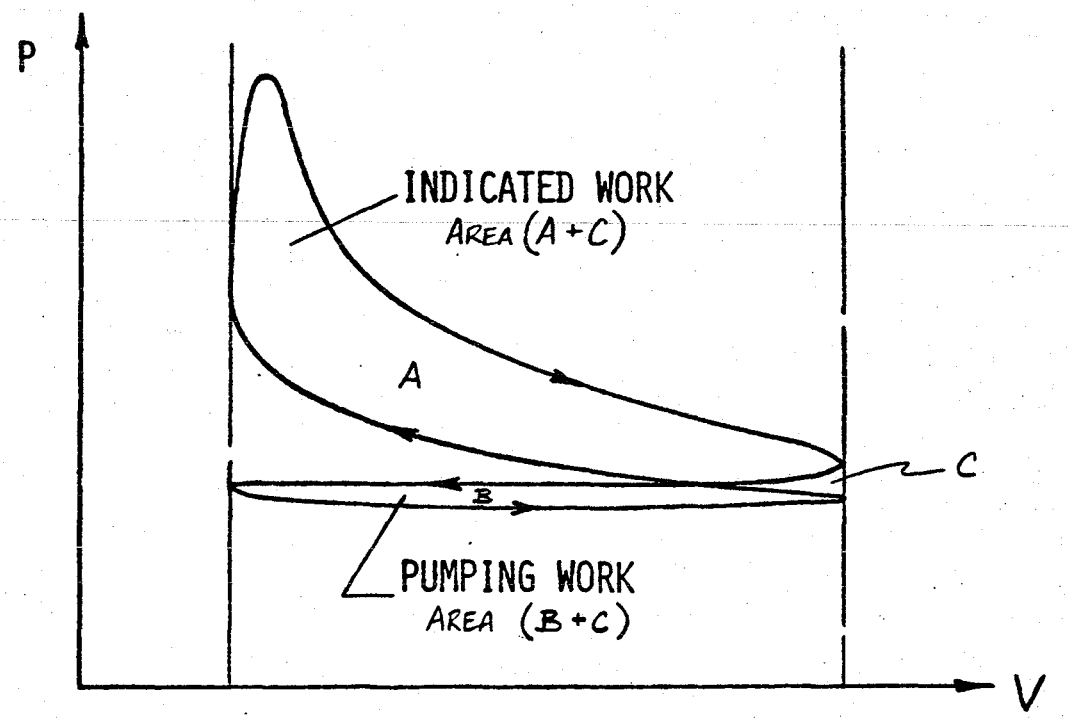

FIGURE E.1 TYPICAL PRESSURE-VOLUME CYCLE DIAGRAM FOR A NATURALLY ASPIRATED AIRCRAFT ENGINE.

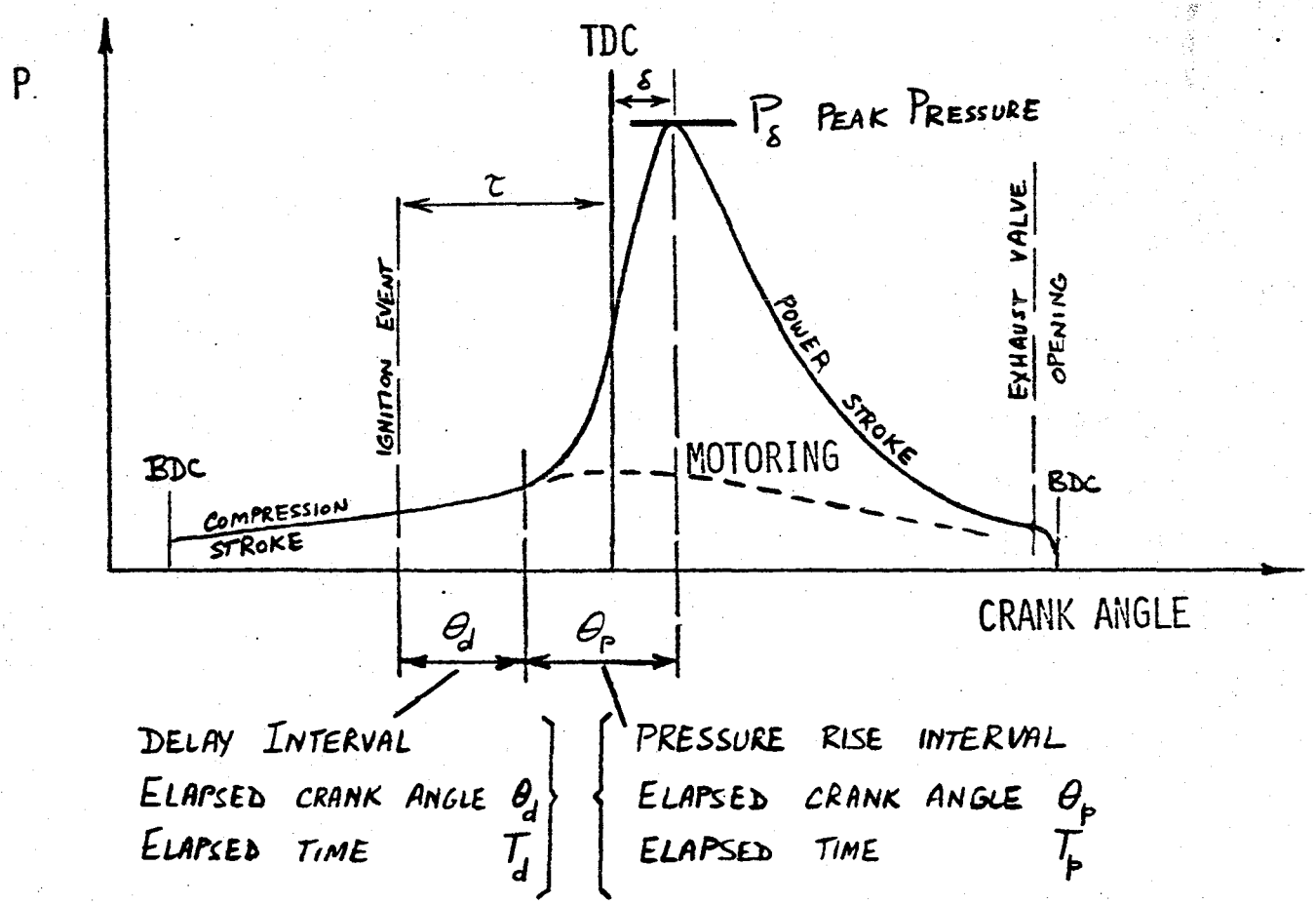

FIGURE E.2 TYPICAL TRACE OF CYLINDER PRESSURE VERSUS CRANK ANGLE.

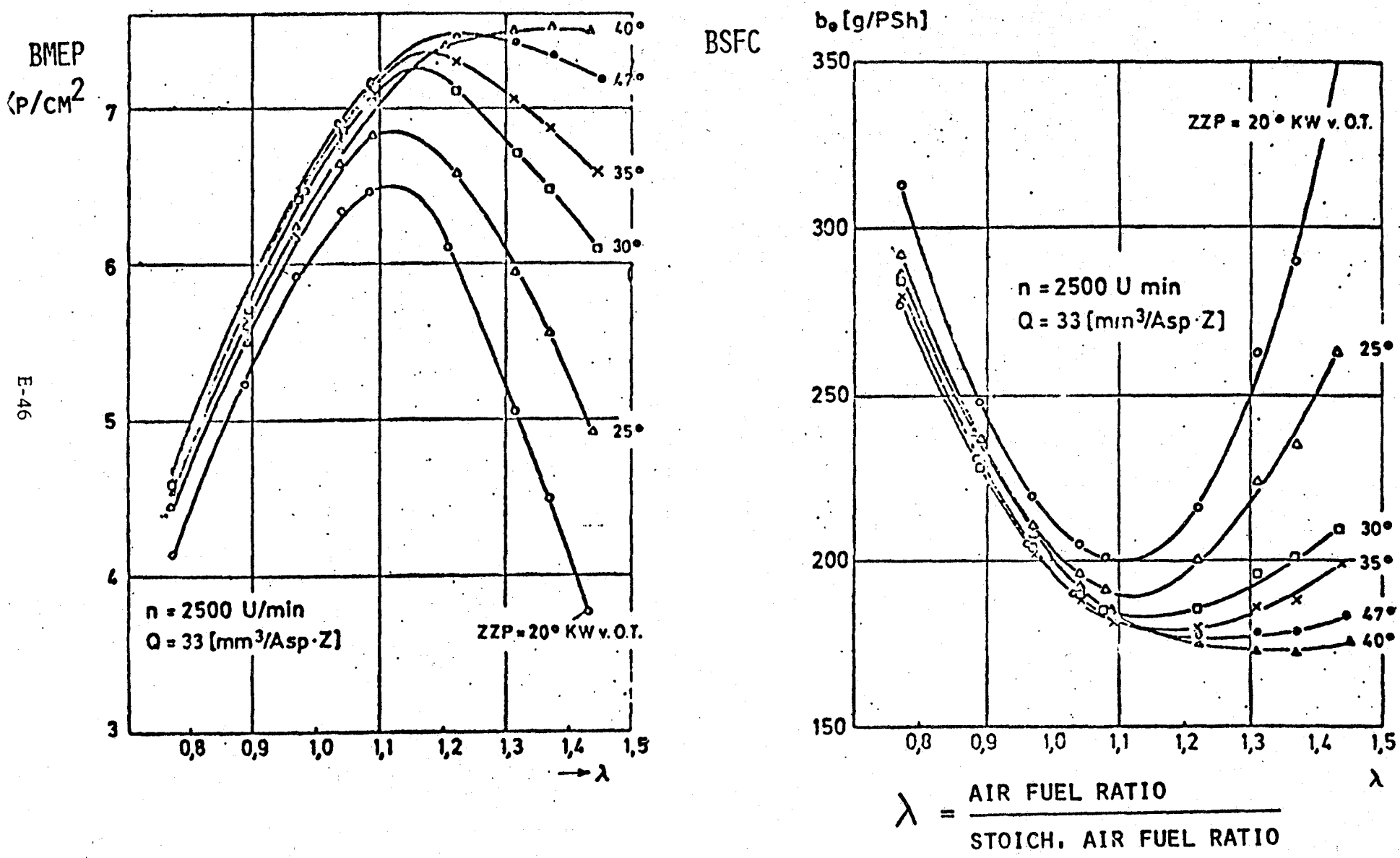

NOTE: FUEL QUANTITY KEPT CONSTANT, AIR QUANTITY VARIED BY THROTTLING. SINGLE SPARK IGNITION.

FIGURE E.3 TYPICAL EFFECTS OF FUEL-AIR RATIO AND IGNITION TIMING ON PERFORMANCE (REF. 45).

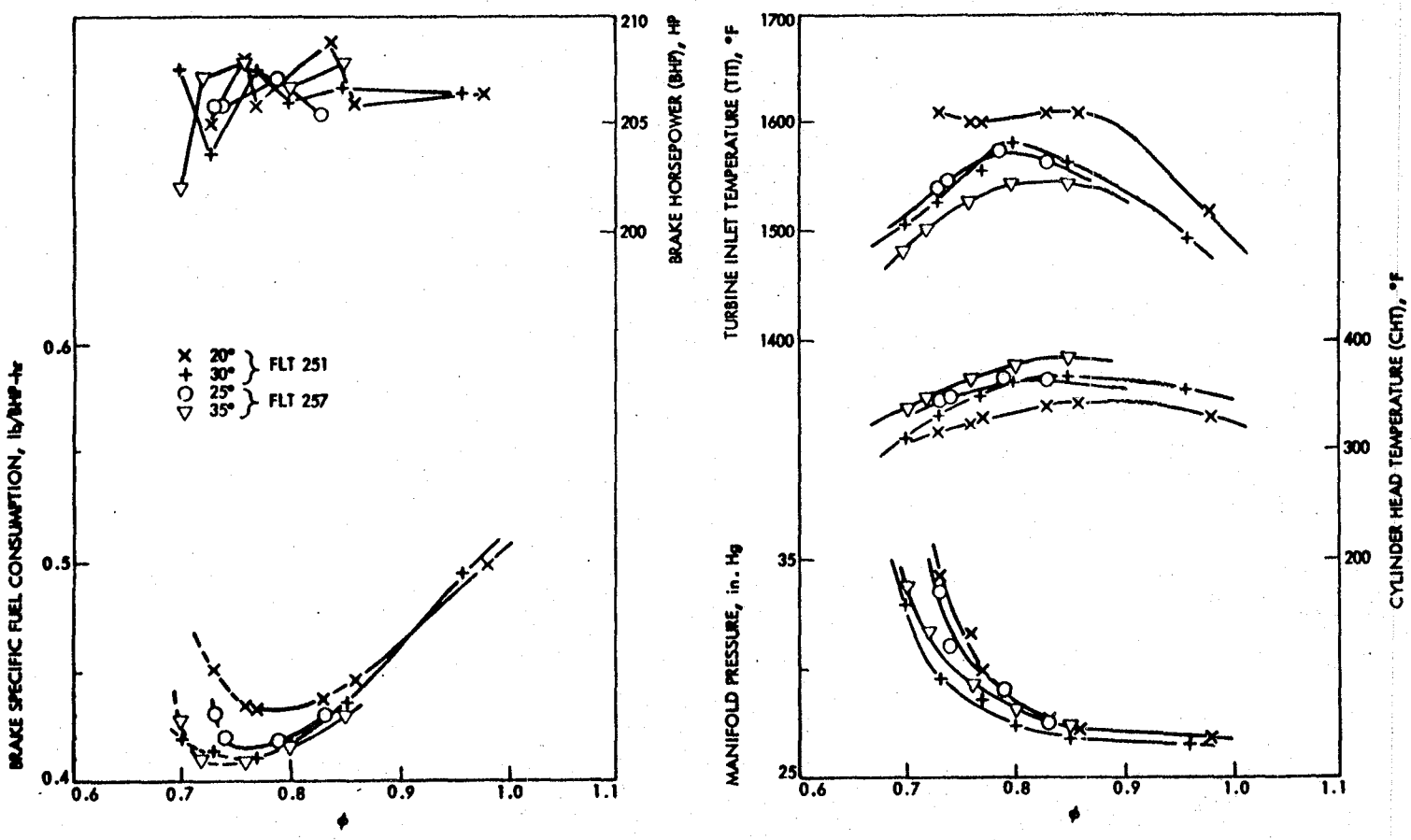

Leanout Curves for 2400 rpm, at 15,000 ft, Constant Power = 55%, and Several Ignition Timings (---Unstable Operation, Roughness)

(REF. 16, page 6-93)

FIGURE E.4

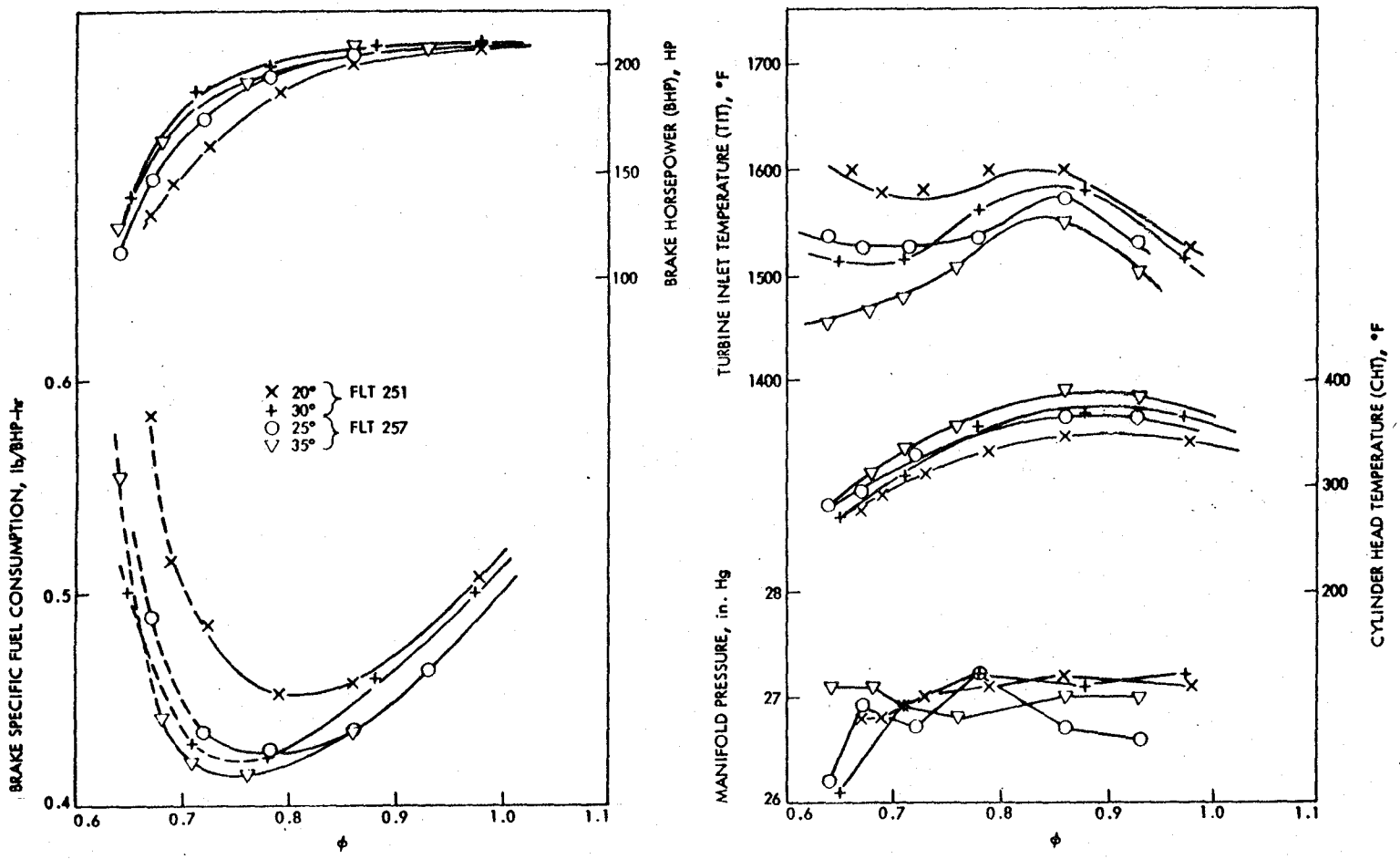

FIGURE E.5

Leanout Curves for 2400 rpm, at 15,000 ft, Constant Manifold Pressure = 27 in. Hg., and Several Ignition Timings (---Unstable Operation, Roughness)

(REF. 16, page 6-92)

SCHEMATIC

TYPICAL VARIATIONS OF INDICATED THERMAL EFFICIENCY WITH EQUIVALENCE RATIO AND IGNITION TIMING

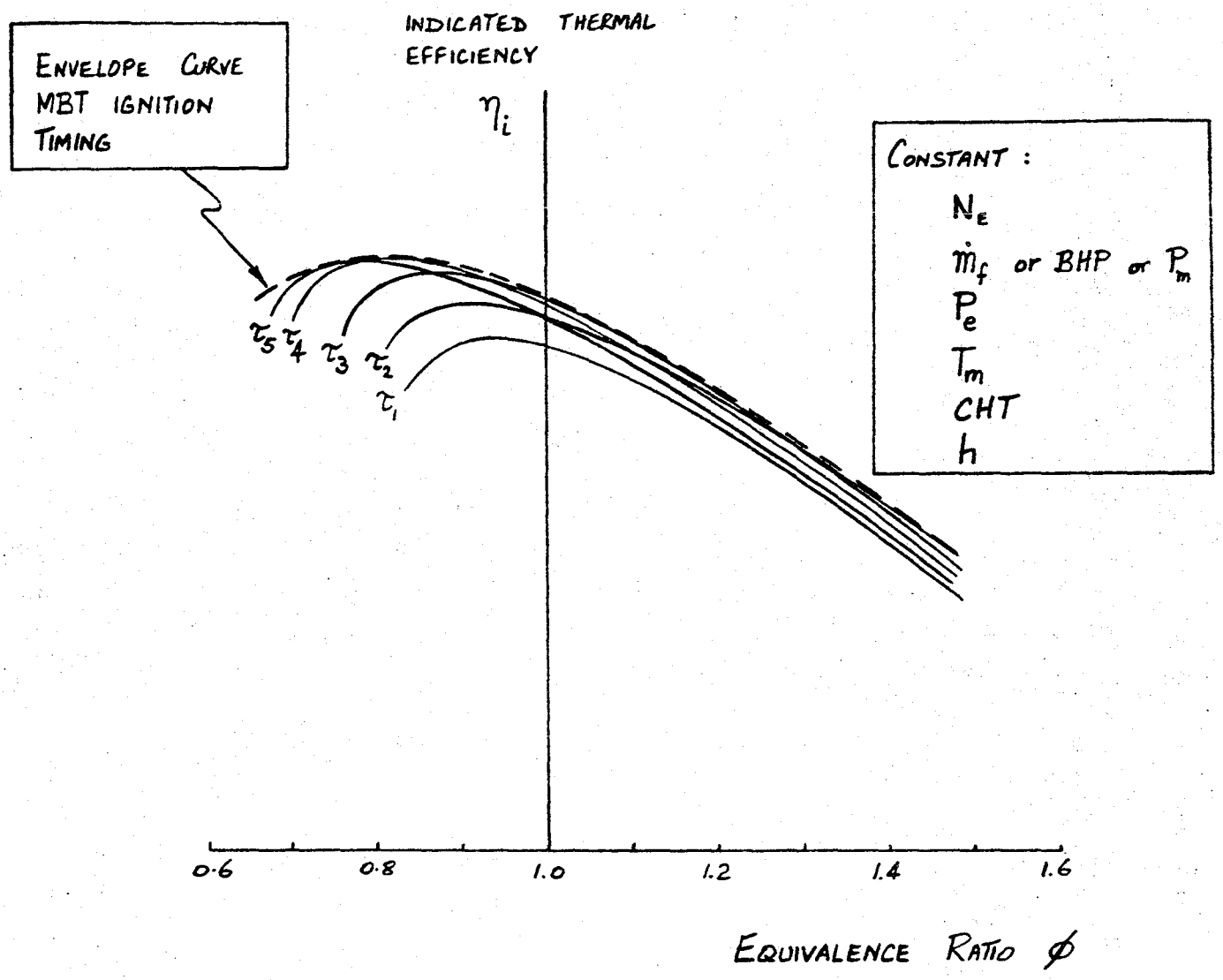

IGNITION TIMING τ DEGREES BTDC

$\tau_1 < \tau_2 < \tau_3 < \tau_4 < \tau_5$

FIGURE E.6

INDICATED THERMAL EFFICIENCY η_i' vs. EQUIVALENCE RATIO

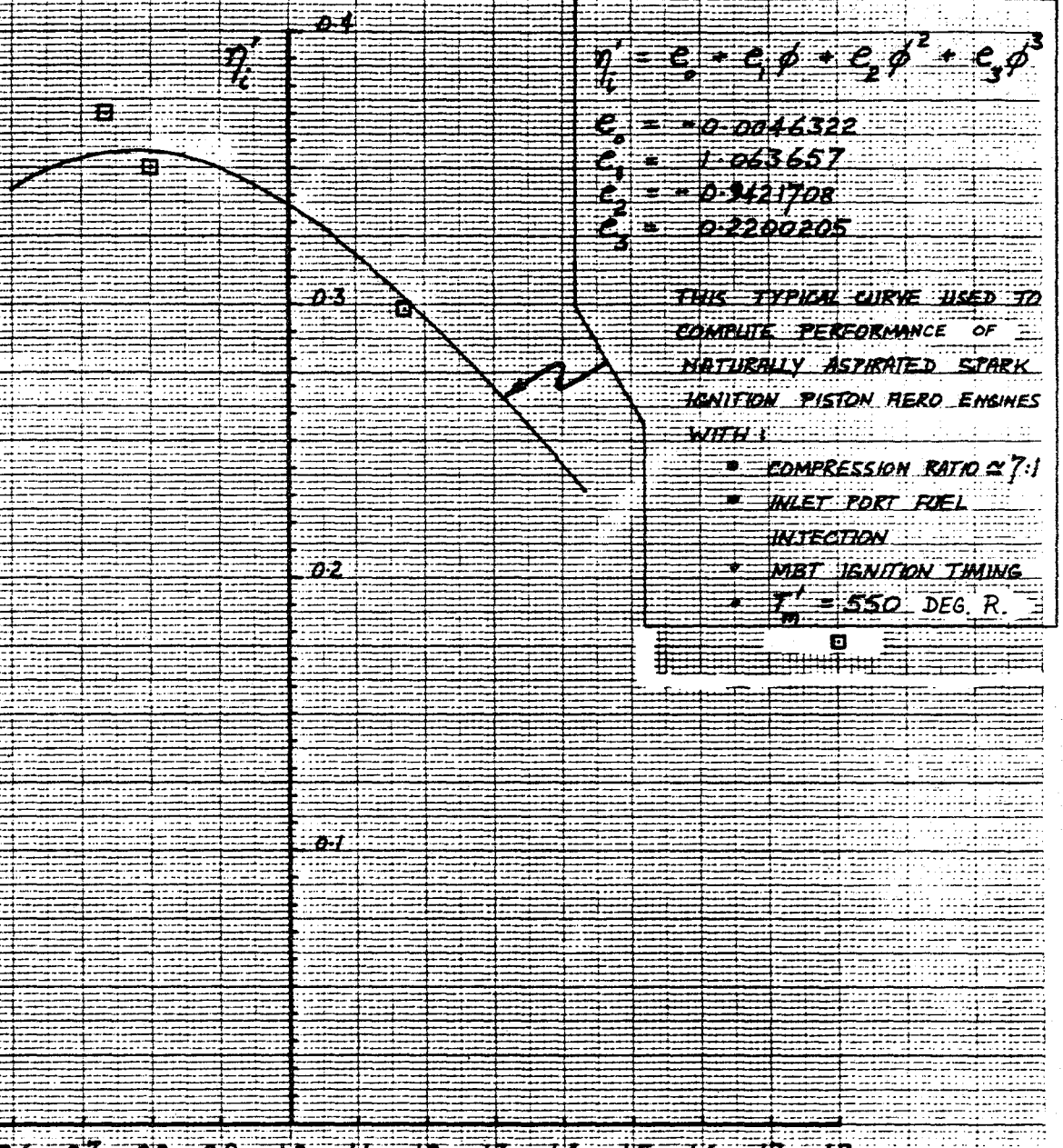

$$\eta_i' = e_0 + e_1\phi + e_2\phi^2 + e_3\phi^3$$

$e_0 = -0.0046322$
$e_1 = 1.063657$
$e_2 = -0.9421708$
$e_3 = 0.2200205$

THIS TYPICAL CURVE USED TO COMPUTE PERFORMANCE OF NATURALLY ASPIRATED SPARK IGNITION PISTON AERO ENGINES WITH:

- COMPRESSION RATIO ≃ 7:1
- INLET PORT FUEL INJECTION
- MBT IGNITION TIMING
- $T_m' = 550$ DEG. R.

□ TAYLOR [13] PAGE 153 (INDICATOR CARD):
CFR ENGINE 3¼ × 4½ INCH
COMPRESSION RATIO 7:1
ENGINE SPEED 1200 RPM
INLET MANIFOLD ABSOLUTE PRESSURE 13.75 LB/IN²
EXHAUST ABSOLUTE BACK-PRESSURE 14.8 LB/IN²
INLET MANIFOLD TEMPERATURE 179 DEG. F = 639 DEG. R
MBT IGNITION TIMING

FIGURE E.7

VARIATION OF INDICATED THERMAL EFFICIENCY WITH ENGINE SPEED

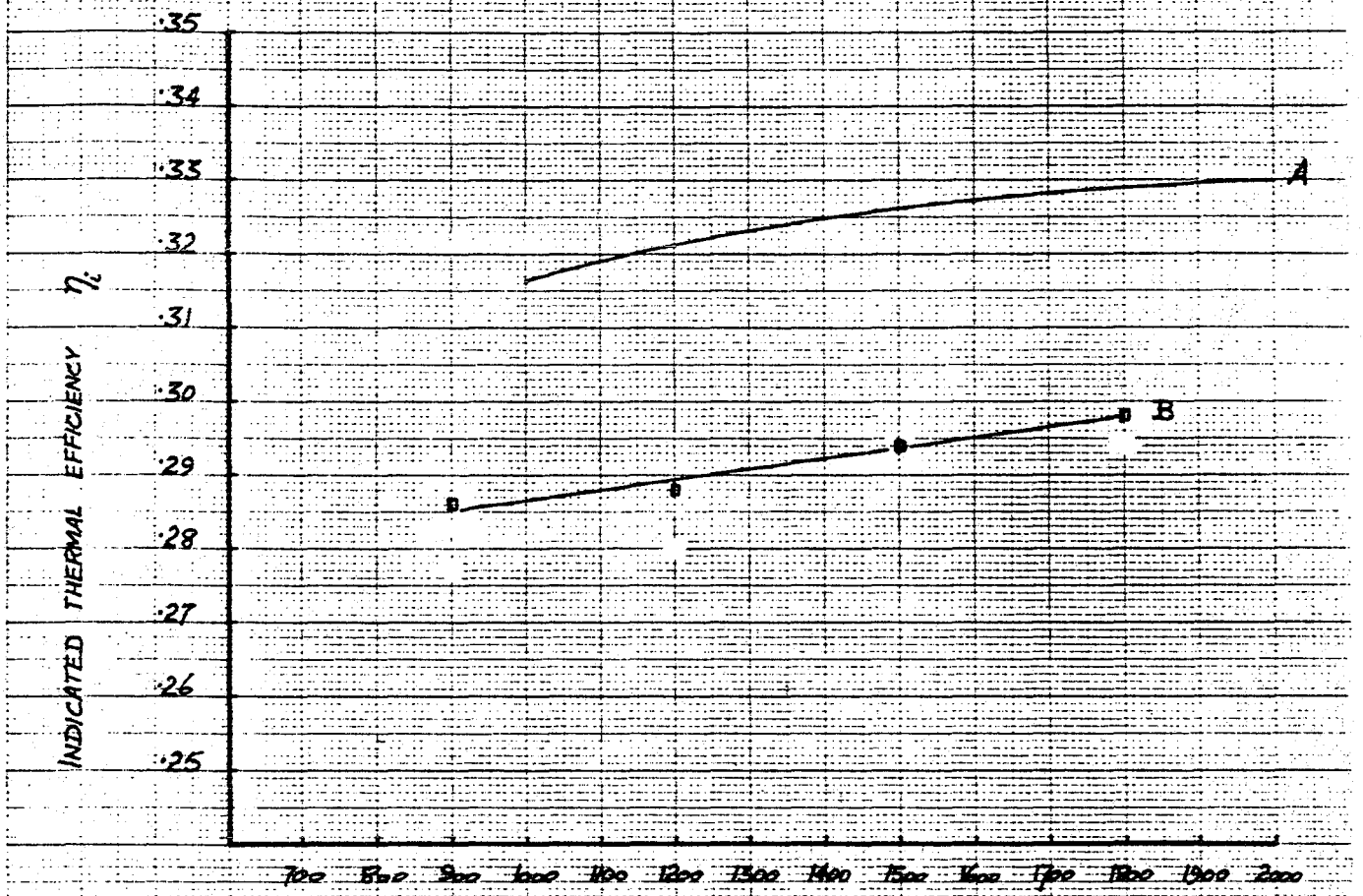

CURVE A

ENGINE TEST DATA

COMPRESSION RATIO 5:1
FUEL : COAL GAS
EQUIVALENCE RATIO 1.0
DESIGN SPEED 1500 RPM
(MBT IGNITION TIMING IMPLIED BY REF 11)

(REF. 11, PAGE 204)

CURVE B

ENGINE TEST DATA

CFR ENGINE 3¼ × 4½ INCH
COMPRESSION RATIO 6:1
INLET MANIFOLD TEMPERATURE 150 DEG. F
EQUIVALENCE RATIO 1.15
FUEL-AIR RATIO 0.075
EXHAUST ABSOLUTE BACK-PRESSURE 14.75 PSIA
CONSTANT VOLUMETRIC EFFICIENCY
MBT IGNITION TIMING

(REF. 13, PAGE 129)

FIGURE E.8

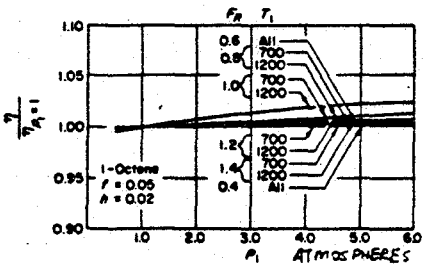

(a) (REF. 13 Page 82)

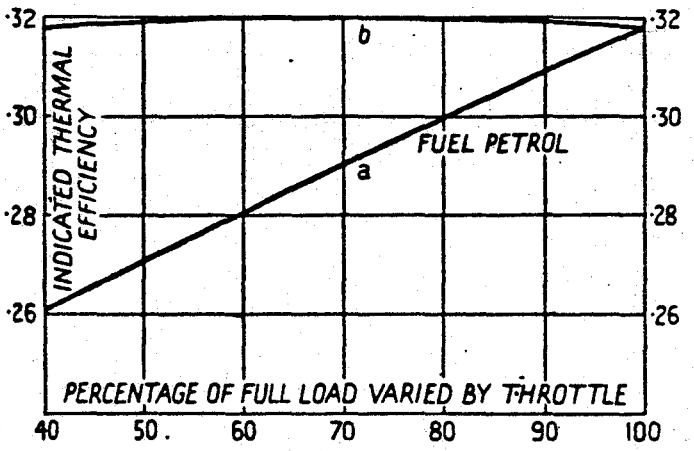

(b) Thermal efficiency under throttled conditions. Speed 1,500 r.p.m. Compression ratio 5:1. (*a*) Ignition fixed as for maximum power at full throttle, and (*b*) ignition adjusted for maximum power at each throttle setting.

FIGURE E.9

(REF. 11, page 185)

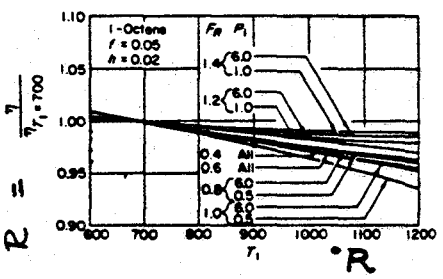

(a) (REF. 13 page 82)

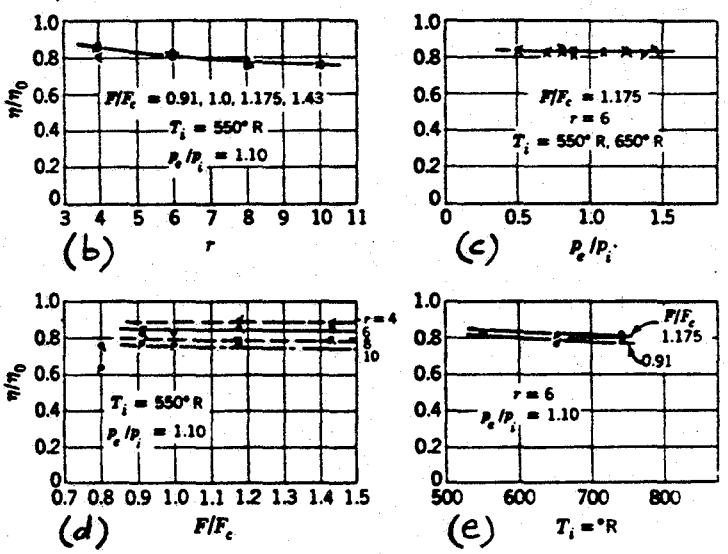

Fig 5-21. Comparison of efficiencies of actual cycles with efficiencies of equivalent fuel-air cycles—spark-ignition engines: η_0 = efficiency of equivalent constant volume fuel-air cycle with octane; η = indicated efficiency of CFR, 3¼ x 4½ in engine, 1200 rpm; fuel, gaseous butane, C_4H_8. (Van Duen and Bartas, ref 5.21)

(REF. 13, page 134)

FIGURE E.10

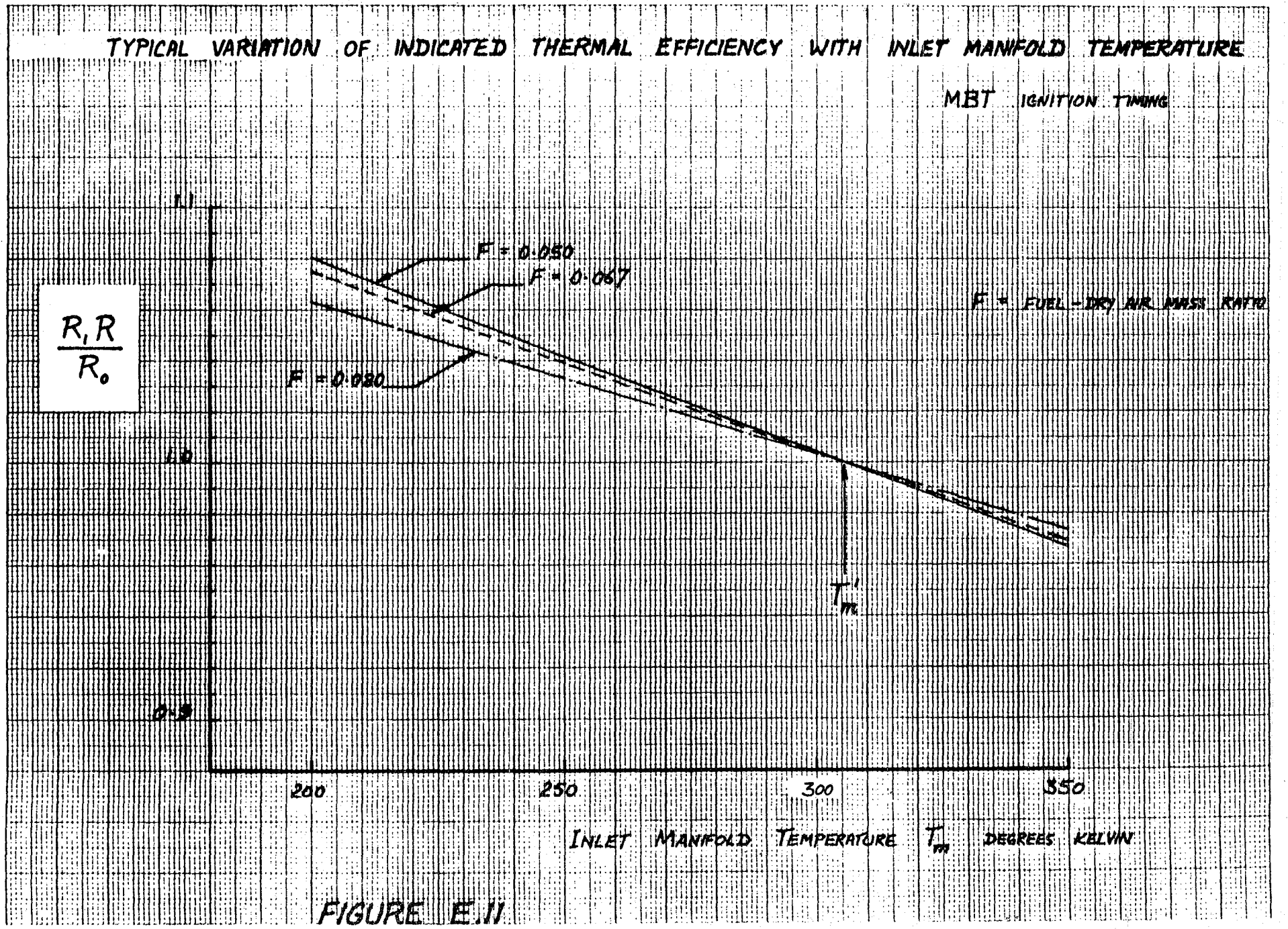
TYPICAL VARIATION OF INDICATED THERMAL EFFICIENCY WITH INLET MANIFOLD TEMPERATURE
MBT IGNITION TIMING
F = FUEL - DRY AIR MASS RATIO
F = 0·050
F = 0·067
F = 0·030
R, R / R₀
1·1
1·0
0·9
T_m'
200
250
300
350
INLET MANIFOLD TEMPERATURE T_m DEGREES KELVIN

FIGURE E.11

SCHEMATIC

POSTULATED TYPICAL VARIATIONS OF INDICATED THERMAL EFFICIENCY η_i WITH ϕ, τ AND P_m

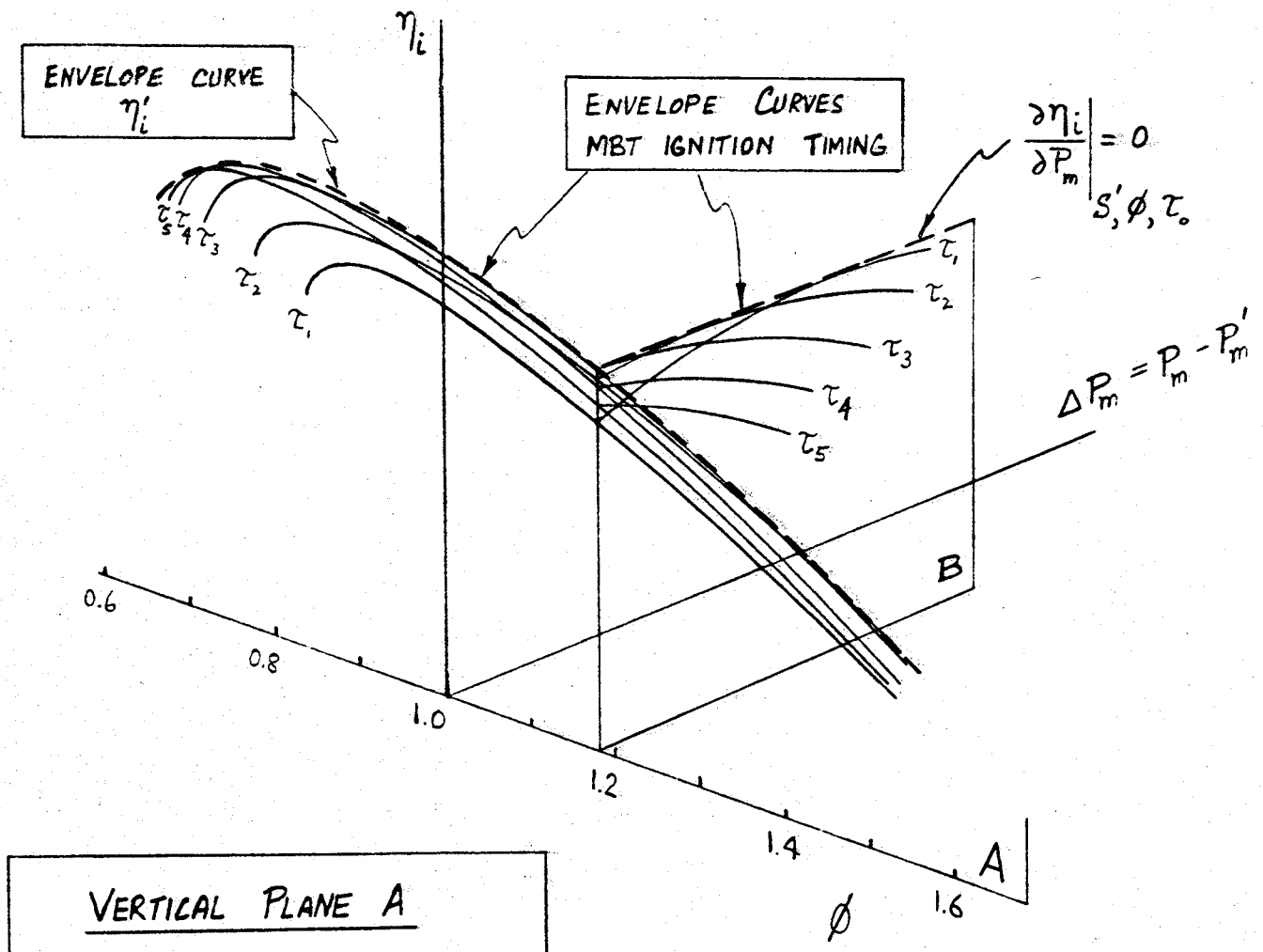

VERTICAL PLANE A

CONSTANT :

$N_E = N_E'$

$P_m = P_m'$

$P_e = P_e'$

$T_m = T_m'$

$CHT = CHT'$

$h = h'$

IGNITION TIMING τ DEGREES BTDC

$\tau_1 < \tau_2 < \tau_3 < \tau_4 < \tau_5$

FIGURE E.12

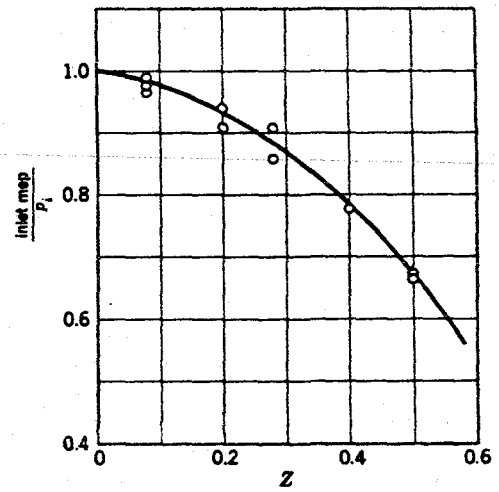

Fig 9-19. Ratio of inlet-stroke mep to inlet pressure: CFR engine 3¼ x 4½ in; r = 4.9; T_i = 580°F; p_e/p_i = 1.0, 0.5, and 0.25; $\gamma \cong 1.2$. (From indicator diagrams taken by Livengood and Eppes in connection with ref 6.44.)

(a) (REF. 13, page 342)

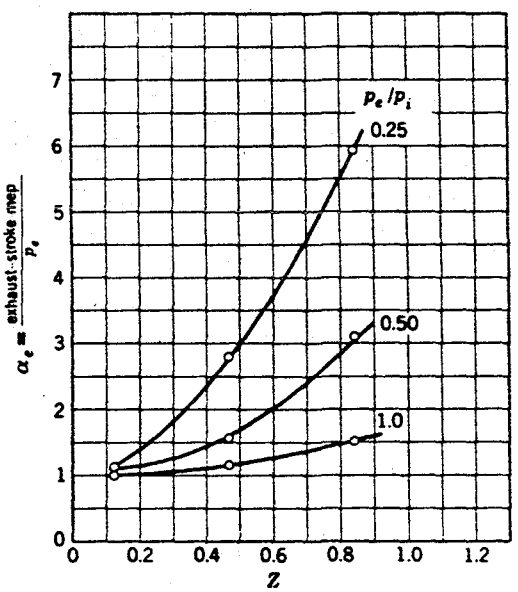

Fig 9-18. Ratio of exhaust-stroke mep to exhaust pressure: CFR engine, 3¼ x 4½ in, r = 4.9; T_i = 580°F; p_e/p_i = 1.0, 0.5, and 0.25; $\gamma \cong 1.2$. (From indicator diagrams taken by Livengood and Eppes in connection with ref 6.44)

(b) (REF. 13, page 341)

FIGURE E.13

(a)

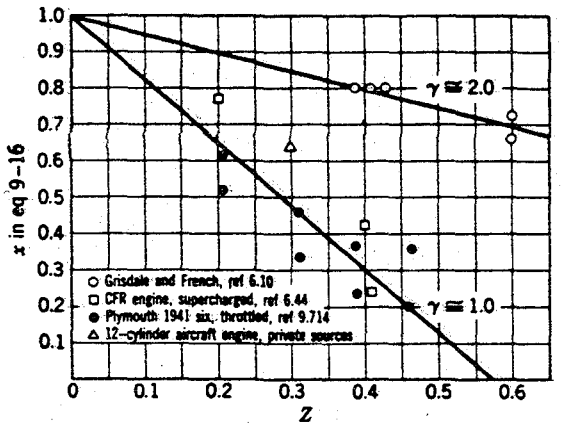

(b)

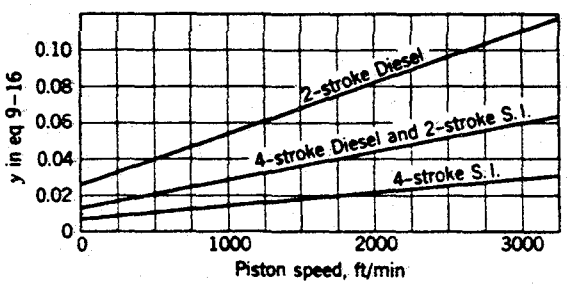

Motoring test correction factors: $\text{fmep} = \text{fmep}_0 + x(p_e - p_i) + y(\text{imep} - 100)$. y taken from Fig 9-10, x from motoring tests. (See Fig 6.24 for γ.)

FIGURE E.14 (REF. 13, page 354)

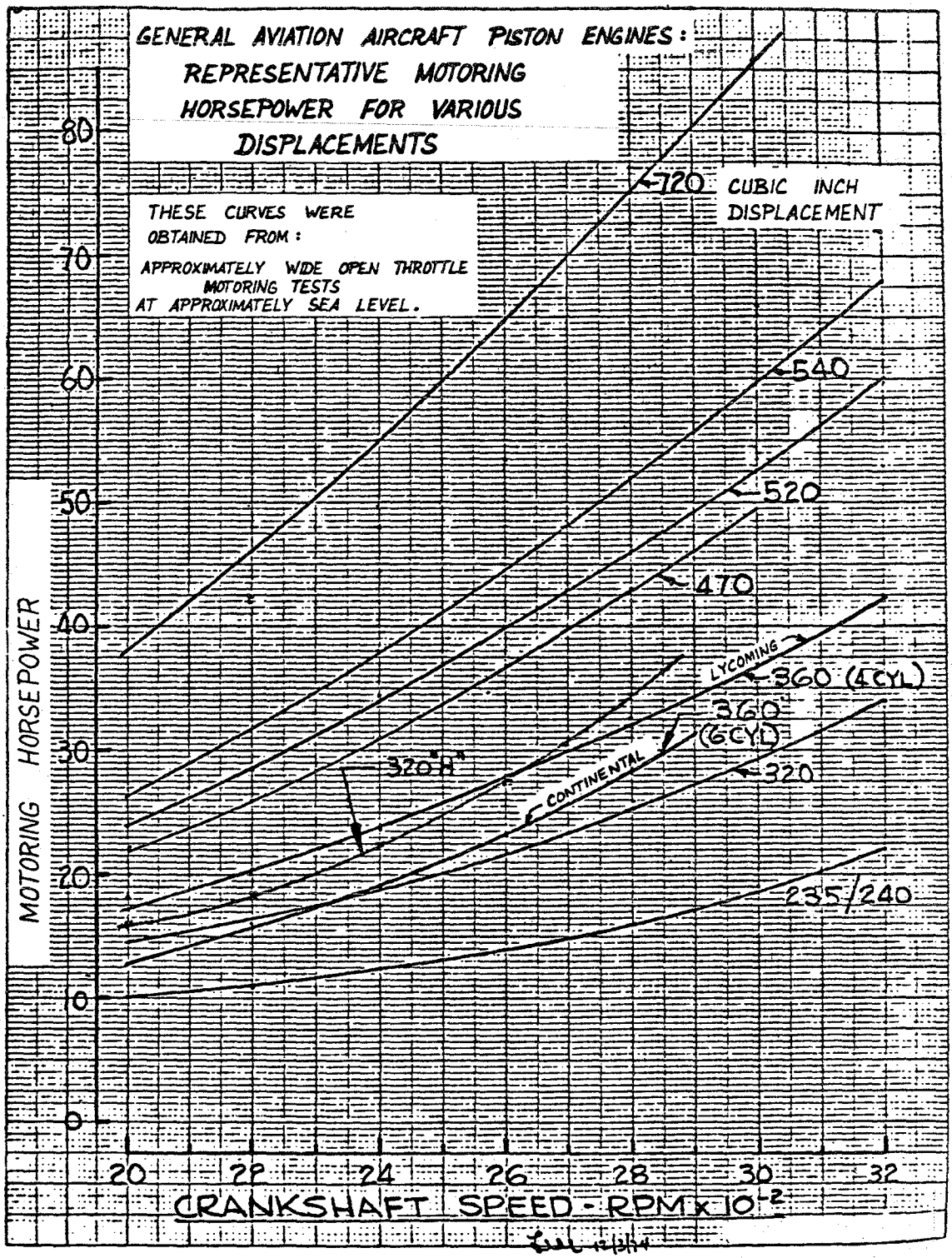

(REF. 28)

FIGURE E.15

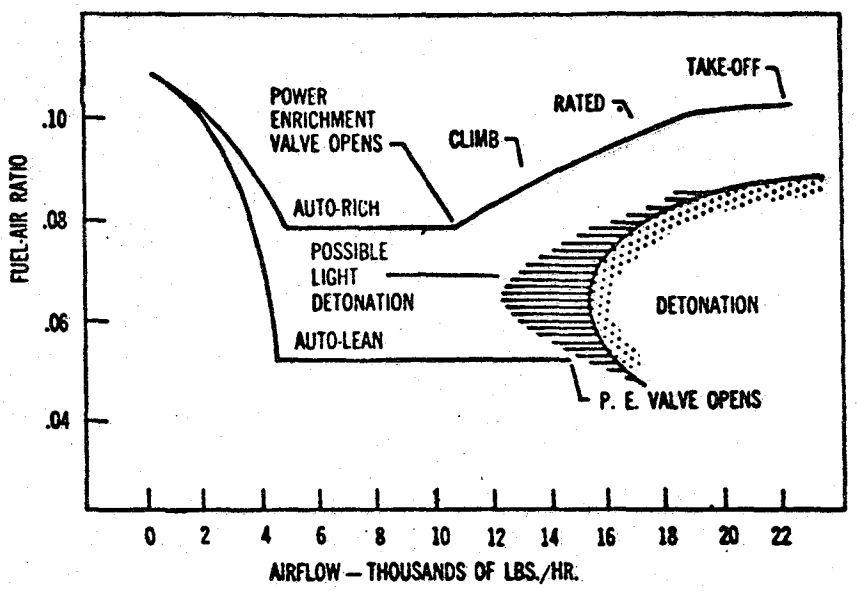

Carburetor Metering Curve Showing the Detonation Area

(REF. 15, page 17)

FIGURE E.16

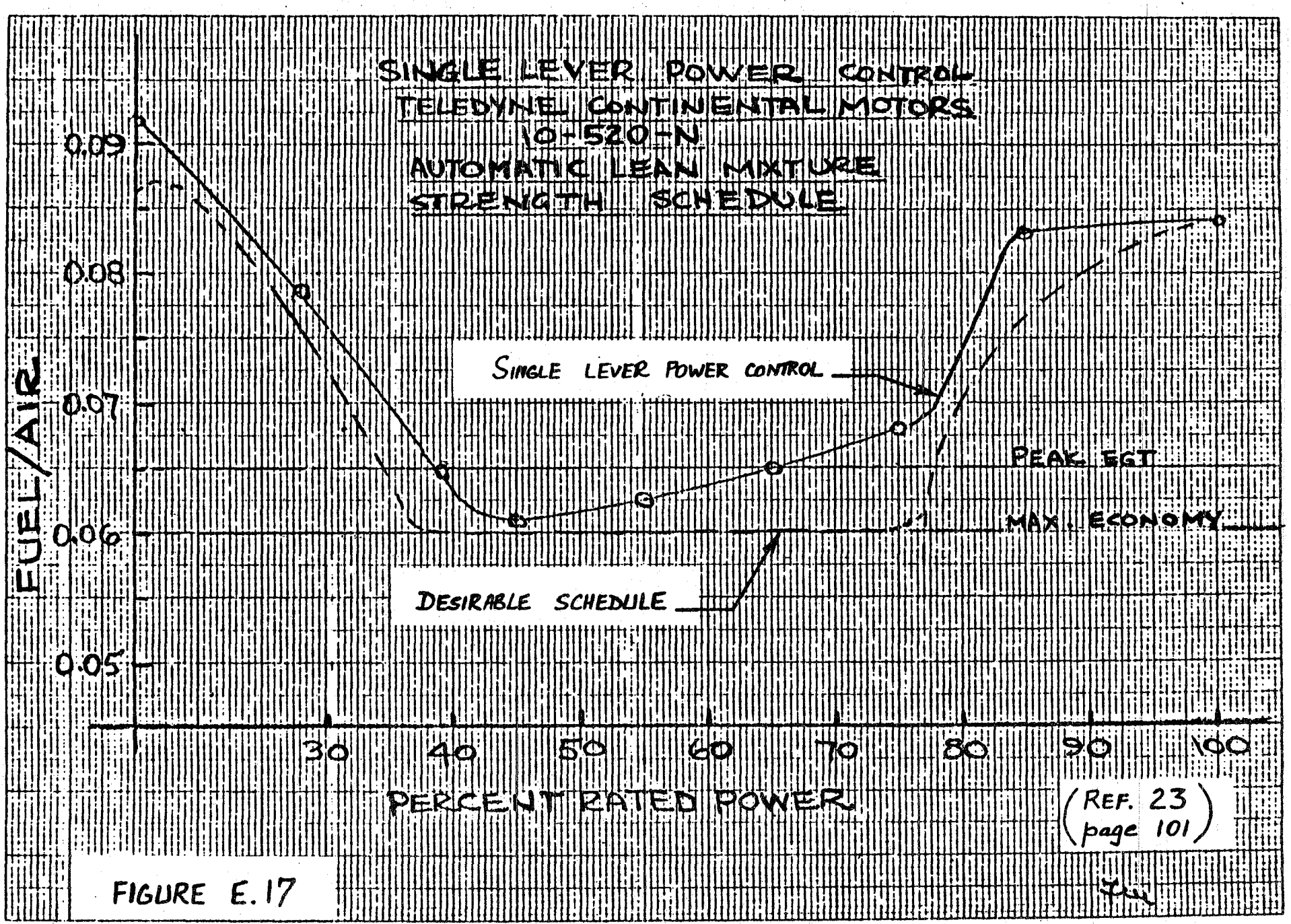
SINGLE LEVER POWER CONTROL
TELEDYNE CONTINENTAL MOTORS
IO-520-N
AUTOMATIC LEAN MIXTURE
STRENGTH SCHEDULE
FUEL/AIR
0.09
0.08
0.07
0.06
0.05
SINGLE LEVER POWER CONTROL
PEAK EGT
MAX. ECONOMY
DESIRABLE SCHEDULE
30
40
50
60
70
80
90
100
PERCENT RATED POWER
(REF. 23 page 101)

FIGURE E.17

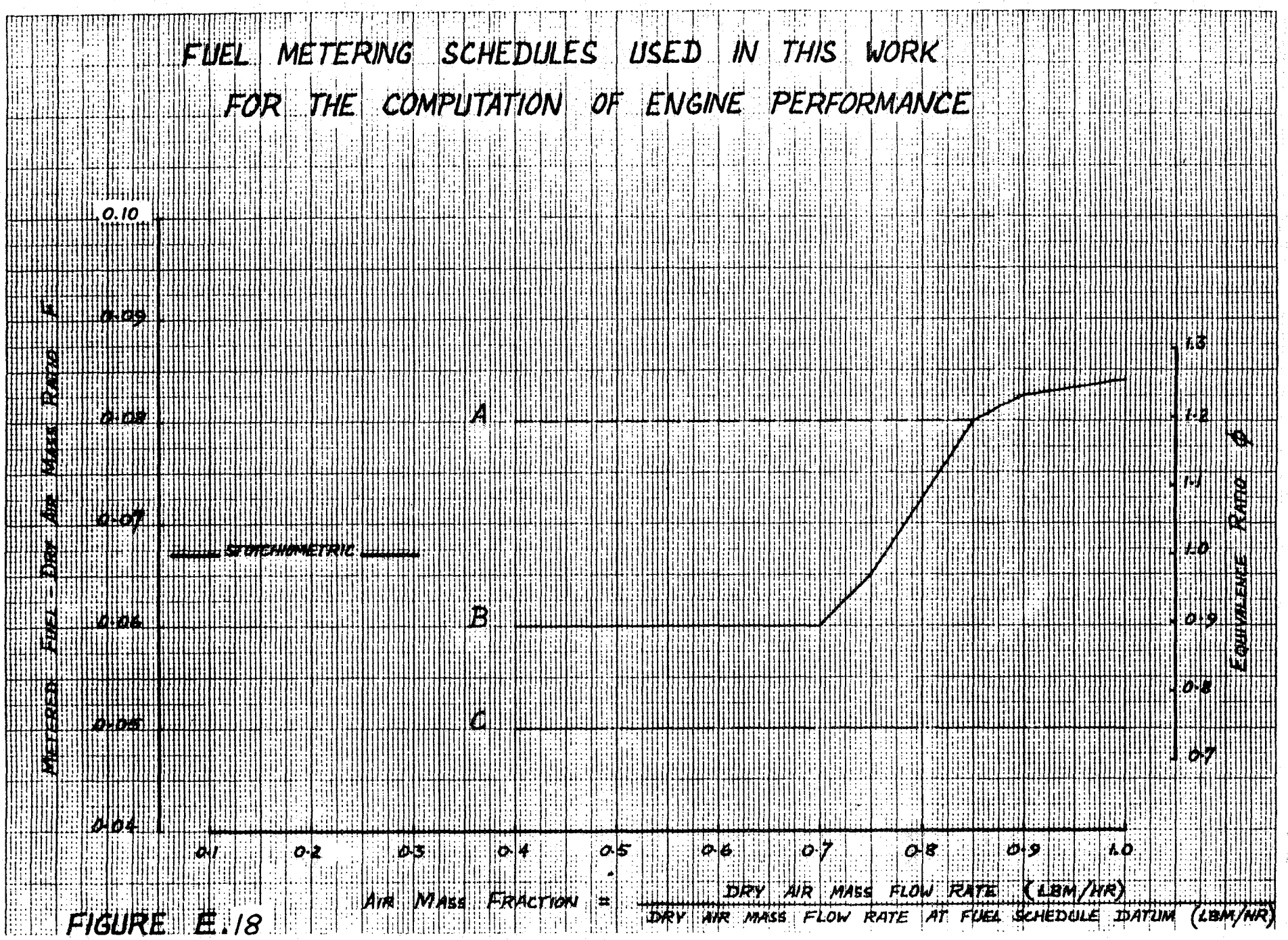
FUEL METERING SCHEDULES USED IN THIS WORK
FOR THE COMPUTATION OF ENGINE PERFORMANCE
METERED FUEL - DRY AIR MASS RATIO
0.10
0.09
0.08
0.07
0.06
0.05
0.04
STOICHIOMETRIC
A
B
C
0.1
0.2
0.3
0.4
0.5
0.6
0.7
0.8
0.9
1.0
AIR MASS FRACTION =
DRY AIR MASS FLOW RATE (LBM/HR)
DRY AIR MASS FLOW RATE AT FUEL SCHEDULE DATUM (LBM/HR)
EQUIVALENCE RATIO Φ
1.3
1.2
1.1
1.0
0.9
0.8
0.7

FIGURE E.18

APPENDIX F

AUTOIGNITION, DETONATION AND KNOCK IN SPARK-IGNITION PISTON ENGINES

Table of Contents

APPENDIX F

AUTOIGNITION, DETONATION AND KNOCK IN SPARK-IGNITION PISTON ENGINES

DEFINITIONS

The phenomena of autoignition, detonation and knock are discussed at length by Obert (29).

Autoignition is a spontaneous chemical reaction (oxidation) in the unburned mixture, ahead of the flame front in the combustion chamber. This reaction may be either explosive (usual) or non-explosive.

Knock is the noise accompanying autoignition. According to Obert (29):

> In general, knock is the term used to signify any unusual sound that arises because of autoignition in the combustion process. In automotive work, borderline knock is defined as audible knock apparent in a quiet test room. In aviation work, such borderline knock would be quite inaudible . . . Here vibration pickups are attached to the engine and, quite arbitrarily, a certain level of indication is specified to be objectionable knock.
>
> . . . A detonating wave has been proposed as the mechanism for explosive autoignition . . . It would be well to . . . explain that the terms *detonation* and *knock* are used synonymously by most engineers although, to the physical chemist, detonation is a unique propagation of combustion by a shock wave at superacoustic velocity.

A complete understanding of autoignition phenomena has not yet been reached. It is well recognized, however, that severe autoignition is destructive in an engine. This is especially true in aircraft engines where light structures are used.

FACTORS INFLUENCING THE OCCURRENCE OF KNOCK

Amongst those factors which influence the occurrence of knock in Spark Ignition (SI) engines, Obert (29) lists temperature, density, time and composition factors here quoted.

A. TEMPERATURE FACTORS. Increasing the temperature of the unburned mixture by any of the following factors will increase the possibility of knock in the SI engine:
   1. Raising the compression ratio . . .
      (a) Supercharging
   2. Raising the inlet air temperature
   3. Raising the coolant temperature
   4. Raising the temperatures of the cylinder and combustion-chamber walls
      (a) Opening the throttle (increasing the load)
   5. Advancing the spark timing . . .

B. DENSITY FACTORS. Increasing the density of the unburned mixture by any of the following will increase the possibility of knock in the SI engine:
   1. Opening the throttle (increasing the load)
   2. Supercharging the engine
      (a) Raising the compression ratio
   3. Advancing the spark timing

C. TIME FACTORS. Increasing the time of exposure of the unburned mixture to autoigniting conditions by any of the following factors will increase the possibility of knock in the SI engine:
   1. Increasing the distance the flame has to travel in order to traverse the combustion chamber
   2. Decreasing the turbulence of the mixture and thus decreasing the speed of the flame . . .
   3. Decreasing the speed of the engine, thus
      (a) decreasing the turbulence of the mixture . . .
      (b) increasing the time available for preflame reactions . . .

D. COMPOSITION. The properties of the fuel and the fuel-air ratio are the primary means for controlling knock, once the compression ratio and engine dimensions are selected. The probability of knock is decreased by
   1. Increasing the octane rating of the fuel . . .
   2. Either rich or lean mixtures . . .
   3. Stratifying the mixture so that the end gas is less reactive
   4. Increasing the humidity of the entering air

ENGINE PERFORMANCE MODELLING

No attempt is made in this study to either predict the occurrence of detonation or to model its effects on engine performance. It is assumed that detonation-free operation prevails at all times.

In justification of this assumption, the flight test experience of Reference 16 is invoked. In those experiments, fuel-air ratios, ignition timings and manifold pressures were employed which were beyond the domains of current General Aviation engine practice. The latter two resulted in the simultaneous occurrence of:

1. Advanced spark
2. High inlet manifold pressure
3. High inlet manifold temperature
4. Moderately high cylinder head temperature.

Each of these conditions is conducive to detonation. Nevertheless Chirivella (16) states that detonation was not observed:

> During the initial flights and at high power settings, detonation equipment was used to monitor the engine operation . . . It was soon realized that the techniques used to gather the experimental data were not detonation-limited. The detonation equipment was then removed from the aircraft.

The engine used in these experiments was a Lycoming TIO-541-E.

The absence of detonation in the flight tests of Reference 16 is probably largely attributable to the use of low fuel-air ratios in conjunction with items 1-4 above. Figure E.16, taken from Reference 15, shows how lean (as well as rich) fuel-air ratios in

the Curtiss-Wright TC18 Compound engine permitted higher air mass flow rates than would have been possible with a stoichiometric mixture, due to the shape of the detonation boundary. In general, detonation is most probable with fuel-air ratios in the vicinity of stoichiometric.

However, while spark advances from 20° BTDC (standard for the Lycoming TIO-541-E) to 35° BTDC were used in the flight tests of Reference 16, the spark advance for maximum torque (MBT timing) was not identified. Obert (29) states that "maximum power [torque] is obtained with the usual SI engine (and fuel) when the spark is adjusted to the point of audible knock." The use of MBT ignition timing thus commonly corresponds to the presence of some level of detonation. Some detonation may therefore have been encountered in the flight tests of Reference 16 had the spark been further advanced to MBT.

The assumption of MBT ignition timing in this work, with its attendant fuel economy advantages, is made in the knowledge that such an operational mode may approach an autoignition condition.

NOMENCLATURE

APA	Airframe-Propeller-Atmosphere
b_t	Tailplane span, ft
b_w	Wing span, ft
BHP	Brake Horsepower
BMEP	Brake Mean Effective Pressure
BSFC	Brake Specific Fuel Consumption
c	Brake specific fuel consumption, lbm/BHP.hr
$\bar{c}$	Mean aerodynamic chord of the wing, ft
c'	Shaft specific fuel consumption, lbm/SHP.hr
C_D	Airframe power-off drag coefficient
$C_{D_{ON}}$	Airframe power-on drag coefficient
C_L	Airframe lift coefficient
C_P	Power coefficient
C_Q	Torque coefficient
C_R	Speed-Thrust coefficient
C_S	Speed-Power coefficient
C_T	Thrust coefficient
CAS	Calibrated Airspeed
CHT	Cylinder Head Temperature
d	Propeller diameter, ft
dh	Increment in center of gravity position h
D_{OFF}	Airframe drag (power-off), lbf

D_{OFF_c}	Corrected airframe drag, lbf
D_{ON}	Airframe drag (power-on), lbf
E	Number of engines, each driving one propeller
EGT	Exhaust Gas Temperature
f_{comp}	Compressibility correction factor
f_D	Slipstream interference factor
f_J	Propeller J-factor
F	Fuel-dry air mass ratio of fresh mixture entering the engine
F_c	Stoichiometric fuel-dry air mass ratio
g_0	Sea level gravitational acceleration, ft/sec^2
G	Transmission gear ratio
GA	General Aviation
h	Distance of the airplane center of gravity aft of the leading edge of the mean aerodynamic chord of the wing, fraction of $\bar{c}$. The quantity h_{ref} is a reference value of h.
h	Atmospheric mass ratio of water vapour/dry air (Chapter 5 and Appendix E only)
H	Geometric altitude above sea level in the standard atmosphere (=density altitude), ft
H_p	Pressure altitude, ft
IHP	Indicated Horsepower
ISA	International Standard Atmosphere
ISCPM	Integrated Subsystem Cruise Performance Model
ISFC	Indicated Specific Fuel Consumption
J	Propeller advance ratio
J_a	Propeller apparent advance ratio

L	Airframe lift, lbf
LHP	Lost Horsepower
$\dot{m}_a$	Air mass flow rate into each engine, lbm/hr
$\dot{m}_{a_c}$	Corrected air mass flow rate into each engine, lbm/hr
$\dot{m}_f$	Fuel mass flow rate into each engine, lbm/hr
$\dot{m}_{f_t}$	Total fuel mass flow rate to all engines, lbm/hr
M_f	Total fuel mass burned during a trip, lbm
M_T	Propeller helical tip Mach number
MAP	Inlet Manifold Absolute (static) Pressure
MBT	Minimum ignition advance for Best Torque
n	Propeller shaft speed, revolutions/second
n	Density Index
N	Propeller shaft speed, RPM
N_c	Commanded propeller shaft speed, RPM
N_E	Engine shaft speed, RPM
NACA	National Advisory Committee for Aeronautics
NASA	National Aeronautics and Space Administration
NEA	Naturally aspirated MBT ignition timing Engine-Atmosphere
NMBTE	Naturally aspirated MBT ignition timing Engine
OAT	Outside Air Temperature (=atmospheric ambient air temperature)
P_a	Installed propeller shaft power, ft lb/sec
P_{atmos}	Atmospheric ambient air absolute pressure, lbf/ft^2
P_{AUX}	Auxiliary equipment power consumed per engine, horsepower
P_{AUX_c}	Corrected auxiliary equipment power, horsepower

P_e	Exhaust absolute static back-pressure, inches Hg
P_E	Brake horsepower (BHP) per engine
P_m	Inlet manifold absolute static pressure, inches Hg
P_R	Airframe power required (power-off), horsepower
P_{R_c}	Corrected airframe power required (power-off), horsepower
$P_{R_{ON}}$	Airframe power required (power-on), horsepower
P_S	Propeller shaft power, horsepower
PCP	Peripheral Computational Package
POH	Pilot Operating Handbook
POHCPM	Pilot Operating Handbook Cruise Performance Model
Q_a	Installed propeller shaft torque (apparent torque), lb ft
Q_E	Engine brake torque, lb ft
Q_{E_c}	Corrected brake torque, lb ft
Q*	Kernel of Q_a, lb ft
R	Propeller tip radius, ft
R_a	Gas constant for dry air, ft.lbf/lbm.degree Kelvin
R*	Point Economy Function (≡Specific Range), ground nautical miles/lbm
RPM	Revolutions Per Minute
S	Airframe reference area = wing area, ft^2
S*	The kernel of R*c, knots/BHP
S^*_c	Corrected S*, knots/BHP

SI	Spark Ignition
T_{atmos}	Atmospheric ambient air temperature at pressure altitude H_p, degrees Kelvin.
T_m	Inlet manifold temperature, degrees Kelvin
T_p	Propulsive thrust, lbf
T_s	Atmospheric ambient air temperature at altitude H in the standard atmosphere, degrees Kelvin
TAS	True Airspeed
TEA	Turbocharged MBT ignition timing Engine-Atmosphere
TIT	Turbine Inlet Temperature
V	True airspeed, ft/sec
V_e	Equivalent airspeed, ft/sec
V_E	Equivalent airspeed, knots
V_G	Groundspeed, knots
V_T	True airspeed, knots
V_w	Geocentric true windspeed along track, knots
V_{w_c}	Corrected geocentric true windspeed along track, knots
W	Airplane gross weight, lbf
WOT	Wide Open Throttle
X	Corrected airspeed, knots
Y	Corrected propeller shaft speed, RPM
Z	Corrected Q*, lb ft
Z	Inlet valve Mach Index

α	Angle of attack, degrees
β	Propeller blade angle, degrees
β^*	Kernel of β, degrees
γ	Airplane flight path angle to horizontal, degrees
Δ	Denotes an increment
ε_p	Index for correcting volumetric efficiency for effects of engine pressure ratio
ε_t	Index for correcting volumetric efficiency for effects of inlet manifold temperature
ξ	Constant which describes the effect of airplane longitudinal center of gravity position on L/D_{ON}
η	Free propeller efficiency
η_a	Installed propeller efficiency
η_i	Indicated thermal efficiency
η_p	Propulsive efficiency
η_p^*	Kernel of η_p
η_t	Tailplane efficiency
η_v	Volumetric efficiency
ζ	Constant which describes the effect of airplane longitudinal center of gravity position on L/D_{OFF}
θ	Angular spacing of straight radial lines approximating the constant β lines in the $C_R^i:J^2$ plot, degrees
Λ	Auxiliary equipment power loading factor
ρ	Atmospheric air density, slugs/ft^3
ρ_0	Atmospheric air density at sea level in the standard atmosphere, slugs/ft^3
σ	Atmospheric air density ratio = ρ/ρ_0

τ	Ignition timing, crankshaft degrees before top dead center
τ_o	MBT ignition timing, crankshaft degrees before top dead center
ϕ	Equivalence ratio
ψ	Airplane heading, degrees True

REFERENCES

1. Durand, W. F., (Editor-in-Chief), Aerodynamic Theory, Vol. 4, Julius Springer, Berlin, 1935. (H. Glauert, "Airplane Propellers," pp. 169-360.)
2. Durand, W. F., (Editor-in-Chief), Aerodynamic Theory, Vol. 5, Julius Springer, Berlin, 1935. (L. V. Kerber, "Airplane Performance," pp. 223-341.)
3. Perkins, C. D. and Hage, R. E., Airplane Performance, Stability and Control, John Wiley & Sons, New York, 1949.
4. Von Mises, R., Theory of Flight, Dover, New York, 1959.
5. Diehl, W. S., Engineering Aerodynamics, The Ronald Press Company, New York, 1936.
6. Hemke, P. E., Elementary Applied Aerodynamics, Prentice Hall, New Jersey, 1956.
7. Dommasch, D. O., et. al., Airplane Aerodynamics, Pitman, London, 1961.
8. Dommasch, D. O., Elements of Propeller and Helicopter Aerodynamics, Pitman, New York, 1953.
9. Glauert, H., The Elements of Aerofoil and Airscrew Theory, Cambridge University Press, 1947.
10. Weick, F. E., Aircraft Propeller Design, McGraw Hill, New York, 1930.
11. Pye, D. R., The Internal Combustion Engine, Vol. 1, Principles, Oxford University Press, London: Humphrey Milford, 1937.
12. Pye, D. R., The Internal Combustion Engine, Vol. 2, The Aero-Engine, Oxford University Press, (Clarendon), 1934.

13. Taylor, C. F., The Internal Combustion Engine in Theory and Practice, Vol. 1, MIT Press, Cambridge, Mass., 1977.

14. Taylor, C. F., The Internal Combustion Engine in Theory and Practice, Vol. 2, MIT Press, Cambridge, Mass., 1977.

15. Curtiss-Wright Corporation (Wright Aeronautical Division), Wood-Ridge, New Jersey, "Basic Theory of Operation-Turbo Compound Engine," 1962.

16. Chirivella, J. E., "Ultralean Combustion in General Aviation Piston Engines," JPL Publication 79-75, Jet Propulsion Laboratory, Pasadena, CA, December 1979.

17. Donovan, A. F., et. al. (Editors), High Speed Aerodynamics and Jet Propulsion, Vol. 8, High Speed Problems of Aircraft and Experimental Methods, Princeton University Press, Princeton, 1961. (I. L. Ashkenas, "Methods of Performance Calculation at High Speed," pp. 3-56.)

18. NASA, USAF, U.S. WEATHER BUREAU, U.S. Standard Atmosphere, 1962, U.S. Government Printing Office, Washington, D.C., 1962.

19. Staley, C. W., "An In Flight Investigation of the Performance of a Simple Thrust Measuring Device for Propeller Driven Airplanes," Department of Mechanical and Aerospace Engineering, T-909, Princeton University, 1970.

20. Laitone, E. V., "Positive Tail Loads for Minimum Induced Drag of Subsonic Aircraft," Journal of Aircraft, Vol. 15, No. 12, 1978.

21. Hamilton Standard Propellers (United Aircraft Corporation), East Hartiord, Connecticut, "Hamilton Standard Method of Propeller Performance Calculation," 1941.

22. Private communication with Dr. J. David Kocurek, Group Engineer, Bell Helicopter, Fort Worth, Texas, October 1981.

23. Monts, Frank, "Energy Conservation in General Aviation Piston Powered Aircraft," First National Conference on Energy Conservation in General Aviation, Transportation Technology Department, Western Michigan University, October, 1977.

24. Bent, R. D. and McKinley, J. L., Aircraft Powerplants, Gregg Division, McGraw Hill, New York, 1978.

25. Avco Lycoming, Williamsport, Pennsylvania, "Horsepower Correction Factors and Operating Techniques for Engine Development and Calibration," Avco Lycoming Report No. 2268, Vol. 1 (Vol. 2), 1960 (1964).

26. Smith, P. H. and Morrison, J. C., The Scientific Design of Exhaust and Intake Systems, G. T. Foulis, Henley-on-Thames, Oxfordshire, 1971.

27. Rezy, B. J. et. al., "Concepts for Reducing Exhaust Emissions and Fuel Consumption of the Aircraft Piston Engine," SAE 790605, 1979.

28. Private communication with Mr. Frank Monts, Mooney Aircraft Corporation, Kerrville, Texas, November 1979.

29. Obert, E. F., Internal Combustion Engines and Air Pollution, Harper and Row, New York, 1973.

30. Woodward Governor Company, Aircraft Controls Division, Rockford, Illinois, "Single Lever Power Control," no date.

31. Woods, R. L., "A Study of Optimum Engine Scheduling and Its Application to Fluidic Fuel Injection", U.S. Army Materiel Command, Harry Diamond Laboratories, Washington, D. C., 1973.

32. Schmidt, F., The Internal Combustion Engine, Chapman and Hall, London, 1965.

33. Wylie Jr., C. R., Advanced Engineering Mathematics, McGraw Hill, New York, Third Edition (International Student Edition), 1966.

34. Wallace, F. J. et. al., "Variable Geometry Turbocharging-The Realistic Way Forward," SAE 810336, 1981.

35. Private communication with Mr. Bernard J. Rezy, Director (Advanced Engineering), Teledyne Continental Motors, Mobile, Alabama, July 1981.

36. Babister, A. W., Aircraft Stability and Control, Pergamon, New York, 1961.

37. Seckel, E., Stability and Control of Airplanes and Helicopters, Academic Press, New York, 1972.

38. Abbott, I. H. and Von Doenhoff, A. E., Theory of Wing Sections, Dover, New York, 1959.

39. Spreiter, J. R. and Sacks, A. H., "The Rolling Up of the Trailing Vortex Sheet and Its Effect on the Downwash Behind Wings," Journal of the Aeronautical Sciences, January 1951.

40. Wood, D. H., "Full Scale Tests of Metal Propellers at High Tip Speeds," NACA TR 375, 1931.

41. Durand, W. F., "Interaction Between Air Propellers and Airplane Structures", NACA TR 235, 1926.

42. Wallace, J. M. and Hobbs, P. V., Atmospheric Science--An Introductory Survey, Academic Press, New York, 1977.

43. Private communication with Mr. Allen Light, Vice President-Engineering, Avco Lycoming Williamsport Division, Pennsylvania, December 1980.

44. Powell, J. D., "Closed Loop Control of Spark Timing," Automotive Engine Control Workshop, Transportation Systems Center, DOT, Cambridge, Mass., July 1975.

45. Zeilinger, K., Beitrag zur Untersuchung der Schadstoff Emissionen eines Ottomotors unter besonderer Berücksichtigung des instationären Motorbetreibes, (Ph.D. Thesis) University of München, Germany, 1974.

* * * * * * * *

1. Report No.	2. Government Accession No.	3. Recipient's Catalog No.
NASA CR-172188		

4. Title and Subtitle	5. Report Date
A Fuel-Efficient Cruise Performance Model for General Aviation Piston Engine Airplanes	August 1983
	6. Performing Organization Code
7. Author(s)	8. Performing Organization Report No.
Richard C. H. Parkinson	1527-T
	10. Work Unit No.
9. Performing Organization Name and Address	
Princeton University Department of Mechanical and Aerospace Engineering Princeton, NJ	11. Contract or Grant No. NGL 31-001-252
	13. Type of Report and Period Covered
12. Sponsoring Agency Name and Address	Contractor Report
National Aeronautics & Space Administration Washington, DC 20546	14. Sponsoring Agency Code

15. Supplementary Notes
Langley Technical Monitor: William E. Howell
Final Report
Dissertation presented to Princeton University for Ph.D. degree.

16. Abstract: This report presents a fuel-efficient cruise performance model which facilitates maximizing the specific range of General Aviation airplanes powered by spark-ignition piston engines and propellers. Airplanes of fixed design only are considered. The uses and limitations of typical Pilot Operating Handbook cruise performance data, for constructing cruise performance models suitable for maximizing specific range, are first examined. These data are found to be inadequate for constructing such models. A new model of General Aviation piston-prop airplane cruise performance is then developed. This model consists of two subsystem models: the airframe-propeller-atmosphere subsystem model; and the engine-atmosphere subsystem model. The new model facilitates maximizing specific range; and by virtue of its implicity and low volume data storage requirements, appears suitable for airborne microprocessor implementation.

17. Key Words (Suggested by Author(s))
Aircraft propulsion
Aircraft propulsion controls
Aircraft propulsion modeling

18. Distribution Statement
Unclassified - Unlimited
Subject Category 07

19. Security Classif. (of this report)	20. Security Classif. (of this page)	21. No. of Pages	22. Price
Unclassified	Unclassified	398	A17

N-305 For sale by the National Technical Information Service, Springfield, Virginia 22161

End of Document